Exploring the Possibilities of Increasing Energy Density and Efficiency in Rechargeable Batteries

ARTICLE COLLECTION

Wiley Analytical Science

Sponsored by:

Ω Metrohm

Contents

COVER IMAGE © GETTY IMAGES

Introduction

Battery research is a rapidly expanding field of research due to the increasing demand for better, more efficient batteries that can provide power to a wide variety of applications. Research is being conducted on several different technologies such as nickel-metal hydride (NiMH), lithium-ion, lithium-polymer, and other types of rechargeable batteries. The focus of battery research is to improve the performance, safety, and longevity of existing battery technologies as well as to explore innovative technologies that could potentially revolutionize the way we store and use energy.

Battery research has focused heavily on energy density in recent years. A battery with a higher energy density can store more energy in a smaller space, making it lighter and more compact. For example, lithium-ion batteries have a much higher energy density than traditional lead-acid batteries which makes them ideal for a wider range of applications such as electric vehicles, where weight and size are important considerations.

In addition to developing new technologies, researchers are also investigating ways to increase the efficiency of existing technology, for example developing techniques to reduce the amount of energy lost during charging and discharging cycles.

This article collection begins with a study on Lithium-ion batteries (LIBs). LIBs with high energy density and safety under fast-charging conditions are highly desirable for electric vehicles. However, owing to the growth of lithium dendrites, increased temperature at high charging rates, and low specific capacity in commercially available anodes, they cannot meet the market demand. In a study by Choi et al. (2022), a one-pot electrochemical self-assembly approach has been developed for constructing hybrid electrodes composed of ultrafine Fe_3O_4 particles on reduced graphene oxide (Fe_3O_4@rGO) as anodes for LIBs.

Zhang, S. et al. (2021) report a bifunctional in situ formed poly(vinylene carbonate) (PVCA)-based buffer layer that is introduced between the LAGP electrolyte and the metallic Li anode to improve interface compatibility and the electrolyte stability. The improved interface contact between LAGP and electrodes and the enhanced stability of LAGP enable all-solid-state lithium metal batteries (ASSLMBs) with excellent electrochemical performance.

Next, Chen et al. (2021) reported an in situ quasi-solid-state polyether electrolyte (SPEE) with a nano-hierarchical design. Developing solid-state electrolytes with good compatibility for high-voltage cathodes and reliable operation of batteries over a wide temperature range are two bottleneck requirements for practical applications of solid-state metal batteries (SSMBs).

All-solid-state lithium batteries (ASSLBs) with polyethylene oxide (PEO)-based solid-state electrolytes generally suffer from severe capacity degradation and interface transfer obstacles during the charge/discharge process. The study by Zhang et al. (2022) provides a facile and economical strategy to solve the problem of the lithium-electrolyte interface.

Aqueous rechargeable batteries boast numerous advantages, such as safety, affordability, and environmental friendliness, but their low energy density limits their effectiveness. To get around this problem, researchers have focused on increasing the concentration of aqueous electrolytes. However, there is a physical solubility limit of 21-32 mol kg^{-1} (m). In a breakthrough study by Cai et al. (2021), a $ZnCl_2$/$ZnBr_2$/$Zn(OAc)_2$ aqueous electrolyte was found to have an unprecedented solubility of up to 75 m, surpassing the physical solubility threshold.

Redox flow batteries (RFB) are receiving wide attention as scalable energy-storage systems to address the intermittency issues of renewable energy sources. However, for widespread commercialization, the redox flow batteries should be economically viable and environmentally friendly. Zinc-based batteries are a good choice for energy storage devices because zinc is earth-abundant and zinc metal has a moderate specific capacity of 820 mA h g^{-1} and a high volumetric capacity of 5851 mA h cm^{-3}. Jeena et al. (2022) reported a zinc-iron (Zn-Fe) hybrid RFB employing Zn/Zn(II) and Fe(II)/Fe(III) redox couples as positive and negative redox systems, respectively, separated by a self-made anion exchange membrane (AEM).

Finally, supercapacitors are potential electrochemical energy storage devices (EESDs) that hold much promise because of their high-power density, long-term cycling stability, high-power attainment, low maintenance costs, and high stability. Ashraf et al. (2021) investigated the use of an asymmetric supercapacitor (HRG//m-WO$_3$ ASC) composed of highly reduced graphene oxide (HRG) as

the positive electrode material and monoclinic tungsten oxide (m-WO$_3$) nanoplates as the negative electrode.

Overall, energy density is an important factor in battery research, and researchers are continuing to develop new technologies and techniques to increase the energy density of existing batteries. This will allow for the development of lighter and more powerful batteries for a variety of applications.

Through the methods and applications presented in this article collection, we hope to educate researchers on new technologies and techniques to increase the energy density of batteries. For more information, we encourage you to visit Metrohm to learn more and explore options to enhance your research.

Róisín Murtagh, Editor
Wiley Analytical Science

References

Choi, W., Ha, J., Kim, Y. T., & Choi, J. (2022). Highly Stable Iron-and Carbon-Based Electrodes for Li-Ion Batteries: Negative Fading and Fast Charging within 12 Min. *ChemSusChem, 15*(19), e202201137. https://chemistry-europe.onlinelibrary.wiley.com/doi/10.1002/cssc.202201137

Zhang, S., Zeng, Z., Zhai, W., Hou, G., Chen, L., & Ci, L. (2021). Bifunctional in situ polymerized interface for stable LAGP-based lithium metal batteries. *Advanced Materials Interfaces, 8*(10), 2100072. https://doi.org/10.1002/admi.202100072

Chen, Y., Huo, F., Chen, S., Cai, W., & Zhang, S. (2021). In-built quasi-solid-state poly-ether electrolytes enabling stable cycling of high-voltage and wide-temperature Li metal batteries. *Advanced Functional Materials, 31*(36), 2102347. https://doi.org/10.1002/adfm.202102347

Zhang, L., Wang, Z., Zhou, H., Li, X., Liu, Q., Wang, P., & Yuan, A. (2022). Synergistic Coupling of Li6. 4La3Zr1. 4Ta0. 6O12 and Fluoroethylene Carbonate Boosts Electrochemical Performances of Poly (Ethylene Oxide)-Based All-Solid-State Lithium Batteries. *ChemElectroChem, 9*(17), e202200641. https://chemistry-europe.onlinelibrary.wiley.com/doi/10.1002/celc.202200641

Cai, S., Chu, X., Liu, C., Lai, H., Chen, H., Jiang, Y., ... & Gao, C. (2021). Water–Salt Oligomers Enable Supersoluble Electrolytes for High-Performance Aqueous Batteries. *Advanced Materials, 33*(13), 2007470. https://doi.org/10.1002/adma.202007470

Jeena, C. B., Elsa, P. J., Moly, P. P., Ambily, K. J., & Joy, V. T. (2022). A dendrite free Zn-Fe hybrid redox flow battery for renewable energy storage. *Energy Storage, 4*(1), e275. https://doi.org/10.1002/est2.275

Ashraf, M., Shah, S. S., Khan, I., Aziz, M. A., Ullah, N., Khan, M., ... & Tahir, M. N. (2021). A High-Performance Asymmetric Supercapacitor Based on Tungsten Oxide Nanoplates and Highly Reduced Graphene Oxide Electrodes. *Chemistry–A European Journal, 27*(23), 6973-6984. https://chemistry-europe.onlinelibrary.wiley.com/doi/10.1002/chem.202005156

ChemSusChem

Research Article
doi.org/10.1002/cssc.202201137

Chemistry
Europe
European Chemical
Societies Publishing

www.chemsuschem.org

Highly Stable Iron- and Carbon-Based Electrodes for Li-Ion Batteries: Negative Fading and Fast Charging within 12 Min

Wonyoung Choi,[a] Jaeyun Ha,[a] Yong-Tae Kim,*[a] and Jinsub Choi*[a]

Lithium-ion batteries (LIBs) with high energy density and safety under fast-charging conditions are highly desirable for electric vehicles. However, owing to the growth of Li dendrites, increased temperature at high charging rates, and low specific capacity in commercially available anodes, they cannot meet the market demand. In this study, a facile one-pot electro-chemical self-assembly approach has been developed for constructing hybrid electrodes composed of ultrafine Fe_3O_4 particles on reduced graphene oxide (Fe_3O_4@rGO) as anodes for LIBs. The rationally designed Fe_3O_4@rGO electrode containing 36 wt% rGO exhibits an increase in specific capacity as cycling progresses, owing to improvements in the active sites, electro-chemical kinetics, and catalytic behavior, leading to a high specific capacity of 833 mAh g^{-1} and outstanding cycling stability over 2000 cycles with a capacity loss of only 0.127% per cycle at 5 A g^{-1}, enabling the full charging of batteries within 12 min. Furthermore, the origin of this abnormal improvement in the specific capacity (called negative fading), which exceeds the theoretical capacity, is investigated. This study opens up new possibilities for the commercial feasibility of Fe_3O_4@rGO anodes in fast-charging LIBs.

Introduction

Since they were first commercialized by the Sony Corporation in 1991, rechargeable lithium-ion batteries (LIBs) have been widely used in portable electronic devices, owing to advantages including high energy density, long cycling life, absence of memory effects, and low environmental impact.[1–3] However, as the application of LIBs has expanded to power sources for energy storage systems (ESSs) and electric vehicles (EVs), the development of new anode materials for next-generation LIBs that meet the requirements of high power density, fast charging, and low cost has become important for overcoming the low consumer acceptance and market penetration of EVs.[4] In particular, to solve the problem of limited charging speed, one of the most crucial factors in the competition between EVs and conventional combustion engines, the US Department of Energy (DOE) proposed an interim goal called extreme fast charging (XFC), in which high-energy-density batteries (ca. 180 Wh kg^{-1}) can be fully charged within 15 min.[4–6] Graphite is currently used as an anode in commercial LIBs because of its high stability, durability, and low cost; however, it has a low specific capacity (372 mAh g^{-1}) and slow charge–discharge process owing to its low diffusion coefficient and high expansion resistance.[7] In addition, there is a safety concern associated with the formation of Li dendrites, which grow quickly while charging at high charging rates owing to the low lithiation potential of graphite (ca. 0.1 V vs. Li/Li$^+$).[8,9] Furthermore, high charging rates increase the temperature inside battery cells, forming a thick solid–electrolyte interphase (SEI) film and deforming the battery pack, thereby adversely affecting the electrochemical performance of LIBs.[10,11]

Magnetite (Fe_3O_4) is a promising alternative candidate owing to its higher potential than graphite, which reduces safety concerns at high charging rates and its ability to store up to eight Li$^+$ ions per formula unit, leading to a high theoretical specific capacity of 924 mAh g^{-1}.[12] Nevertheless, the application of Fe_3O_4 anode material in practical LIBs suffers from low conductivity and large volume changes during the charging/discharging process, resulting in pulverization and aggregation of the electrode with poor cycling stability.[13,14] One of the most promising strategies to overcome these drawbacks is to design nanosized Fe_3O_4 particles combined with different forms of carbon materials with high electronic conductivity and high surface area to improve electrochemical kinetics by effectively shortening Li diffusion pathways and enhancing mechanical integrity.[15–19] In particular, graphene, which has excellent electronic conductivity and outstanding mechanical flexibility, is an ideal substrate for anchoring nanosized Fe_3O_4, contributing to fast electronic transport and increased electrical contact area between the electrode and electrolyte.[20,21]

Several studies have been conducted to achieve a capacity close to the theoretical value by adjusting the morphology and crystallinity of electrode materials.[22–24] However, in certain circumstances, mainly in transition metal oxide anodes, the anomalous behavior of the capacity increases beyond the theoretical capacity of the material itself, which occurs as cycling progresses. Contrary to the expected loss of capacity due to fatigue, the origin of this abnormal cycling-induced capacity increase, termed negative fading, remains controversial because of integrated circumstance originated by structural

[a] W. Choi, J. Ha, Dr. Y.-T. Kim, Prof. Dr. J. Choi
Department of Chemistry and Chemical Engineering
Inha University, 22212 Incheon (Republic of Korea)
E-mail: yongtaekim@inha.ac.kr
jinsub@inha.ac.kr

ChemSusChem

Research Article
doi.org/10.1002/cssc.202201137

**Chemistry
Europe**
European Chemical
Societies Publishing

reorganization, reoxidation of active material, and surface layer related reaction at the interfaces.[25,26] In general, because negative fading is significantly influenced by the structural morphology of the electrode and the catalytic activity of metals formed from metal oxides during cycling, preparing metal oxide@carbon composites is an effective approach for maximizing the electrode/electrolyte contact area and preventing the agglomeration of metal oxide nanoparticles. Su et al. prepared Fe_3O_4-graphene nanocomposites by hydrothermal method. They show that graphene sheets effectively prevent the aggregation of Fe_3O_4 nanoparticles, guaranteeing the fast electron transfer. Also, the Fe_3O_4 on the graphene sheets prevent the restacking of graphene sheets, resulting in loss of active surface site.[27] In addition. Jing et al. suggest a one-step high temperature solvothermal process to prepare Fe_3O_4/Graphene composites, and the prepared Fe_3O_4/Graphene composites deliver a capacity of 907 mAh g^{-1} at 0.1 C after 65 cycles.[28] Luo et al. employ the electrode consisted of mesoporous nanostructure Fe_3O_4 on three-dimensional graphene foam with excellent cycling stability. The hybrid electrode delivers a capacity of 870 mAh g^{-1} at 500 cycles at 1 C. Also, they demonstrate the possibility of full charge within 1 min, showing a capacity of 190 mAh g^{-1} at 60 C.[29]

Inspired by the above, we designed and fabricated ultrafine Fe_3O_4 particles (20–30 nm in size) uniformly arranged on reduced graphene oxide (rGO) sheets (Fe_3O_4@rGO) via a one-spot electrochemically assisted self-assembly method under ambient conditions. The mild strategy allowed further reduction of rGO, which corresponds to the additional oxidation of Fe_3O_4 particles, resulting in increased electrical conductivity of the electrode. The rationally designed Fe_3O_4@rGO electrode containing 36 wt% rGO serving as a highly conductive network exhibited an excellent reversible capacity of 833 mAh g^{-1} with outstanding long-term stability at 5 A g^{-1} for 2000 cycles and 301 mAh g^{-1} even at 20 A g^{-1}, which is comparable to that of commercial graphite. In addition, the origin of the anomalous cycling-induced capacity increase is discussed from the viewpoint of the increased surface area, which is caused by pulverization during repeated cycling, amorphization providing multiple channels for the transport of Li$^+$, and the catalytic behavior of Fe atoms generated from Fe_3O_4 during cycling.
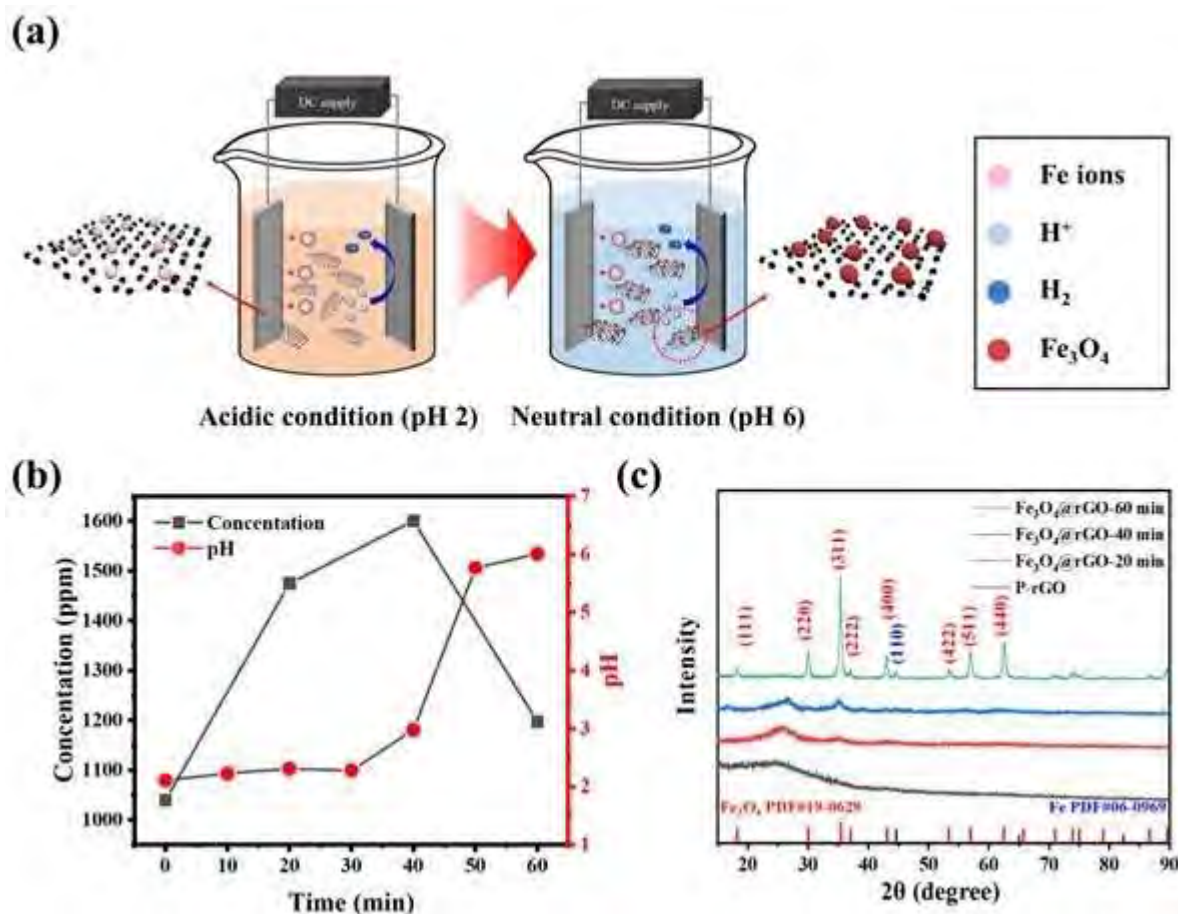
Results and Discussion

Synthesis and physical characterization

Nanostructured Fe_3O_4-carbon composites can be prepared through diverse approaches, including hydrothermal treatment, spray pyrolysis, and chemical vapor deposition (CVD).[15–19] In this study, Fe_3O_4@rGO was prepared using a straightforward one-step electrochemical method under ambient conditions. As shown in Figure 1a, Fe ions were eluted from Fe foil into aqueous rGO solution at a constant current density of 25 mA cm^{-2}, which induced a relatively low corresponding voltage of approximately 10 V, owing to the presence of chloride ions. The Fe ions introduced in the aqueous rGO

solution self-assembled with a uniform distribution on the rGO sheets with a negative zeta potential via electrophoretic interactions (see the Supporting Information, Table S1). However, the biased negative potential leads to a severe hydrogen evolution reaction at the counter electrode. Thus, when the reaction approached the endpoint after approximately 40 min, the pH of the rGO aqueous solution increased from acidic to neutral (Figure S1). The concentration of Fe ions, measured by ICP-OES (Figure 1b), rapidly decreased owing to the consumption of Fe_3O_4 on the surface of rGO sheets when the pH of the aqueous rGO solution was changed from acidic to neutral, which can be ascribed to the low solubility of Fe_3O_4 in the neutral solution. Owing to the synergetic effect of supersaturated Fe ions inducing a short burst of nucleation and homogeneous distribution of Fe ions on the rGO sheets, ultrafine spherical Fe_3O_4 nanoparticles (20–30 nm in size) with a large degree of mesoporosity and a wide pore size distribution were uniformly formed on the entire surface of the rGO sheets without any agglomeration, whereas there were severe agglomerations of Fe_3O_4 particles formed without adding rGO to the solution (Figure S2a–c). Surface area of samples was evaluated by N$_2$ adsorption-desorption isotherm plots. The Brunauer–Emmett–Teller (BET) surface area of Fe_3O_4@rGO (148.1 m^2 g^{-1}) is much larger than that of the Fe_3O_4 (39.1 m^2 g^{-1}; Figure S2d and e).

The effect of rGO on the morphology of Fe_3O_4@rGO was investigated by adjusting the amount of rGO in solution. Herein, the samples of rGO powder with 35, 50, 65, and 80 mg in 200 ml DI water are denoted as Fe_3O_4@rGO-35, Fe_3O_4@rGO-50, Fe_3O_4@rGO-65, and Fe_3O_4@rGO-80, respectively. As the amount of rGO increased, the density of the formed Fe_3O_4 nanoparticles decreased because of the increased surface area of the rGO sheets (Figure S3). Thermogravimetric analysis (TGA) under an air atmosphere was used to estimate the Fe_3O_4 content of the various samples (Figure S4). The weight loss observed from 500 to 700 °C can be ascribed to the decomposition of carbonaceous content to form carbon dioxide and the simultaneous conversion of Fe_3O_4 to Fe_2O_3[30,31] Therefore, the Fe_3O_4 content in the obtained samples calculated from the weight of Fe_2O_3, which is the final product after heat treatment, were 76.24, 67.37.6, 64.18, and 54.98% for Fe_3O_4@rGO-35, Fe_3O_4@rGO-50, Fe_3O_4@rGO-65, and Fe_3O_4@rGO-80, respectively.

The XRD patterns in Figure 1c show the crystal structure of Fe_3O_4@rGO-65 obtained at a constant current density of 25 mA cm^{-2} at different times. For pristine rGO (P-rGO), a typical broad diffraction peak is observed at 25.6°, corresponding to the (002) plane of a few-layered rGO sheet. After 20 and 40 min, there were no significant changes in the peaks, except for a small peak at 35.5° which corresponds to Fe_3O_4 (311), indicating that the formation of Fe_3O_4 nanoparticles started after 40 min. However, for Fe_3O_4@rGO-65 after 60 min, distinct peaks corresponding to Fe_3O_4 (JCPDS No. 19-0629) and Fe (JCPDS NO.06-0696) appeared. This demonstrates that Fe_3O_4 nanoparticles were effectively formed after 40 min as the pH changed from acidic to neutral. In addition, because the nanoparticles formed on the surface of rGO can prevent the restacking of the graphene sheets, the diffraction peak at 25.6°

ChemSusChem

Research Article
doi.org/10.1002/cssc.202201137

Chemistry Europe
European Chemical
Societies Publishing

Figure 1. (a) Schematic representation of the one-step electrochemical preparation of ultrafine Fe_3O_4 nanoparticles on rGO sheets. (b) Correlation between Fe ion concentration and pH change according to the electrochemical elution of Fe. (c) XRD analysis of P–rGO and Fe_3O_4@rGO-65 obtained at a constant current density for different times.

detected in the stacked RGO sheets disappeared in the XRD pattern of Fe_3O_4@rGO-65 after 60 min. The mean crystallite size (D) of the Fe_3O_4 nanoparticles was determined using the Debye–Scherrer equation [Eq. (1)]:[32–34]

$$D = K\lambda/\beta\cos\theta \tag{1}$$

where K is the shape factor (0.9), λ is the wavelength of employed X-rays (0.154 nm), β is the full width at half maximum of the diffraction peak, and θ is the diffraction angle from the XRD data. The mean crystalline size (D) of Fe_3O_4 was calculated to be around 205 Å on the (111) crystalline plane, indicating the formation of ultrafine Fe_3O_4 nanoparticles.

TEM analysis was performed to characterize the morphology and composition of Fe_3O_4@rGO-65. A representative TEM image of Fe_3O_4@rGO-65 obtained for a reaction time of 60 min (Figure 2a) demonstrates that Fe_3O_4 particles with an average size of approximately 25 nm were homogeneously distributed on the surface of the rGO sheets, which is in good agreement with the SEM and XRD results. Note that the voids between the nanoparticles act as electrolyte reservoirs,[17] promoting Li^+ diffusion by shortening the diffusion path[35] and effectively

accommodating volume expansion during cycling in the LIB.[17,36] The HR-TEM image (Figure 2b) shows lattice fringes with a d-spacing of 0.483 nm, corresponding to the (311) plane of Fe_3O_4, with a distinct rGO sheet serving as a substrate to anchor the Fe_3O_4 nanoparticles. Energy-dispersive X-ray spectroscopy (EDX) mapping results (Figure 2c) show the uniform atomic distribution of oxygen (36.72%), carbon (31.69%), and iron (31.58%) across the entire structure, implying uniform deposition and distribution of the Fe_3O_4 nanoparticles on the rGO sheets.

The electronic properties and chemical composition of Fe_3O_4@rGO-65 were characterized by Raman spectroscopy and XPS (Figure 3 and Figure S5). The Raman spectra (Figure 3a) present two dominant peaks corresponding to the D and G bands of graphene, respectively. The G band is related to the vibration of scattered E_{2g} phonons by sp^2-hybridized carbon, whereas the D band corresponds to the breathing mode of κ-point phonons of A_{1g} symmetry and defects associated with vacancies and grain boundaries.[37–39] The relative peak intensity for the D and G bands (I_D/I_G ratio), indicating the degree of defectiveness of rGO, increased from 1.26 for pristine rGO to 1.40 for Fe_3O_4@rGO-65, owing to the presence of defects caused
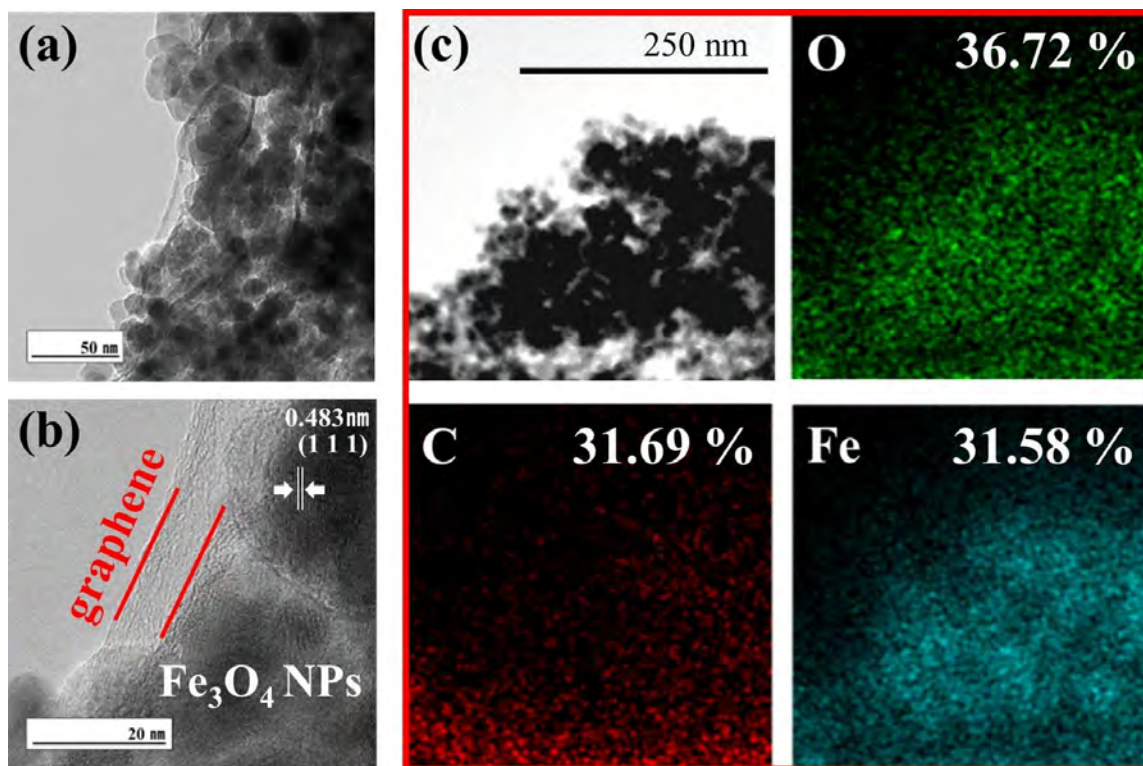
ChemSusChem

Research Article
doi.org/10.1002/cssc.202201137

**Chemistry
Europe**
European Chemical
Societies Publishing

Figure 2. (a) TEM and (b) HR–TEM images and (c) corresponding EDS elemental mapping of Fe_3O_4@rGO-65.

by the incorporation of Fe_3O_4 nanoparticles. Note that the red-shifted G-band for Fe_3O_4@rGO-65 to 1583 cm^{-1} compared to the G-band of pristine rGO (1595 cm^{-1}) indicates the removal of oxygen-functional groups,[40,41] resulting from the partial reduction of rGO with better electrical conductivity, which is accompanied by the oxidation of Fe_3O_4.

The reduction of rGO induced by the corresponding oxidation of Fe in the Fe_3O_4@rGO-65 composite, with high binding energy of an oxygen atom, was further verified by XPS analysis (Figure 3b–e).[42] In the high-resolution C1s XPS spectra of pristine rGO and Fe_3O_4@rGO-65 (Figure 3b), the shift of the deconvoluted peaks to lower binding energies in COOH, C—O, and C═O of Fe_3O_4@rGO suggests deoxygenation of rGO.[40,43,44] Meanwhile, in the high-resolution Fe2p XPS spectrum (Figure 3c–e and Figure S6), the Fe2p$_{3/2}$ (711.28 eV) and Fe2p$_{1/2}$ (724.94 eV) peaks of Fe_3O_4@rGO-65, corresponding to the magnetite phase, appeared at higher binding energies compared to Fe_3O_4 prepared without rGO, demonstrating additional oxidation of Fe_3O_4 on the rGO sheets. This is in good agreement with the relative area ratio (Fe^{3+}/Fe^{2+}) of Fe_3O_4@rGO-65, which was 1.96, whereas that of Fe_3O_4 was 1.64, indicating the conversion of Fe^{2+} to Fe^{3+} along with the reduction of rGO.[45,46] These results indicate that the spontaneous oxidation of Fe_3O_4 and the reduction of rGO are caused by potential differences in the intrinsic sp^2-hybridized carbon with an increase in electrical conductivity.[47,48]

Electrochemical performance

To investigate the Li storage mechanism, the electrochemical properties of Fe_3O_4@rGO in LIBs were measured in a half-cell (vs. Li/Li$^+$). Figure 4a shows the initial five CV curves under a scan rate of 0.1 mV s^{-1} at potential ranges from 0.01 to 3 V (vs. Li/Li$^+$) for Fe_3O_4@rGO-65 anode. From the first cathodic sweep, the peaks at 0.80 V are ascribed to the formation of Li$_x$Fe$_3$O$_4$ resulting from the insertion of Li$^+$ into the Fe_3O_4 lattice [Eq. (2)]:[49]

$$Fe_3O_4 + xLi^+ + xe^- \rightarrow Li_xFe_3O_4 \tag{2}$$
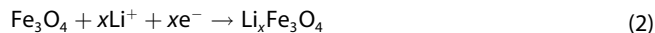
Another strong peak at 0.64 V is assigned to the reduction of Li$_x$Fe$_3$O$_4$ to Fe and the formation of SEI mainly composed of Li$_2$O according to Equation (3):[50–52]

$$(8-x)Li^+ + Li_xFe_3O_4 + (8-x)e^- \rightarrow 4Li_2O + 3Fe^0 \tag{3}$$
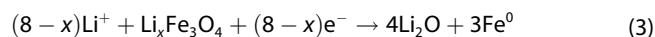
The sharp peak at approximately 0 V indicated the insertion of Li$^+$ into the rGO framework. The cathodic peak in the subsequent cycles was shifted to 0.76 V with a decreased intensity owing to the structural reconstruction and polarization of Fe_3O_4 nanoparticles after Li$^+$ insertion during the first cycle.[17] In the following anodic sweep, the peaks at 1.61 and 1.85 V are related to the oxidation of Fe to Fe^{2+} and Fe^{3+}, respectively.[53] After the first cycle, the CV curves overlapped
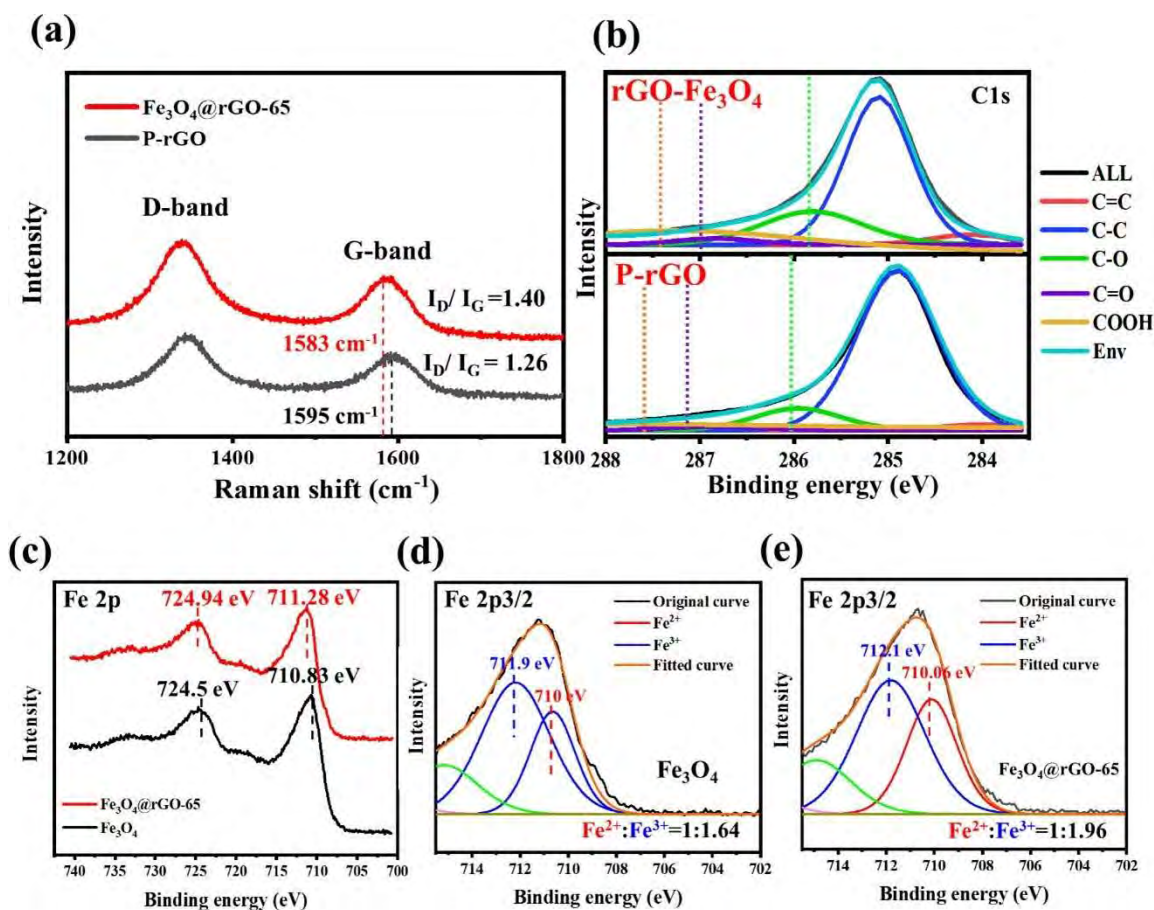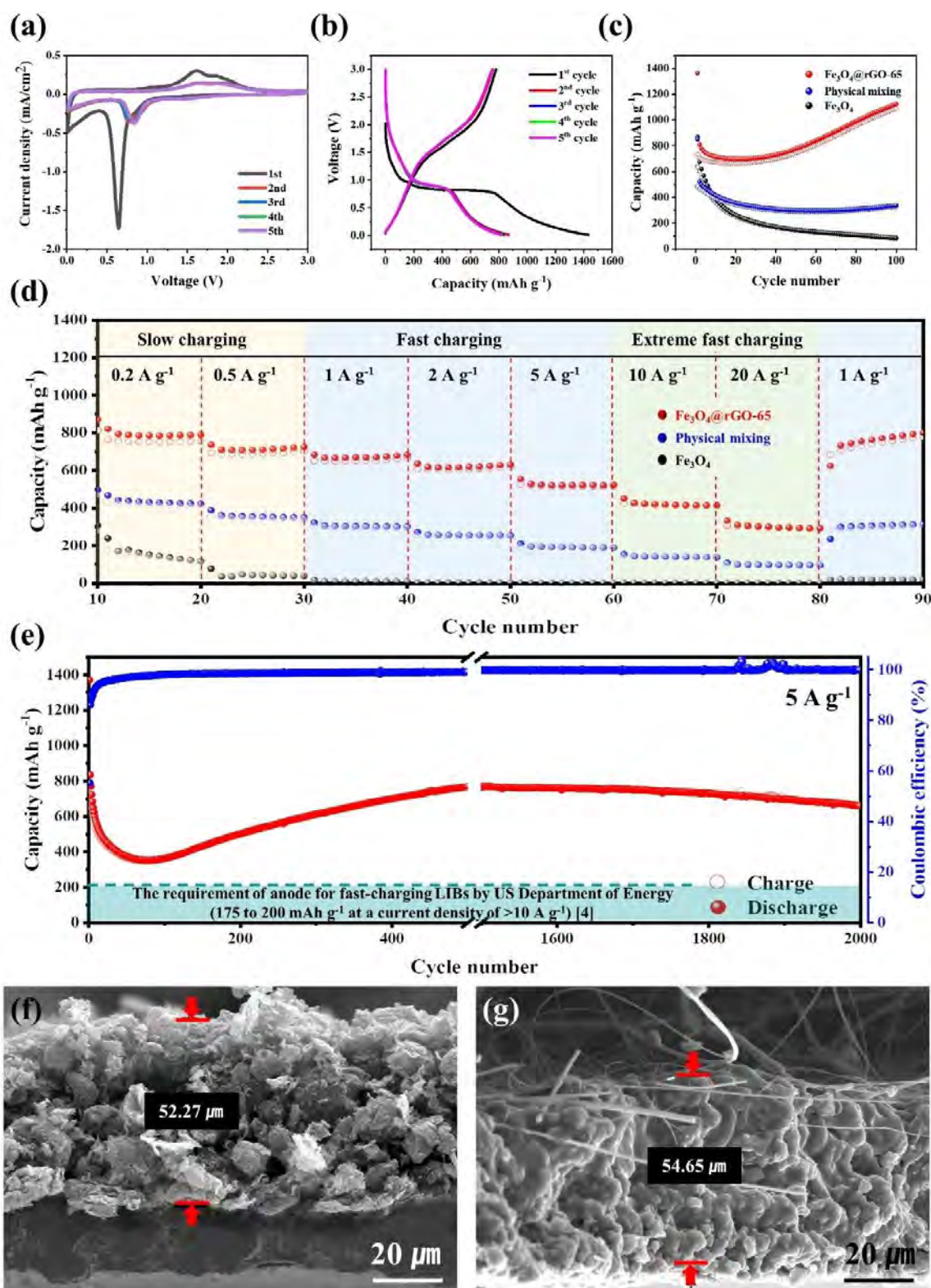
ChemSusChem

Research Article
doi.org/10.1002/cssc.202201137

Chemistry Europe
European Chemical
Societies Publishing

Figure 3. (a) Raman spectra and (b) C1s XPS analysis of P—rGO and Fe_3O_4@rGO-65. (c–e) Fe2p XPS spectra of Fe_3O_4@rGO-65.

well, demonstrating the good cycling reversibility of the Fe_3O_4@rGO-65 anode.

The initial five galvanostatic discharge–charge profiles of the Fe_3O_4@rGO-65 anode at a current density of $0.1\,A\,g^{-1}$, in which the plateaus are consistent with those of the CV curves, are shown in Figure 4b. The first discharge and charge capacities of the Fe_3O_4@rGO-65 anode were 1375 and $780\,mAh\,g^{-1}$, respectively, with a coulombic efficiency (CE) of 57%. The specific capacity loss in the initial cycle is attributed to irreversible Li^+ insertion into the rGO nanosheets and the formation of the SEI layer, which causes irreversible decomposition of the electrolyte. However, the CE rapidly increased and gradually stabilized at approximately 100% in subsequent cycles. To verify this superiority, the cycling performance of Fe_3O_4@rGO-65 was compared with two other conditions at a current density of $1\,A\,g^{-1}$: 1) Fe_3O_4 prepared without rGO and 2) physical mixing of Fe_3O_4 with rGO powder with identical proportions of Fe_3O_4 and rGO for the Fe_3O_4@rGO-65 anode. The Fe_3O_4@rGO-65 anode exhibited an extremely high specific capacity with a gradual increase, reaching a reversible discharge capacity of approximately $1100\,mAh\,g^{-1}$ after 100 cycles (Figure 4c). The electrodes obtained from Fe_3O_4 and the simple mixture showed a rapid decay of the specific capacity, followed by a plateau onwards with reversible discharge capacities of

roughly 90 and $310\,mAh\,g^{-1}$, respectively. The superior cycling stability of Fe_3O_4@rGO-65 is attributed to the flexible rGO with high conductivity and nanosized Fe_3O_4 particles uniformly distributed on the rGO sheets, which effectively accommodated the mechanical stress induced by the volume expansion during charge–discharge cycles, suppressing the pulverization of the electrode.[14,54]

The rate capability of Fe_3O_4@rGO-65 anode was evaluated at various current densities in the voltage range of 0.01–3 V (vs. Li/Li^+), ranging from 0.2 to $20\,A\,g^{-1}$ after the activation process at $0.1\,A\,g^{-1}$ for 10 cycles. Herein, $0.1\,A\,g^{-1}$ approximately corresponds to a rate of about 0.1 C.[55] The average reversible specific capacities of Fe_3O_4@rGO-65 at slow (0.2 and $0.5\,A\,g^{-1}$), fast (1, 2, and $5\,A\,g^{-1}$), and rapid charging (XFC, 10 and $20\,A\,g^{-1}$) were approximately 752, 688, 653, 604, 519, 416, 301 $mAh\,g^{-1}$, respectively (Figure 4d). After returning the rate from 20 to $1\,A\,g^{-1}$, the specific capacity recovered to $745\,mAh\,g^{-1}$, exhibiting good rate performance and excellent reversibility. The specific capacity at $1\,A\,g^{-1}$ after cycling up to $20\,A\,g^{-1}$ was slightly higher than that measured before cycling because of negative fading, which is discussed later. Fast charging for the commercialization of EV batteries is considered to be less than 15 min for fully charged batteries.[56] The high fast-charging capability of the Fe_3O_4@rGO-65 anode was tested at $5\,A\,g^{-1}$ (ca.

ChemSusChem

Research Article
doi.org/10.1002/cssc.202201137

Chemistry
Europe

European Chemical
Societies Publishing

Figure 4. Electrochemical properties of Fe$_3$O$_4$@rGO-65: (a) CV curves. (b) Galvanostatic charge–discharge profiles. (c–e) Comparison of electrochemical properties of Fe$_3$O$_4$@rGO-65 with Fe$_3$O$_4$ and physical mixture electrode: (c) Cycling performance at 1 A g^{-1}. (d) Rate performance from 0.2 to 20 A g^{-1}, returning to 1 A g^{-1}. (e) Long–term cycling stability of Fe$_3$O$_4$@rGO-65 at 5 A g^{-1} (fast–charging) for 2000 cycles. SEM images of Fe$_3$O$_4$@rGO-65 (f) before and (g) after 2000 cycles at 5 A g^{-1}.

ChemSusChem

Research Article
doi.org/10.1002/cssc.202201137

Chemistry
Europe
European Chemical
Societies Publishing

5 C) for 2000 cycles. After the specific capacity decreased during the initial 75 cycles and gradually increased in the subsequent cycles, owing to the formation of the SEI layer and negative fading, the Fe$_3$O$_4$@rGO-65 anode exhibited an excellent fast-charging capacity of 833 mAh g^{-1} at the 700th cycle and outstanding long-term stability with only 0.179% capacity loss per cycle at 5 A g^{-1} (ca. 5 C) for 2000 cycles (Figure 4e). The rate capability and long-term stability of the Fe$_3$O$_4$@rGO-65 anode were compared to those of previously reported fast-charging anodes (Tables S2 and S3). Thus, Fe$_3$O$_4$@rGO-65 met the near-term target for XFC from the USABC for the 2023 calendar year with the goal of ⊿80% state of charge (SOC) in 15 min.[6] SEM images of Fe$_3$O$_4$@rGO-65 before and after 2000 cycles at 5 A g^{-1} are shown in Figure 4f and 4 g, respectively. The thickness of the electrode increased by 4.55% from 52.27 to 54.65 μm without the formation of visible Li dendrites, demonstrating that Fe$_3$O$_4$@rGO-65 is commercially feasible and safe. Fast-charging and high-energy density LIBs, as well as efficient alleviation of the volume change during cycling without loss of the active material, were caused by pulverization.

Capacity increase of Fe$_3$O$_4$@rGO by negative fading

To further investigate the electrochemical performance of the Fe$_3$O$_4$@rGO anodes containing different amounts of rGO, the cycling performances of various electrodes (Fe$_3$O$_4$, Fe$_3$O$_4$@rGO-35, Fe$_3$O$_4$@rGO-50, Fe$_3$O$_4$@rGO-65, and Fe$_3$O$_4$@rGO-80) at a current density of 1 A g^{-1} were characterized for 300 cycles (Figure 5a). For the Fe$_3$O$_4$ and Fe$_3$O$_4$@rGO-35 anodes, the specific capacity decreased quickly in the initial cycles and then stabilized at low specific capacities of approximately 54 and 262 mAh g^{-1}, respectively. This can be ascribed to the formation of dense Fe$_3$O$_4$ particles, which leads to pulverization of the electrode, resulting from severe volume expansion during cycling. However, the Fe$_3$O$_4$@rGO-50, Fe$_3$O$_4$@rGO-65, and Fe$_3$O$_4$@rGO-80 electrodes delivered improved capacities of approximately 1096, 1346, and 1593 mAh g^{-1}, respectively, at the 200th cycle with a stable cycling performance over 300 cycles, showing that the capacity slightly decreased during the initial few cycles and gradually improved in subsequent cycles. The Fe$_3$O$_4$@rGO-65 anode showed the highest specific capacity because of the optimized amount of rGO sheets that can stabilize the Fe$_3$O$_4$ nanoparticles to avoid aggregation and pulverization during repeated charge–discharge processes while enhancing the conductivity of the electrode material to accelerate the electrochemical kinetics.[57]

Notably, as the cycling proceeds, there is an abnormal improvement in the specific capacity, called negative fading, which exceeds the theoretical value of Fe$_3$O$_4$ (924 mAh g^{-1}) based on conventional conversion reactions.[12] To elucidate the lithium storage mechanism and diffusion kinetics, which lead to momentous negative fading through electrode activation, the CV of Fe$_3$O$_4$@rGO-65 was measured at different charge–discharge cycles at 1 A g^{-1}. The intensity of the anodic peak (i_{pa}) at about 1.75 V and the internal area of the curve gradually increase as a function of the number of cycles (Figure 5b),

suggesting a progressive increase in the active surface area (A) and/or diffusion coefficient (D). This can be explained by the Randles–Sevcik equation [Eq. (4)]:

$$i_{pa} = (2.69 \times 10^5) n^{3/2} A C D^{1/2} \nu^{1/2} \quad (4)$$

where n is the electron stoichiometry during the redox reaction (constant), A is the active surface area of the electrode, C is the concentration of the diffusion species regarded as a constant because of the excess solid lithium counter electrode, D is the diffusion coefficient of Li$^+$, and ν is the scan rate.[58–60]
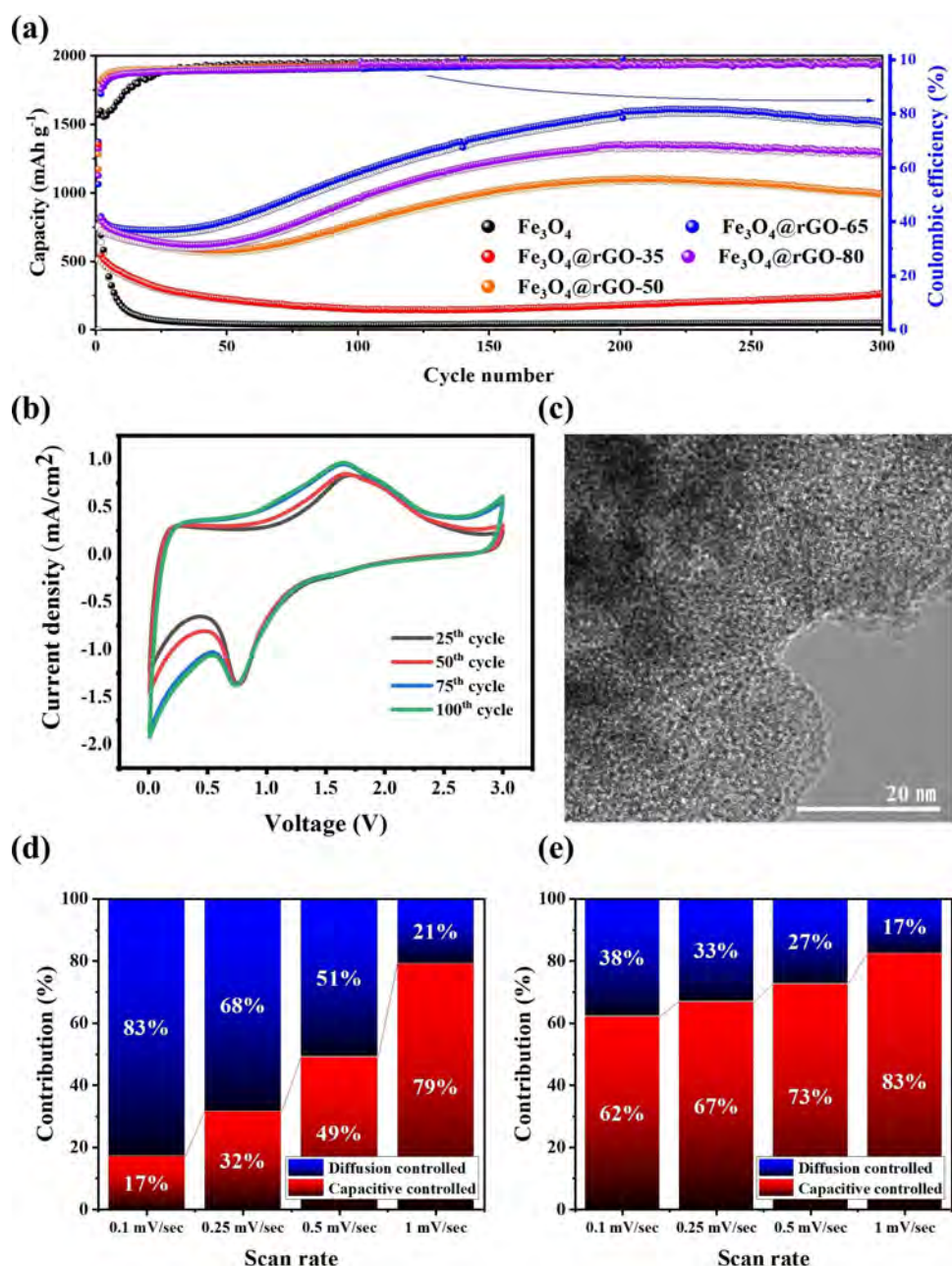
To better understand the origin of the negative fading due to surface area enlargement and fast diffusion coefficient, TEM analysis was performed. The particle size of Fe$_3$O$_4$ significantly decreased from approximately 25 nm to a few nanometers (Figure 5c), owing to pulverization, which occurred because of the mechanical stress caused by volume expansion during repeated charge–discharge while maintaining their adhesion to rGO sheets. As the size of the domains decreased, the spacing between the nanoparticles loosened, and the electrode changed into a porous structure with a larger surface area, resulting in the formation of new electrochemically active sites where Li$^+$ can be stored, shortening the path for the diffusion of Li$^+$ with enhanced charge transfer kinetics.

To verify the storage mechanism involved in the Fe$_3$O$_4$@rGO-65 anode, quantitative analysis was performed by separating the diffusion-controlled reaction and pseudocapacitive contribution by using Equation (5):

$$i(V) = k_1 \nu + k_2 \nu^{1/2} \quad (5)$$

where $i(V)$ is the response current of the potential at a diverse scan rate and k_1 and k_2 correspond to the proportions of pseudo-capacitance and diffusion behavior, respectively.[61–66] 62% of the total charge storage corresponded to the pseudocapacitive contribution at 0.1 mV s^{-1} after 200 cycles (Figure S7), which was higher than that after 50 cycles (17%). Additionally, the ratio of the pseudocapacitive contribution increases with the sweeping speed, and the contributions of the pseudocapacitance at 0.1, 0.25, 0.5, and 1 mV s^{-1} after 200 cycles are 62%, 67%, 73%, and 83%, respectively, which are higher than those after 50 cycles (Figure 5d). These results indicate that pseudocapacitive behavior is prominent in the Fe$_3$O$_4$@rGO-65 anode as the cycle progresses, which originates from structural amorphization into small domains with large interfaces within the cluster.

Amorphous materials are also advantageous in terms of electrochemical kinetics because of the absence of grain boundaries and the presence of percolation pathways that facilitate Li$^+$ diffusion.[67,68] The galvanostatic discharge–charge profiles of Fe$_3$O$_4$@rGO-65 (Figure 6a) indicate that the plateau disappeared as the cycles proceeded, converting the crystalline Fe$_3$O$_4$ to an amorphous state. The HR-TEM images before and after 100 cycles further confirmed the transition of the phase from crystalline to amorphous (Figure 6b,c). Thus, the charge–discharge induced amorphization of ultrafine Fe$_3$O$_4$ promotes the reversible conversion reaction of Equations (2) and (3) by

ChemSusChem

Research Article
doi.org/10.1002/cssc.202201137

**Chemistry
Europe**
European Chemical
Societies Publishing

Figure 5. (a) Cycling performance of the various electrodes (Fe_3O_4, Fe_3O_4@rGO-35, Fe_3O_4@rGO-50, Fe_3O_4@rGO-65, and Fe_3O_4@rGO-80) at a current density of 1 A g^{-1} for 300 cycles with negative fading. (b) CV curves of Fe_3O_4@rGO-65 after different cycles. (c) TEM image showing amorphization after 200 cycles. (c, d) Contribution ratio of the capacitive and diffusion–controlled capacities at various rates after (d) 50 cycles and (e) 200 cycles.

providing multiple channels for the transport of Li$^+$ and mitigating pulverization of the electrode, resulting in an elevated and stable specific capacity during long-term cycling.[69]

EIS was performed to provide further insight into the effective transport of electrons and Li$^+$, enhancing the reaction kinetics. In the Nyquist plot (Figure 6d), the semicircles in the high-frequency region are caused by the charge-transfer resistance (R_{ct}), indicating that the kinetics of the electrode decreased significantly after 100 cycles. Moreover, the diffusion

coefficient (D) of Li$^+$ was estimated from the Warburg region in the low-frequency region using the Equations (6) and (7):[70–72]

$$Z' = R_s + R_{ct} + \sigma\omega^{-1/2} \tag{6}$$

$$D = 0.5(RT/An^2F^2C\sigma)^2 \tag{7}$$

where R is the gas constant, D is the diffusion coefficient, T is the thermodynamic temperature, A is the electrode surface, n is the number of electrons, F is the Faraday constant, C is the concentration of Li$^+$, ω is the angular frequency in the low-

ChemSusChem

Research Article
doi.org/10.1002/cssc.202201137

**Chemistry
Europe**
European Chemical
Societies Publishing
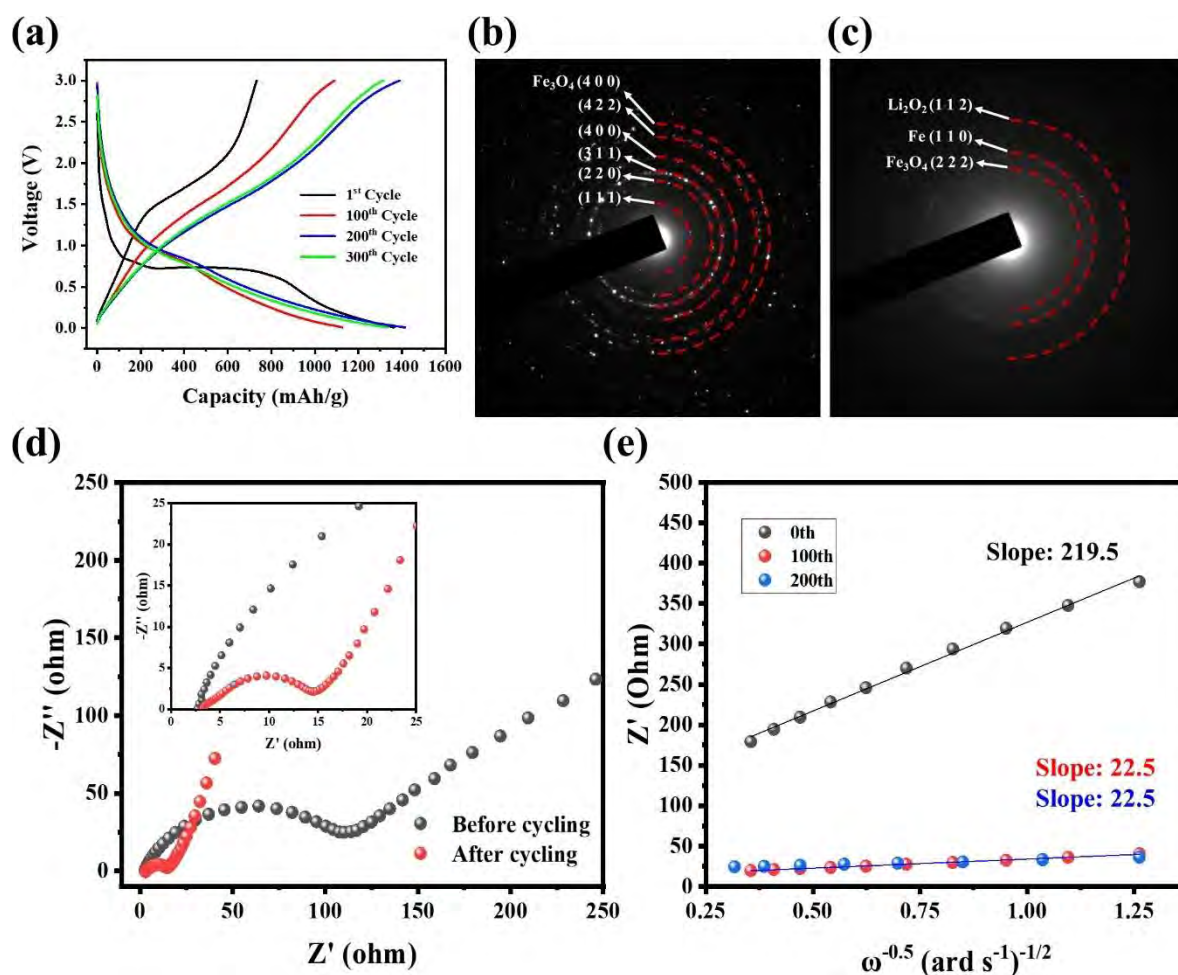
Figure 6. Electrochemical properties of Fe₃O₄@rGO-65: (a) Galvanostatic charge–discharge profiles after different cycling. (b, c) SAED patterns (b) before and (c) after cycling. (d) Nyquist plots before and after cycling. Inset shows the magnification view. (e) The curves of Z' plotted against $\omega^{-1/2}$ in the low-frequency region.

frequency region, and σ can be plotted as Z' *vs* $\omega^{-1/2}$. After cycling, the value of the Warburg impedance coefficient for Fe₃O₄@rGO-65 is 22.5 $\Omega\,cm^2\,s^{-0.5}$ (Figure 6e), which is ten times smaller than that before cycling (219.5 $\Omega\,cm^2\,s^{-0.5}$), providing an efficient transport pathway for electrons and Li⁺. The resistance values and diffusion coefficient are shown in Table S4, which was estimated using the equivalent circuit in Figure S8.

Another reason for the negative fading of the Fe₃O₄@rGO-65 anode could be partially ascribed to the catalytic properties of Fe. It is generated from Fe₃O₄, which enables reversible formation/decomposition of lithium oxide between Li₂O and Li₂O₂.[26,73] Most transition oxides used as anodes decompose into Li₂O and metals, which are usually regarded as inert for lithium storage. However, recent research has shown that metal nanoparticles generated from metal oxides during cycling serve as electrocatalysts for the reversible conversion of SEI components, resulting in extra capacity.[74,75] In Figure 5b, the reduction peak below 0.01 V and the corresponding oxidation peak around 2.8–3.0 V appeared prominently as the specific capacity increased after sufficient cycles because of the following

reaction in which the ultrafine Fe nanoparticles act as a catalyst [Eq. (8)].

$$2Li_2O \rightarrow Li_2O_2 + 2Li^+ + 2e^-, \ E = 2.87 \text{ V} \tag{8}$$
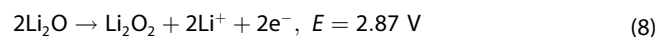
Therefore, it can be concluded that the ultrafine Fe₃O₄ nanoparticles uniformly anchored on rGO sheets result in a cycling-induced capacity increase (negative fading) through the catalytic reversible formation/decomposition of lithium oxide and the enhanced electrochemical kinetics caused by pulverization and amorphization, increasing the surface area and transport channels for electrons and Li⁺.

Conclusion

A facile one-spot electrochemical approach was used to construct a self-assembled ultrafine Fe₃O₄ network on rGO sheets as a promising anode material for high-energy density, fast-charging LIBs. Fe ions, which were eluted from the Fe foil at a constant current of 25 mA cm⁻², self-assembled on the rGO

ChemSusChem

Research Article
doi.org/10.1002/cssc.202201137

**Chemistry
Europe**

European Chemical
Societies Publishing

surface owing to electrostatic interactions. Fe_3O_4 nanoparticles with a size of 25 nm were formed when the pH of the aqueous rGO solution changed from acidic to neutral owing to severe hydrogen evolution at the counter electrode. During the formation of Fe_3O_4 nanoparticles, partial reduction of rGO was induced by the simultaneous oxidation of Fe_3O_4, restoring the intrinsic sp^2-hybridized carbon with enhanced electrical conductivity. The optimized Fe_3O_4@rGO-65 anode exhibited stable cycling properties with a high specific capacity owing to the synergy of the nanosized Fe_3O_4 nanoparticles anchored on flexible rGO with high conductivity, alleviating the volume change during cycling. In addition, a high specific capacity of 833 mAh g^{-1} was delivered at the 700th cycle at 5 A g^{-1}, which corresponds to charging within 12 min, and was maintained for 2000 cycles with a capacity loss of only 0.127% per cycle. Notably, a specific capacity of 301 mAh g^{-1}, comparable to that of a commercial graphite anode, was achieved at 20 A g^{-1}, which was fully charged in 3 min. As the cycles progressed, the Fe_3O_4 nanoparticles were pulverized to a size of a few nanometers while preserving their attachment to the rGO sheets and increasing the number of electrochemically active sites, thereby increasing the specific capacity. The amorphization of the electrode promotes the reversible conversion reaction by providing an efficient transport pathway for electrons and Li$^+$. Moreover, the catalytic ability of Fe atoms to reversibly convert Li_2O to Li_2O_2, generated from Fe_3O_4 during cycling, increases the specific capacity. This straightforward synthesis method can be applied to construct other transition-metal-based hybrid anodes, and will significantly enhance the commercialization of LIBs for fast-charging EVs.

Experimental Section

Electrochemical synthesis of Fe_3O_4@rGO

Before applying the electrochemical synthesis method, pure Fe foil (99.5%, Avention) was cut into dimensions of 1.5 cm × 1.5 cm and degreased in sequence with acetone and ethanol by ultrasonication for 5 min. The electrolyte was prepared by mixing 0.55 g of $FeCl_3$ (97%, Sigma-Aldrich) with different amounts of pristine rGO powder (Digichem Co.) in 200 mL of deionized (DI) water through ultrasonication for 60 min. Fe_3O_4@rGO was electrochemically prepared by applying a constant current density of 25 mA cm^{-2} using a two-electrode system composed of cleaned Fe pieces as the working and counter electrodes under ultrasonication for 60 min. Thereafter, the produced Fe_3O_4@rGO powder was washed separately several times with DI water via centrifugation and then obtained through vacuum-assisted filtration using a polytetrafluoroethylene (PTFE) filter membrane with a 0.2 μm pore size. The resulting Fe_3O_4@rGO powder was dried and stored in a vacuum oven at 40°C before its physical and electrochemical characteristics were analyzed. Pure Fe_3O_4 powder was prepared using an identical procedure without adding pristine rGO powder to the electrolyte to investigate the role of rGO in enhancing the electrochemical properties of Fe_3O_4@rGO as an anode material for LIBs.

Physical characterization

The morphological characteristics of the prepared samples were observed using field-emission scanning electron microscopy (FE-SEM, S-4300SE, Hitachi, Japan) at the Core Facility Center for Sustainable Energy Materials of Korea Basic Science Institute (KBSI) and field-emission transmission scanning electron microscopy (FE-TEM, JEM-2100F, JEOL, Japan) equipped with an energy-dispersive X-ray spectrometer (EDS). The crystalline structure and chemical state of the composite were analyzed using X-ray diffraction with a Cu Kα radiation source (λ = 1.54056 Å)(XRD, X'Pert Pro MRD, PANalytical, Netherlands), X-ray photoelectron spectroscopy using an Al Kα X-ray source (1486.6 eV) (XPS, K-Alpha, Thermo Fisher Scientific, USA), and Raman spectroscopy (LabRAM HR Evolution, HORIBA, Japan) with a 532 nm laser. A Brunauer-Emmett-Teller (BET) analyzer (3Flex, Micromeritics, USA), thermogravimetry and differential thermal analysis (TG/DTA, Seiko, Japan), and particle analyzer (ELS—Z, Otsuka, Japan) were used to measure the specific surface area, thermal stability, and zeta potential, respectively.

Electrochemical measurements

Electrochemical experiments were conducted using standard CR2032 coin-type cells with the prepared Fe_3O_4@rGO as the working electrode, a lithium disk as the counter and reference electrodes, and a glass fiber filter (GF/A, Whatman) as a separator soaked with a fixed amount of organic electrolyte composed of ethylene carbonate (EC) and diethyl carbonate (50:50, w/w) with dissolved 1 M LiPF$_6$ at 25°C. All half-cells were assembled or disassembled in an argon-filled glove box ($O_2 < 0.5$ ppm, $H_2O < 0.5$ ppm). The as-prepared powders were mixed with a conductive additive (carbon black) and polymer binder (polyvinylidene difluoride) in a weight ratio of 8:1:1 in N-methyl-2-pyrrolidone (NMP) to form a homogeneous slurry, which was then coated onto a Cu foil current collector. The average mass loading of the active materials on the electrode was 0.5 mg cm^{-2}.

The galvanostatic charge–discharge tests were performed on a battery cycling system (WBCS 3000, WonATech, South Korea) in the potential range of 0.01–3 V (vs. Li/Li$^+$) at several current rates ranging from 0.1 to 20 A g^{-1}. Cyclic voltammetry (CV) measurements were conducted on an electrochemical workstation (SP-150, Bio-Logic, Seyssinet–Pariset, France) in the potential range of 0.01–3 V (vs. Li/Li$^+$) at scan rates ranging from 0.1 to 1 mV s^{-1}. Electrochemical impedance spectroscopy (EIS) curves were obtained using an electrochemical workstation (PGSTAT302 N Autolab, Metrohm, Switzerland) in the frequency range of 0.1 Hz–100 kHz under an AC stimulus with an amplitude of 5 mV.

Conflict of Interest

The authors declare no conflict of interest.

ChemSusChem

Research Article
doi.org/10.1002/cssc.202201137

Chemistry
Europe
European Chemical
Societies Publishing

Data Availability Statement

The data that support the findings of this study are available on request from the corresponding author. The data are not publicly available due to privacy or ethical restrictions.

[1] C. Yang, X. Zhang, J. Li, J. Ma, L. Xu, J. Yang, S. Liu, S. Fang, Y. Li, X. Sun, *Electrochim. Acta* **2020**, *346*, 136244.

[2] Y. S. Duh, X. Liu, X. Jiang, C. S. Kao, L. Gong, R. Shi, *J. Energy Storage* **2020**, *30*, 101422.

[3] S. Zhao, J. Quan, T. Wang, D. Song, J. Huang, W. He, G. Li, *Environ. Sci. Pollut. Res. Int.* **2021**, *29*, 9448.

[4] J. Ren, Z. Wang, P. Xu, C. Wang, F. Gao, D. Zhao, S. Liu, H. Yang, D. Wang, C. Niu, *Nano-Micro Lett.* **2022**, *14*, 5.

[5] Y. Liu, Y. Zhu, Y. Cui, *Nat. Energy* **2019**, *4*, 540.

[6] A. Masias, J. Marcicki, W. Paxton, *ACS Energy Lett.* **2021**, 321.

[7] S. Y. Hwang, H. R. Lee, Y. K. Lee, G. B. Lee, S. Lee, H. J. Kim, H. I. Joh, *Int. J. Energy Res.* **2021**, *45*, 4718.

[8] X. Liu, L. Yin, D. S. Ren, L. Wang, Y. Ren, W. Q. Xu, S. Lapidus, H. W. Wang, X. M. He, Z. H. Chen, G. L. Xu, M. G. Ouyang, K. Amine, *Nat. Commun.* **2021**, *12*, 4235.

[9] J. Ming, Z. Cao, W. Wahyudi, M. Li, P. Kumar, Y. Wu, J. Y. Hwang, M. N. Hedhili, L. Cavallo, Y. K. Sun, *ACS Energy Lett.* **2018**, *3*, 335.

[10] Y. Li, X. Feng, D. Ren, M. Ouyang, L. Lu, X. Han, *ACS Appl. Mater. Interfaces* **2019**, *11*, 46839.

[11] Y. Tian, C. Lin, H. Li, J. Du, R. Xiong, *Appl. Energy* **2021**, *300*, 117386.

[12] G. Chen, M. Zhou, J. Catanach, T. Liaw, L. Fei, S. Deng, H. Luo, *Nano Energy*. **2014**, *8* 126.

[13] L. Hou, L. Lian, L. Zhang, G. Pang, C. Yuan, X. Zhang, *Adv. Funct. Mater.* **2015**, *25*, 238.

[14] G. Zhou, D. W. Wang, F. Li, L. Zhang, N. Li, Z. S. Wu, L. Wen, G. Q. Lu, H. M. Cheng, *Chem. Mater.* **2010**, *22*, 5306.

[15] Y. Jiao, H. Zhang, T. Dong, P. Shen, Y. Cai, H. Zhang, S. Zhang, *J. Mater. Sci.* **2017**, *52*, 3233.

[16] K. Karthikeyan, D. Kalpana, S. Amaresh, Y. S. Lee, *RSC Adv.* **2012**, *2*, 12322–12328.

[17] L. Li, H. Wang, Z. Xie, C. An, G. Jiang, Y. Wang, *J. Alloys Compd.* **2020**, *815*, 152337.

[18] J. Z. Wang, C. Zhong, D. Wexler, N. H. Idris, Z. X. Wang, L. Q. Chen, H. K. Liu, *Chem. Eur. J.* **2011**, *17*, 661.

[19] W. Yang, Y. Zhong, C. He, S. Peng, Y. Yang, F. Qi, P. Feng, C. Shuai, *J. Adv. Res.* **2020**, *24*, 191.

[20] Y. Lu, L. Yu, X. W. D. Lou, *Chem* **2018**, *4*, 972.

[21] Y. Fang, X. Y. Yu, X. W. D. Lou, *Matter* **2019**, *1*, 90.

[22] H. Kim, W. Choi, J. Yoon, J. H. Um, W. Lee, J. Kim, J. Cabana, W. S. Yoon, *Chem. Rev.* **2020**, *120*, 6934.

[23] Y. Liu, J. Xue, T. Zheng, J. Dahn, *Carbon* **1996**, *34*, 193.

[24] S. Goriparti, E. Miele, F. De Angelis, E. Di Fabrizio, R. P. Zaccaria, C. Capiglia, *J. Power Sources* **2014**, *257*, 421.

[25] S. Laruelle, S. Grugeon, P. Poizot, M. Dolle, L. Dupont, J. Tarascon, *J. Electrochem. Soc.* **2002**, *149*, A627.

[26] L. Su, Y. Zhong, Z. Zhou, *J. Mater. Chem. A* **2013**, *1*, 15158.

[27] J. Su, M. Cao, L. Ren, C. Hu, *J. Phys. Chem. C* **2011**, *115*, 14469.

[28] L. Jing, A. Fu, H. Li, J. Liu, P. Guo, Y. Wang, X. Zhao, *RSC Adv.* **2014**, *4*, 59981.

[29] J. Luo, J. Liu, Z. Zeng, C. Ng, L. Ma, H. Zhang, J. Lin, Z. Shen, H. Fan, *Nano Lett.* **2013**, *13*, 6136.

[30] Y. Dong, R. Ma, M. Hu, H. Cheng, Q. Yang, Y. Y. Li, J. A. Zapien, *Phys. Chem. Chem. Phys.* **2013**, *15*, 7174.

[31] L. Qin, S. Liang, X. Tan, G. Yan, *Electrochemistry* **2017**, *85*, 397.

[32] S. Mustapha, M. Ndamitso, A. Abdulkareem, J. Tijani, D. Shuaib, A. Mohammed, A. Sumaila, *Adv. Nat. Sci. Nanosci. Nanotechnol.* **2019**, *10*, 045013.

[33] U. Holzwarth, N. Gibson, *Nat. Nanotechnol.* **2011**, *6*, 534.

[34] J. Hargreaves, *Catal. Struct. React.* **2016**, *2*, 33.

[35] J. Feng, S. Xiong, Y. Qian, L. Yin, *Electrochim. Acta* **2014**, *129*, 107.

[36] Y. Zhang, Y. Shi, X. C. Hu, W. P. Wang, R. Wen, S. Xin, Y. G. Guo, *Adv. Energy Mater.* **2020**, *10*, 1903325.

[37] S. Brown, A. Jorio, M. Dresselhaus, G. Dresselhaus, *Phys. Rev. B: Condens. Matter Mater. Phys.* **2001**, *64*, 073403.

[38] A. Guedes, B. Valentim, A. Prieto, S. Rodrigues, F. Noronha, *Int. J. Coal Geol.* **2010**, *83*, 415.

[39] M. J. Matthews, M. A. Pimenta, G. Dresselhaus, M. Dresselhaus, M. Endo, *Phys. Rev. B: Condens. Matter Mater. Phys.* **1999**, *59*, R6585.

[40] M. M. MacInnes, S. Hlynchuk, S. Acharya, N. Lehnert, S. Maldonado, *ACS Appl. Mater. Interfaces* **2017**, *10*, 2004.

[41] K. Krishnamoorthy, M. Veerapandian, K. Yun, S. J. Kim, *Carbon* **2013**, *53*, 38.

[42] J. C. Yoon, X. Dai, K. N. Kang, J. Hwang, M. J. Kwak, F. Ding, J. H. Jang, *ACS Nano* **2021**, *15*, 11655.

[43] T. Homola, J. Pospíšil, R. Krumpolec, P. Souček, P. Dzik, M. Weiter, M. Černák, *ChemSusChem* **2018**, *11*, 941.

[44] A. Ganguly, S. Sharma, P. Papakonstantinou, J. Hamilton, *J. Phys. Chem. C* **2011**, *115*, 17009.

[45] S. Majumder, M. Sardar, B. Satpati, S. Kumar, S. Banerjee, *J. Phys. Chem. C* **2018**, *122*, 21356.

[46] G. Chen, J. Peng, C. Song, F. Zeng, F. Pan, *J. Appl. Phys.* **2013**, *113*, 104503.

[47] S. Pei, H. M. Cheng, *Carbon* **2012**, *50*, 3210.

[48] C. K. Chua, M. Pumera, *Chem. Soc. Rev.* **2014**, *43*, 291.

[49] C. He, S. Wu, N. Zhao, C. Shi, E. Liu, J. Li, *ACS Nano* **2013**, *7*, 4459.

[50] B. B. Kopuklu, A. Tasdemir, S. A. Gursel, A. Yurum, *Carbon* **2021**, *174*, 158.

[51] F. X. Ma, H. B. Wu, C. Y. Xu, L. Zhen, X. W. D. Lou, *Nanoscale* **2015**, *7*, 4411.

[52] J. Luo, J. Liu, Z. Zeng, C. F. Ng, L. Ma, H. Zhang, J. Lin, Z. Shen, H. J. Fan, *Nano Lett.* **2013**, *13*, 6136.

[53] J. Mao, D. Niu, N. Zheng, G. Jiang, W. Zhao, J. Shi, Y. Li, *Chem. Eng.* **2019**, *7*, 3424.

[54] L. Yang, J. Hu, A. Dong, D. Yang, *Electrochim. Acta* **2014**, *144*, 235.

[55] E. Kang, Y. S. Jung, A. S. Cavanagh, G. H. Kim, S. M. George, A. C. Dillon, J. K. Kim, J. Lee, *Adv. Funct. Mater.* **2011**, *21*, 2430.

[56] Y. Huang, H. Yang, Y. Zhang, Y. Zhang, Y. Wu, M. Tian, P. Chen, R. Trout, Y. Ma, T. H. Wu, *J. Mater. Chem. A* **2019**, *7*, 11250.

[57] X. Lu, D. Liu, T. Han, M. Zhu, S. O. Ryu, J. Huang, *J. Alloys Compd.* **2018**, *765*, 1061.

[58] Y. Liu, J. Xu, X. Qin, H. Xin, X. Yuan, J. Zhang, D. Li, C. Song, *J. Mater. Chem. A* **2015**, *3*, 9682.

[59] D. Li, L. Dai, X. Ren, F. Ji, Q. Sun, Y. Zhang, L. Ci, *Energy Environ. Sci.* **2021**, *14*, 424.

[60] K. Ahmad, P. Kumar, S. M. Mobin, *Nanoscale Adv.* **2020**, *2*, 502.

[61] J. Li, S. Hwang, F. M. Guo, S. Li, Z. W. Chen, R. H. Kou, K. Sun, C. J. Sun, H. Gan, A. P. Yu, E. A. Stach, H. Zhou, D. Su, *Nat. Commun.* **2019**, *10*, 2224.

[62] V. Augustyn, P. Simon, B. Dunn, *Energy Environ. Sci.* **2014**, *7*, 1597.

[63] J. Wang, J. Polleux, J. Lim, B. Dunn, *J. Phys. Chem. C* **2007**, *111*, 14925.

[64] T. Brezesinski, J. Wang, S. H. Tolbert, B. Dunn, *Nat. Mater.* **2010**, *9*, 146.

[65] Z. Zhao, X. Teng, Q. Xiong, H. Chi, Y. Yuan, H. Qin, Z. Ji, *Sustain. Mater. Technol.* **2021**, *29*, e00313.

[66] Y. Xiang, Z. Yang, S. Wang, M. S. A. Hossain, J. Yu, N. A. Kumar, Y. Yamauchi, *Nanoscale* **2018**, *10*, 18010.

[67] Y. Jiang, D. Zhang, Y. Li, T. Yuan, N. Bahlawane, C. Liang, W. Sun, Y. Lu, M. Yan, *Nano Energy* **2014**, *4*, 23.

[68] H. Xiong, M. D. Slater, M. Balasubramanian, C. S. Johnson, T. Rajh, *J. Phys. Chem. Lett.* **2011**, *2*, 2560.

[69] Z. Huang, H. Gao, Z. Yang, W. Jiang, Q. Wang, S. Wang, J. Ju, Y. U. Kwon, Y. Zhao, *Mater. Des.* **2019**, *180*, 107973.

[70] B. Cong, Y. Hu, S. Sun, Y. Wang, B. Wang, H. Kong, G. Chen, *Nanoscale* **2020**, *12*, 16901.

[71] B. Kurc, M. Pigłowska, *J. Power Sources* **2021**, *485*, 229323.

[72] M. Reddy, R. Jose, A. Le Viet, K. I. Ozoemena, B. Chowdari, S. Ramakrishna, *Electrochim. Acta* **2014**, *128*, 198.

[73] Y. Huang, Z. Xu, J. Mai, T. K. Lau, X. Lu, Y. J. Hsu, Y. Chen, A. C. Lee, Y. Hou, Y. S. Meng, *Nano Energy* **2017**, *41*, 426.

[74] Y. Cheng, B. Chen, M. Zhu, L. Chang, D. Zhang, C. Wang, S. Wang, L. Wang, *Appl. Mater. Res.* **2021**, *25*, 101205.

[75] Y. Qiao, K. Jiang, H. Deng, H. Zhou, *Nat. Catal.* **2019**, *2*, 1035.

Bifunctional In Situ Polymerized Interface for Stable LAGP-Based Lithium Metal Batteries

Shengnan Zhang, Zhen Zeng, Wei Zhai, Guangmei Hou,* Lina Chen,* and Lijie Ci*

All-solid-state lithium metal batteries (ASSLMBs) have attracted intensive research attention since their incomparable energy density and the further advance of ASSLMBs is severely dependent on the development of solid electrolytes. Unfortunately, as one of the most studied solid electrolytes, the practical applications of (NASICON)-type $Li_{1.5}Al_{0.5}Ge_{0.5}P_3O_{12}$ (LAGP) electrolyte is hindered by not only its inferior interfacial contact with electrodes but also its undesirable instability toward Li metal anodes. In this work, a bifunctional in situ formed poly(vinylene carbonate) (PVCA)-based buffer layer is introduced between the LAGP electrolyte and the metallic Li anode to improve interface compatibility and the electrolyte stability. The improved interface contact between LAGP and electrodes and the enhanced stability of LAGP enable ASSLMBs with excellent electrochemical performance. The Li/LAGP/Li symmetric cell with the PVCA-based interlayer can maintain a low overpotential of 80 mV for 800 h at 0.05 mA cm^{-2}. Inspiringly, the as-assembled ASSLMBs with LiFePO$_4$ as the cathode also present excellent cyclic stability with a high initial discharge capacity of 150 mAh g^{-1} at 0.5 C and superior capacity retention of 96% after 200 cycles.

1. Introduction

Benefiting from the highest theoretical capacity (3860 mAh g^{-1}) and the lowest redox potential (−3.04 V vs standard hydrogen electrode), lithium metal is believed to be an ideal anode material for new rechargeable batteries.[1,2] However, several safety hazards, such as short-circuit, explosion, and low Coulombic efficiencies when working in liquid organic electrolyte hinder the practical application of Li metal seriously.[3–6] Recently, solid electrolytes (SEs) have gained extensive attention owing to some unattainable features in liquid organic electrolytes, including the nonflammable character and high mechanical strength, which makes SEs promising to solve the mentioned safety issues of Li metal.[7,8] As the key component in ASSLMBs, SEs are usually categorized into inorganic solid electrolytes, polymer solid electrolytes, and inorganic–polymer composite electrolytes. Benefiting from their outstanding room temperature ionic conductivity (>10^{-4} S cm^{-1}), high shear modulus, and high Li-ion transference numbers (≈1), inorganic solid electrolytes (ISEs) have attracted wide research attention.[9,10] (NASICON)-type LAGP electrolyte, Na superionic conductor, is one of the most promising SEs, because it possesses superior properties, such as high room-temperature ionic conductivity, high stability in air, wide electrochemical stability window, and low cost.[11–15] Nevertheless, the practical applications of LAGP electrolytes in Li metal batteries are limited since the rough solid–solid interface and the chemical instability of LAGP toward Li metal.[16–19] As Ge^{4+} ions in LAGP can be spontaneously reduced by Li metal to a lower chemical state by metallic Li at the interface of electrolyte/anode,[20,21] a mixed (ionic/electronic) conducting interphase (MCI) emerges composed of the reaction product, and the continuously formed mixed phase will degrade the performance of ASSLMBs quickly.[22] Detailed characterization further revealed that the local volumetric expansion during the reduction process can induce the fracture of LAGP, resulting in an ever-increasing interfacial resistance, destruction of LAGP structure, and failure of cells.[23,24] In addition, the reduction imposes a high potential thermal runaway risk on the integrated cells due to the released oxygen from the interphase at a high temperature (>200 °C).[20] Consequently, it is urgent to stabilize the interface between the LAGP electrolyte and Li metal

S. Zhang, Z. Zeng, Prof. L. Ci
Key Laboratory for Liquid-Solid Structural Evolution & Processing of Materials (Ministry of Education)
Research Center for Carbon Nanomaterials
School of Materials Science and Engineering
Shandong University
Jinan 250061, China
E-mail: lci@sdu.edu.cn

W. Zhai
Department of Chemistry
City University of Hong Kong
83 Tat Chee Avenue, Kowloon, Hong Kong 999077, China
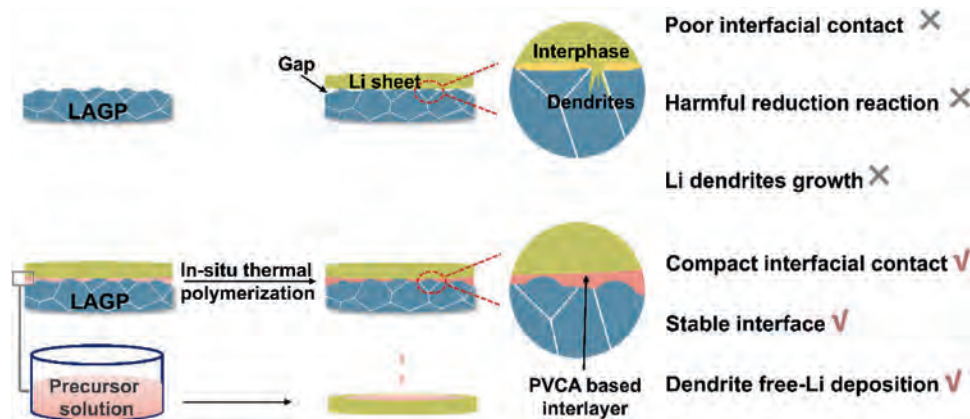
Dr. G. Hou
School of Light Industry and Engineering
Qilu University of Technology (Shandong Academy of Sciences)
Jinan 250353, China
E-mail: houmeiDream2011@126.com

Dr. L. Chen, Prof. L. Ci
State Key Lab of Advanced Welding and Joining
School of Materials Science and Engineering
Harbin Institute of Technology (Shenzhen)
Shenzhen 518055, China
E-mail: linachen@hit.edu.cn

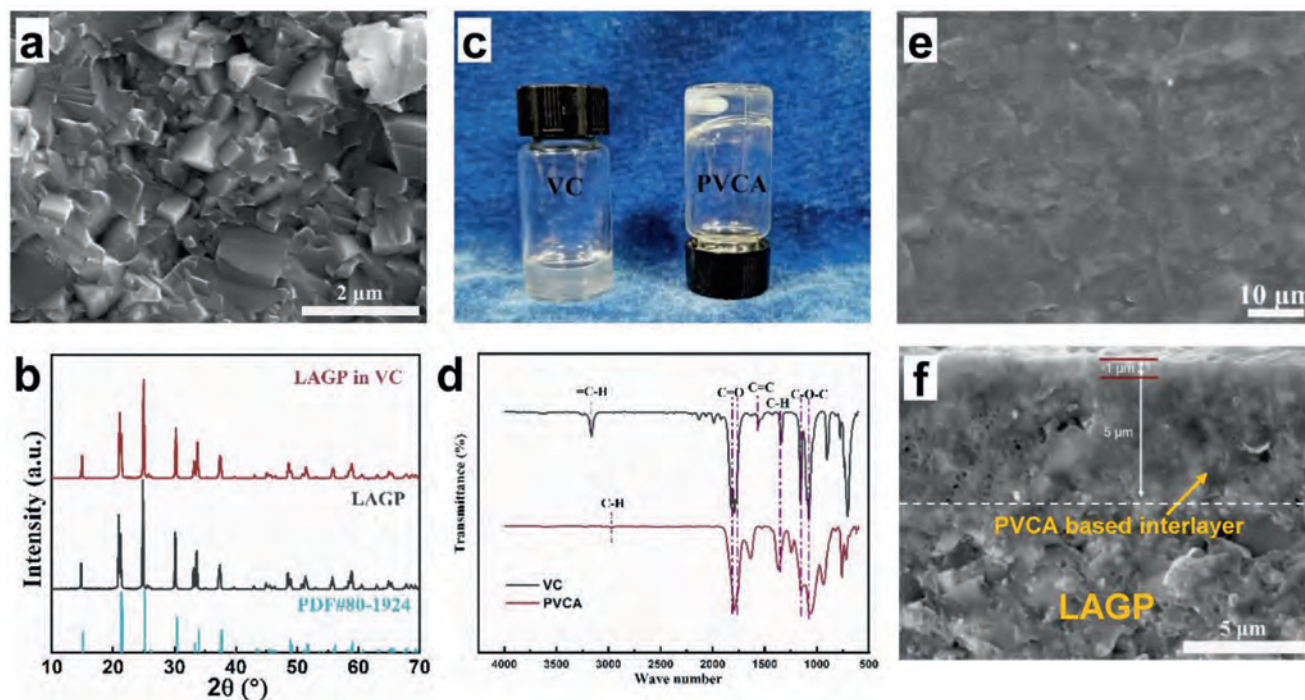**Figure 1.** Schematic of the preparation of PVCA-based interlayer and its protection for stable anode.

for high-performance SSLMBs. Adopting a buffer layer between Li metal anode and SSEs is deemed to be an effective strategy to solve the aforementioned problems.[25,26] Until now, much effort has been dedicated to designing various buffer layers, such as 3D polymer-gel layers,[27] poly(oxyethylene) (PEO) buffer layer,[16] Al$_2$O$_3$ nanolayer,[28,29] and germanium (Ge) thin film.[14] Nevertheless, due to the poor elastic feature of solid inorganic buffer layers, the formed interface at the buffer layers and the LAGP SSEs can be severely damaged by the volume change of the anode during the repeated Li plating/stripping processes, leading to a rapidly increased interfacial resistance.[30] Though the mechanical flexibility of these polymer-based buffer layers is satisfying, hundreds of microns thickness can severely compromise the energy density of ASSLMBs.[12,31] Worsely, it is hard to build a perfect face to face contact between polymer membranes and SSEs to decrease the interfacial resistance drastically.[32]

Herein, bifunctional PVCA-based buffer layer is introduced through in situ polymerization of carbonate (VC) monomer and azodiisobutyronitrile (AIBN) initiator (**Figure 1**).[33,34] The buffer layer with 5 wt% FEC is denoted as PVCA-5, while without FEC denoted as PVCA-0. The in situ formed ionically conductive PVCA-5 buffer layer can build a perfect compact electrode/electrolyte interface contact. Furthermore, the formed solid electrolyte interphase (SEI) from decomposition of FEC and resulted LiF can stabilize Li anode effectively.[35,36] As a result, the assembled symmetric cells exhibit an ultralow interfacial resistance and excellent interface compatibility with a stable voltage profile at 80 mV after nearly 850 h. What is more, with modification of the PVCA-based buffer layer, the Li/LAGP/LiFePO$_4$ (LFP) hybrid solid full cells can deliver an impressively high initial capacity of 150 mAh g^{-1} with and superior capacity retention of 96% after 200 cycles at 0.5 C. The facile in situ polymerized-interlayer approach presented in this work provides a resultful access to stabling SSEs/anode interface in ASSLMBs.

2. Results and Discussion

The prepared LAGP pellet was first characterized. SEM image in **Figure 2**a represents that the sintered LAGP electrolyte is composed of primary crystals with obvious grain boundaries. To further confirm the phase purity, XRD was employed to characterize the synthesized LAGP pellet. As indicated in Figure 2b, the XRD pattern of the prepared LAGP pellet can perfectly match with the standard pattern,[37] confirming the successful preparation of LAGP. As shown in Figure S1 (Supporting Information), the as-prepared LAGP SSE possessed a high ionic conductivity of 2.5×10^{-4} S cm^{-1} at 20 °C. Furthermore, the ionic conductivities at variable temperature ranging from 20 °C to 80 °C were tested (Figure S1, Supporting Information), and the activation energy is calculated to be 0.37 eV (Figure S2, Supporting Information), which matches well with that in previous reports.[38] To prove the in situ polymerization is feasible, liquid VC monomer polymerization process was also studied. As indicated in Figure 2c, PVCA-based interlayer is obtained from polymerizing liquid VC monomers after catalyzed by a thermally initialized radical initiator at 60 °C for 48 h. The polymerization reaction is also confirmed by the Fourier transform infrared (FTIR) spectra, from which the unsaturated =C—H vibration band of VC at 3164 cm^{-1} disappears, and a new peak appears at around 3002 cm^{-1}, which is the evidence of the polymerization reaction, which well matches with previously reported results (Figure 2d).[33] To confirm the in situ polymerization of VC on the surface of LAGP and study the built perfect surface contact, SEM observation was employed. As indicated in Figure 2e, SEM image shows that LAGP with the PVCA-5 buffer layer has a much flatter surface than the prepared LAGP, which is the evidence of the polymerization reaction. Considering liquid penetration, part of the precursor monomers can diffuse into the gaps between the electrolyte particles, enabling the in situ polymerized buffer layer with improved contact with the electrolyte. As displayed in Figure 2f, the invisible surface gap between the LAGP and the PVCA-5 buffer proves that perfect surface contact has been built between the buffer layer and the LGAP pellet. Compared to the undesirable contact between these conventionally employed polymer-based buffer layers and the electrolytes, the improved contact will benefit the decrease of surface resistance. Compared with the thick polymer-based buffer layers used in the reported literature,[31] another advantage of the in situ polymerized buffer layer is that the ultrathin thickness (Figure 2f and Figure S3, Supporting Information) will not degrade the energy density of the ASSLMBs. The ionic conductivity of the prepared electrolytes at variable temperature from

**ADVANCED
SCIENCE NEWS**
www.advancedsciencenews.com

**ADVANCED
MATERIALS
INTERFACES**
www.advmatinterfaces.de

Figure 2. Characterization of the LAGP solid electrolyte and PVCA-based material. a) SEM image of the fabricated LAGP pellet. b) XRD patterns of the fabricated pellets, the standard references of NASICON-type $LiGe_2(PO_4)_3$ structure (PDF#80-1924) and the LAGP pellets in VC after 24 h. c) Digital image of monomer solution and PVCA-based polymer material. d) FTIR spectra comparison of VC and PVCA. e) Surface SEM image of the LAGP pellet with PVCA-based interlayer. f) Cross sectional SEM image of how PVCA-based buffer layer combined with the LAGP pellet.

30 °C to 80 °C is shown in Figure S4 (Supporting Information). The LAGP/PVCA-5 electrolyte delivers a high ionic conductivity of 3.34×10^{-4} S cm^{-1} at 50 °C, and the temperature dependence of ionic conductivity conforms to Arrhenius' law, which ensure that the Li ions can rapidly transmit through the PVCA-5 interlayer. The electrochemical window of the investigated electrolyte was measured by Linear sweep voltammetry (LSV). As displayed in Figure S5 (Supporting Information), the LAGP/PVCA-5 electrolyte can maintain stability up to ≈4.8 V versus Li/Li$^+$, which can meet requirements of the most cathode materials.[4] To investigate the chemical stability of the prepared LAGP pellet toward VC monomer solution, LAGP was submerged in VC solution for 24 h. After that, the Raman spectra reveal that the characteristic peaks are unchanged (Figure S6b, Supporting Information). XRD test was also employed for further confirmation. Figure S6a (Supporting Information) shows that there is no new peak change, indicating LAGP and VC are chemically compatible.

The in situ polymerized PVCA-based buffer layer can benefit the performance of ASSLMBs owing to the improved stability of LAGP and the decreased resistance. **Figure 3**a and Figure S7 (Supporting Information) show the voltage profiles at 0.05 mA cm^{-2} current densities for 2 h per cycle. For the Li/LAGP/Li symmetric cell without any buffer layer, because of the rigid solid–solid contact between LAGP electrolyte and Li anode, it exhibits a high overpotential early in the electrochemical process, which increases to 100 mV after several cycles (Figure S7, Supporting Information). In addition, the voltage polarization rapidly increased and the cell triggered the protection cutoff voltage after cycling for 265 h (Figure S8, Supporting

Information). This phenomenon can be mainly attributed to impedance increment resulted from the inevitable interface side reactions and the volume change of Li anode.[3] The introduction of 5 µm PVCA-0 interlayer can improve the interfacial wettability between LAGP electrolyte and Li anode to some extent, but the polarization of Li/PVCA-0/LAGP/PVCA-0/Li cell increases after cycling 120h. This result suggests that the PVCA-0 interlayer cannot remain the chemical stability during charge and discharge. On the contrary, the symmetric cell modified by the PVCA-5 interlayer shows a very small overpotential and the voltage platform is only about 20 mV under the same conditions (Figure S7, Supporting Information). Furthermore, the Li/PVCA-5/LAGP/PVCA-5/Li cell maintains a stable voltage profile at 80 mV after nearly 850 h, confirming a compatible and kinetically stable interface (Figure 3a). The results confirm the remarkable role of PVCA-5 in reducing interface resistance. Figure 3b exhibits the voltage–time profile on galvanostatic cycling with step-ascending current densities were investigated at different currents. The Li/PVCA-5/LAGP/PVCA-5/Li cell could stably cycle for 600 h, while the overpotential is only about 75 mV even at the current density of 0.2 mA cm^{-2} (Figure S9, Supporting Information). In sharp contrast, the overpotential of Li/LAGP/Li increases rapidly and to be micro short-circuit at 0.2 mA cm^{-2} (Figure 3b). Interestingly, when reducing the current density to 0.05 mA cm^{-2}, the voltage platform returns to 20 mV and could continuously stable cycle for more than 400 h (Figure S10, Supporting Information), showing the advances of the interlayer in terms of stabling Li anode and accommodating the volume change of Li anode.

2100072
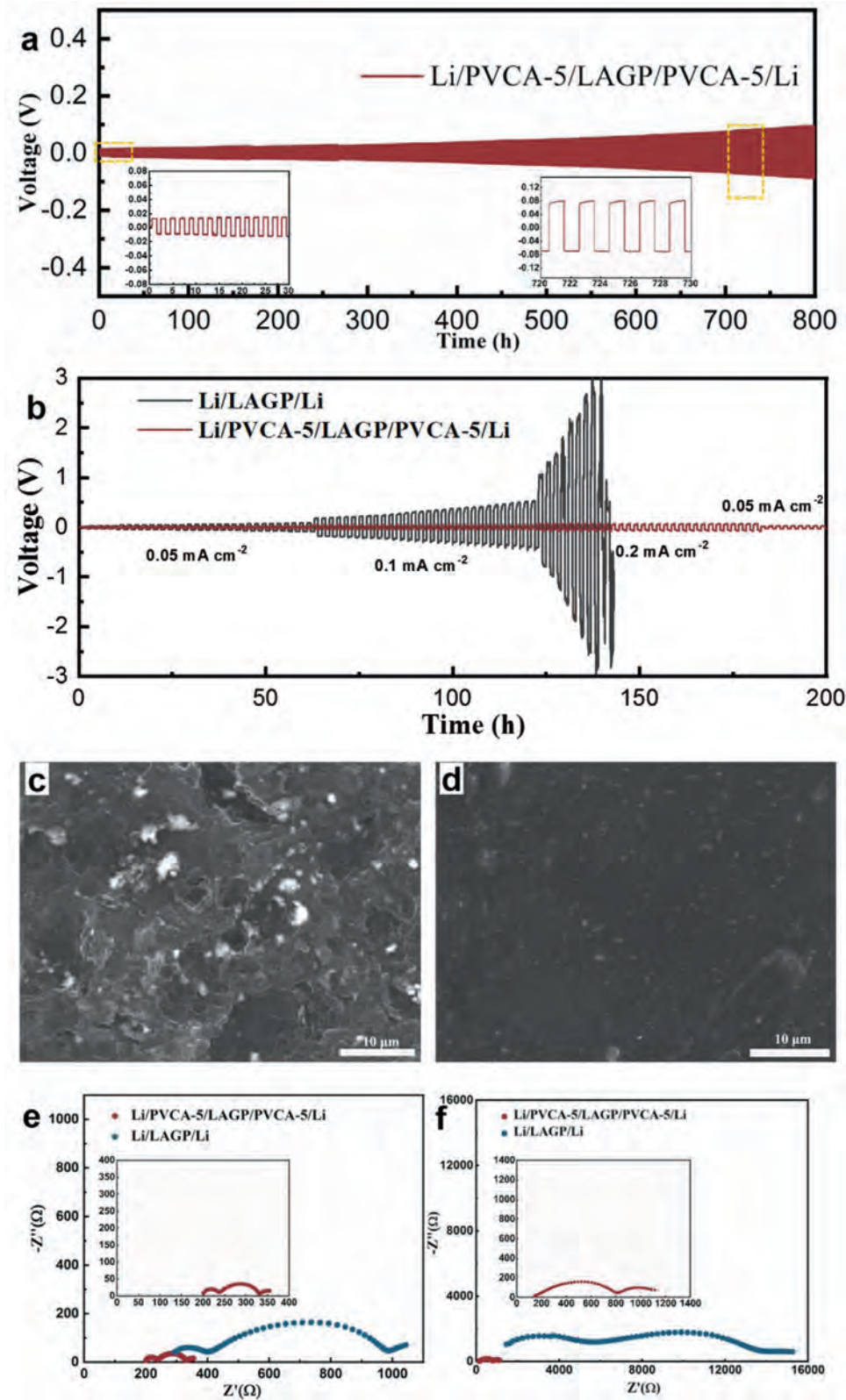
Figure 3. Voltage profiles of a) Li/PVCA-5/LAGP/PVCA-5/Li symmetric cells at b) 0.05 mA cm^{-2} and at different current densities at 50 °C. Surface SEM images of lithium foil obtained from c) Li/LAGP/Li and d) Li/PVCA-5/LAGP/PVCA-5/Li symmetrical cells after cycling for 50 h at 0.1 mA cm^{-2}. Electrochemical impedance spectra of the LAGP/Li symmetric cells with and without the PVCA-5 buffer layer e) before cycling and f) after cycled 50 h at 0.1 mA cm^{-2}.

In order to verify the effect of the PVCA-5 interlayer for preventing the undesirable interface side reaction, the surface SEM images of LAGP electrolyte and Li metal were observed after cycling for 50 h. As shown in Figure 3c, a mass of porous dead lithium can be found on Li metal, which is ascribed to the nonuniform Li deposition on the surface of Li.[20] In sharp contrast, the Li metal cycled in the LAGP/PVCA-5 electrolyte presents a compact surface with no visible dead lithium (Figure 3d). The morphology difference of LAGP surface with and without PVCA-5 coating is shown in Figure S11 (Supporting Information). The surface morphology of LAGP in direct contact with Li metal after dozens of cycles is no longer flat but very crushing, resulting from the serious reaction between LAGP and Li metal during cycling. Meanwhile, enlarged and rough particles appear on the surface, which can be ascribed to the reduced products of LAGP by Li metal. The volume expansion during side reaction creates a localized and nonuniform stress, driving crack formation in the LAGP pellet (Figure S11a, Supporting Information). The cracks in the pellet interrupt ion flow channels, resulting in an increased impedance and overpotential.[23] In addition, the cracks can change the local electrical field rapidly, leading to a nonuniform distribution of electrons and ions at the interface.[39,40] Conversely, the LAGP electrolyte separated from Li metal by coated PVCA-5 interlayer maintains a relatively flat appearance after several cycles, no obvious change was observed compared to the pristine LAGP pellet (Figure S11b,c, Supporting Information). EIS test also demonstrated the role of the PVCA-5 interlayer in enhancing interface stability. Figure 3e,f shows that the total impedance of Li/LAGP/Li fresh cell is 1082 Ω, and then the impedance increases to 14 370 Ω after cycled for 50 h at 30 °C. The high and rapidly rising resistance is due to the poor interfacial contact, and more importantly, the formed of MCI film leads to a continuous chemical reaction between LAGP and Li metal.[41] However, after introducing PVCA-5 based interlayer, the semicircle at high frequency in Nyquist plots was used to calculate the bulk resistance and grain boundary resistance of LAGP pellet, the second semicircle represents the interfacial resistance between LAGP pellet and PVCA-5 coating, which is 48 Ω before cycling. The resistance left corresponds the interfacial resistance of the formed SEI from decomposition of FEC and the interface impedance of SEI film is 22 Ω before cycling. The overall interfacial resistance of Li/PVCA-5/LAGP/PVCA-5/Li then slightly increases to 400 Ω after cycling 50 h, while that of Li/LAGP/Li is 7120 Ω after cycling 50 h. Such confirms that the PVCA-5 based interlayer is efficient in impeding the reduction of LAGP by Li metal and stabilizing the interface. To further evaluate the interfacial stability with and without PVCA-5 interlayer, the electrochemical impedance spectroscopy (EIS) tests were investigated using different electrolyte systems with various time intervals after cell assembly. As displayed in Figure S12a (Supporting Information), the interfacial impedance of Li/LAGP/Li cell is reached up to 1040 Ω after 24 h elapsed time, which can be assigned to the rigid contact between LAGP pellet and Li anode, and the instability of LAGP with lithium metal. While the interfacial impedance of Li/PVCA-5/LAGP/PVCA-5/Li cell is 164.3 Ω. The low interfacial impedance confirms the functionality of the PVCA-5 interlayer on Li metal surface in achieving face to face contact. Because of the sustained

chemical reaction between LAGP and lithium metal, the interfacial impedance of Li/LAGP/Li cell increases rapidly to 5023 Ω after 288 h elapsed time. In contrast, the interfacial impedance of Li/PVCA-5/LAGP/PVCA-5/Li cell is below 300 Ω after 288 h elapsed time, which illustrates that the PVCA-5 interlayer can be chemical compatible towards to lithium metal.

As mentioned previously, the formed solid electrolyte interphase (SEI) from decomposition of FEC and resulted LiF can stabilize Li anode effectively. In order to analyze the SEI film components on the cycled Li anode, in depth X-ray photoelectron spectroscopy (XPS) was conducted to get a comprehensive understanding of the surface chemistry at the interface (**Figure 4**). The Li 1s and F 1s XPS spectrum of the metallic Li harvested from the Li/LAGP/Li cell are displayed in Figure 4a,c. As shown in Figure 4a, the peaks in Li 1s spectra around 54.5 and 55.4 eV may correspond to Li_2O_2 and Li_2CO_3, respectively.[22] Meanwhile, compared to the Li 1s spectrum of pristine LAGP pellet (Figure S13h, Supporting Information), new peaks of Li_2O_2 and Li_2CO_3 (derived from residual carbon produced during the preparation of LAGP) appear in Li 1s spectrum of LAGP pellet after cycling (Figure S13f, Supporting Information).[20] These inorganic components on lithium anode are generally regarded as the side products of LAGP with Li metal and can lead to a loose and uneven surface on the Li anode, which was consistent with SEM image in Figure 3c. Furthermore, Ge 3d XPS spectrum of LAGP pellet after cycling presents a reduction peak representing Ge^0 at 29.1 eV instead of Ge^{4+} [≈32.5 eV (Figure S13c, Supporting Information)], which also verifies that Ge^{4+} on the surface of the pellet was reduced by the Li metal.[20] When PVCA-based material was employed as the interlayer between the LAGP electrolyte and Li metal, there is no new peak appearing, confirming the protective function of the PVCA-5 interlayer (Figure S13d,e, Supporting Information). More importantly, for the LAGP/PVCA-5/Li symmetric cells, new peaks assigned to $ROCO_2Li$ and LiF appear in Li 1s (54.9 eV, 55.8 eV)(Figure 4b).[42] And the peaks in F 1s spectra appearing at 685.3 eV and 687.8 eV indicate the existence of LiF and C−F. LiF can be attributed to the decomposition product of FEC during cycling and plays a critical role in creating a robust SEI film. Benefiting from the high interfacial energy and the low diffusing energy to Li metal, the LiF-enriched SEI can promote the uniform deposition of Li ion on the Li surface effectively. What is more, due to the excellent electrical insulation property (≈10^{-31} S cm^{-1}) of LiF, it is effectively to block electrons from crossing the SEI layer.[35,43] Protected by such smooth and robust SEI, the assembled symmetric cell exhibits a homogeneous Li stripping/plating and no lithium dendrite is formed during cycling. The SEM image above (Figure 3c,d) also confirms this conclusion.

The stable electrochemical properties of the aforementioned symmetric cells with PVCA-5 buffer layer enable its application in full cells. The hybrid solid-state full cells assembled with and without PVCA-based interlayer were cycled at 50 °C and the cycling and rate performance are shown in **Figure 5**. It is worth noting that 2 µL precursor solution was dropped toward the cathode when assembling the full cells, which could effectively improve the interfacial contact. The elastic property of PVCA-5 could also help relieve some of the stress from the electrode expansion/contraction. Figure 5a presents the voltage

ADVANCED
SCIENCE NEWS
www.advancedsciencenews.com

ADVANCED
MATERIALS
INTERFACES
www.advmatinterfaces.de
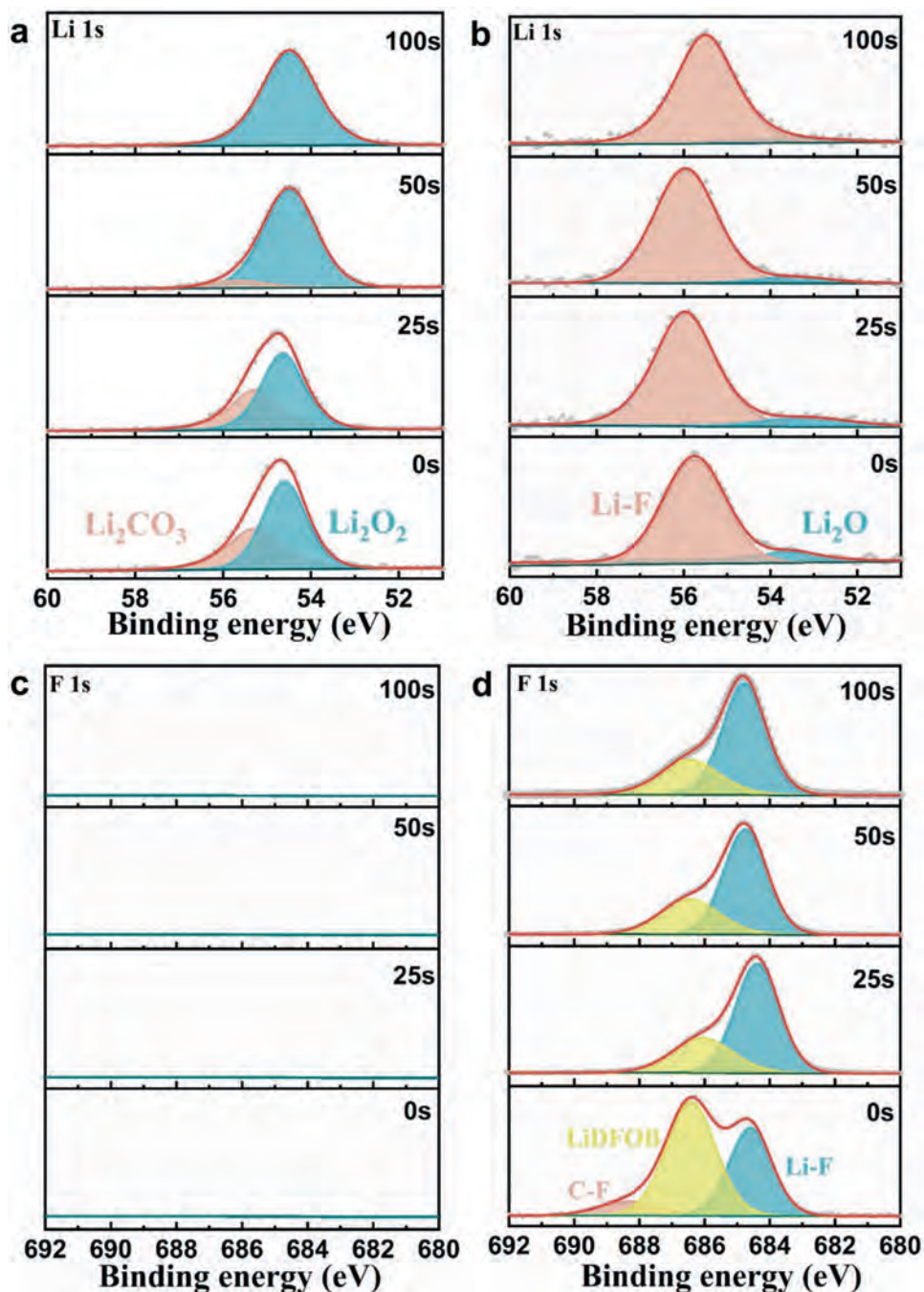
Figure 4. SEI characterization. a,b) Li 1s and c,d) F 1s in-depth XPS spectra on the surface of various Li metal anodes, recovered from a,c) Li/LAGP/Li and b,d) Li/PVCA-5/LAGP/PVCA-5/Li symmetric cells after 50 h.

curves for the Li/PVCA-5/LAGP/LFP cell at 0.5 C, from which a representative charge and discharge voltage platforms can be observed. Modified by the PVCA-5 interlayer, the hybrid cell presents a discharge capacity of 153 mAh g^{-1} at first cycle with a high initial Coulombic efficiency (ICE) of 99.45%. Furthermore, after 80 cycles, the discharge capacity remains 144 mAh g^{-1}, realizing a capacity retention of 94.1%. These results indicate that the interlayer not only provides an intimate contact of Li/LAGP interface, but also exhibits the excellent stability

toward Li anode. However, the cells without PVCA-5 interlayer exhibit the initial discharge capacity of 118 mAh g^{-1} and the electrochemical performance declines quickly, indicating a lower cycling stability resulted from continuous side reactions between the LAGP electrolyte and the electrodes (Figure 5b).[44] Figure 5c,d shows the rate performance of Li/LFP cells and the corresponding charge–discharge curves with and without the PVCA-5 interlayer. The cell using bare Li anode presents rapidly deteriorative rate performance with the increase of current

**ADVANCED
SCIENCE NEWS**

www.advancedsciencenews.com

**ADVANCED
MATERIALS
INTERFACES**

www.advmatinterfaces.de
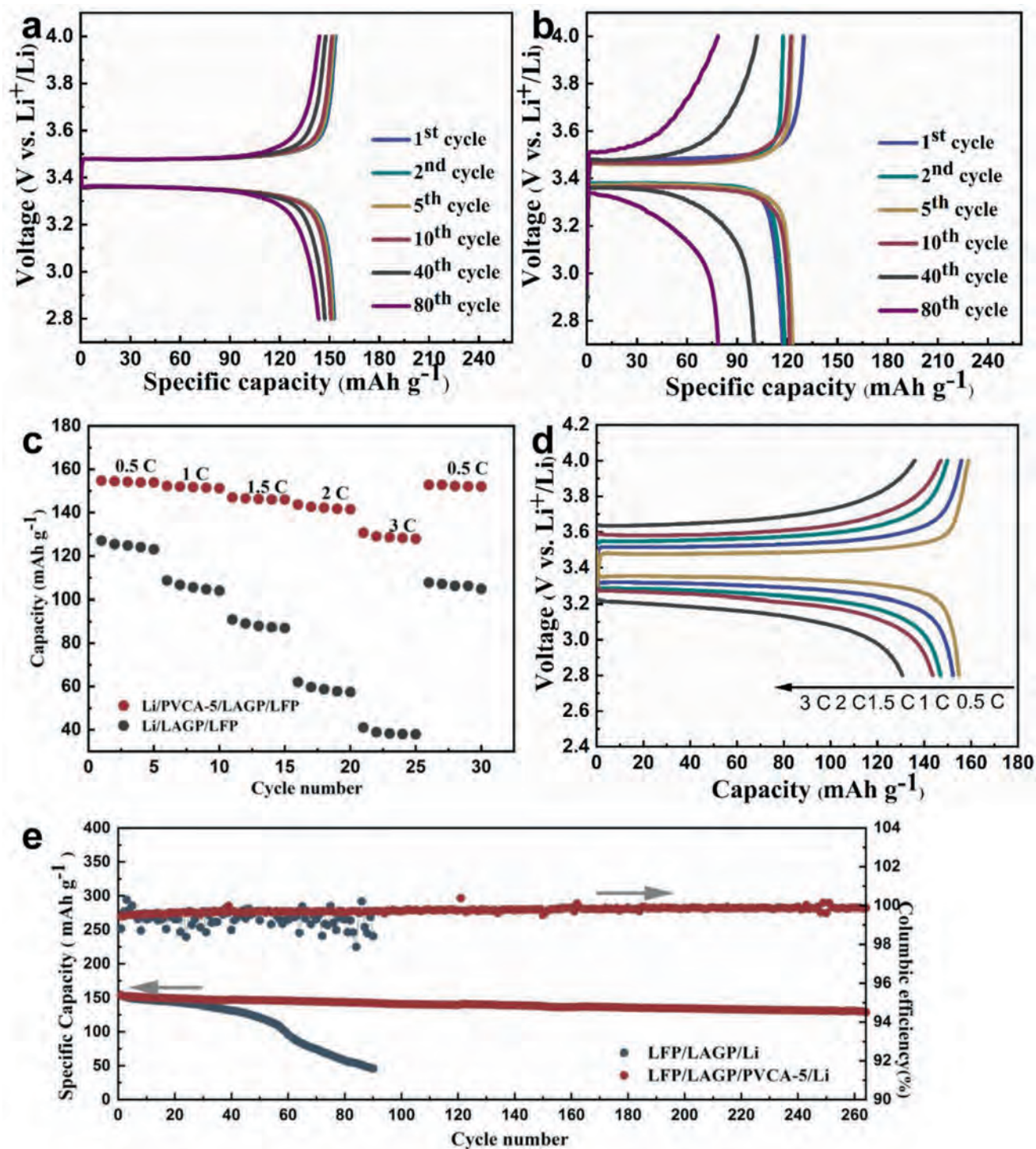
Figure 5. Charge/discharge profiles of a) Li/PVCA-5/LAGP/LFP cell and b) Li/LAGP/LFP cell at 0.5 C at 50 °C. c) Rate performance of Li/LAGP/LFP ASSLMBs with and without PVCA-based layer from 0.5 to 3 C at 50 °C. d) Charge/discharge curves of Li/PVCA-5/LAGP/LFP cell at different rates. e) Cyclic performance Li/LAGP/LFP ASSLMBs with and without interlayer.

density, only showing a capacity of 38 mAh g⁻¹ at 3 C. The high interfacial resistance at anode side is responsible for the degradation of capacity. Notably, as the current density increases, the cell with the PVCA-based buffer layer still exhibits a high discharge capacity of 152 mAh g⁻¹, 148 mAh g⁻¹, 143 mAh g⁻¹,

132 mAh g⁻¹ at 1 C, 1.5 C, 2 C, 3 C, respectively. When the current density drops back to 0.5 C, the discharge capacity also returns to a higher value of 153 mAh g⁻¹. These results demonstrate the role of PVCA-5 interlayer in improving Li ionic lithiation/delithiation capability between the electrolyte and electrodes.

**ADVANCED
SCIENCE NEWS**

www.advancedsciencenews.com

**ADVANCED
MATERIALS
INTERFACES**

www.advmatinterfaces.de

Figure 5e shows the comparison of long cycling stability in different ASSLMBs. The Li/PVCA-5/LAGP/LFP cell delivers a high capacity of 150 mAh g^{-1} at 0.5 C and favorable capacity retention of 91.2% after 200 cycles, while the capacity of Li/LAGP/LFP decays rapidly from 150 mAh g^{-1} to 57 mAh g^{-1} within 80 cycles (Figure 5e). Compared with the full cell using bare Li anode, the electrodes modified by the PVCA-5 interlayer also have an improved Coulombic efficiency stability. In order to prove the feasibility of the interfacial engineering in practical application, the cycling performance of the Li/PVCA-5/LAGP/LFP cell at 1.5 C is exhibited in Figure S14 (Supporting Information). The initial discharge capacity is 144.6 mAh g^{-1} with Coulombic efficiency of 99.8%, and the capacity retention is 88.3% after 45 cycles. In addition, full cells with a LiCoO$_2$ (LCO) cathode and a LiNi$_{0.33}$Mn$_{0.33}$Co$_{0.33}$O$_2$ (NMC) cathode were tested at 50 °C (Figures S15 and S16, Supporting Information). At 0.3 C, the first-cycle discharge capacity of the Li/PVCA-5/LAGP/LCO cell is 130 mAh g^{-1} and remains at 125.6 mAh g^{-1} after four cycles, while the Li/LAGP/LCO delivers only 81 mAh g^{-1} and drops to 50.1 mAh g^{-1} after four cycles (Figure S15, Supporting Information). The Li/PVCA-5/LAGP/NMC and Li/LAGP/NMC were also tested at 50 °C at 0.2 C. The initial discharge capacity of PVCA-5/LAGP reaches to 140.1 mAh g^{-1} and remains at 130 mAh g^{-1} after four cycles. However, the capacity of the cell without PVCA-5 interlayer exhibits the initial discharge capacity of 100.2 mAh g^{-1} and declines to 70.4 mAh g^{-1} quickly (Figure S16, Supporting Information). All of the data above illustrate that the presence of an in situ polymerized PVCA-5 interlayer can effectively prevent the reduction of LAGP by Li so that LAGP can function normally in ASSLBs.

3. Conclusion

In this work, we propose a novel strategy of interface design by in situ radical polymerization. The monomer solution dropped between the LAGP electrolyte and the metallic Li anode can fill the voids completely at the interface and the as-fabricated PVCA-based layer is electronic insulating but well ionic conducting. Not only can the interlayer acts as barricades to prevent the side reactions, but also it enables lithium ion diffuse homogeneously and relieves the volumetric changes of anodes during cycling. The Li/PVCA-5/LAGP symmetric cell exhibits outstanding cycling performance for over 800h of repeatable Li plating/stripping. Besides, the Li/LAGP/LFP cell with PVCA-5 interlayer also displays improved rate performance, as well as a high capacity retention after 200 cycles. This work demonstrates that the modifying design by the in-situ polymerization can improve the performance of ASSLMBs significantly.

4. Experimental Section

Synthesis of LAGP pellets: The LAGP raw powder was purchased from Shenzhen Kejing Material Technology Co., Ltd. The LAGP pellet was synthesized by pressing 0.5 g raw powder using a die (diameter: 16 mm; thickness: ≈1 mm). Then, the pressed pellet was sintered at 900 °C for 12 h at air atmosphere in a muffle furnace. The obtained LAGP pellet was ground to 980 µm thick and the bare LAGP pellets were polished with 600, 800, 1000, and 1500 mesh sandpaper before use.

Preparation of Poly(Vinylene Carbonate) (PVCA)-Based Interlayer Materials: Difluorooxalato borate lithium salt (LiDFOB, 99.9%) was purchased from Innochem (Beijing) Technology Co., Ltd. LiDFOB (0.143 g) was first dissolved into 1 mL vinylene carbonate (VC, 99.9%, Aladdin (Shanghai) Biochemical Technology Co., Ltd.), ≈9.6% (w/w)), followed by adding 2 mg AIBN (99%, Aladdin (Shanghai) Biochemical Technology Co., Ltd.) as thermal initiator into the above mixture. Subsequently, 5 wt% fluoroethylene carbonate (FEC) was added into the mixture to obtain homogeneous and transparent precursor solution and the obtained mixture was stirred for 4–6 h in an argon-filled glove box (H$_2$O < 1 ppm and O$_2$ < 1 ppm). Afterward, the precursor solution was dropped on Li anodes and then the modified anodes were achieved. Later, these assembled batteries were kept constantly at 60 °C for 48 h to achieve the polymerization of the monomers. As a result, a thin PVCA-5 interlayer was in situ constructed between LAGP pellet and Li anode. The PVCA buffer layer without FEC (denoted as PVCA-0) was prepared in the same way as above.

Materials Characterization: The phase structure of LAGP pellets was obtained by X-ray diffraction (XRD) measurement on an X-ray diffractometer (Bruker D8 Advance, Germany) using Cu Kα radiation (λ = 0.154 nm) at a power of 40 KeV. Fourier transform infrared spectra were obtained on Bruker VERTEX 70 at room temperature. Raman spectra were collected using a Renishaw InVia Reflex system equipped with a 532 nm laser. The morphology of the electrolytes and lithium anodes were characterized by a field-emission scanning electron microscope (FE-SEM, Hitachi SU-70). X-ray photoelectron spectroscopy analysis was performed on Thermo Scientific K-Alpha+ using a monochromatic Al K(alpha) X-ray source.

Cell Assembly: Symmetric cells were assembled with two lithium sheets as both electrodes in the LAGP pellet in CR2032 coin-type cells. The LiFePO$_4$ (LFP) cathode of the ASSLIBs was prepared by coating slurry containing 80 wt% LiFePO$_4$ (LFP), 10 wt% super P, and 10 wt% poly-vinylidene fluoride (PVDF) on the Al foil, next the prepared material underwent vacuum-drying at 80 °C for 12 h, and the mass loading was ≈1.2 mg cm^{-2}. The LiCoO$_2$ (LCO) cathode material was prepared by coating slurry containing 80 wt% LCO, 10 wt% super P, and 10 wt% PVDF on the Al foil. The following steps were the same as LFP and the cathode loading was ≈1.4 mg cm^{-2}. The LiNi$_{0.33}$Mn$_{0.33}$Co$_{0.33}$O2 (NMC) cathode was prepared by mixing NMC, super P and PVDF at a mass ratio of 8:1:1. The left steps were also the same as LFP and the mass loading of obtained cathode material was ≈1.2 mg cm^{-2}. After that, the ASSLIBs using Li anodes, LAGP with or without PVCA-5 interlayer and three types of cathodes were assembled in the CR2032 coin cell in an argon-filled glovebox.

Electrochemical Measurement: Symmetrical Au/LAGP/Au cell was assembled by sputtering Au onto the two sides of LAGP pellet to measure the ionic conductivity of the LAGP solid electrolyte as a function of temperature in the range 20–80 °C. The ionic conductivity of electrolytes samples was measured by electrochemical impedance spectra on an electrochemical workstation (Autolab, Metrohm) with an alternating current (AC) amplitude of 10 mV in the frequency from 0.1Hz to 1.0 MHz. The Li–Li symmetric cells were tested on the charge/discharge unit by applying various current in the range of 0.05–0.2 mA cm^{-2} using a LAND-CT2001A multichannel battery tester (Wuhan, China). For full cells, the integrated Li/LFP full cells were charged and discharged at a rate of 0.5 C (1 C = 170 mAh g^{-1}), and the cycle rate was set as 0.5, 1, 1.5, 2, and 3 C, during which the voltage ranges from 2.8 to 4.0 V. All electrochemical tests were performed after the cells were kept at 50 °C for 30 min.

Supporting Information

Supporting Information is available from the Wiley Online Library or from the author.

Acknowledgements

Conflict of Interest

The authors declare no conflict of interest.

Data Availability Statement

Research data are not shared.

Keywords

[1] H. Huo, Y. Chen, R. Li, N. Zhao, J. Luo, J. G. Pereira da Silva, R. Mücke, P. Kaghazchi, X. Guo, X. Sun, *Energy Environ. Sci.* **2020**, *13*, 127.

[2] J. Wan, J. Xie, X. Kong, Z. Liu, K. Liu, F. Shi, A. Pei, H. Chen, W. Chen, J. Chen, X. Zhang, L. Zong, J. Wang, L.-Q. Chen, J. Qin, Y. Cui, *Nat. Nanotechnol.* **2019**, *14*, 705.

[3] G. Hou, X. Ma, Q. Sun, Q. Ai, X. Xu, L. Chen, D. Li, J. Chen, H. Zhong, Y. Li, Z. Xu, P. Si, J. Feng, L. Zhang, F. Ding, L. Ci, *ACS Appl. Mater. Interfaces* **2018**, *10*, 18610.

[4] Q. Liu, D. Zhou, D. Shanmukaraj, P. Li, F. Kang, B. Li, M. Armand, G. Wang, *ACS Energy Lett.* **2020**, *5*, 1456.

[5] L. Yang, Y. Song, H. Liu, Z. Wang, K. Yang, Q. Zhao, Y. Cui, J. Wen, W. Luo, F. Pan, *Small Methods* **2020**, *4*, 1900751.

[6] Z. Zhang, Y. Shao, B. Lotsch, Y.-S. Hu, H. Li, J. Janek, L. F. Nazar, C.-W. Nan, J. Maier, M. Armand, L. Chen, *Energy Environ. Sci.* **2018**, *11*, 1945.

[7] Q. Zhao, S. Stalin, C.-Z. Zhao, L. A. Archer, *Nat. Rev. Mater.* **2020**, *5*, 229.

[8] C. Sun, J. Liu, Y. Gong, D. P. Wilkinson, J. Zhang, *Nano Energy* **2017**, *33*, 363.

[9] A. Manthiram, X. Yu, S. Wang, *Nat. Rev. Mater.* **2017**, *2*, 16103.

[10] S. Xin, Y. You, S. Wang, H.-C. Gao, Y.-X. Yin, Y.-G. Guo, *ACS Energy Lett.* **2017**, *2*, 1385.

[11] Z. Gao, H. Sun, L. Fu, F. Ye, Y. Zhang, W. Luo, Y. Huang, *Adv. Mater.* **2018**, *30*, 1705702.

[12] Q. Cheng, A. Li, N. Li, S. Li, A. Zangiabadi, T.-D. Li, W. Huang, A. C. Li, T. Jin, Q. Song, W. Xu, N. Ni, H. Zhai, M. Dontigny, K. Zaghib, X. Chuan, D. Su, K. Yan, Y. Yang, *Joule* **2019**, *3*, 1510.

[13] Y. J. Hao, S. Wang, F. Xu, Y. J. Liu, N. N. Feng, P. He, H. S. Zhou, *ACS Appl. Mater. Interfaces* **2017**, *9*, 33735.

[14] Y. Liu, C. Li, B. Li, H. Song, Z. Cheng, M. Chen, P. He, H. Zhou, *Adv. Energy Mater.* **2018**, *8*, 1702374.

[15] H. S. Kim, Y. Oh, K. H. Kang, J. H. Kim, J. Kim, C. S. Yoon, *ACS Appl. Mater. Interfaces* **2017**, *9*, 16063.

[16] Z. H. Zhang, Y. R. Zhao, S. J. Chen, D. J. Xie, X. Y. Yao, P. Cui, X. X. Xu, *J. Mater. Chem. A* **2017**, *5*, 16984.

[17] Y. Xiao, Y. Wang, S.-H. Bo, J. C. Kim, L. J. Miara, G. Ceder, *Nat. Rev. Mater.* **2020**, *5*, 105.

[18] Y. Shen, Y. Zhang, S. Han, J. Wang, Z. Peng, L. Chen, *Joule* **2018**, *2*, 1674.

[19] H. S. Jadhav, R. S. Kalubarme, A. H. Jadhav, J. G. Seo, *Electrochim. Acta* **2016**, *199*, 126.

[20] H. Chung, B. Kang, *Chem. Mater.* **2017**, *29*, 8611.

[21] L. He, Q. Sun, C. Chen, J. A. S. Oh, J. Sun, M. Li, W. Tu, H. Zhou, K. Zeng, L. Lu, *ACS Appl. Mater. Interfaces* **2019**, *11*, 20895.

[22] P. Hartmann, T. Leichtweiss, M. R. Busche, M. Schneider, M. Reich, J. Sann, P. Adelhelm, J. Janek, *J. Phys. Chem. C* **2013**, *117*, 21064.

[23] J. Tippens, J. C. Miers, A. Afshar, J. A. Lewis, F. J. Q. Cortes, H. P. Qiao, T. S. Marchese, C. V. Di Leo, C. Saldana, M. T. McDowell, *ACS Energy Lett.* **2019**, *4*, 1475.

[24] J. A. Lewis, F. J. Q. Cortes, M. G. Boebinger, J. Tippens, T. S. Marchese, N. Kondekar, X. M. Liu, M. F. Chi, M. T. McDowell, *ACS Energy Lett.* **2019**, *4*, 591.

[25] Z. Jiang, Q. Han, S. Wang, H. Wang, *ChemElectroChem* **2019**, *6*, 2970.

[26] M. J. Du, K. M. Liao, Q. Lu, Z. P. Shao, *Energy Environ. Sci.* **2019**, *12*, 1780.

[27] Q. Yu, D. Han, Q. Lu, Y.-B. He, S. Li, Q. Liu, C. Han, F. Kang, B. Li, *ACS Appl. Mater. Interfaces* **2019**, *11*, 9911.

[28] X. Han, Y. Gong, K. Fu, X. He, G. T. Hitz, J. Dai, A. Pearse, B. Liu, H. Wang, G. Rubloff, Y. Mo, V. Thangadurai, E. D. Wachsman, L. Hu, *Nat. Mater.* **2016**, *16*, 572.

[29] Y. L. Liu, Q. Sun, Y. Zhao, B. Q. Wang, P. Kaghazchi, K. R. Adair, R. Y. Li, C. Zhang, J. R. Liu, L. Y. Kuo, Y. F. Hu, T. K. Sham, L. Zhang, R. Yang, S. G. Lu, X. P. Song, X. L. Sun, *ACS Appl. Mater. Interfaces* **2018**, *10*, 31240.

[30] B. H. Zhou, D. He, J. Hu, Y. S. Ye, H. Y. Peng, X. P. Zhou, X. L. Xie, Z. G. Xue, *J. Mater. Chem. A* **2018**, *6*, 11725.

[31] W. D. Zhou, S. F. Wang, Y. T. Li, S. Xin, A. Manthiram, J. B. Goodenough, *J. Am. Chem. Soc.* **2016**, *138*, 9385.

[32] Y. Hu, Y. Zhong, L. Qi, H. Wang, *Nano Res.* **2020**, *13*, 3230.

[33] J. Chai, Z. Liu, J. Ma, J. Wang, X. Liu, H. Liu, J. Zhang, G. Cui, L. Chen, *Adv. Sci.* **2017**, *4*, 1600377.

[34] S. Matsui, T. Muranaga, H. Higobashi, S. Inoue, T. Sakai, *J. Power Sources* **2001**, *97-98*, 772.

[35] X.-Q. Zhang, X.-B. Cheng, X. Chen, C. Yan, Q. Zhang, *Adv. Funct. Mater.* **2017**, *27*, 1605989.

[36] Y. Lu, Z. Tu, L. A. Archer, *Nat. Mater.* **2014**, *13*, 961.

[37] B. Key, D. J. Schroeder, B. J. Ingram, J. T. Vaughey, *Chem. Mater.* **2012**, *24*, 287.

[38] Q. Liu, Q. Yu, S. Li, S. Wang, L. Zhang, B. Cai, D. Zhou, B. Li, *Energy Storage Mater.* **2020**, *25*, 613.

[39] R. H. Basappa, T. Ito, H. Yamada, *J. Electrochem. Soc.* **2017**, *164*, A666.

[40] E. Kazyak, R. Garcia-Mendez, W. S. LePage, A. Sharafi, A. L. Davis, A. J. Sanchez, K.-H. Chen, C. Haslam, J. Sakamoto, N. P. Dasgupta, *Matter* **2020**, *2*, 1025.

[41] D. Cao, X. Sun, Q. Li, A. Natan, P. Xiang, H. Zhu, *Matter* **2020**, *3*, 57.

[42] Q. Huang, K. Turcheniuk, X. Ren, A. Magasinski, A.-Y. Song, Y. Xiao, D. Kim, G. Yushin, *Nat. Mater.* **2019**, *18*, 1343.

[43] X. B. Cheng, C. Yan, X. Chen, C. Guan, J. Q. Huang, H. J. Peng, R. Zhang, S. T. Yang, Q. Zhang, *Chem* **2017**, *2*, 258.

[44] F. Hu, Y. Li, Y. Wei, J. Yang, P. Hu, Z. Rao, X. Chen, L. Yuan, Z. Li, *ACS Appl. Mater. Interfaces* **2020**, *12*, 12793.

In-Built Quasi-Solid-State Poly-Ether Electrolytes Enabling Stable Cycling of High-Voltage and Wide-Temperature Li Metal Batteries

Yong Chen, Feng Huo, Shimou Chen,* Weibin Cai,* and Suojiang Zhang*

Developing solid-state electrolytes with good compatibility for high-voltage cathodes and reliable operation of batteries over a wide-temperature-range are two bottleneck requirements for practical applications of solid-state metal batteries (SSMBs). Here, an in situ quasi solid-state poly-ether electrolyte (SPEE) with a nano-hierarchical design is reported. A solid-eutectic electrolyte is employed on the cathode surface to achieve highly-stable performance in thermodynamic and electrochemical aspects. This performance is mainly due to an improved compatibility in the electrode/electrolyte interface by nano-hierarchical SPEE and a reinforced interface stability, resulting in superb-cyclic stability in Li‖Li symmetric batteries (>4000 h at 1 mA cm^{-2}/1 mAh cm^{-2}; >2000 h at 1 mA cm^{-2}/4 mAh cm^{-2}), which are the same for Na, K, and Zn batteries. The SPEE enables outstanding cycle-stability for wide-temperature operation (15–100 °C) and 4 V-above batteries (Li‖LiCoO$_2$ and Li‖LiNi$_{0.8}$Co$_{0.1}$Mn$_{0.1}$O$_2$). The work paves the way for development of practical SSMBs that meet the demands for wide-temperature applicability, high-energy density, long lifespan, and mass production.

1. Introduction

Solid-state lithium metal batteries (SSLMBs) show promising prospects in high-energy-density and highly-safe energy storage devices owing to their reliable electrochemical performance, inherent safety, and excellent abuse tolerance.[1–6] Plentiful solid-state electrolytes (SSEs) have been spawned by the never-ceasing surge on materials and chemistry. But SSLMBs

have been suffering from inferior interfacial stabilities between SSEs and other battery components.[7–11] For achieving intimate interface contact and the compatibility with metallic lithium, an efficient and easy-industrialized strategy is in situ solid poly-ether electrolytes (SPEEs), which formed in electrochemical cells upgrading process by using conventional ether-based electrolytes, like 1,3-dioxolane (DOL) via cationic ring-opening polymerization reaction.[3,12–15] However, it has two ineluctable problems including incomplete polymerization and residue of initiators, resulting in a "trade-off" between ion conductivity and stability. Lewis-acidic Li salts (e.g., LiPF$_6$ and LiDFOB) and organic metal compounds (e.g., Al(OTf)$_3$ and Sn(OTf)$_4$) are the two common initiators, which always trigger violent reactions. They display rapid initiator failure, short curing time, and inferior polymerization degrees.[16–18] On the other hand, high content of initiator residue also complicates the matters. In contrast, reducing the number of initiators results in excess unpolymerized DOL. It discounts practical applications of SPEE, presenting inferior electrochemical performances at elevated-temperature (especially over 70 °C) and high-voltage condition (4 V-above class).[15,18] In order to stabilize the oxidizing of 4 V-above class cathodes, coating an artificial cathode-electrolyte interphases (CEI) seems an efficient approach, however, it would introduce some new issues, such as high-temperature processing, damage of energy density, and ionic conductivity.[19–22] Furthermore, the stable-cycling performances of high-voltage and wide-temperature Li metal batteries are almost out of reach. These factors lead to inferior cycle performances of solid polymer electrolytes, especially poly-ethers, in high voltage and wide-temperature operating conditions.[7]

Herein, we design a nano-hierarchical SPEE with a solid eutectic electrolyte as an interface encapsulation on the surface of the cathode to mitigate interfacial instability in thermodynamic and electrochemical aspects. The nano-hierarchical SPEE with high polymerization degree and a soothing curing time is initiated by a trace amount of a designed hybrid initiator system, which shows excellent catalytic activity and well-controlled polymerization. Consequently, the SPEE demonstrates superb-cyclic stability for Li‖Li symmetric batteries (>4000 h at 1 mA cm^{-2}/1 mAh cm^{-2}; >2000 h at 1 mA cm^{-2}/4 mAh cm^{-2}), which also can support the Na, K, and

Y. Chen, Prof. W. Cai
School of Chemical and Environmental Engineering
China University of Mining and Technology
Beijing 100083, China
E-mail: caiweibin@cumtb.edu.cn, caiweibin2000@126.com
Prof. F. Huo, Prof. S. Chen, Prof. S. Zhang
Beijing Key Laboratory of Ionic Liquids Clean Process
Key Laboratory of Green Process and Engineering
Institute of Process Engineering
Chinese Academy of Sciences
Beijing 100190, China
E-mail: chenshimou@ipe.ac.cn; sjzhang@ipe.ac.cn
Prof. S. Chen
State Key Laboratory of Chemical Resource Engineering
Beijing University of Chemical Technology
Beijing 100029, China

The ORCID identification number(s) for the author(s) of this article can be found under https://doi.org/10.1002/adfm.202102347.

Zn symmetric batteries. Benefiting from solid eutectic assistance, the as-designed SPEE is advantageous to mitigate the interfacial instability and facilitate Li⁺ ion conductivity, and thus enabling super-cyclic stability for 4 V-above batteries (Li‖LiCoO$_2$ and Li‖LiNi$_{0.8}$Co$_{0.1}$Mn$_{0.1}$O$_2$) and wide-temperature operation (15–100 °C). Significantly, Li|SPEE|LiFePO$_4$ batteries display outstanding long lifespan with capacity retention of 85% after 1200 cycles at 1 C and Li|SPEE|LiCoO$_2$ batteries display capacity retention of 91.7% over 200 cycles with coulombic efficiencies (CE > 99%).

2. Results and Discussion

2.1. Fabrication of SSLMBs Via Nano-Hierarchical SPEE and CIE

The fabricating route of nano-hierarchical SPEE is illustrated in **Figure 1**a. Two types of additives were designed as efficacious initiators by adding a tiny amount in LiTFSI/DOL: 300 ppm AlI$_3$ and 600 ppm LiPF$_6$ (SPEE-1); LiDFOB (SPEE-2), as a demonstration of a library of candidates. Subsequently, the additive and the prepared LiTFSI/DOL solution formed a homogeneous precursor, which was injected into batteries with a solid eutectic encapsulated cathode and Li metal anode. The polymerization reaction is illustrated in Figure S1a, Supporting Information. LiDFOB was introduced to form a solid eutectic electrolyte for preparing the cathode interface encapsulation (CIE). The solid-state characteristic of the solid eutectic electrolyte at elevated room temperature

(RT) is demonstrated by differential scanning calorimetry (DSC), as shown in Figure S2a, Supporting Information. It's worth mentioning that the CIE was solid-state when battery assemblies and the CIE was just used to wet the surface of the cathode materials, which were all for inhibiting the dissolution of CIE. Then, after curing over 10 h at RT, a solid polymer electrolyte with two different molecular weights was in situ obtained. Gel permeation chromatography (GPC) was conducted to demonstrate that low weight-averaged molecular weights (M_w) of SPEE were formed at the interface which was conducive to ionic conductivity and high M_w was formed in the bulk electrolyte which guaranteed excellent capacity of dendrite inhibition (Table S1, Supporting Information).[23,24] Thus, the nano-hierarchical SPEE was obtained. To further investigate the compatibility between CIE and SPEE, electrochemical impedance spectroscopy (EIS) and scanning electron microscope (SEM) image of the full battery fracture surface were conducted. Figure 1b shows no evident change in EIS impedance (35–40 Ω) of Li|SPEE|LiNi$_{0.8}$Co$_{0.1}$Mn$_{0.1}$O$_2$(NCM811) full batteries in comparison to the absence and presence of CIE case. And the battery fracture surface presents a well-connected interface contact (Figure 1c), indicating that the fast conduction of Li⁺ ions has remained.

The nano-hierarchical SPEE design is highly dependent on polymerization chemistry. It's important to improve the polymerization degree and reduce the initiator addition.[15,18,25] Thus, the reduced initiators should have excellent catalytic activity and stability in order to conquer the impact of porous electrodes and highly reactive metallic lithium that terminates the
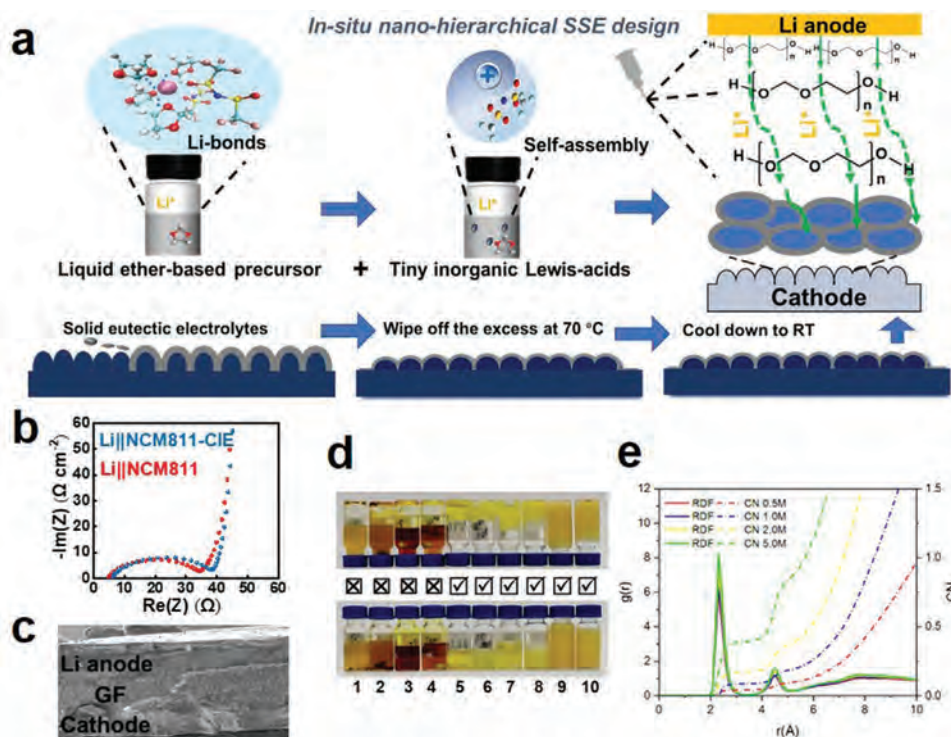
Figure 1. The nano-hierarchical SPEE design. a) Schematic illustration of the fabrication of nano-hierarchical SPEE and CIE. b) EIS spectra of Li‖NCM811 with and without CIE. c) SEM image of the Li|nano-hierarchical SPEE|NCM811-CIE battery. d) The optical photographs of the products (1: 600 ppm AlI$_3$ in DOL; 2:3000 ppm AlI$_3$ in DOL; 3:600 ppm AlI$_3$ in 2 м LiI/DOL; 4:3000 ppm AlI$_3$ in 2 м LiI/DOL; 5:600 ppm AlI$_3$ in 2 м LiTFSI/DOL; 6:600 ppm AlI$_3$ in 1 м LiTFSI/DOL; 7:600 ppm AlI$_3$ in 1 м LiFSI/DOL; 8:600 ppm AlI$_3$ in 1 м LiOTf/DOL; 9:600 ppm AlI$_3$ in 1 м NaTFSI/DOL; 10:600 ppm AlI$_3$ in 1 м KFSI/DOL). e) The RDFs and CNs obtained by MD.

**ADVANCED
SCIENCE NEWS**

www.advancedsciencenews.com

**ADVANCED
FUNCTIONAL
MATERIALS**

www.afm-journal.de

polymer chain growth of SPEE. In this context, the initiator is designed in a hybrid form. As a proof of concept, Li salts with bulk organic anions (e.g, TFSI$^-$, FSI$^-$, and OTf$^-$) were pre-dissolved in DOL solvents, as efficacious initiators should combine a counter anion with bulk ion structure and low nucleophilicity.[26,27] Thus, when an additive containing a required Lewis-acid cation is added, the pre-dissolved bulk anions can drive self-assembly with the cations to form hybrid initiators. It was demonstrated by AlI$_3$ acted as hypothetical additives and soluble LiI with small anions acted as control (Figure 1d). The polymerization is only observed in the bulk anion case.[28,29] On the other hand, the dissolved Li salts have mass of Li-bonds in Li$^+$-ether complex pairs, which will chemically activate the liquid precursor. Li-bonds were identified by classical molecular dynamics (MD) simulations. The global snapshots of four precursors are shown in Figure S3a, Supporting Information, with different concentrations. A distinct change in the distribution of Li$^+$-ethers (represent Li-bonds) was captured in the related local snapshots from the first coordination shell of Li$^+$ (Figure S3b, Supporting Information), indicating the formation of Li-bonds.[30] The radial distribution functions (RDFs) of Li-O$_{DOL}$ in different salt concentrations and the corresponding coordination number (CN) were calculated (Figure 1e).[31–34] The first spikes of RDFs increase with salt concentrations, and the platform of CN is higher, suggesting the increased number of Li-bonds.[35] To further investigate the effect of Li-bonds, 3 M KFSI/DOL, and 3 M LiFSI/DOL were as contrast. Only 3 M LiFSI/DOL was cured because of a weaker Lewis acidity of K$^+$ ion (Figure S3c, Supporting Information).[36] Consequently, the activation of Li-bonds and the self-assembly of hybrid initiators enable tiny amounts to realize the high polymerization degree. A library of inorganic Lewis-acid additives (e.g., AlI$_3$, ZnI$_2$, SnI$_4$, CuF$_2$, ZnF$_2$, SnF$_2$, AgPF$_6$, KPF$_6$, LiDFOB, and LiBF$_4$) was demonstrated to have high polymerization degree (>90%, calculated from nuclear magnetic resonance (NMR) results), as shown in Figures S4 and S5, Supporting Information.
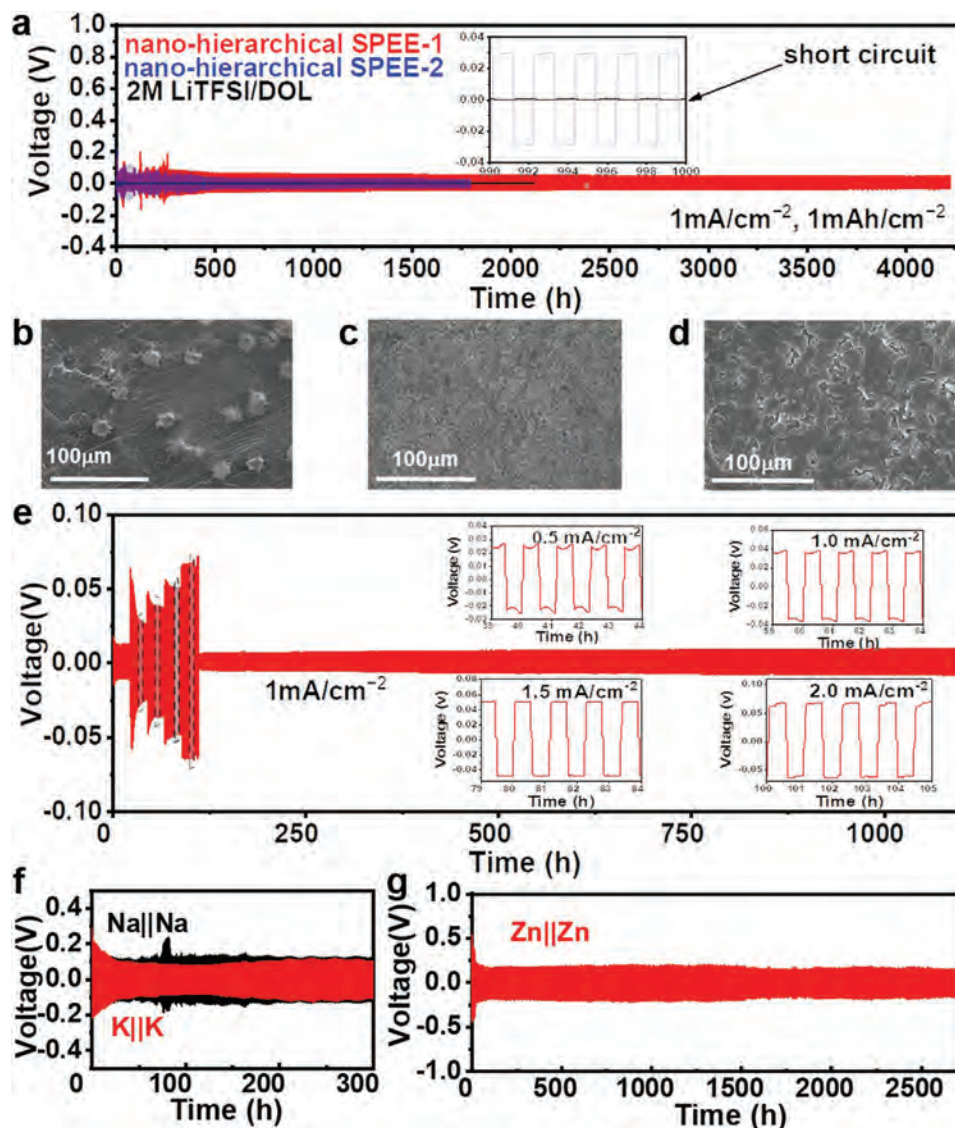
All initiator candidates have been further optimized by introducing inorganic metal compounds with Lewis-acids cations and anions simultaneously to reduce the additive amount, while the high polymerization degree of SPEE is guaranteed. In a typical experiment, AlI$_3$ was combined with LiPF$_6$ to form a binary catalysis system.[37] It's worth mentioning that AlI$_3$ is also a catalyst for the hydrolyzing reaction of LiPF$_6$ (Formula 1 in Figure S1b, Supporting Information). Furthermore, LiDFOB has remarkable thermal stability with a functionality of CEI-forming additive, which is also proposed here.[38] NMR, Raman, and Fourier transform infrared spectroscopic analysis (FTIR) were all conducted to confirm the occurrence of the polymerization reaction initiated by these two types of initiators (Figure S6a–d, Supporting Information). All results detect the distinguished changes of characteristic signals, indicating the dismission of the ring species belonged to DOL and the appearance of long-chain structures assigned to SPEEs. The polymerization degrees are over 92%. The curing time is mostly over 10 h at RT. The M_w of SPEEs obtained in our work is around 77–80 k, larger than most previously reported results, which ensures the high thermal stability of the SPEEs (Table S1, Supporting Information).[15–17] The thermogravimetric analysis (TGA) further confirmed this result (Figure S6e,f, Supporting Information).

2.2. Electrochemical Stability of Metal Anode with Nano-Hierarchical SPEE

The improved reversibility of Li plating/stripping was demonstrated by galvanostatic polarization experiments of symmetric Li cells (**Figure 2**a). The stable cycles are over 4000 and 1800 h at a current density of 1.0 mA cm^{-2}/1.0 mAh cm^{-2} in the SPEE-1 and SPEE-2 cases, respectively. The inset of Figure 2a shows the magnified image of voltage versus time curve. EIS impedance measures were simultaneously investigated during 300 cycles (Figure S7a, Supporting Information). It keeps stable around 41 Ω after 150 cycles, which further confirms that the reversible process is stable even the battery underwent several unexpected temperature fluctuations (uncontrolled ≈15 °C). In comparison, the symmetric Li cell with the liquid precursor as electrolyte exhibits a low overpotential of 3 mV. which is arisen from the formation of one or more internal short circuits (the inset of Figure 2a).[39] The lithium deposition morphology after 30 cycles presents distinct mossy Li deposits in liquid precursor case (Figure 2b). By contrast, a smooth and dense Li anode remained even after 500 cycles in both SPEE-1 and SPEE-2 cases (Figure 2c,d). The asymmetric Li∥Cu cell was performed to evaluate the CE of metallic Li anode. The average CE is 98.51% (SPEE-1) and 99.08% (SPEE-2), respectively (Figure S7b, Supporting Information), indicating the enhanced compatibility with Li anodes than the routine SPEE electrolytes. Furthermore, the Li$^+$ transference number (t_{Li^+}) was also evaluated via the electrochemical combination method.[18,40] The t_{Li^+} of SPEE is up to 0.64 (Figure S7c, Supporting Information). These results suggest that the improvement of Li plating/stripping reversibility in Li∣SPEE∣Li cells are contributed by the increased compatibility with Li anode and the favorable t_{Li^+}.

Furthermore, SPEE converted from 1 M precursors marked as SPEE(1 M) also displays amorphous state in Celgard 2400 or glass fiber membrane (GF), as measured by DSC (Figure S7d, Supporting Information). Only a glass transition peak (T_g) and a tiny melting peak (T_m) are observed, indicating the intrinsic amorphous state. Figure S7e,f, Supporting Information, also provides the DSC results of SPEE(1 M) in absence of porous membrane and SPEE converted from 2 M precursors without porous framework. Without porous framework, SPEE converted from 2 M precursors marked as SPEE(2 M) displays a similar curve, indicating the intrinsic amorphous state. By contrast, SPEE(1 M) displays two typical peaks associated with T_m and recrystallization (T_c) of polymers, indicating the crystallization is formed in absence of porous membrane.[12,16] NMR results (Figure S7g,h, Supporting Information) verify that the polymerization degree is almost unaffected by porous membrane.

The reduction of Li-salt concentration is in favor of ionic conductivities. The temperature dependence of ionic conductivities is shown in Figure S7i, Supporting Information, indicating the remarkable ionic conductivities. The rate performance of Li∣SPEE(from 1 M precursors)∣Li was conducted to reveal the compatibility of metallic Li anode. However, cells suffer a short circuit when 1.5 w% LiDFOB is added (Figure S8a, Supporting Information). It's mainly due to the reduced Li-bonds effect in 1 M LiTFSI/DOL compared with 2 M LiTFSI/DOL. Increasing the initiators up to 2.5 w%, SPEE-2 displays remarkable rate performance with modest Li metal
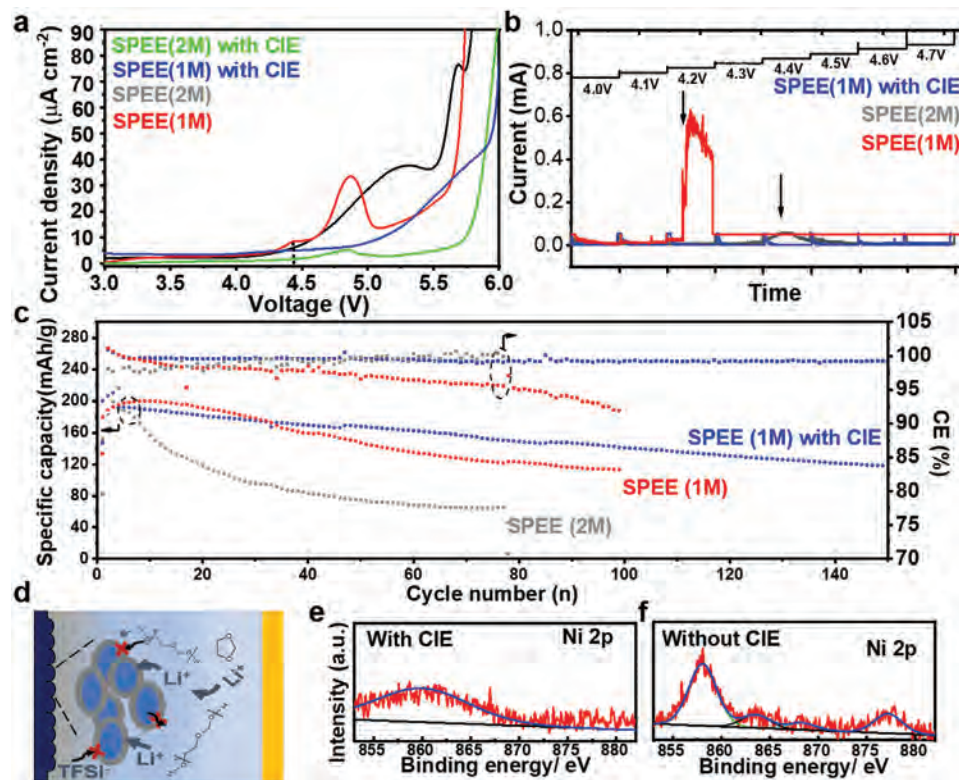
**ADVANCED
SCIENCE NEWS**
www.advancedsciencenews.com

**ADVANCED
FUNCTIONAL
MATERIALS**
www.afm-journal.de

Figure 2. Cycling stability of symmetric metallic cells. a) Voltage versus time of Li‖Li cells operated under 1.0 mA cm^{-2} with 1.0 mAh cm^{-2}. The insert plot shows magnifications of the specific cycles. SEM image of metallic Li anode harvested from batteries after 30 cycles in the liquid precursors (b), 500 cycles in SPEE-1 (c), and 500 cycles in SPEE-2 (d). e) Rate performance of Li|SPEE(1 M)|Li. f,g) Voltage versus time in symmetric Na, K, and Zn cells at 0.1 mA cm^{-2}.

stripping/deposition overpotentials (≈55 mV, 2.0 mA cm^{-2}, magnified views in Figure 2e). A stable cycling performance at a current density of 1.0 mA cm^{-2}/4.0 mAh cm^{-2} is also provided (over 2000 h, Figure S8b, Supporting Information). In comparison, about 10 times overpotentials are displayed in 2 M precursors case (Figure S8c, Supporting Information). Thus, this strategy was extended into other NaTFSI and KFSI, as shown in Figure 1c. NMR results demonstrate high polymerization degrees (Figure S5, Supporting Information). Voltage profiles of symmetric cells with SPEE(Na$^+$ and K$^+$) at the current density of 0.1 mA cm^{-2} are provided in Figure 2f,g also provides the voltage–time profile of Zn|SPEE(Zn^{2+})|Zn cell. The stable cycles are over 3000 h at a current density of 0.1 mA cm^{-2}, demonstrating a promising application in other metal batteries.[41,42]

2.3. Stability of High-Voltage Cathode Systems with Nano-Hierarchical SPEE

The electrochemical stability of SPEE at the oxidative potentials was evaluated by linear sweep voltammetry (LSV), and electrochemical floating test.[43] **Figure 3**a shows that SPEE(1 M) and SPEE(2 M) with CIE show rather low current flow beyond 5 V versus Li$^+$/Li^0, and 5.7 V versus Li$^+$/Li^0, respectively. By contrast, the electrochemical stability windows narrow to 4.5 V even the polymer is converted from 1.5 w% LiDFOB in 2 M LiTFSI/DOL precursors, which the concentrated Li salts and LiDFOB are both in favor of the oxidative stability in full batteries. Furthermore, the oxidative current platforms arise from 4.3 V in both SPEE without CIE cases, before the steep current increase due to electrolyte decomposition occurs. Results

**ADVANCED
SCIENCE NEWS**

www.advancedsciencenews.com

**ADVANCED
FUNCTIONAL
MATERIALS**

www.afm-journal.de

Figure 3. Cycling stability with 4.0 V-above cathodes. a) LSV curves. b) Electrochemical floating analysis. c) Li‖NMC811 batteries work at 0.2 C, and d) the illustration of protected strategies for NCM811 cathodes. e,f) XPS analyses of the surface of Li anode.

reported in Figure 3b further demonstrates that only SPEE with CIE can remain the limited leakage currents from 4.0 to 4.7 V. Without CIE, the in situ polymerization of 1 M LiTFSI/DOL in Li‖NCM batteries encounter a large leakage current at 4.2 V, and the in situ polymerization of 2 M LiTFSI/DOL just retards this decomposition to 4.4 V. Based on these results, it suggests that CIE design can improve the oxidative stability of SPEE efficiently.

Li‖NCM811 batteries were conducted further to characterize the improved stability. The cell exhibits high CEs (>99%) over 100 cycles without a rapid capacity attenuation when the encapsulated cathode is used (Figure 3c). On the contrary, low CEs are observed in SPEE(1 M) and rapid capacity attenuation is subjected in SPEE(2 M) without using CIE. The encapsulated cathode would inhibit the side-reactions between SPEE and Ni-rich nickel-cobalt-manganese oxides cathode system, involving the oxidative reaction of poly-ether at high-voltage battery systems and irreversible fluorination between TFSI⁻ and transition metals. The possible protecting mechanism is shown in Figure 3d.[18,38,44] X-ray photoelectron spectroscopy (XPS) analysis was conducted to probe the surface of Li anodes harvested from batteries after 30 cycles (Figure 3e,f). With CIE, signal belonged to Ni element is detected. In comparison, the signal in the absence of CIE case becomes stronger, indicating that the dissolution of transition metal from cathode side is more serious and results in the evident dissolution of transition metal from cathode side to the surface of Li anode.[45–47] Thus, the impeded effect of the nano-hierarchical SPEE with CIE improves the cycle stability.

The long-cycling performance of the nano-hierarchical SPEE design with CIE was further investigated by Li‖LiCoO₂(4.25 V) batteries. **Figure 4**a shows the repeated cyclic voltammetry (CV) curves of Li‖LiCoO₂-CIE battery in the first 5 cycles. The high overlapping indicates the reversible charge/discharge process. Figure 4b displays high reversibility of charge/discharge profiles with a specific capacity of 132 mAh g⁻¹ at 0.5 C and 91.7% capacity retention over 200 cycles at 15 °C. The CEs are all up to 99%. When the operating temperature is up to 45 °C, high-rate performances are obtained (Figure S9c, Supporting Information). Simultaneously, super-long cycle life is obtained with 89% capacity retention over 700 cycles (Figure 4c). The in situ polymerization of 1 M LiTFSI/DOL, on the other hand, delivers a rapid capacity decay with low CEs in Li‖LiCoO₂ without CIE.

2.4. Cycling-Stability of Wide-Temperature Operation with Nano-Hierarchical SPEE

Apart from the cycling stability of SSE in 4 V-above class cathode systems, wide-temperature operation is another key indicator for practical applications. The type of initiator is important for the thermostability of SPEE due to the similar structure of polyoxymethylene that could encounter depolymerization in acidic media. Even though LiPF₆ and LiBF₄ are effective Lewis-acidic initiators, these two Li salts are both thermolabile. Furthermore, in-built SPEE design always has residual initiators and liquid precursors. 1.0 w% LiPF₆, and LiBF₄ were chosen to
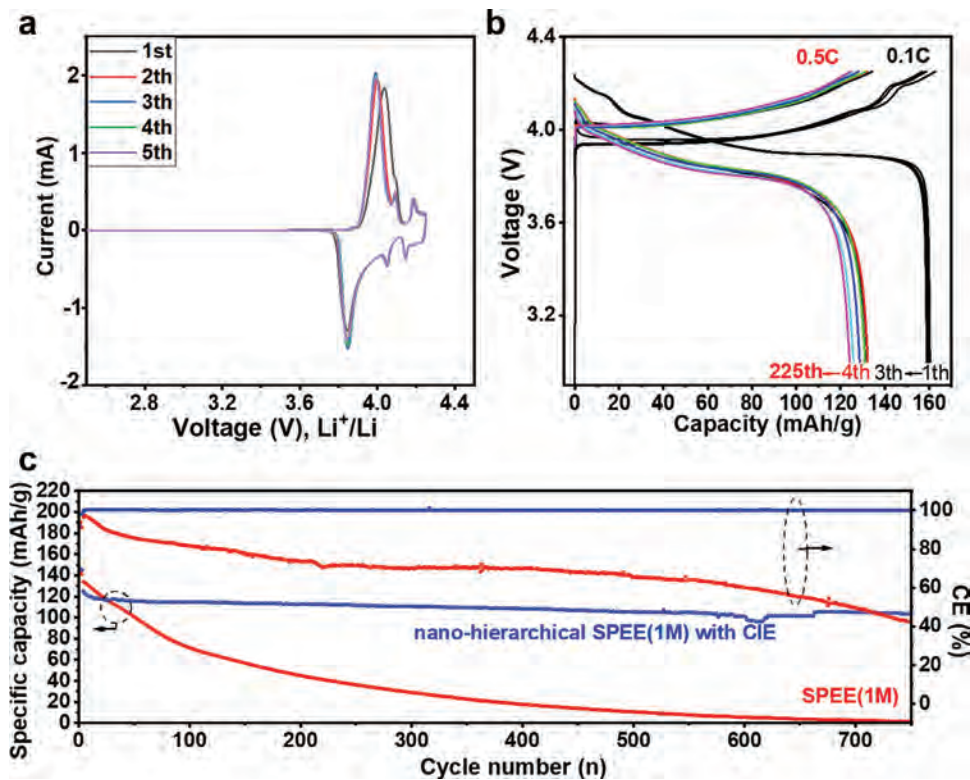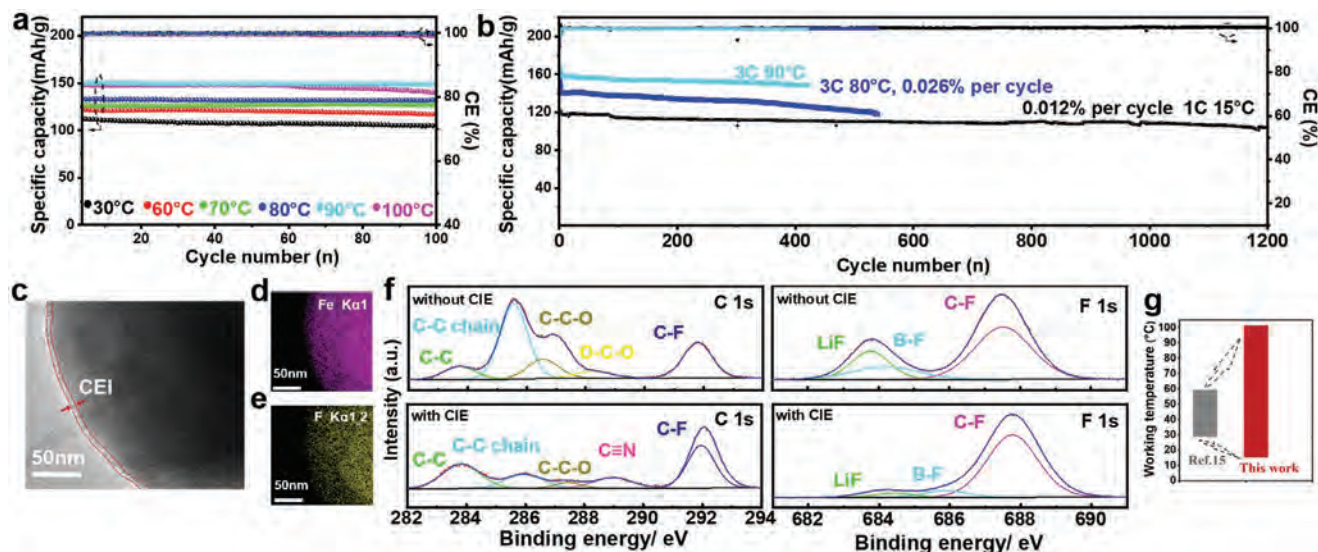
Figure 4. Long-cycling performance of 4.0 V-above cathodes. a) CV of Li|SPEE(1 M)|LiCoO$_2$ at RT, and b) the related discharge/charge profiles. c) Long-term cycling at 0.5 C and 45 °C using SPEE (1 M) without CIE as a control (A charge/discharge rate of 1 C corresponds to a specific current of 274 mA g^{-1}).

illustrate the already reported thermo-sensitivity of only 70 °C. Even though sudden increase of EIS isn't observed from 50 to 90 °C by investigating ss‖ss and Li‖Li cells (Figure S10a,d, Supporting Information), the Li‖Li cells suffered battery cracking after two days standing at 100 °C (Figure S10e, Supporting Information). Furthermore, recurrence of part-fluidities after the two SPEEs standing for 6 months validates the instability (Figure S10f,g, Supporting Information). TGA was conducted to investigate the thermal stability of the two SPEEs comparing with the original states (Figure S11, Supporting Information). The results indicate that the polymer chains of the two SPEEs are degraded gradually. When the two SPEEs were stored at 80 °C, M_w became small (Table S1, Supporting Information). A more rigorous investigation is conducted in Li‖LiFePO$_4$ full batteries, which displays no capacity after few cycles when LiPF$_6$ and LiBF$_4$ are as initiators (Figure S12a, Supporting Information). In comparison, stable cycles at 80 °C beyond 200 cycles with a reversible capacity of 162 mAh g^{-1} at 1 C are both observed in both SPEE-1 and SPEE-2 case (Figure S12b, Supporting Information).

In addition, the additive amount also impacts the thermostability of SPEE. Figure S12b, Supporting Information, demonstrates that even though LiDFOB has a high thermostability, an inferior long-cycling at 80 °C has been found when increasing LiDFOB from 1.5 to 5.0 w%.[48] Thus, it's necessary to reduce the additive amount. In fact, our two recommended types of initiators enable the effective dose is tiny and the residual amounts would further reduce because of the reaction between additives

and Li electrode, as illustrated in Formula 2–4 of Figure S1b, Supporting Information. To investigate this, Li|SPEE(600 ppm AlI$_3$)|Li batteries at 50 °C were conducted. Elemental mappings of Li anodes obtained from cells at different cycling indicate uniform distribution of Al–Li nano-alloying and surface affinity of I$^-$, and their enrichment at the interface during 50 cycles (Figures S13 and S14, Supporting Information). Consequently, the synergistic effect of initiator type, additive amount, and the element enrichment at the interface ensures the cycling of Li|SPEE(A$_{300}$/P$_{600}$)|LiFePO$_4$ at elevated temperature. The batteries can work from 50 to 90 °C batteries (Figure S15, Supporting Information).[15]

With CIE, the temperature tolerance of Li|nano-hierarchical SPEE|LiFePO$_4$ batteries at 3 C is enhanced up to 100 °C (**Figure 5**a). The long-cycling performances are provided in Figure 5b and Figure S16, Supporting Information. At 15 °C, a specific capacity of 118 mAh g^{-1} at 1 C is presented with 87.2% capacity retention after 1200 cycles. The SPEEs also maintain stable battery cycling of 80 and 90 °C for over 520 and 420 cycles at 3 C with high CEs (>99%), respectively. Conversely, low CEs (<98%) are delivered after 200 cycles at 80 °C when the batteries are without using CIE (Figure S12c, Supporting Information). Even though 2 M precursors are used to improve the oxidative stability, a thick and irregular CEI is formed after 50 cycles without CIE, as detected by transmission electron microscopy (TEM) (Figure S17, Supporting Information). Comparatively, the surface of encapsulated cathodes has a thin CEI, indicating the SPEE isn't subjected to significant

**ADVANCED
SCIENCE NEWS**

www.advancedsciencenews.com

**ADVANCED
FUNCTIONAL
MATERIALS**

www.afm-journal.de

Figure 5. Wide temperature operation with long cycles. a) The tolerance of Li|SPEE|LiFePO$_4$ batteries as a function of temperature worked at 3 C; b) long-term cycling. c) TEM image of cathode harvested from Li|SPEE|LiFePO$_4$-CIE after 50 cycles and the related EDS mapping (d,e). f) XPS analyses of cathode surface after 10 cycles. g) Comparison of the work with previously reported polyether-based SPEs.

decomposition (Figure 5c) and the related EDS mappings in Figure 5d,e). XPS results further confirm that a lower content of Li–F containing compound derived from LiTFSI and C—C chain containing organic species derived from the ether-based electrolyte are detected in the CIE case (Figure 5f).[49–51] Thus, the nano-hierarchical SPEE demonstrates long-life cycles of full batteries with wide-temperature operation, from 15 to 100 °C, as shown in Figure 5g.

To demonstrate the abuse tolerance of the as-obtained SPEE, rate performances of Li||LiCoO$_2$ batteries with a high active cathode material loading of 7.0 mg cm^{-2} were investigated. The batteries display a reversible capacity of 118 mAh g^{-1} at 0.2 C rate and RT (**Figure 6**a). Furthermore, the SPEE with CIE enables outstanding high-rate performance of Li||LiFePO$_4$

cells (108 mAh g^{-1}, at 5 C and RT) compared with the absence of CIE case, indicating that the batteries have an intimate interface contact and improved ionic conduction between two electrodes (Figure 6b). As these accomplishments, a pouch cell blended nearly 180° successfully lighting three custom-made lights was conducted at RT (Figure 6c), indicating that the integral construction of the batteries also endows remarkable flexibility for the full batteries with the SPEE. Figure 6d also shows the working lights powered by button batteries at 100, 80, and 15 °C, respectively. They all demonstrate the reinforced thermodynamic and electrochemical stabilities of the in-bulit SPEE. All improvements in our SPEE design are compared in Figure S18 and Table S2, Supporting Information.
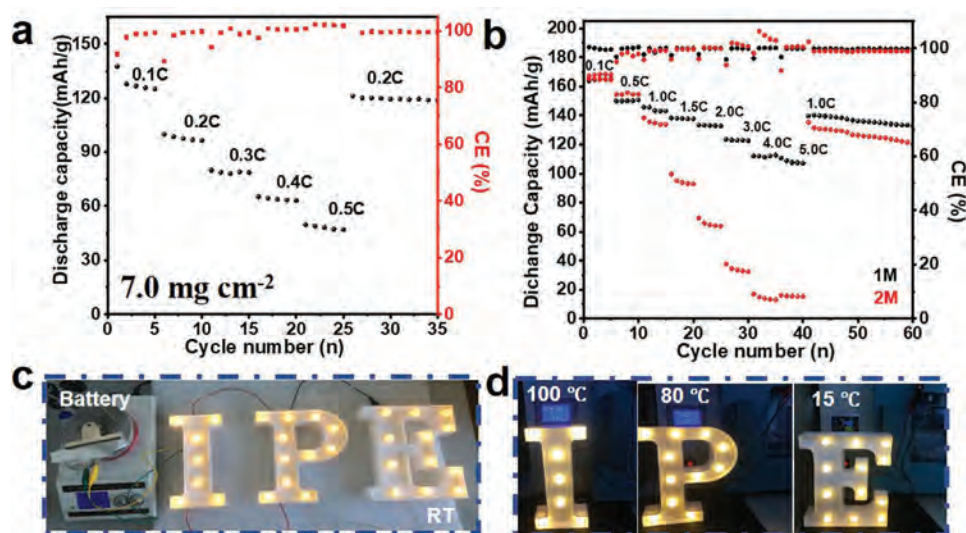
Figure 6. Abuse tolerance of full batteries. Rate performances of a) Li|SPEE|LiCoO$_2$-CIE with an active material loading of 7.0 mg cm^{-2}; b) Li||LiFePO$_4$ with and without CIE cells. c,d) The optical images of battery powering lights with abuse operation.

**ADVANCED
SCIENCE NEWS**
www.advancedsciencenews.com

**ADVANCED
FUNCTIONAL
MATERIALS**
www.afm-journal.de

3. Conclusions

In summary, this work demonstrates a nano-hierarchical quasi-solid-state polymer electrolyte with solid eutectic for the interface protection on the surface of the cathodes via in situ polymerization of traditional liquid ether-based precursors. The nano-hierarchical SPEE presents highly compatible electrolyte/electrode interfaces in thermodynamic and electrochemical aspects, showing a promising wide application in Li, Na, K, and Zn metal batteries. Outstanding lifespan of wide-temperature Li‖LiFePO$_4$ batteries (15–100 °C, at 3 C) and other 4 V-above batteries (Li‖LiCoO$_2$ and Li‖LiNi$_{0.8}$Co$_{0.1}$Mn$_{0.1}$O$_2$) were demonstrated by using the nano-hierarchical SPEE. Our study paves an unexplored scope for developing practical solid-state metal batteries (SSMBs) that meet the demands for wide-temperature applicability, high-energy density, long lifespan, and scale manufacture.

4. Experimental Section

Materials and Chemicals: 1,3-dioxolane (DOL) and Li salts were all provided by Shanghai Song Jing New Energy Technology Co., Ltd. ZnI$_2$, MgI$_2$, SnI$_4$, CuF$_2$, ZnF$_2$, SnF$_4$, AgPF$_6$, and KPF$_6$ were all obtained from Aladdin.

Synthesis of Nano-Hierarchical SPEE and CIE: A desired stoichiometric amount of LiTFSI salts was dissolved into DOL with vigorous stirring overnight to get LiTFSI/DOL solution. Excess water in the solution was dislodged through fresh metallic lithium standing for 7 days. Then, a desired stoichiometric number of initiators was added into the solution to prepare the precursors at RT. Finally, the precursors were injected into batteries with Li metal as an anode. For multivalent metal ions (e.g., Zn^{2+}), their Lewis acidities are stronger than Li$^+$, resulting in a violent polymerization. Thus, 1.5 w% LiDFOB in 1 M LiTFSI/DOL and 1 M Zn(TFSI)$_2$/DOL were prepared with equal volume ratio to obtain SPEE containing Zn^{2+}.

For CIE, the solid eutectic electrolyte was obtained by mixing 5 mol% LiDFOB in SN at 70 °C and then stirring overnight to get a transparent solution. The melted solid eutectic electrolyte was dropped on the surface of the cathodes. The cathodes were only interracially wetted by the solid eutectic electrolytes, extra solution was removed at 70 °C, ensuring solid property of SSMBs. Finally, the treated cathodes were cooled naturally to RT. All the processes of cathode treatment were conducted in the argon gas-filled glove box. It's worth mentioning that porous and alkalescent cathodes cause the incomplete polymerization while the CIE also ensures the formation of nano-hierarchical SPEE in a full battery due to the solid encapsulation.

Battery Assembly and Electrochemical Measurements: Coin 2025-type cells were assembled using Li foil as an anode and GF (Whatman) or Celgard 2400 as separator in argon gas-filled glove box. LiFePO$_4$, LiCoO$_2$, and NCM cathodes were prepared by mixing the active particles with polyvinylidene fluoride and Super P (Aladdin) in a weight ratio of 8:1:1 with appropriate amount NMP and mixed with magnetic stirring. Finally, the cathode slurry coated on a carbonated aluminum foil was dried at 80 °C overnight in a vacuum oven. The cathodes were controlled at 2–3 mg·cm^{-2} of active material. The high active material loading of LiCoO$_2$ was 7.0 mg cm^{-2}. Galvanostatic discharge/charge tests were performed using a Neware battery tester. Li‖LiFePO$_4$, Li‖ LiCoO$_2$, and Li‖NMC were operated with the voltage range between 2.5 and 4.0 V, 3.0 and 4.25 V (and high voltage LiCoO$_2$: 3.0–4.45 V), 2.5 and 4.3 V versus Li/Li$^+$, respectively. The cycle test of Li‖LiFePO$_4$ at high temperatures was operated between 2.5 and 4.2 V to overcome the big polarization. The electrochemical floating experiments were conducted in Li‖NCM batteries, which were charged to 4.0 V first, then held at progressively higher voltages, each for a period of 10 h. Metrohm Auto lab M204 electrochemical workstation

was used for CV (0.1 mV s^{-1}), LSV (a scan rate of 0.1 mV s^{-1}), and EIS. The test conditions of EIS were tested in a frequency range of 10^5–0.1 Hz with amplitude of 5 mV. Their ionic conductivities were tested in the stainless steels (ss)|SPEE+GF|ss cell assemblies and calculated from the EIS measurements according to the following equation: $\sigma = d/(R_b \cdot S)$. Here, σ is for the ionic conductivity, d is the thickness between two stainless steels, S is the contact area between the electrolyte and stainless steels, and R_b refers to the bulk resistance, and the nickel foam was used to replace the stainless-steel spring when cell assembled. The test conditions of EIS were open-circuit voltage in a frequency range of 10^5–1 Hz with amplitude of 5 mV. The test conditions of EIS were open-circuit voltage in a frequency range of 10^5–1 Hz with amplitude of 5 mV. The Li CE was performed in Li‖Cu cells.[10] An amount of lithium (Q_T, 1 mAh cm^{-2}, 0.1 mA cm^{-2}) was first deposited on Cu electrode. Then, the Li‖Cu cell was plated/stripped with a small capacity (Q_C, 0.1 mAh cm^{-2}, 0.1 mA cm^{-2}) for n cycles ($n = 10$). Afterward, the remaining Li (Q_S) on Cu substance was charged until the cut-off voltage of 1.0 V. Finally, the average CE was estimated as:

$$CE_{average} = \frac{nQ_C + Q_S}{nQ_C + Q_T} \tag{1}$$

The t_{Li^+} of the SPEE was tested by a conventional electrochemical method combined with direct current (DC) polarization and alternating current impedance measurements for Li|SPEE|Li symmetrical cells at RT. The t_{Li^+} was calculated as:

$$t_{Li^+} = \frac{I_S(\Delta V - I_0 R_1^0)}{I_0(\Delta V - I_S R_1^S)} \tag{2}$$

where ΔV is the applied voltage (5 mV), I_o and I_s were the initial current and steady current, respectively, during DC polarization process. R_1^0 and R_1^S were the charge transfer resistances of Li‖Li cell before and after DC polarization, respectively.

Materials Characterization: For ^{1}H NMR and ^{13}C NMR characterization, dimethyl sulfoxide-d$_6$ was used as solvent and they were performed on Bruker advance III HD 600 MHz NMR spectrometer. FTIR was recorded using a Thermo Scientific spectrometer. Raman spectroscopy was tested using a Renishaw in Via confocal Raman microscope. GPC was performed by first dissolving the synthesized SPEEs in DMF (GC) and eluting the solutions in a Waters ambient temperature GPC equipped with triple detection capability for absolute polymer molecular weight determination. DSC was tested using a Q1000 Modulated DSC (TA Instruments). TGA (Setaram Labsys) was performed under an N$_2$ atmosphere at a temperature increase of 5 °C min^{-1}. SEM and elemental mappings were achieved using Hitachi SU8020 (Japan). TEM was conducted by JEM-2100HR, Japan. XPS spectrometer was achieved using Thermo Fisher Scientific ESCALAB 250Xi system with Al Ka radiation ($h\nu = 1486.6$ eV) as the X-ray source.

Simulation: Four concentrations of MD simulations were carried out with the freely-available LAMMPS code.[52] Initial systems were constructed with cubic boxes using the PACKMOL package.[53] All non-bonded van der Waals interactions were based on the Lennard-Jones (LJ) potential together with the Lorentz-Berthelot combining rule $\sigma_{ij} = \frac{(\sigma_i + \sigma_j)}{2}$ and $\varepsilon_{ij} = \sqrt{\varepsilon_i \varepsilon_j}$ for the LJ size and energy parameters, respectively. Meanwhile, the electrostatic interactions were treated with Particle-Particle Particle-Mesh (PPPM) method. The equation of motions was evolved using a Velocity-Verlet integrator with a timestep of 2 fs. All systems were first equilibrated at 298 K for more than 10 ns including energy minimizations, relaxation in the NVT ensemble followed by a period of NPT runs. Berendsen thermostat and barostat were employed to regulate the temperature and pressure of the systems with damping constants of 100 and 1000 fs, respectively.[54] The production runs for the computation of the micro-structures were performed in the NPT ensemble for 10 ns at a constant pressure of 1 bar and temperature of 298 K after the equilibration. The RDFs and CN were calculated from production runs.

[1] J. Lopez, D. G. Mackanic, Y. Cui, Z. Bao, *Nat. Rev. Mater.* **2019**, *4*, 312.

[2] Z. Zou, Y. Li, Z. Lu, D. Wang, Y. Cui, B. Guo, Y. Li, X. Liang, J. Feng, H. Li, C. W. Nan, M. Armand, L. Chen, K. Xu, S. Shi, *Chem. Rev.* **2020**, *120*, 4169.

[3] P. M. Attia, A. Grover, N. Jin, K. A. Severson, T. M. Markov, Y. H. Liao, M. H. Chen, B. Cheong, N. Perkins, Z. Yang, P. K. Herring, M. Aykol, S. J. Harris, R. D. Braatz, S. Ermon, W. C. Chueh, *Nature* **2020**, *578*, 397.

[4] S. Chen, K. Wen, J. Fan, Y. Bando, D. Golberg, *J. Mater. Chem. A* **2018**, *6*, 11631.

[5] P. Jaumaux, Q. Liu, D. Zhou, X. Xu, T. Wang, Y. Wang, F. Kang, B. Li, G. Wang, *Angew. Chem., Int. Ed.* **2020**, *59*, 9134.

[6] P. Jaumaux, J. Wu, D. Shanmukaraj, Y. Wang, D. Zhou, B. Sun, F. Kang, B. Li, M. Armand, G. Wang, *Adv. Funct. Mater.* **2020**, *31*, 2008644.

[7] Z. Li, H. Zhang, X. Sun, Y. Yang, *ACS Energy Lett.* **2020**, *5*, 3244.

[8] A. Sumboja, J. Liu, W. G. Zheng, Y. Zong, H. Zhang, Z. Liu, *Chem. Soc. Rev.* **2018**, *47*, 5919.

[9] Q. Zhou, J. Ma, S. Dong, X. Li, G. Cui, *Adv. Mater.* **2019**, *31*, 1902029.

[10] D. Zhou, D. Shanmukaraj, A. Tkacheva, M. Armand, G. Wang, *Chem* **2019**, *5*, 2326.

[11] J. Qiu, X. Liu, R. Chen, Q. Li, Y. Wang, P. Chen, L. Gan, S. J. Lee, D. Nordlund, Y. Liu, X. Yu, X. Bai, H. Li, L. Chen, *Adv. Funct. Mater.* **2020**, *30*, 1909392.

[12] L. Ma, S. Chen, X. Li, A. Chen, B. Dong, C. Zhi, *Angew. Chem., Int. Ed.* **2020**, *59*, 23836.

[13] Z. Zou, Y. Li, Z. Lu, D. Wang, Y. Cui, B. Guo, Y. Li, X. Liang, J. Feng, H. Li, C. W. Nan, M. Armand, L. Chen, K. Xu, S. Shi, *Chem. Rev.* **2020**, *120*, 4169.

[14] Q. Liu, B. Cai, S. Li, Q. Yu, F. Lv, F. Kang, Q. Wang, B. Li, *J. Mater. Chem. A* **2020**, *8*, 7197.

[15] J. Zhou, T. Qian, J. Liu, M. Wang, L. Zhang, C. Yan, *Nano Lett.* **2019**, *19*, 3066.

[16] Q. Zhao, X. Liu, S. Stalin, K. Khan, L. A. Archer, *Nat. Energy* **2019**, *4*, 365.

[17] K. Khan, Z. Tu, Q. Zhao, C. Zhao, L. A. Archer, *Chem. Mater.* **2019**, *31*, 8466.

[18] C. Z. Zhao, Q. Zhao, X. Liu, J. Zheng, S. Stalin, Q. Zhang, L. A. Archer, *Adv. Mater.* **2020**, *32*, 1905629.

[19] H.-H. Ryu, N.-Y. Park, T.-C. Noh, G.-C. Kang, F. Maglia, S.-J. Kim, C. S. Yoon, Y.-K. Sun, *ACS Energy Lett.* **2020**, *6*, 216.

[20] X. Pan, H. Sun, Z. Wang, H. Huang, Q. Chang, J. Li, J. Gao, S. Wang, H. Xu, Y. Li, W. Zhou, *Adv. Energy Mater.* **2020**, *10*, 2002416.

[21] Y. Han, S. Heng, Y. Wang, Q. Qu, H. Zheng, *ACS Energy Lett.* **2020**, *5*, 2421.

[22] Y. Q. Zhang, Y. Tian, Y. Xiao, L. J. Miara, Y. Aihara, T. Tsujimura, T. Shi, M. C. Scott, G. Ceder, *Adv. Energy Mater.* **2020**, *10*, 1903778.

[23] K. Pan, L. Zhang, W. Qian, X. Wu, K. Dong, H. Zhang, S. Zhang, *Adv. Mater.* **2020**, *32*, 2000399.

[24] F. Xian, J. Li, Z. Hu, Q. Zhou, C. Wang, C. Lu, Z. Zhang, S. Dong, C. Mou, G. Cui, *Chem. Commun.* **2020**, *56*, 4998.

[25] J. G. Han, K. Kim, Y. Lee, N. S. Choi, *Adv. Mater.* **2019**, *31*, 1804822.

[26] Y. Yamashita, M. Okada, M. Hirota, *Die Macromolecular Chem* **1969**, *122*, 284.

[27] M. Okada, Y. Yamashita, Y. Ishii, *Die Macromolecular Chem* **1966**, *94*, 181.

[28] L. Ma, M. S. Kim, L. A. Archer, *Chem. Mater.* **2017**, *29*, 4181.

[29] Z. Wang, Z. Xu, X. Jin, J. Li, Q. Xu, Y. Chong, C. Ye, W. Li, D. Ye, Y. Lu, Y. Qiu, *J. Mater. Chem. A* **2020**, *8*, 9218.

[30] X. Chen, Y. K. Bai, C. Z. Zhao, X. Shen, Q. Zhang, *Angew. Chem., Int. Ed.* **2020**, *59*, 11192.

[31] X. Wang, F. Chen, G. M. A. Girard, H. Zhu, D. R. MacFarlane, D. Mecerreyes, M. Armand, P. C. Howlett, M. Forsyth, *Joule* **2019**, *3*, 2687.

[32] C. V. Amanchukwu, X. Kong, J. Qin, Y. Cui, Z. Bao, *Adv. Energy Mater.* **2019**, *9*, 1902116.

[33] J. Holoubek, M. Yu, S. Yu, M. Li, Z. Wu, D. Xia, P. Bhaladhare, M. S. Gonzalez, T. A. Pascal, P. Liu, Z. Chen, *ACS Energy Lett.* **2020**, *5*, 1438.

[34] X. Ren, S. Chen, H. Lee, D. Mei, M. H. Engelhard, S. D. Burton, W. Zhao, J. Zheng, Q. Li, M. S. Ding, M. Schroeder, J. Alvarado, K. Xu, Y. S. Meng, J. Liu, J.-G. Zhang, W. Xu, *Chem* **2018**, *4*, 1877.

[35] J. Alvarado, M. A. Schroeder, T. P. Pollard, X. Wang, J. Z. Lee, M. Zhang, T. Wynn, M. Ding, O. Borodin, Y. S. Meng, K. Xu, *Energy Environ. Sci.* **2019**, *12*, 780.

[36] Y. Xu, H. Dong, M. Zhou, C. Zhang, Y. Wu, W. Li, Y. Dong, Y. Lei, *Small Methods* **2019**, *3*, 1800349.

[37] M. Ishikawa, S.-i. Machino, M. Mor, *J. Electroanal. Chem.* **1999**, *473*, 279.

[38] L. Yu, S. Guo, Y. Lu, Y. Li, X. Lan, D. Wu, R. Li, S. Wu, X. Hu, *Adv. Energy Mater.* **2019**, *9*, 1900257.

[39] Y. Song, L. Yang, W. Zhao, Z. Wang, Y. Zhao, Z. Wang, Q. Zhao, H. Liu, F. Pan, *Adv. Energy Mater.* **2019**, *9*, 1900671.

[40] W. Tang, S. Tang, X. Guan, X. Zhang, Q. Xiang, J. Luo, *Adv. Funct. Mater.* **2019**, *29*, 1900648.

[41] W. Du, E. H. Ang, Y. Yang, Y. Zhang, M. Ye, C. Li, *Energy Environ. Sci.* **2020**, *13*, 3330.

[42] L. Ma, S. Chen, N. Li, Z. Liu, Z. Tang, J. A. Zapien, S. Chen, J. Fan, C. Zhi, *Adv. Mater.* **2020**, *32*, 1908121.

[43] Z. Zhang, L. Hu, H. Wu, W. Weng, M. Koh, P. C. Redfern, L. A. Curtiss, K. Amine, *Energy Environ. Sci.* **2013**, *6*, 1806.

[44] C. F. N. Marchiori, R. P. Carvalho, M. Ebadi, D. Brandell, C. M. Araujo, *Chem. Mater.* **2020**, *32*, 7237.

[45] J. Y. Liang, X. D. Zhang, X. X. Zeng, M. Yan, Y. X. Yin, S. Xin, W. P. Wang, X. W. Wu, J. L. Shi, L. J. Wan, Y. G. Guo, *Angew. Chem., Int. Ed.* **2020**, *59*, 6585.

**ADVANCED
SCIENCE NEWS**

www.advancedsciencenews.com

**ADVANCED
FUNCTIONAL
MATERIALS**

www.afm-journal.de

[46] Y. Cui, Y. Wang, S. Gu, C. Qian, T. Chen, S. Chen, J. Zhao, S. Zhang, *J. Power Sources* **2020**, *453*, 227852.

[47] S. Wang, S. Chen, W. Gao, L. Liu, S. Zhang, *J. Power Sources* **2019**, *423*, 90.

[48] D. Wang, H. Liu, M. Li, D. Xia, J. Holoubek, Z. Deng, M. Yu, J. Tian, Z. Shan, S. P. Ong, P. Liu, Z. Chen, *Nano Energy* **2020**, *75*, 104889.

[49] H. Wu, Y. Xu, X. Ren, B. Liu, M. H. Engelhard, M. S. Ding, P. Z. El-Khoury, L. Zhang, Q. Li, K. Xu, C. Wang, J. G. Zhang, W. Xu, *Adv. Energy Mater.* **2019**, *9*, 1902108.

[50] J. Fu, X. Ji, J. Chen, L. Chen, X. Fan, D. Mu, C. Wang, *Angew. Chem., Int. Ed.* **2020**, *59*, 22194.

[51] H. Zhang, X. Judez, A. Santiago, M. Martinez-Ibañez, M. Á. Muñoz-Márquez, J. Carrasco, C. Li, G. G. Eshetu, M. Armand, *Adv. Energy Mater.* **2019**, *9*, 1900763.

[52] S. Plimpton, *J. Comput. Phys.* **1995**, *117*, 1.

[53] L. Martínez, R. Andrade, E. G. Birgin, J. M. Martínez, *J. Comput. Chem.* **2009**, *30*, 2157.

[54] H. J. C. Berendsen, J. P. M. Postma, W. F. van Gunsteren, A. DiNola, J. R. Haak, *J. Chem. Phys.* **1984**, *81*, 3684.

ChemElectroChem

Research Article
doi.org/10.1002/celc.202200641

Chemistry
Europe
European Chemical
Societies Publishing

www.chemelectrochem.org

Synergistic Coupling of $Li_{6.4}La_3Zr_{1.4}Ta_{0.6}O_{12}$ and Fluoroethylene Carbonate Boosts Electrochemical Performances of Poly(Ethylene Oxide)-Based All-Solid-State Lithium Batteries

Lu Zhang,[a] Zhitao Wang,[a] Hu Zhou,[b] Xiaogang Li,[a] Qian Liu,[a] Ping Wang,[c] and Aihua Yuan*[a]

All-solid-state lithium batteries (ASSLBs) with poly(ethylene oxide) (PEO)-based composites solid-state electrolytes have received much attention owing to their higher energy density and better safety compared with conventional liquid electrolytes. However, ASSLBs with PEO-based solid-state electrolytes generally suffer from severe capacity degradation and interface transfer obstacles during the charge/discharge process. In this work, fluoroethylene carbonate (FEC) is employed as a reducing additive to in-situ form LiF-rich and stable solid-state electrolyte interface (SEI). Benefiting from the integrated advantages of $Li_{6.4}La_3Zr_{1.4}Ta_{0.6}O_{12}$ (LLZTO) and FEC binary additives, the number of lithium-ion transference increases to 0.48, which facilitates the stable cycling of Li‖Li symmetrical batteries over 900 h at 0.1 mA cm^{-2}. The synergistic interplay of LLZTO and FEC constructs a stable LiF-rich SEI film, effectively addressing the interfacial problems caused by lithium dendrites and promoting the transport of Li ions. Therefore, the high ionic conductivity and self-healing anode-electrolyte interface are achieved. This study provides a facile and economical strategy to solve the problem of the lithium-electrolyte interface. It is of great scientific significance for the development of dendrite-free solid-state lithium metal batteries.

Introduction

Empowering green energy to reach its full potential is significant for addressing the growing environmental problems. Increasing demand for rechargeable battery storage and charging efficiency stimulates the dramatic development of lithium-ion batteries (LIBs) with high energy density.[1] Lithium is the lightest metal with the highest specific capacity (3860 mAh g^{-1}) and the lowest chemical potential (Li$^+$/Li couple -3.05 V vs. standard hydrogen electrode, SHE), which is a promising anode candidate of high-performance lithium-ion batteries.[2] However, lithium metal anode suffers from uneven deposition/stripping in organic electrolytes during the electrochemical cycles and the formed lithium dendrites penetrate the separator and cause the combustion or explosion.[3] Along with the outstanding safety performance and high energy density, the development of all-solid-state lithium batteries (ASSLBs) has emerged as a radical solution to simultaneously take count of

the above issues. As the vital component of ASSLBs, the solid-state electrolyte (SSE) faces a great challenge in the aspects of ionic conductivity and interfacial compatibility.[4] Based on great progress in the past decades, composite solid-state electrolytes (CSEs) have been employed to consistently solve the ionic conductivity by combining the integrated merits of polymers and ceramics.[5]

Poly(ethylene oxide) (PEO)-based electrolytes with excellent flexibility and processing property are particularly receiving much attention recently.[6] Various ceramic fillers have been introduced into PEO-based electrolytes to prepare CSEs with high ionic conductivity.[7] For instance, Zhuang et al. prepared the PEO-LiTFSI-10 wt.%$Li_{6.75}La_3Zr_{1.75}Ta_{0.25}O_{12}$ with an ionic conductivity of 3.03×10^{-4} S cm^{-1} at 55 °C.[8] Zhou et al. reported PEO-LiTFSI-$Li_{1.3}Al_{0.3}Hf_{1.7}(PO_4)_3$ with the ionic conductivity of 1.3×10^{-4} S cm^{-1} at 30 °C, and the assembled ASSLB retained with 80% capacity after 200 cycles.[9] Nevertheless, the large-scale applications of CSEs are still hampered by some urgent issues. It is found that CSEs may react with lithium metal and then cause a continuous decomposition during the cycles, resulting in poor interfacial compatibility and serious capacity degradation of ASSLBs. Thus, it is vitally necessary to optimize the interface between CSEs and lithium metal.[10]

LiF-rich solid-state electrolyte interface (SEI) has been documented to be significantly effective to inhibit the growth of lithium dendrites and stabilize the electrolyte-anode interface.[11] Fan et al. introduced a LiF-rich SEI layer between CSEs and lithium metal anode through a simple coating/infiltrating of LiFSI into Li_3PS_4.[12] Besides, Wang et al. reported the formation of LiF-rich SEI on lithium metal by modifying lithium metal with copper lithium fluoride (CuF_2) based on the

[a] L. Zhang, Z. Wang, Dr. X. Li, Q. Liu, Prof. Dr. A. Yuan
School of Environmental and Chemical Engineering
Jiangsu University of Science and Technology
Zhenjiang 212003, PR China
E-mail: aihua.yuan@just.edu.cn
[b] Dr. H. Zhou
School of Materials Science and Technology
Jiangsu University of Science and Technology
Zhenjiang 212003, PR China
[c] Dr. P. Wang
Institute of Medicine & Chemical Engineering
Zhenjiang College
Zhenjiang, 212028, PR China

ChemElectroChem

Research Article
doi.org/10.1002/celc.202200641

**Chemistry
Europe**
European Chemical
Societies Publishing

reaction of CuF_2 and lithium.[13] However, these strategies require extra steps to treat the lithium and electrolyte separately. Therefore, it is extremely urgent to develop an effective approach to boost the interface performance of solid-state electrolytes. Fluoroethylene carbonate (FEC) as a functional additive is commonly used in the field of liquid electrolytes.[14] Specifically, FEC can combine with Li^+ to form a solvation sheath and allow for a homogeneous lithium deposition.[15] Accordingly, Li et al. introduced FEC into $Li_{0.35}La_{0.55}TiO_3$ backbone-based CSE to enable the self-healing of the CSE/Li interface.[16] Therefore, FEC holds a great promise as an additive to improve the solid electrolyte-lithium interface in the system of CSEs.

In this work, the combination of FEC and PEO-LiTFSI-$Li_{6.4}La_3Zr_{1.4}Ta_{0.6}O_{12}$ (LLZTO) affords the formation of CSEs with high ionic conductivity and interfacial stability. Especially, LLZTO inhibits the crystallization of PEO to increase the ionic conductivity. In addition, FEC as a plasticizing agent further reduces the crystallinity of PEO and weakens the interaction between Li^+ and PEO chains.[17] Meanwhile, FEC is preferentially reduced to in-situ form a stable LiF-rich SEI, boosting the interfacial stability.[18] Combining the intrinsic and integrated advantages of LLZTO and FEC, the synergistic coupling of both components results in a high ionic conductivity, excellent interfacial stability, and superior cycling ability of CSEs. The ion conductivity is 1.06×10^{-3} S cm^{-1} at 60°C and 7.74×10^{-5} S cm^{-1} at 30°C. The lithium-ion transference number of electrolytes increases to 0.48 at 60°C. Symmetric Li∥Li batteries are capable of cycling for 900 h, along with a low voltage hysteresis of 57 mV at 0.1 mA cm^{-2} at 60°C. The LiFePO$_4$(LFP)∥Li battery delivers a steady capacity of 118 mAh g^{-1} for 400 cycles at 60°C.

Results and Discussion

Figure S1a–c show the electrochemical performances of PEO-based electrolyte with different concentrations of LLZTO. The results indicate that PEO-10 wt.% LLZTO CSE displays the best performance with an ionic conductivity of 6.36×10^{-5} S cm^{-1} at 30°C and 8.36×10^{-4} S cm^{-1} at 60°C. This is mainly because the addition of an appropriate amount of LLZTO particles inhibits the crystallization of PEO and increases the amorphous region.

Exceeding above addition may lead to the agglomeration of LLZTO and phase separation between ceramic particles and the matrix, which eventually decreases the ionic conductivity. This is consistent with the previous reports.[19] In addition, the symmetric Li∥Li battery with PEO-10 wt.% LLZTO CSE exhibits the best cycle stability over 700 h and the lowest polarization voltage of 48 mV. Likewise, the LEP∥Li battery with PEO-10 wt.% LLZTO CSE delivers a superior performance. The discharge specific capacity is 139.5 mAh g^{-1} after 100 cycles at 0.2 C, with 91.3% of the maximum specific capacity during the whole cycling process. Figure S1d–f show the electrochemical performances of PEO-based electrolyte with different concentrations of FEC. The PEO-2 wt.% FEC CSE exhibits the highest ionic conductivity of 1.60×10^{-5} S cm^{-1} at 30°C and 3.29×10^{-4} S cm^{-1} at 60°C. In addition, the Li–Li battery with PEO-2 wt.% FEC CSE presents a polarized voltage of 58 mV and keeps stable for 300 h. In comparison, the LEP∥Li battery with PEO-2 wt.% FEC CSE has a discharge capacity of 128.8 mAh g^{-1} after 100 cycles, with 85.6% of the maximum specific capacity. FEC improves battery performance by inhibiting parasitic side reactions between the cathode and electrolyte, and the excessive FEC may lead to concentrated polarization.[20] The above results reveal that the optimization of 10 wt.% LLZTO and 2 wt.% FEC affords the superior battery performance. Thus, 10 wt.% LLZTO and 2 wt.% FEC are used in the subsequent experiments.

Figure 1a shows the optical photographs of as-prepared CSEs. With the addition of LLZTO and FEC, the color of CSEs is gradually converted from translucent to milky white. At the same time, CSEs maintain the excellent structural flexibility (Figure 1b, Figure 1c). Scanning electron microscopy (SEM) image of CSEs membrane prepared by tape casting is shown in Figure 1d–g. The surface of the doped electrolyte remains smooth and clear without apparent voids. The elements are uniformly distributed without severe agglomeration according to the elemental mapping distribution (Figure S2). In addition, both LLZTO and FEC greatly improved the tensile strength of PEO-based solid-state electrolytes, P–L–F electrolyte approaching 7.0 MPa compared to 1.8 MPa for P-Only (Figure S3). The boosting of mechanical strength can effectively relieve the growth of lithium dendrites.[21]
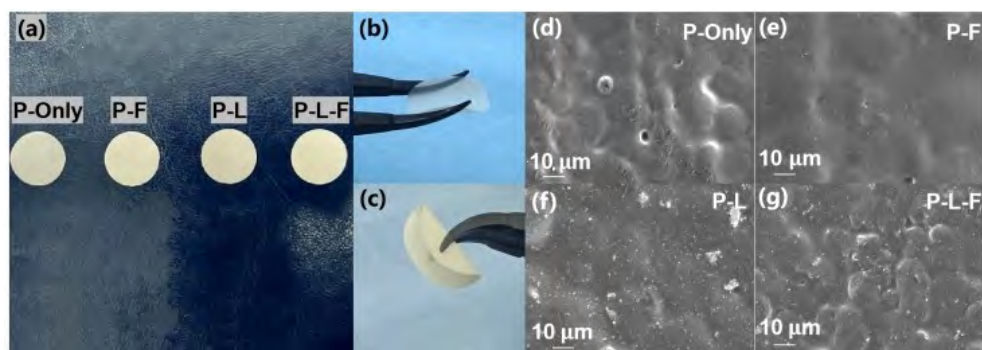
Figure 1. Digital photos of (a) CSEs; the membranes of (b) P-Only and (c) P–L–F electrolytes; SEM images of CSEs with (d) P-only, (e) P–F, (f) P–L and (g) P–L–F.

ChemElectroChem

Research Article
doi.org/10.1002/celc.202200641

**Chemistry
Europe**
European Chemical
Societies Publishing

The ionic transport of PEO-based solid-state electrolytes can be improved by reducing the crystallinity of PEO and increasing the proportion of amorphous phases.[22] As shown in X-ray diffraction (XRD) patterns (Figure 2a), the addition of LLZTO and FEC significantly reduces the intensity of characteristic peaks at 19.5° and 23.7° as compared to those of the electrolytes with PEO-only, P–F, and P–L. The result indicates the decrease of PEO crystallinity and the increase of ionic conductivity.[22b] Fourier transform infra-red (FT-IR) spectra are also performed to investigate the effects of LLZTO and FEC on the electrochemical performances of PEO-based solid-state electrolytes (Figure 2b). The presence of CH_2 deformation peak at 1342 cm^{-1} and C–O–C stretching triple peak at 1100 cm^{-1} (split into three peaks at 1190 cm^{-1}, 1110 cm^{-1}, and 1050 cm^{-1}) reveals the high crystallinity of PEO. Compared to the electrolyte with P-Only, the peaks assigned to the C–O–C stretching mode for the P–F, P–L, and P–L–F electrolytes show a negligible shift in peak position except an apparent decrease in intensity.[23] It suggests the interaction between -OH groups of LLZTO and oxygen group of PEO has weakened the complexation of Li$^+$. FEC can combine with Li$^+$ to form solvation and weaken the coordination of Li$^+$. Meanwhile, the glass transition temperature (T_g) is the threshold value at the beginning of segment movement. The low T_g also facilitates an increase in ionic conductivity. As shown in Figure 2c and Figure S4, where the T_g drops from −42 °C to −43 °C after the addition of both LLZTO and FEC. The melting temperatures (T_m) of P–L–F electrolyte membranes are significantly lower than those of the P–L electrolyte, and similar results are obtained on P–F versus P-Only (Table S1).

Figure 2d illustrates the thermal stability of CSEs. The CSEs are relatively stable up to 300 °C, where the PEO and LiTFSI are decomposed at 350–450 °C and 400–450 °C, respectively. In comparison, LLZTO particles are thermally stable above 600 °C. Therefore, the LLZTO filler can act as a safety barrier between the electrodes under extreme conditions, and FEC does not affect the thermal stability. Overall, the P–L and P–L–F electrolytes have superior thermal stability and fully meet the safety requirements for the development of lithium battery applications.

Ionic conductivity is a critical parameter to evaluate the performance of solid-state electrolytes. The conductivity can be calculated from the electrochemical impedance plots at different temperatures (20–80 °C.) (Figure S5). The ionic conductivity of P–L, P–F, and P–L–F electrolytes increases by varying degrees compared to the P-Only electrolyte (Figure 3a). The P–L–F electrolyte has the highest ionic conductivity of 1.06× 10^{-3} S cm^{-1} at 60 °C and 7.74×10^{-5} S cm^{-1} at 30 °C. The conductive mechanism of PEO-LiTFSI can be summarized by the combination and fracture of EO–Li bonds and molecular chain movement, which is restricted to amorphous regions. In the presence of LLZTO, Li$^+$ can transport through PEO, LLZTO, and the interfaces between PEO and LLZTO.[5d,24] Moreover, LLZTO inhibits the crystallization of PEO to significantly increase the ionic conductivity.[22] Meanwhile, FEC as a plasticizing agent has pro-lithium properties. Coupled with the theoretical calculations, the binding energy of FEC with Li$^+$ is shown in Table S2. The lower LUMO energy of FEC favors the preferential reduction. Also, the value of reduction electrode potential (E_{re}) is calculated to be 0.56 eV by theoretical calculation. FEC competes benignly with the EO unit in PEO for binding under the action of the carbonyl group, thus facilitating the charge transport and the results are consistent with the XRD data. Besides, the curves have an inflection point around 50 °C which attributes to the crystallinity of PEO at higher temperatures. In other words, the composite electrolyte has distinctively different ionic conductivities in the region of 50–80 °C and 30–50 °C, which agree with the previous results.[7a] The ionic conductivity

Figure 3. (a) Arrhenius plots and (b) electrochemical windows of CSEs; DC polarization curves of the electrolytes with (c) P-Only, (d) P–F, (e) P–L, and (f) P–L–F at 60 °C (Inset: AC impedance spectra of symmetric batteries before and after polarization).
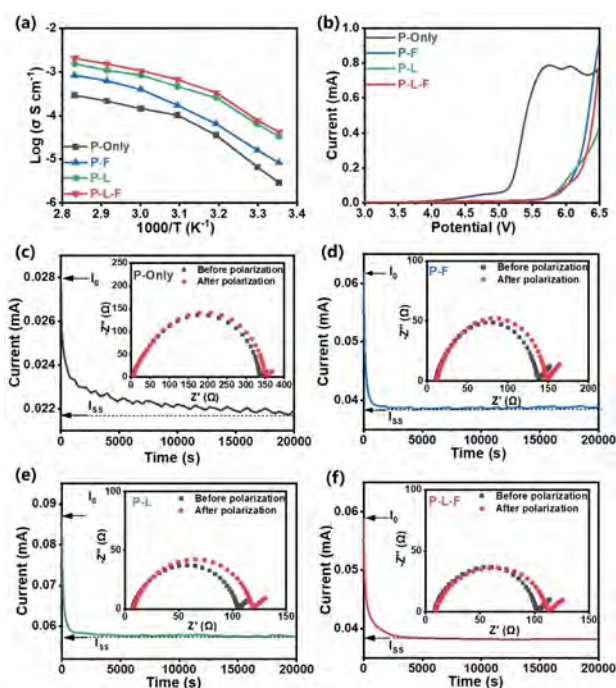

Figure 2. (a) XRD patterns, (b) FT-IR spectra, (c) DSC curves, and (d) TGA curves of CSEs.

ChemElectroChem

Research Article
doi.org/10.1002/celc.202200641

**Chemistry
Europe**
European Chemical
Societies Publishing

(σ) and activation energy(E_a) of CSEs are listed in Table S3 and the activation energy of P–L–F is calculated to be 0.30 eV at 60 °C.

Electrolytes can contact both anodic and cathodic active materials at the same time, which might result in side reactions if the working electric potentials of active materials fall beyond the electrochemical stability windows. The electrochemical windows of CSEs measured at 60 °C are shown in Figure 3b. The decomposition potential of the P-Only electrolyte starts at 4.1 V. When LLZTO and FEC are added, the decomposition potentials of the electrolytes raised to 5.2 V and 5.4 V, respectively. Notably, the decomposition potential of the P–L–F electrolyte raised to 5.5 V when both FEC and LLZTO are added (Table S4). This may be ascribed to the high potential of LLZTO as well as the Lewis acid-base interaction between electrolyte ion species and surface groups of LLZTO, which enhances the salt dissociation and stabilizes the anion.[25] The dense SEI film formed by FEC can stabilize the electrolyte/electrode interface by blocking the side reactions. It indicates that the P–L–F electrolyte has the widest electrochemical window and the strongest electrochemical stability, suggesting that P–L–F can be used in most battery cathodes such as LiFePO$_4$ (3.8), LiNiMn (4.8), etc.

The lithium-ion transference number (t_{Li^+}) is an important criterion for evaluating the cycle performance of ASSLB. The t_{Li^+} close to 1 means that the electrolyte is more efficient in transferring charge between the positive and negative electrodes. The direct current (DC) polarization curves and electrochemical impedance spectroscopy (EIS) plots before and after DC polarization experiments at 60 °C for the CSEs are shown in Figure 3c–f. The response of the current to applied polarization is observed to decrease initially and remain stable in the following measurements. In addition, the impedance increases variously after DC polarization. The small t_{Li^+} value forms an ion concentration gradient within the electrolyte, indicating a poor performance for ASSLBs. The calculated t_{Li^+} for P-Only electrolyte is 0.14. After the incorporation of LLZTO and FEC, the P–L and P–F electrolytes are 0.27 and 0.29, respectively. When both FEC and LLZTO are added, the value of t_{Li^+} for the P–L–F electrolyte is 0.48, significantly superior to the previous studies (Table S5).[6b,7a] Both LLZTO and FEC can facilitate the increase of lithium-ion transference number. LLZTO as active fillers interacts with the chain fragments of PEO polymer to promote the local chain relaxation and segmental movement of the polymer.[24] FEC as plasticizing agents can enhance the flexibility of PEO to boost the movement of the fragments and promote the adequate dissociation of LiTFSI. So, more Li$^+$ will be liberated from the binding of anions, and these free Li$^+$ ions further combine with PEO for bulk transport, improving the ionic conductivity and lithium-ion transference number.

The ability to inhibit the growth of lithium dendrites is critical for solid-state electrolyte-based ASSLB with lithium metal as the anode. The Li symmetric batteries are assembled to investigate the CSE–Li interfacial stability by Li–Li dissolution/deposition. The current-voltage distributions for CSEs at a current density of 0.1 mA cm^{-2} are shown in Figure 4a. The P-only electrolyte delivers a fluctuated polarization voltage and
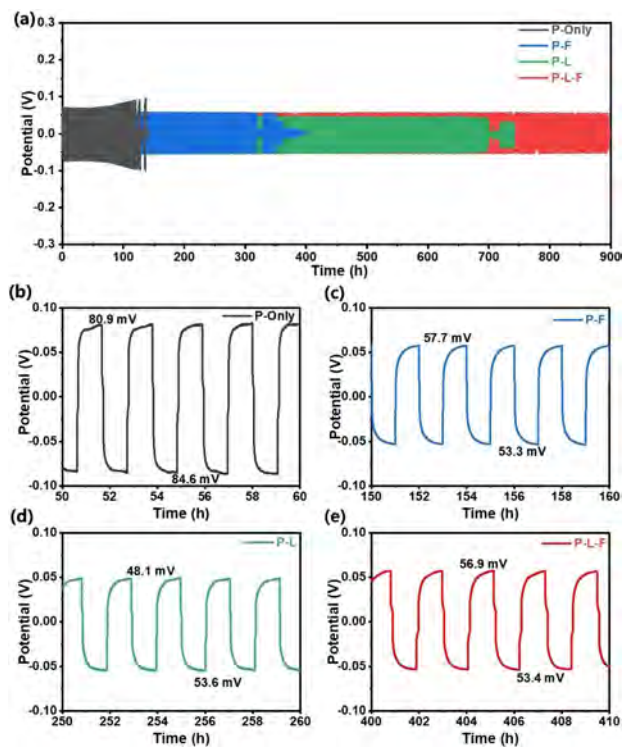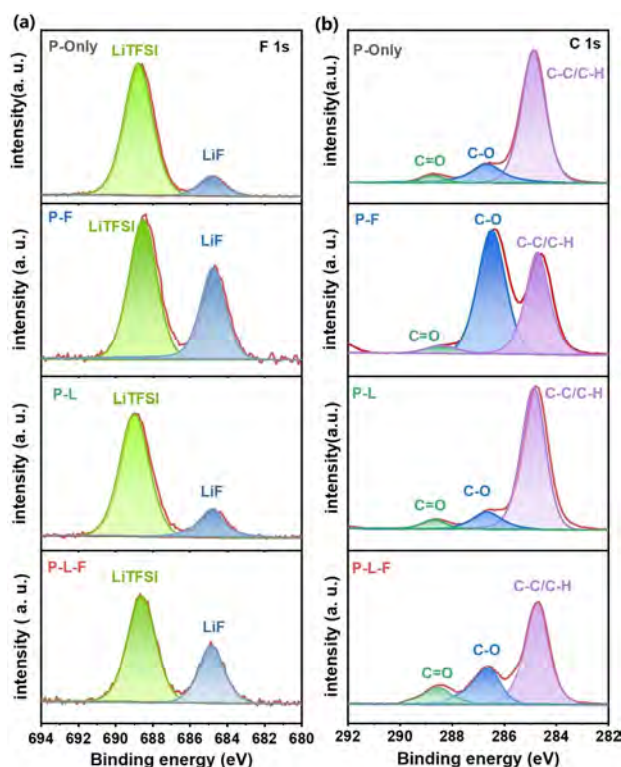

Figure 4. (a) Symmetric Li∣∣Li batteries test of lithium plating/stripping for CSEs at 0.1 mA cm^{-2} under 60 °C, and the voltage profiles of batteries with (b) P-Only, (c) P–F, (d) P–L, and (e) P–L–F.

shows a short circuit in a short period due to the penetration of lithium dendrites (Figure 4b). The P–F electrolyte delivers a stable voltage response of 58 mV during 300 h of internal cycles (Figure 4c), and the P–L electrolyte affords a stable voltage response of 48 mV during 690 h of internal cycles (Figure 4d). In addition, the P–L–F electrolyte exhibits a very stable voltage response of 57 mV during 900 h of initial cycles at 0.1 mA cm^{-2} (Figure 4e) and shows a stable voltage response of 85 mV over 300 h at 0.2 mA cm^{-2} (Figure S6). The above results demonstrate a favorable electrochemical stability for the P–L–F electrolyte against Li metal. This suggests that a considerably stable and Li$^+$ conductive SEI layer may be generated from PEO-based composite solid electrolyte with LLZTO and FEC additives, which is more effective to suppress side reactions during the Li dissolution/deposition process. In general, FEC can form solvation sheath with Li$^+$, which enables uniform lithium deposition and prevents the growth of lithium dendrites. Zhang et al. has determined from SEAD, XPS, and EDS characterizations that LiF and LiN$_x$O$_y$ are uniformly mixed and dispersed in the SEI component generated by FEC, providing a rich interface for rapid diffusion of lithium ions.[16a] Li et al. also confirmed that FEC could form a weaker chemical bond FEC-Li$^+$ with lithium ions during the cycling, and this coordination played an important role in the self-healing process at the interface.[16b] More experimental and theoretical calculations prove above results, where the high reduction potential of FEC allows a preferential formation of stable LiF-rich SEI film, promoting the interfacial stability.[16c–f]

ChemElectroChem

Research Article
doi.org/10.1002/celc.202200641

Chemistry
Europe
European Chemical
Societies Publishing

For better understanding the synergistic effect of LLZTO and FEC on regulating Li plating/stripping, the composition of SEI layer in each electrolyte is examined by X-ray photoelectron spectroscopy (XPS). Similar peak positions of C, O, and F are observed for the SEI layer with CSEs (Figure S7). As shown in Figure 5a, the F 1s spectra of CSEs can be fitted and divided into two peaks assigned to TFSI⁻ and LiF. With the addition of FEC, the F 1s spectra for P–F and P–L–F electrolytes show a high peak intensity at 684.8 eV related to LiF. It can be inferred that the SEI layer formed on the surface of both electrolytes contains a significant amount of LiF because of the FEC reduction. According to the previous studies, the SEI derived from FEC is featured with LiF which has a high Young's modulus of about 64.9 Gpa to suppress lithium dendrites.[11b,14c] The large TFSI⁻ anion at 688.8 eV is delocalized chargeable and has a weak bond to Li⁺. The peak intensity of TFSI⁻ is reduced after the addition of LLZTO, which is due to the fact that LLZTO promotes the preferential decomposition of LiTFSI, and more Li⁺ becomes free from the bondage of anions.[19] This free-Li⁺ couple with PEO to realize the effective transport in bulk PEO. An appropriate amount of LiF is beneficial for reducing the interfacial impedance and improving the interfacial stability, which is also consistent with the EIS analyses and t_{Li}^+ results discussed above.
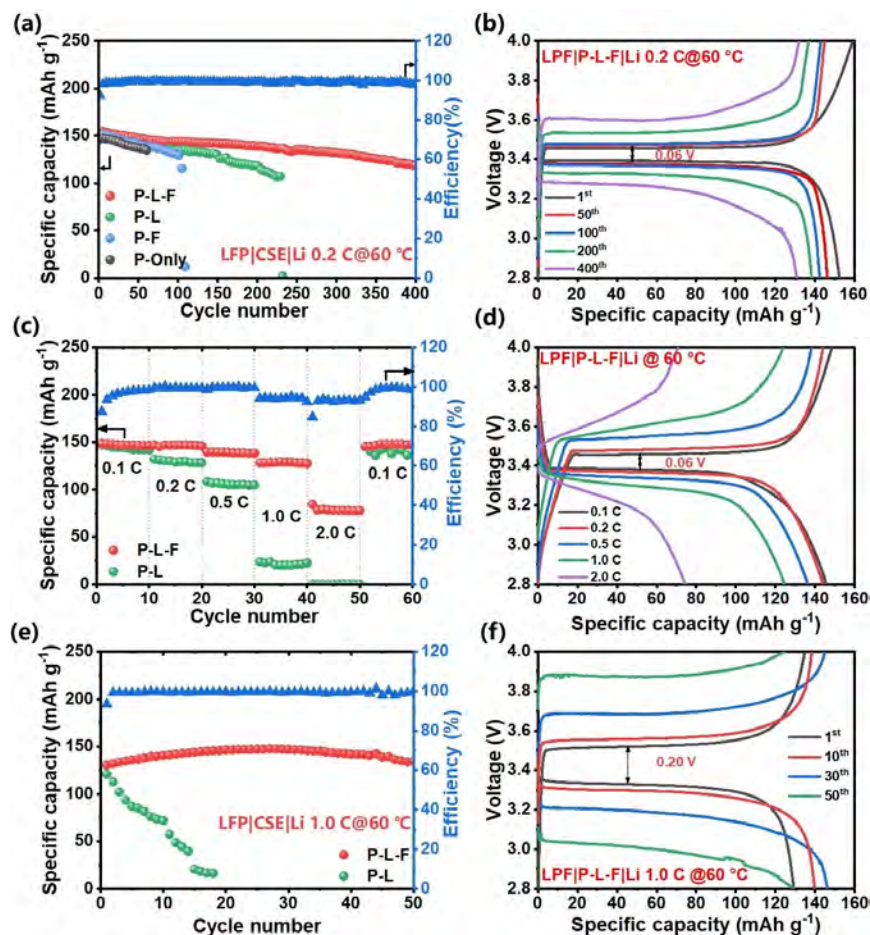
Figure 5b shows the XPS C1s spectra of the composite solid electrolyte, which are fitted into three types: C=O (288.8 eV), C–O (286.2 eV), and C–C/C–H (284.8 eV). The presence of C=O bonds is related to LiCO₃ as well as the decomposition of FEC.

The prominent increase of intensity for the C=O peak suggests an increase of Li⁺ conductive inorganic species.[15a] The peak intensity of C–C/C–H is significantly reduced, indicating that FEC preferentially reduces to form a stable SEI film and inhibits the decomposition of electrolytes. Meanwhile, the compact SEI with high inorganic components facilitates the charge transfer as well as prevents the continuous decomposition of electrolyte,[18] thereby promoting the charge transference at the electrolyte interface and decreasing the capacity decay during subsequent high voltage cycles. Benefiting from the synergistic coupling of LLZTO and FEC, an SEI layer with LiF and inorganic species can be formed to stabilize the lithium cathode/electrolyte interface, further improving the stability and ionic conductivity of electrolyte for efficient Li⁺ transportation.

To evaluate the feasibility of the practical application of CSEs in solid-state lithium batteries, the LEP‖Li ASSLB is assembled using the commercial LFP as cathode and lithium as the negative electrode. Figure 6a shows a comparison of the cycling performance and coulombic efficiency at a current density of 0.2 C (1.0 C = 170 mAh g⁻¹) at 60 °C. The batteries with P-Only electrolyte deliver an initial discharge capacity of 146.3 mAh g⁻¹, together with an extremely poor cycling stability (Figure S8a) and a large polarization of 0.15 V (Figure S8b). The batteries with P–F electrolyte deliver an initial discharge capacity of 150.5 mAh g⁻¹ with a capacity retention of 85.6% after 100 cycles. The coulomb efficiency remains stable with a polarization of 0.09 V during the cycling (Figure S8c, Figure S8d). The capacity is near zero at the 119th cycle, indicating that the battery has failed by lithium dendrites. The batteries with P–L electrolyte deliver an initial discharge capacity of 146.8 mAh g⁻¹ with a capacity retention of 91.3% after 100 cycles and a stable Coulombic efficiency (Figure S8e). Figure S8f shows that the charge-discharge voltage curves become unstable at the 100th cycle, which predicts the followed failure of the battery. The batteries with P–L–F electrolyte delivered an initial discharge capacity of 153.4 mAh g⁻¹. The reversible capacity is maintained at 143.6 mAh g⁻¹ with a capacity retention rate of 93.63% after 100 cycles, 139.1 mAh g⁻¹ with a capacity retention rate of 90.68% after 200 cycles, and 118.8 mAh g⁻¹ with a capacity retention rate of 77.44% after 400 cycles. The coulombic efficiencies are consistently above 98%. The cycle life has an apparent improvement compared to the reported PEO-based solid-state electrolytes (Table S6). Specifically, the all-solid-state battery exhibits a superior long-term cycling and rate capability performances to the other ceramic-blended PEO-based composite solid-state electrolytes in the presence of FEC, strongly demonstrating the self-healing mechanism of FEC during the charge-discharge process.[16b] Figure 6b shows the corresponding charge/discharge curves of the battery with P–L–F electrolyte, which can be identified at the corresponding typical charge/discharge platforms of LFP at around 3.38/3.45 V. Compared to the performance of the ASSLB with P–L electrolyte, the addition of FEC results in a significant increase in battery performance, indicating that FEC alleviates the battery deterioration situation with PEO-based solid-state electrolytes.

Figure 5. High-resolution XPS spectra of (a) F 1s and (b) C 1s in CSEs. The samples were obtained from symmetric Li‖Li batteries cycled at 0.1 mA cm⁻² for 10 cycles.

ChemElectroChem

Research Article
doi.org/10.1002/celc.202200641

Chemistry Europe
European Chemical
Societies Publishing

Figure 6. (a) Cycling performance and Coulomb efficiency of Li|CSEs|LiFePO₄ at 0.2 C under 60 °C; (b) the corresponding charge-discharge curves of Li|P–L-F|LiFePO₄ at 0.2 C under 60 °C; (c) rate capability at various current densities of Li|P–L-F|LiFePO₄ and Li|P–L|LiFePO₄ at 60 °C; (d) the corresponding charge-discharge curves under different current rates of Li|P–L-F|LiFePO₄ under 60 °C; (e) cycling performance and Coulomb efficiency, and (f) the corresponding charge-discharge curves of Li|P–L-F|LiFePO₄ at 1.0 C under 60 °C.

Poor rate capability, one of the main drawbacks of the lithium-rich cathode, is usually attributed to the excessive oxidation of the electrolyte at high voltage and the complicated side reaction on the cathode surface. Figure 6c shows the rate capabilities of LFP|P–L-F|Li and LFP|P–L|Li at 60 °C with the rates ranging from 0.1 C to 2.0 C. The batteries with P–L–F electrolyte exhibit a specific capacity of 148.6 mAh g⁻¹ at 0.1 C, 146.8 mAh g⁻¹ at 0.2 C, and 139.4 mAh g⁻¹ at 0.5 C, 128.2 mAh g⁻¹ at 1.0 C, and 78.9 mAh g⁻¹ at 2.0 C. The capacity can be quickly recovered to 147.7 mAh g⁻¹ when the rate returns to 0.1 C. However, the rate performance of the battery with P–L electrolyte is significantly worse. This is evidence of high-rate stability for ASSLB with P–L–F composite electrolyte. Figure 6d in the charge and discharge curves at various rates of the battery with P–L–F electrolyte. The batteries present two charge voltage plateaus at around 3.38 and 3.46 V under the operation of 0.1 C, corresponding to the Fe^{2+}/Fe^{3+} redox couple reactions on the cathode. Significant improvements in cycling efficiency and stability compared to P–L electrolytes attribute to the high ionic conductivity and lithium-ion transference number of P–L–F. Compared to the polarization voltage

of the P–L electrolyte, the SEI film generated by the addition of FEC does not increase the electrolyte resistance and interfacial resistance. A comparison of the cycling performances at a current density of 1.0 C at 60 °C are shown in Figure 6e and Figure 6f, where the P–L–F electrolyte is stable for more than 50 cycles. The above results reveal that the battery with P–L–F electrolyte affords a superior cycling performance and holds a promise for fabricating practical solid-state lithium batteries.

Actually, LLZTO and FEC synergistically produce positive effects on the improvements of ionic conductivity and stability to lithium. On the one hand, LLZTO significantly improves the ionic conductivity by reducing the crystallinity of PEO, whereas FEC as a plasticizer enables PEO-based solid-state electrolytes softer and more conducive to lithium ion transport. In fact, FEC contributes greatly to the lithium stability, and the lower reduction potential of FEC allows it to be preferentially reduced to generate dense SEI film containing LiF and fluorinated organic matter during the cycles. This high-quality interfacial layer modifies the polymer/lithium cathode interface and mitigates the lithium concentration gradient. Meanwhile, it is stable with lithium metal, which promotes uniform distribution

ChemElectroChem

Research Article
doi.org/10.1002/celc.202200641

**Chemistry
Europe**
European Chemical
Societies Publishing

of Li^+ and inhibits the occurrence of side reactions. Furthermore, the improved mechanical properties induced by LLZTO also facilitates the inhibition of lithium dendrites.

Conclusion

To summarize, a facile and efficient strategy is proposed to boost the electrochemical performance of the solid-state electrolyte, protecting the electrolyte from severe deterioration caused by lithium dendrites and establishing a stable solid electrolyte/lithium metal interface. The battery assembled with P—L—F electrolyte delivers a superior long-term cycling stability. The synergistic interplay of FEC and LLZTO endows the PEO-based solid-state electrolyte with high ionic conductivity and lithium-ion transference number, which expands the electrochemical window, enhances electrochemical cycling stability and protects lithium metal from lithium dendrites. The P—L—F electrolyte with high bulk and interfacial ionic conductivity enables a steady Li plating/stripping behavior with a low voltage hysteresis, and also displays highly oxidative stability beyond 5.0 V. In addition, there are no side reactions occurred in PEO with additions of FEC and LLZTO.

Experimental Section

Preparation of CSEs

CSEs were prepared by adding LLZTO ($Li_{6.4}La_3Zr_{1.4}Ta_{0.6}O_{12}$, 500 nm, 99.99%, MTI) and fluoroethylene carbonate (FEC, 99%, Macklin) into the matrix of PEO (Mw=600000, Sigma)-lithium bis(trifluoromethane-sulfonyl)imide (LiTFSI, 99%, Sigma). PEO and LiTFSI were weighed at molecular ratio of [EO]: [Li]=15:1. LLZTO and FEC with various ratios were added, where the weight contents of LLZTO and FEC were 5–20 wt.% and 1–4 wt.% concerning the composite membrane, respectively. Based on the performance tests, the optimal ratio was selected for the further tests.

PEO and LiTFSI were dissolved in acetonitrile (ACN, Aldrich) for 24 h. Subsequently, LLZTO and FEC were added to the solution to obtain a milky white gel (the weight ratios of LLZTO and FEC were 10 wt.% and 2 wt.%, respectively). Then, the gel was poured onto a Teflon mold with being spread evenly with a spatula, and placed in the argon glove box. After 18 h, the solution was transferred into a chamber at 45 °C in the argon glove box for 2 h, followed by a complete drying. Finally, a white flexible composite film of about 120 μm thickness was formed as the electrolytes. To make the comparison more intuitive and convenient, four solid-state electrolytes were prepared, named PEO(P-Only), PEO-LLZTO(P—L), PEO-FEC(P—F), and PEO-LLZTO-FEC(P—L—F).

Preparation of Positive Electrode Materials

Active cathode material $LiFePO_4$ (LFP, MTI), conductive additive Super-P (Cochin Black, LION), and polyvinylidene fluoride (PVDF, Sigma) binder were mixed at a weight ratio of 7:2:1, which were then added into N-1-methyl-2-pyrrolidone (99.5%, Macklin) for 12 h to form a homogeneous cathode slurry. The slurry was coated on the aluminum foil and dried in a vacuum oven at 80 °C for 24 h. The loading of cathode materials is about 1.1 g cm^{-3}.

Materials Characterizations

A scanning electron microscope (SEM, Zeiss Merlin Compact) equipped with an energy dispersive spectrometer (EDS, Oxford X–Max) was employed to determine the morphology and elemental mapping distribution. XRD patterns were collected on a Shimadzu XRD-6000 diffractometer with Cu-K_α radiation to identify the crystal structure. FTIR spectrometer (NICOLET 380) was used to examine the chemical structures. X-ray photoelectron spectrometer (XPS, ESCALAB250) with monochromatic Al-K_α radiation was applied for investigating the chemical composition. Thermogravimetric analysis (TGA, Pyris Diamond TGA analyzer) and differential scanning calorimetry (DSC, PerkinElmer) were performed to investigate the thermal stability. The mechanical strength of HPEs was investigated by CMT6103 at a stretching speed of 1 mm s^{-1}.

Electrochemical Measurements

To evaluate the ionic conductivity, the CSE was assembled in a sandwich structure by two pieces of stainless steel under nominal pressure of 70 kg cm^{-2}. EIS was performed to calculate the ionic conductivity by assembling stainless steel SS‖SS batteries at a frequency range of 10–10^6 Hz with an amplitude of 10 mV from 25 to 80 °C. The ionic conductivity was determined using the following equation:

$$\sigma = L/(R_b \, S) \tag{1}$$

where σ (S cm^{-1}) is the ionic conductivity, R_b (Ω) is the value of the bulk resistance, L (cm) is the thickness of the CSE membrane, and S (cm^{-2}) is the area of the symmetrical electrode. The activation energy(E_a) is calculated by the equation:

$$\sigma = A\exp[(-Ea)/kT] \tag{2}$$

where σ (S cm^{-1}) is the ionic conductivity, A is the pre-exponential constant, Ea is the activation energy for lithium-ion conduction, k is the Boltzmann constant, and T is the absolute temperature. To determine the electrochemical window of CSE, linear sweep voltammetry (LSV) was performed by assembling SS‖Li batteries in the voltage range of 2.5–6.5 V at a scan rate of 0.1 mV s^{-1}. The Li^+ transference number was calculated by testing EIS and DC polarization of symmetric Li‖Li batteries according to the following formula:

$$t_{Li}^+ = I_{ss} \, (\Delta V - I_0 \, R_0)/I_0 \, (\Delta V - I_{ss} \, R_{ss} \,) \tag{3}$$

Where t_{Li}^+ presents the Li^+ transference number, $\triangle V$ (V) is the applied DC polarization voltage of 10 mV. I_0 (A) and I_{ss} (A) refer to the initial and steady current, respectively, while R_0 (Ω) and R_{ss} (Ω) indicate the resistance before and after polarization, respectively. Symmetric Li‖Li batteries were assembled to determine the lithium striping/plating cycling at a current density of 0.1 mA cm^{-2} and 60 °C. The cycling performance of all-solid-state LEP‖Li batteries with CSEs was examined at 60 °C and a current density of 0.2 C (1 C=170 mAh g^{-1}) in the voltage range of 2.8–4.0 V. No extra pressure was applied on the batteries during the electrochemical tests. All batteries were assembled in the Air-filled glovebox and tested on a LANHE CT2003 A instrument. LSV, EIS and DC polarization were tested on an Autolab workstation (Metrohm).

ChemElectroChem

Research Article
doi.org/10.1002/celc.202200641

Chemistry
Europe

European Chemical
Societies Publishing

Theoretical Calculations

Density functional theory (DFT) calculations were carried out using the Gaussian 09 package. The geometric structures and frequency calculations were optimized at the B3LYP/6-311++G(d) level. To investigate the effects of bulk solvents, the structures were optimized by using the integral equation formalism for polarizable continuum model (IEFPCM), with a dielectric constant of 32 (EC/EMC/DMC (1:1:1, by volume)). Atomic charge distributions were obtained by the natural population analysis (NPA). The calculated reduction potential (E_{re}) was converted from the absolute oxidation potential of the species (vs. Li/Li$^+$):

$$E_{re} = [G(M) - G(M^-)]/F\text{-}1.4 \tag{4}$$

Where G(M) and G(M$^-$) represented the free energies of the species M and its reduced form M$^-$ at 298.15 K, respectively, and F is the Faraday constant.

Acknowledgements

Conflict of Interest

The authors declare no conflict of interest.

Data Availability Statement

The data that support the findings of this study are available from the corresponding author upon reasonable request.

[1] a) J. M. Tarascon, M. Armand, *Nature* **2001**, *414*, 359–367; b) J. B. Goodenough, Y. Kim, *Chem. Mater.* **2010**, *22*, 587–603.
[2] a) D. Lin, Y. Liu, Y. Cui, *Nat. Nanotechnol.* **2017**, *12*, 194–206; b) Y. Tang, L. Zhang, J. Chen, H. Sun, T. Yang, Q. Liu, Q. Huang, T. Zhu, J. Huang, *Energy Environ. Sci.* **2021**, *14*, 602–642.
[3] a) K. Fu, Y. Gong, B. Liu, Y. Zhu, S. Xu, Y. Yao, W. Luo, C. Wang, S. D. Lacey, J. Dai, Y. Chen, Y. Mo, E. Wachsman, L. Hu, *Sci. Adv.* **2017**, *3*, 1601659; b) C. Zhao, X. Yao, H. Yang, X. Jiao, L. Wang, *Compos. Commun.* **2021**, *26*, 100789.
[4] a) J. Lau, R. H. DeBlock, D. M. Butts, D. S. Ashby, C. S. Choi, B. S. Dunn, *Adv. Energy Mater.* **2018**, *8*, 1800933; b) J. Wan, J. Xie, D. G. Mackanic, W. Burke, Z. Bao, Y. Cui, *Mater. Today* **2018**, *4*, 1–16; c) L. Chen, W. Li, L. Z. Fan, C.-W. Nan, Q. Zhang, *Adv. Funct. Mater.* **2019**, *29*, 1901047.
[5] a) J. Zhang, N. Zhao, M. Zhang, Y. Li, P. K. Chu, X. Guo, Z. Di, X. Wang, H. Li, *Nano Energy* **2016**, *28*, 447–454; b) K. Fu, Y. Gong, J. Dai, A. Gong, X. Han, Y. Yao, C. Wang, Y. Wang, Y. Chen, C. Yan, Y. Li, E. D. Wachsman, L. Hu, *Proc. Natl. Acad. Sci. USA* **2016**, *113*, 7094–7099; c) D. Lin, W. Liu, Y. Liu, H. R. Lee, P.-C. Hsu, K. Liu, Y. Cui, *Nano Lett.* **2016**, *16*, 459–465; d) L. Chen, Y. Li, S. P. Li, L. Z. Fan, C. W. Nan, J. B. Goodenough, *Nano Energy* **2018**, *46*, 176–184.
[6] a) Z. Wan, D. Lei, W. Yang, C. Liu, K. Shi, X. Hao, L. Shen, W. Lv, B. Li, Q. H. Yang, F. Kang, Y. B. He, *Adv. Funct. Mater.* **2019**, *29*, 1805301; b) B. Chen, H. Huang, Y. Wang, Z. Shen, L. Li, Y. Wang, X. Wang, X. Li, Y. Wang, *ChemElectroChem* **2022**, *9*, 2101277.
[7] a) F. Chen, D. Yang, W. Zha, B. Zhu, Y. Zhang, J. Li, Y. Gu, Q. Shen, L. Zhang, D. R. Sadoway, *Electrochim. Acta* **2017**, *258*, 1106–1114; b) D. Xu, J. Su, J. Jin, C. Sun, Y. Ruan, C. Chen, Z. Wen, *Adv. Energy Mater.* **2019**, *9*, 1900611; c) M. Inal, Z. Gun Gok, N. Perktas, G. Elif Kartal, N. Banu Verim, S. Murat, T. Apaydin, M. Yigitoglu, *J. Nanosci. Nanotechnol.* **2021**, *21*, 3041–3049.
[8] H. Zhuang, W. C. Ma, J. W. Xie, X. Y. Liu, B. B. Li, Y. Jiang, S. S. Huang, Z. W. Chen, B. Zhao, *J. Alloys Compd.* **2021**, *860*, 157915.
[9] Q. Zhou, Q. Li, S. Liu, X. Yin, B. Huang, M. Sheng, *J. Power Sources* **2021**, *482*, 228929.
[10] a) R. Chen, Q. Li, X. Yu, L. Chen, H. Li, *Chem. Rev.* **2020**, 120, 6820–6877; b) S. F. Lou, F. Zhang, C. K. Fu, M. Chen, Y. L. Ma, G. P. Yin, J. J. Wang, *Adv. Mater.* **2021**, *33*, 2000721; c) X. Jiao, J. Wang, G. Gao, X. Zhang, C. Fu, L. Wang, Y. Wang, T. Liu, *ACS Appl. Mater. Interfaces* **2021**, *13*, 60054–60062.
[11] a) G. Hou, X. Ma, Q. Sun, Q. Ai, X. Xu, L. Chen, D. Li, J. Chen, H. Zhong, Y. Li, Z. Xu, P. Si, J. Feng, L. Zhang, F. Ding, L. Ci, *ACS Appl. Mater. Interfaces* **2018**, *10*, 18610–18618; b) C. Cui, C. Yang, N. Eidson, J. Chen, F. Han, L. Chen, C. Luo, P. F. Wang, X. Fan, C. Wang, *Adv. Mater.* **2020**, *32*, 1906427; c) L. Wang, L. Wang, R. Wang, R. Xu, C. Zhan, W. Yang, G. Liu, *Int. J. Min. Met. Mater.* **2021**, *28*, 1584–1602.
[12] X. Fan, X. Ji, F. Han, J. Yue, J. Chen, L. Chen, T. Deng, J. Jiang, C. Wang, *Sci. Adv.* **2018**, *4*, aau9245.
[13] J. Wang, X. Yan, Z. Zhang, R. Guo, H. Ying, G. Han, W.-Q. Han, *ACS Appl. Mater. Interfaces* **2020**, *12*, 41323–41332.
[14] a) Y. Xu, J. Liu, L. Zhou, L. Zeng, Z. Yang, *J. Electroanal. Chem.* **2017**, *791*, 109–116; b) X. Zhang, X. Chen, X. Cheng, B. Li, X. Shen, C. Yan, J. Huang, Q. Zhang, *Angew. Chem. Int. Ed.* **2018**, *57*, 5301–5305; *Angew. Chem.* **2018**, *130*, 5399–5403; c) P. Shi, F. Liu, Y. Feng, J. Zhou, X. Rui, Y. Yu, *Small* **2020**, *16*, 2001989.
[15] a) A. Bordes, K. Eom, T. F. Fuller, *J. Power Sources* **2014**, *257*, 163–169; b) Z. Zhu, Y. Tang, Z. Lv, J. Wei, Y. Zhang, R. Wang, W. Zhang, H. Xia, M. Ge, X. Chen, *Angew. Chem. Int. Ed.* **2018**, *57*, 3656–3660; *Angew. Chem.* **2018**, *130*, 3718–3722; c) X. Zhang, X. Chen, L. Hou, B. Li, X. Cheng, J. Huang, Q. Zhang, *ACS Energy Lett.* **2019**, *4*, 411–416.
[16] a) X. Q. Zhang, X. Chen, X. B. Cheng, B. Q. Li, X. Shen, C. Yan, *Angew. Chem. Int. Ed.* **2018**, *57*, 5301–5305; *Angew. Chem.* **2018**, *130*, 5399–5403; b) H. Li, W. Liu, X. Yang, J. Xiao, Y. Li, L. Sun, X. Ren, P. Zhang, H. Mi, *Chem. Eng. J.* **2021**, *408*, 127254; c) Z. Y. Li, H. R. Zhang, X. L. Sun, Y. Yang, *ACS Energy Lett.* **2020**, *5*, 3244–3253; d) W. Liu, B. Qiu, J. W. Yan, C. X. He, P. X. Zhang, H. W. Mi, *Dalton Trans.* **2021**, *50*, 14296–14302; e) S. J. Xu, Z. H. Sun, C. G. Sun, F. Li, K. Chen, Z. H. Zhang, G. J. Hou, H. M. Cheng, F. Li, *Adv. Funct. Mater.* **2020**, *30*, 2007172; f) Y. Y. Wang, K. X. Huang, P. X. Zhang, H. W. Li, H. W. Mi, *Appl. Surf. Sci.* **2022**, *574*, 151593.
[17] H. J. Woo, A. K. Arof, *Spectrochim. Acta Part A* **2016**, *161*, 44–51.
[18] J. Park, I. Choi, M. J. Lee, M. H. Kim, T. Lim, K. H. Park, J. Jang, S. M. Oh, S. K. Cho, J. J. Kim, *Electrochim. Acta* **2014**, *132*, 338–346.
[19] Z. Zhang, Y. Huang, H. Gao, J. X. Huang, C. Li, P. B. Liu, *Ceram. Int.* **2020**, *46*, 11397–11405.
[20] Y. Li, F. Lian, L. Ma, C. Liu, L. Yang, X. Sun, K. Chou, *Electrochim. Acta* **2015**, *168*, 261–270.
[21] Z. Wang, H. Zhou, C. Meng, L. Zhang, Y. Cai, A. Yuan, *ChemElectroChem* **2020**, *7*, 2660–2664.
[22] a) Z. Xue, D. He, X. Xie, *J. Mater. Chem. A* **2015**, *3*, 19218–19253; b) S. Cheng, D. M. Smith, C. Y. Li, *Macromolecules* **2014**, *47*, 3978–3986.
[23] S. Ramesh, T. F. Yuen, C. J. Shen, *Spectrochim. Acta Part A* **2008**, *69*, 670–675.
[24] J. Zheng, M. Tang, Y.-Y. Hu, *Angew. Chem. Int. Ed.* **2016**, *55*, 12538–12542; *Angew. Chem.* **2016**, *128*, 12726–12730.
[25] Z. Jian, P. S. Fedkiw, *Solid State Ionics* **2004**, *166*, 275–293.

Water–Salt Oligomers Enable Supersoluble Electrolytes for High-Performance Aqueous Batteries

Shengying Cai, Xingyuan Chu, Chang Liu, Haiwen Lai, Hao Chen, Yanqiu Jiang, Fan Guo, Zhikang Xu,* Chunsheng Wang,* and Chao Gao*

Aqueous rechargeable batteries are highly safe, low-cost, and environmentally friendly, but restricted by low energy density. One of the most efficient solutions is to improve the concentration of the aqueous electrolytes. However, each salt is limited by its physical solubility, generally below 21–32 mol kg^{-1} (m). Here, a $ZnCl_2/ZnBr_2/Zn(OAc)_2$ aqueous electrolyte with a record super-solubility up to 75 m is reported, which breaks through the physical solubility limit. This is attributed to the formation of acetate-capped water–salt oligomers bridged by Br^-/Cl^--H and $Br^-/Cl^-/O$-Zn^{2+} interactions. Mass spectrometry indicates that acetate anions containing nonpolarized protons prohibit the overgrowth and precipitation of ionic oligomers. The polymer-like glass transition temperature of such inorganic electrolytes is found at ≈ -70 to $-60\,°C$, without the observation of peaks for salt-crystallization and water-freezing from 40 to $-80\,°C$. This supersoluble electrolyte enables high-performance aqueous dual-ion batteries that exhibit a reversible capacity of 605.7 mAh g^{-1}, corresponding to an energy density of 908.5 Wh kg^{-1}, with a coulombic efficiency of 98.07%. In situ X-ray diffraction and Raman technologies reveal that such high ionic concentrations of the supersoluble electrolyte enable a stage-1 intercalation of bromine into macroscopically assembled graphene cathode.

Aqueous electrolytes resolve the concerns of battery raised over safety, cost, and environmental impact.[1–3] However, their adoption has been slower due to the lack of high-energy-density electrochemical couples that has resulted from the narrow electrochemical stability window of water (1.23 V) and low capacity of cathodes.[4] An effective method to address this problem is to adjust interactions between dissociated ions and water, which have a significant influence on parameters of electrolytes, such as viscosity, solubility, chemical reactivity, and stability.[5] In

Dr. S. Y. Cai, X. Y. Chu, C. Liu, H. W. Lai, Dr. H. Chen, Dr. Y. Q. Jiang,
Dr. F. Guo, Prof. Z. K. Xu, Prof. C. Gao
MOE Key Laboratory of Macromolecular Synthesis and Functionalization
Department of Polymer Science and Engineering
Zhejiang University
38 Zheda Road, Hangzhou 310027, China
E-mail: xuzk@zju.edu.cn; chaogao@zju.edu.cn
Prof. C. S. Wang
Department of Chemical and Biomolecular Engineering
University of Maryland
College Park, MD 20740, USA
E-mail: cswang@umd.edu

The ORCID identification number(s) for the author(s) of this article can be found under https://doi.org/10.1002/adma.202007470.

contrast to classical aqueous electrolytes (molarity of 1 mol L^{-1}), water-in-salt electrolytes characterized by a high molality of 20–30 mol kg^{-1} (m) greatly improved the energy density of aqueous batteries, by extending the electrochemical stability window to 3.0 V.[6] Furthermore, a hydrate salt could dissolve another salt of similar chemical properties to form eutectic systems.[7] Thus water-in-bisalt and hydrate melt electrolytes with higher salt concentrations as well as wider electrochemical stability windows were successfully obtained, pushing the energy density of aqueous cells closer to their non-aqueous counterparts.[8,9] As water-in-(bi)salt electrolytes have approached their physical solubility limits, it is a big challenge to further increase electrolyte contents in water. Additionally, in comparison to extending the potential window, using concentrated electrolytes to increase the capacity of aqueous energy storage devices, especially which are based on non-lithium elements have rarely been exploited.

Herein, we report a supersoluble electrolyte prepared by $ZnCl_2$ (zinc chloride), $ZnBr_2$ (zinc bromide), and $Zn(OAc)_2$ (zinc acetate) that breaks through physical solubility limits by formation of acetate-capped water-salt oligomers. This strategy significantly improves salt concentrations up to 75 m, which is much higher than those of previously reported water-in-(bi)salt/hydrate melt electrolytes (21–40 m).[6,8–11] Polymer-like structures as well as characters of such inorganic electrolytes are revealed by Raman spectroscopy, nuclear magnetic resonance (NMR) spectrum, electrospray ionization mass spectrometry (ESI-MS), and differential scanning calorimetry (DSC). An aqueous lithium-free battery charged by zinc deposition and halogen conversion-intercalation was first constructed with the water–salt oligomer electrolyte, demonstrating a high reversible capacity of 605.7 mAh g^{-1} at 1 A g^{-1}, a cutoff voltage of 1.85 V, and a lifespan more than 500 cycles.
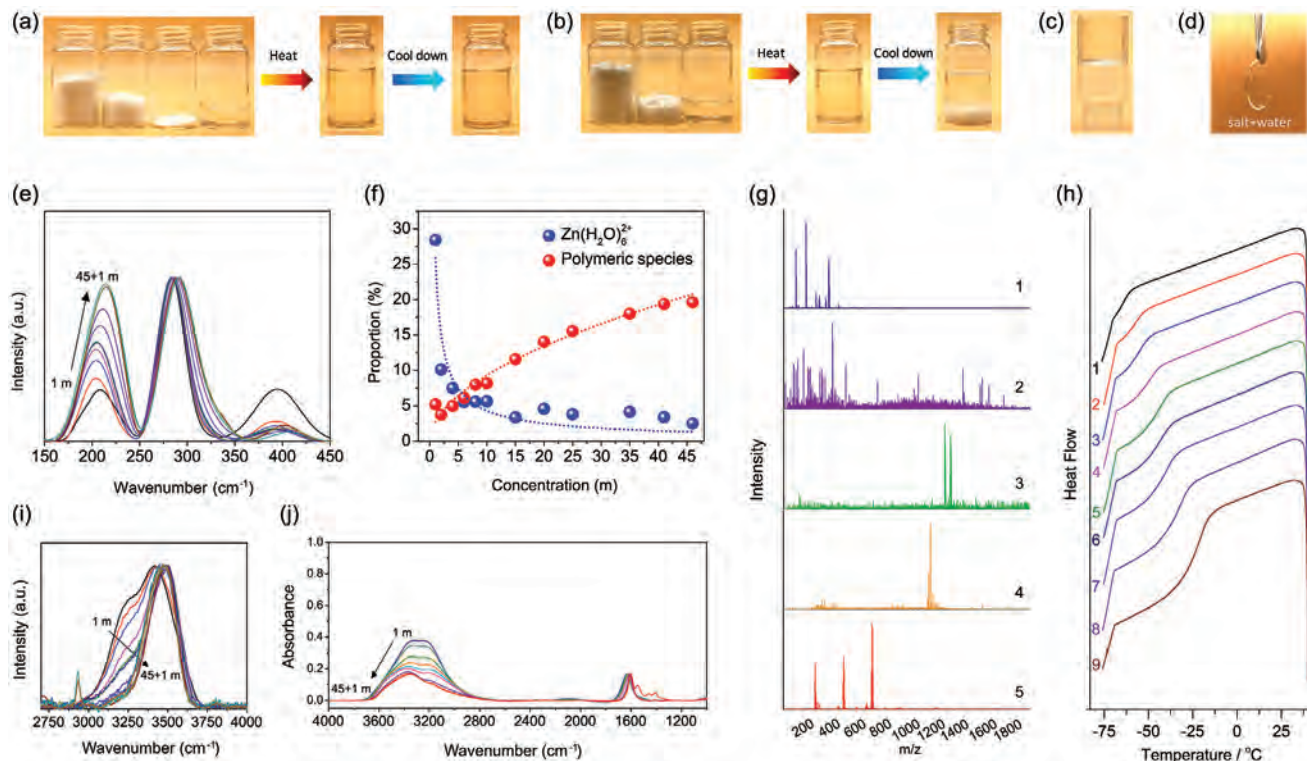
$ZnCl_2$ or $ZnBr_2$ is able to form a water-in-salt electrolyte with a maximum molality of ≈ 20 m (Figure S1a,b, Supporting Information). By utilizing the eutectic effect, a $ZnCl_2/ZnBr_2$ (molar ratio of 3:1) water-in-bisalt electrolyte was made and extended the concentration limit from 20 to 35 m (Figure S1c, Supporting Information). In these solutions, thermal stability of water molecules increases with salt molality due to the reconstructed hydration environments, endowing aqueous electrolytes with heat-tolerance. Therefore, a 45 m $ZnBr_{0.5}Cl_{1.5}$+1 m

Figure 1. Electrolyte characterizations. a) WSOE$_{45}$-1 prepared by stoichiometric amounts of ZnCl$_2$, ZnBr$_2$, Zn(OAc)$_2$, and water. b) 40 m ZnBr$_{0.5}$Cl$_{1.5}$ suspension prepared by stoichiometric amounts of ZnCl$_2$, ZnBr$_2$, and water. c) WSOE$_{40}$-20 consisted of 20 m ZnCl$_2$, 20 m ZnBr$_2$, and 20 m Zn(OAc)$_2$. d) WSOE$_{50}$-25 consisted of 25 m ZnCl$_2$, 25 m ZnBr$_2$, and 25 m Zn(OAc)$_2$. e) Raman spectra of zinc derivatives in electrolytes, including: 1) ZnBr$_n^{2-n}$ (150, 172, 184, and 206 cm^{-1}), 2) ZnCl$_n^{2-n}$ (266, 278, 286, 305, 345 cm^{-1}), 3) polynuclear aggregate (230 cm^{-1}), and 4) Zn(H$_2$O)$_6^{2+}$ (390–410 cm^{-1}).[11–13] Peak differentiating analysis is shown in Figure S4, Supporting Information. f) Variation trends of Zn(H$_2$O)$_6^{2+}$ and polymeric species contents in 1–46 m electrolytes, obtained by the integral area of separated peaks in Figure S3, Supporting Information. g) Mass spectra of 1 m ZnBr$_{0.5}$Cl$_{1.5}$ aqueous solution (curve 1), 40 m ZnBr$_{0.5}$Cl$_{1.5}$ suspension (supernatant, curve 2), WSOE$_{45}$-1 (curve 3), WSOE$_{45}$-2 (curve 4), and WSOE$_{45}$-10 (curve 5). h) DSC results of WSOE$_{45}$-1 (curve 1), WSOE$_{45}$-2 (curve 2), WSOE$_{45}$-4 (curve 3), WSOE$_{45}$-6 (curve 4), WSOE$_{45}$-8 (curve 5), WSOE$_{45}$-10 (curve 6), WSOE$_{45}$-15 (curve 7), WSOE$_{45}$-20 (curve 8), and WSOE$_{45}$-30 (curve 9). i,j) Raman and FTIR spectra of water molecules in electrolytes. Peak differentiating analysis is shown in Figures S6–S9, Supporting Information.

Zn(OAc)$_2$ water–salt oligomer electrolyte (WSOE; WSOE$_X$-Y is used after here, where X denotes the total molality of ZnCl$_2$ and ZnBr$_2$, and Y denotes the molality of Zn(OAc)$_2$) was successfully prepared by heating stoichiometric amounts of ZnCl$_2$, ZnBr$_2$, Zn(OAc)$_2$, and ionized water at 60 °C for 2 h and then 120 °C for 72 h. As a result, a transparent and colorless liquid is obtained even at room temperature, corresponding to a high density of 2.602 g cm^{-3} (**Figure 1**a). The WSOE$_{45}$-1 is stable at 25 °C for at least 24 h as shown in Figure S2a,b, Supporting Information. Ionic conductivities of the WSOE$_{45}$-1 and 1–35 m ZnBr$_{0.5}$Cl$_{1.5}$ are listed in Table S1, Supporting Information. The transference number of positive charge in WSOE$_{45}$-1 was measured to be 0.343 by a Zn|WSOE$_{45}$-1|Zn symmetric cell according to Equation (S1), Supporting Information (corresponding data used for calculation are displayed in Figure S3, Supporting Information). The crucial role of Zn(OAc)$_2$ in this condition is illustrated in Figure 1b, where salt precipitation occurred in a 40 m ZnBr$_{0.5}$Cl$_{1.5}$ aqueous solution without the addition of Zn(OAc)$_2$ during cooling process. The salt molality of WSOE was further improved to 60–75 m by adjusting the molar ratio of zinc salts, and the electrolyte transforms from a liquid to quasi-solid or hydrogel state (Figure 1c,d).

Molecular structures of 1–35 m ZnBr$_{0.5}$Cl$_{1.5}$ aqueous electrolytes, WSOE$_{40}$-1, and WSOE$_{45}$-1 were investigated by spectroscopies. Figure 1e and Figure S4, Supporting Information, show Raman band assignments and corresponding analysis results for zinc derivatives. The vibration band located at about 390 cm^{-1} is assigned to zinc hydrate, which underwent an intensity weakening and blue shift from 390 to 410 cm^{-1} when the salt molality was increased from 1 to 46 m. This phenomenon is ascribed to the weakened hydrolysis and enhanced hydration of Zn^{2+} in concentrated electrolytes.[11,14] Meanwhile, the areal proportion of polymeric species at 230 cm^{-1} increases from 5.2 to 19.6% (Figure 1f), implying the formation of zinc-based oligomers in concentrated electrolytes. This is further supported by ESI-MS. For 1 m ZnBr$_{0.5}$Cl$_{1.5}$, peaks are observed at 200.9–464.8 m/z (Figure 1g, 1), whereas molecular ions of 40 m ZnBr$_{0.5}$Cl$_{1.5}$ supernatant are tested to be 208.9, 438.2, 545.3, 794.3, 957.5, 1119.9, 1471.8, 1623.3, and 1795.2 m/z (Figure 1g, 2). Oversized ionic oligomers might lead to salt precipitation, thus are invisible in the supernatant of suspension. By contrast, peaks of WSOE$_{45}$-1 are mainly observed at 1328.8 m/z (Figure 1g, 3), accompanied by negligible signals around 1400–1800 m/z. The function of Zn(OAc)$_2$ is ascribed

**ADVANCED
SCIENCE NEWS**

www.advancedsciencenews.com

**ADVANCED
MATERIALS**

www.advmat.de

to be capping agents that prevent the overgrowth of ionic oligomers. To verify this assumption, additional $Zn(OAc)_2$ (1 and 9 m) was introduced into $WSOE_{45}$-1, resulting in continuously decreased molecular weights of ionic oligomers (Figure 1g, 4 and 5). Table S2, Supporting Information, shows calculated constitutions of $WSOE_{45}$-1. As a result, both of OAc^- and H_2O are found in these water–salt oligomers as indispensable components. In addition, Raman peaks located at 305 cm^{-1} and 206 cm^{-1} were originated from vibrations of molten $ZnCl_2$ and $ZnBr_2$.[15,16] Remarkable intensification of these peaks was observed with the increment of salt concentration (Figure S4, Supporting Information), indicating a structural transformation from traditional aqueous solution into molten salts. Thermal properties of electrolytes are characterized by differential scanning calorimetry (Figure 1h, 1). In contrast to dilute aqueous solutions (1 m $ZnCl_2$, 1 m $ZnBr_2$, and 1 m $ZnBr_{0.5}Cl_{1.5}$ in Figure S5, Supporting Information), no peaks are observed corresponding to salt-crystallization or water-freeze of $WSOE_{45}$-1 over the entire range examined ($\approx$–80 to 40 °C). Alternatively, glass transition temperature (T_g) of $WSOE_{45}$-1 was measured at $\approx$–70 to –60 °C, suggesting a polymer-like amorphous character of ionic oligomer-based electrolytes. The T_g rises up with the increase of $Zn(OAc)_2$ content and electrolyte concentrations (Figure 1h, 2–9), which is consistent with the increased viscosity of electrolytes.

Association states of water molecules are further examined by O-H vibrations (Figure 1i,j), that reflect the chemical environments of hydrogen and oxygen atoms within different acceptor–donor pairs.[17–22] From 1 to 46 m, the areal proportion of coupled O-H stretch (Raman band at 3250 cm^{-1}; Figure S6, Supporting Information) significantly decreased from 53.8% to 5.9% (Figure S7, Supporting Information), indicating the elapse of water clusters by increasing salt concentrations. However, that of nearly non-H-bonded O—H stretch (Raman band at 3520 cm^{-1}; Figure S6, Supporting Information) only increased from 12.8% to 27.9% (Figure S7, Supporting Information), leaving an areal proportion of 66.2% for other states (Raman band at 3425 cm^{-1}; Figure S6, Supporting Information). We attribute this phenomenon to the formation of $Br^-/Cl^-\cdots H$ pairs in $WSOE_{45}$-1 as an alternative interaction for the $O\cdots H$ pair, that results in a frequency downshift of uncoupled O-H stretch. This interaction reconstructs the solvent framework of solution and connects halogen anions with water molecules to be the segment of water–salt oligomer. Fourier-transform infrared (FTIR) spectra confirmed that the H-bonded O-H content (absorption signals at 3205–3370 cm^{-1}; Figure S8, Supporting Information) in 1–46 m electrolytes only varied from 71.5% to 62.3% (Figure S9, Supporting Information), due to the opposite variate of $O\cdots H$ and $Br^-/Cl^-\cdots H$ pairs.

Electronic environments of water molecules in 1–46 m aqueous electrolytes are characterized by NMR. As shown in Figure S10a, Supporting Information, the ^1H signal is found to move toward lower chemical shifts (from 4.75 to 3.95 ppm) with increasing salt molality. This phenomenon is ascribed to the increment of surrounding electronic density and enhanced shielding of protons in water molecules, consistent with the formation of halogen–hydrogen bonds deduced by Raman and FTIR. Meanwhile, the ^{17}O signal is found to move toward higher chemical shifts (from 5.72 to 17.60 ppm) (Figure S10b,

Supporting Information), indicating a decreased surrounding electronic density as well as weakened shielding of oxygen atoms which are resulted from the enhanced interaction between zinc cations and water molecules in water-salt oligomers. Peak broadening of both ^1H and ^{17}O signals are attributed to the insufficient relaxation time aroused by dramatically increased solution viscosity of concentrated electrolytes.[10]

The relationship between solution structure and salt molality is further revealed from molecular dynamics simulations (**Figure 2**a,b). Typical molecular configurations of the $WSOE_{45}$-1 and 5 m $ZnBr_{0.5}Cl_{1.5}$ are displayed in Figure 2c,d, respectively. For $WSOE_{45}$-1, significantly decreased $N_{O/H}$ is found in comparison to the 5 m electrolyte (Figure 2e; Figure S11a, Supporting Information), consistent with the disappearance of coupled O-H vibration verified by FTIR and Raman spectra. With salt molality increased from 5 to 46 m, hydration number of Zn^{2+} decreases from 5.51 to 1.15, and matches well with one of the oligomer structures calculated by ESI-MS results. Intensified $Cl^-/Br^-\cdots H$ and $Cl^-/Br^-/O_W\cdots Zn^{2+}$ interactions at 46 m are predicted by increased $N_{Cl/H}$, $N_{Br/H}$, $N_{Cl/Zn}$, $N_{Br/Zn}$ as well as reduced d_{Ow-Zn} (from 1.935 to 1.835 Å) (Figure 2f–j and Figure S11b–f, Supporting Information) that bond electrolyte ions with water molecules to be water–salt oligomers. For $WSOE_{45}$-1, O_{ace} is observed inside the primary hydration sheath of Zn^{2+} ($d_{Oace-Zn}$ = 1.665 Å). Nonpolarized protons in acetate anions are unfavorable for the formation of $-CH_3\cdots Cl^-/Br^-$ interactions, thus avoid the overgrowth of ionic oligomers to form precipitations in $WSOE_{45}$-1. Structural scheme of dilute $ZnBr_{0.5}Cl_{1.5}$ aqueous solution, uncapped and acetate-capped WSOE are supplied in Figure S12, Supporting Information, on the basis of experimental and simulation results. Figure S13, Supporting Information, shows the thermo gravimetric analysis) of $WSOE_{45}$-1 and 5 m $ZnBr_{0.5}Cl_{1.5}$ aqueous solution. A gentler profile is observed in the former, indicating the higher stability of water molecules in water-salt oligomers.

The advantages of $WSOE_{45}$-1 are demonstrated through a dual-ion battery (DIB) which is constructed by a self-standing graphene cathode (PGA) combined with a graphene fiber fabric (GFF) in the negative side (Figures S14 and S15, Supporting Information). Electrochemical impedance spectroscopy (EIS) measurements of the DIB in different time were performed to further validate the stability of $WSOE_{45}$-1 at 25 °C before other electrochemical tests. Similar Nyquist plots were obtained at 0, 6, 12, and 24 h in the area of high frequency (Figure S16, Supporting Information), which indicate a stable state of the assembled cell (including the electrolyte) with unchanged intrinsic/charge transfer resistance (R_s and R_{ct}). Although the increased slope of Nyquist plots at low frequency was observed as time passed, it is ascribed to the wettability of electrodes by $WSOE_{45}$-1. The battery mechanism is illustrated in **Figure 3**a. Upon charging, Br^- is oxidized to a near-zero state Br^0 and the latter intercalates into the graphite lattice of PGA cathode, resulting in a $C_n[Br]$ graphite-intercalated compound (GIC).[23] This procedure corresponds to the increased current of cathodic cyclic voltammetry (CV) curves between 1.0 and 1.35 V (versus Ag/AgCl), obtained by a three-electrode system (red plot in Figure 3b). Meanwhile, the Zn/GFF anode is formed in situ by electrodeposition of Zn on GFF below -0.65 V (versus Ag/AgCl) (blue plot in Figure 3b). During discharge, Br de-intercalates
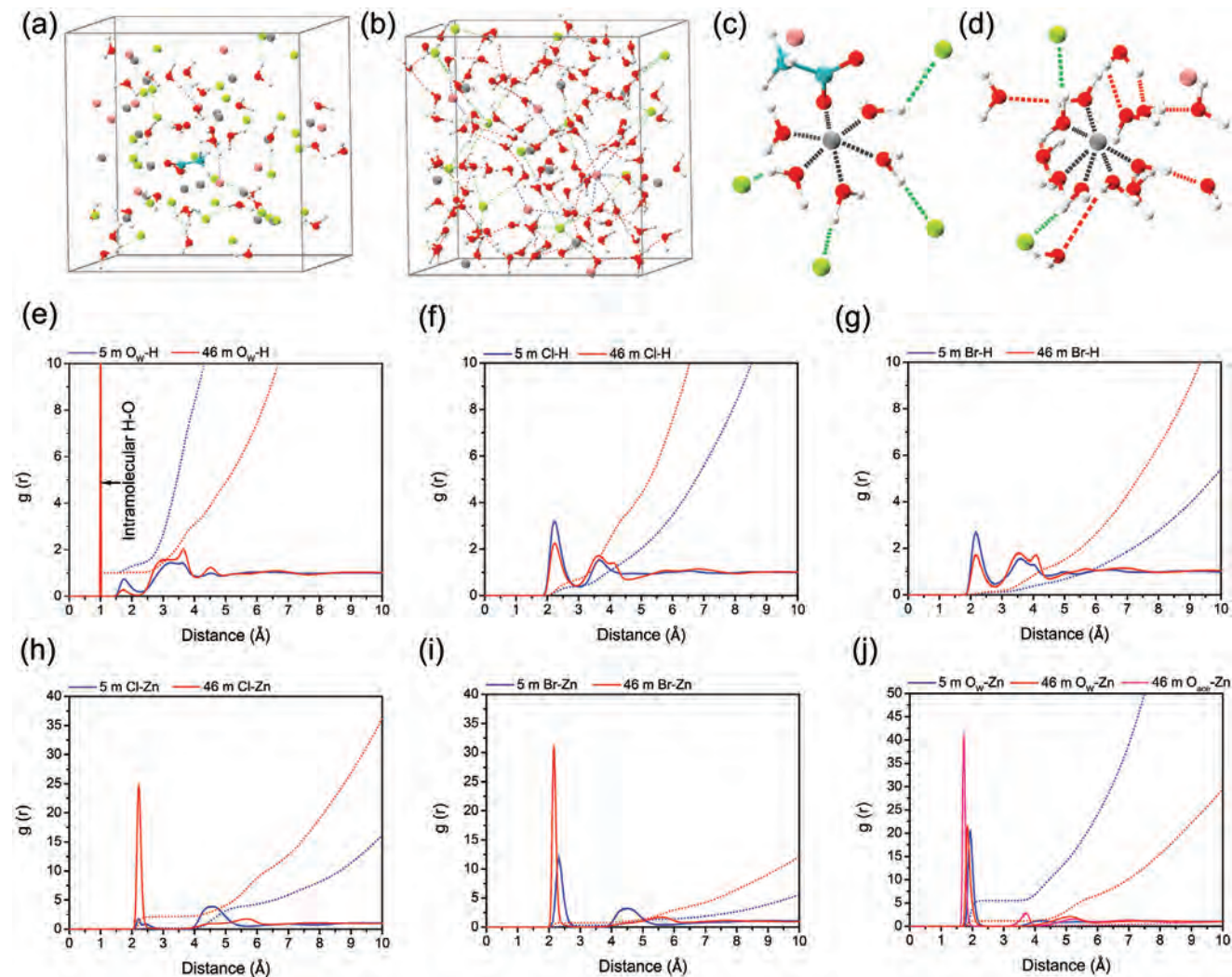
Figure 2. Molecular dynamics simulation. a,b) Snapshots of the WSOE$_{45}$-1 (a) and 5 m ZnBr$_{0.5}$Cl$_{1.5}$ aqueous solution (b) during MD simulations. Atom colors: Zn, gray; O, red; H, white; C, blue; Cl, green; Br, purple. Interactions: O···H, red line; Cl$^-$···H, green line; Br$^-$···H, blue line; O···Zn^{2+}, gray line. c,d) Typical molecular conformations extracted from patterns A and B. e–g) Radial distribution functions (solid line) and integral curves (dashed line) of H atoms, h–j) Zn atoms in 5 m ZnBr$_{0.5}$Cl$_{1.5}$ aqueous electrolytes and WSOE$_{45}$-1. Abbreviations: O$_W$ denotes oxygen atoms from water molecule, and O$_{ace}$ denotes oxygen atoms from acetate anions.

from the graphene interlayer and reduces into Br$^-$, consistent with the reduction peak of anodic CV curves under 1.0 V (versus Ag/AgCl). Simultaneously, Zn on the GFF is oxidized to Zn^{2+} again, verified by the oxidation peak that locates at −0.65 to −0.40 V (versus Ag/AgCl).

According to the Nernst equation (Equations (S2) and (S3), Supporting Information), increment of Zn^{2+} and Br$^-$ concentrations in electrolytes will result in an increased redox potential of Zn/Zn^{2+} as well as a decreased redox potential of Br$^-$/Br. Meanwhile, due to the decreased water content in electrolytes, potentials of hydrogen and oxygen evolutions move in opposite directions to that of Zn/Zn^{2+} and Br$^-$/Br, respectively. All of these variations are beneficial for avoiding water electrolysis as the process shown in Figure S17, Supporting Information. The oxidation of Br$^-$ on Ti current collector is almost irreversible as shown in Figure S18, Supporting Information, (black plot in Figure 3b), illustrating an important

role of graphene host in the reversibility of cathodic reactions. In addition, CV profile of the Zn/GFF|WSOE$_{45}$-1|PGA cell is evaluated by a two-electrode system (green curve in Figure 3b) and indicates a reaction range of 1.70–1.85 V for battery charge and 1.70–1.20 V for discharge. Figure 3c,d shows the charge/discharge behaviors of DIBs when cutoff voltages were gradually increased from 1.81 to 1.85 V at 1 A g^{-1}. The specific capacity increased from 306.2 to 605.7 mAh g^{-1} (corresponding to a GIC of C$_{3.7}$Br, calculated by Equation (S4), Supporting Information) during this process (based on the cathode mass). Given both parameters of high-specific capacity and satisfactory coulombic efficiency (CE ≈97–98%) confirmed by the galvanostatic charge–discharge (GCD) technology, 1.85 V was considered as an ideal cutoff voltage for the Zn/GFF|WSOE$_{45}$-1|PGA cell. For comparison, GCD curves of DIBs beyond 1.85 V are shown in Figure S19, Supporting Information. The coulombic efficiency decreases in these

ADVANCED
SCIENCE NEWS
www.advancedsciencenews.com

ADVANCED
MATERIALS
www.advmat.de
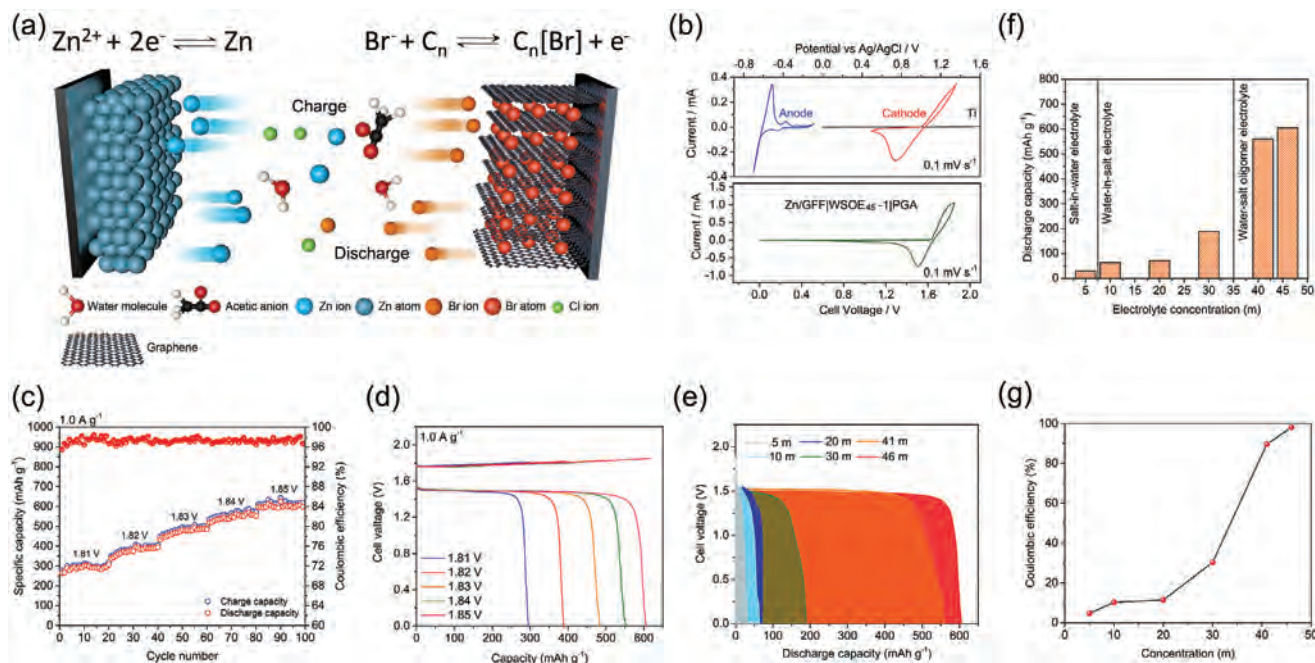
Figure 3. High-capacity aqueous dual-ion battery enabled by WSOE$_{45}$-1. a) Schematic diagram for the dual-ion battery enabled by WSOE$_{45}$-1, PGA cathode, and Zn/GFF anode. b) Cyclic voltammetry curves of anode, cathode, current collector, and dual-ion battery using the WSOE$_{45}$-1 as electrolyte. c,d) Charge and discharge capacities of the Zn/GFF|WSOE$_{45}$-1|PGA dual-ion battery at various voltages. e,f) Discharge capacity of assembled dual-ion batteries using 5–46 m electrolytes. g) Coulombic efficiency of assembled dual-ion batteries using 5–46 m electrolytes.

situations. We attribute this phenomenon to the completely saturated lattice of Br-GIC which cannot accommodate and stabilize more bromine at higher voltages.

In order to demonstrate the crucial role of supersoluble electrolyte in the reversible halogen conversion-intercalation chemistry,[23] DIBs based on 5, 10, 20, 30 m ZnBr$_{0.5}$Cl$_{1.5}$, WSOE$_{40}$-1, and WSOE$_{45}$-1 were fabricated. As shown in Figure 3e–g and Figure S20, Supporting Information, the discharge capacity of Zn/GFF|electrolyte|PGA cells significantly increases from 29.5 to 605.7 mAh g^{-1} upon the increment of salt concentrations from 5 to 46 m, meanwhile the coulombic efficiency increases from 4.72% to 98.07%. We ascribe this phenomenon to the suppressed shuttle effect and promoted intercalation of Br in the condition of concentrated electrolytes. Because most Br$^-$ ions are conserved as anionic halozinc complexes (such as ZnBr$_n^{2-n}$, as confirmed by the Raman spectra in Figure S4, Supporting Information) in concentrated zinc-based electrolytes, it is hard for the oxidized bromine to form polybromides (Br$_3^-$, Br$_5^-$, etc.) by coordinating Br$^-$ anions that widely exist in dilute aqueous solutions, which alleviates the shuttle effect of the polybromides. On the contrary, in dilute situations, Br or Br$_2$ species formed by oxidation of Br$^-$ anions during charging are inclined to dissolve in the aqueous solution rather than intercalate into the graphite lattice. Moreover, Br$_2$ that shuttled to the negative side will further corrode the anode, resulting in an inefficient deposition of metallic zinc.

The rate capability of DIBs was evaluated by increasing the current density from 1.0 to 2.0 A g^{-1}, and corresponding results are shown in **Figure 4**a. The rate capability of our dual-ion batteries is compromised by ionic conductivity of water–salt oligomer electrolytes (1.28 mS cm^{-1}) due to high salt concentrations.

Thus, the energy density is significantly decreased when higher current densities are employed. Although higher capacity above 605.7 mAh g^{-1} was achieved at even slower rates, the reversibility of batteries decreased in this condition (such as 0.5 A g^{-1} in Figure S21a, Supporting Information). We ascribe this phenomenon to reduced-overpotentials for Br$^-$ oxidation at low current densities, by which an excess of Br is produced at original potentials. A voltage-controlled strategy was used at 0.5 A g^{-1} to limit the over-oxidation of Br$^-$ and ensure the reversibility of batteries (Figure S21b,c, Supporting Information). In other words, the specific capacity has to be controlled around 605.7 mAh g^{-1} to avoid the decrement of coulombic efficiency. The Zn/GFF|WSOE$_{45}$-1|PGA cells demonstrated excellent cycle stability (Figure 4b), with 74.5% of initial capacity retained after 500 cycles at 1 A g^{-1}. The structure of graphene cathode was well maintained after the cycling test (Figure S22a–c, Supporting Information). The stability of Zn stripping/plating in WSOE$_{45}$-1 was also affirmed by a Zn|WSOE$_{45}$-1|Zn symmetric cell as shown in Figure S22d, Supporting Information. To explore the causes of capacity recession during long-term tests, X-ray photoelectron spectroscopy (XPS) was used to characterize the cycled PGA cathode. As a result, C−Br covalent bonds (286.9 and 70.0 eV in Figures S22e and 22f, Supporting Information, respectively) were found in the cycled PGA at a discharged state,[24,25] which account for the recession of battery capacity by weakening the reversibility of Br-intercalation/deintercalation. This problem should be overcome in the future work. We measured the EIS of PGA cathode in WSOE$_{45}$-1 with a three-electrode setup at different states of charge (SOC). As a result, the interfacial resistance between PGA cathode and electrolyte ($R_{ct,1}$ in Figure 4c) decreases with SOC (from 224.7 to 211.3 Ω), which can be explained by infiltration
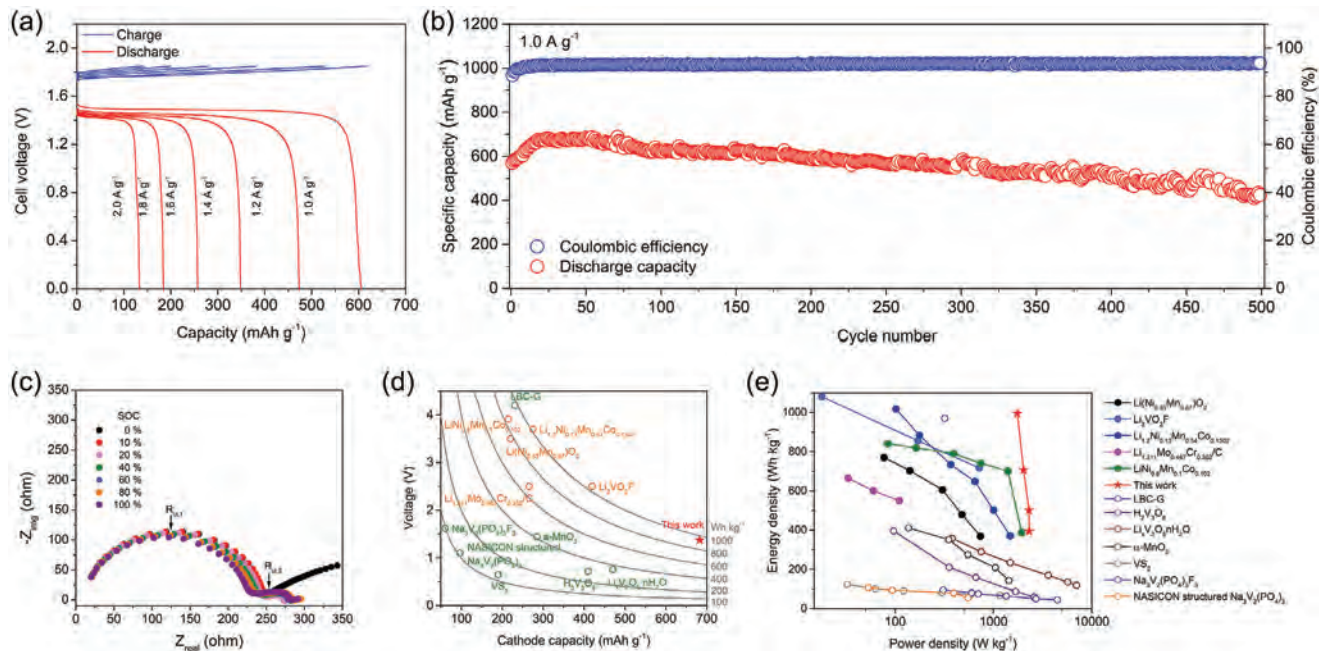
Figure 4. Electrochemical performance. a) Galvanostatic charge–discharge profiles of the dual-ion battery at various rates. b) Cycling stability of the dual-ion battery at 1 A g^{-1}. c) Nyquist plots of the PGA cathode in WSOE$_{45}$-1 at various SOCs, obtained by a three-electrode setup. The Zn foil and Ag/AgCl were used as the counter electrode and reference electrode, respectively. d) Energy density of the Br-intercalated PGA cathode compared with various state-of-the-art cathode using both non-aqueous (yellow circles) and aqueous (green circles) electrolytes. e) Ragone plots of the Br-intercalated PGA cathode compared with various non-aqueous (solid circles) and aqueous (hollow circles) cathodes. All of the above data were based on the WSOE$_{45}$-1. The anode used for NASICON-structured Na$_3$V$_2$(PO$_4$)$_3$, Na$_3$V$_2$(PO$_4$)$_3$F$_3$, VS$_2$, α-MnO$_2$, Li$_x$V$_2$O$_5\cdot n$H$_2$O, and H$_2$V$_3$O$_8$ in (d) and (e) is zinc metal, and that used for LiNi$_{0.8}$Mn$_{0.1}$Co$_{0.102}$, Li$_{1.211}$Mo$_{0.467}$Cr$_{0.302}$/C, Li$_{1.2}$Ni$_{0.13}$Mn$_{0.54}$Co$_{0.1302}$, Li$_2$VO$_2$F, and Li[Ni$_{1/3}$Mn$_{2/3}$]O$_2$ in (d) and (e) is lithium metal. Only the LBC-G is coupled with a graphite anode.

of the WSOE$_{45}$-1 into electrodes. Simultaneously, the intrinsic resistance of the Nyquist plot is also gradually reduced (from 22.8 to 20.1 Ω), which is caused by the increased electrical conductivity of graphene assembly after Br-intercalation.[25] During charge, a new interfacial resistance ($R_{ct,2}$ in Figure 4c) is observed and increases with SOC (from 31.3 to 51.1 Ω). This result is attributed to accumulated halogen species on the cathode. More detailed analyses of the Nyquist plots are provided in Figure S23, Supporting Information. The most significant advantage of our DIBs is the high specific capacity of PGA cathode in WSOE$_{45}$-1, which is benefited from the ultrahigh ionic concentration of electrolyte. The energy density of PGA cathode was calculated to be 908.5 Wh kg^{-1} (the theoretical cell-level energy density is 109.2 Wh kg^{-1} or 238.2 Wh L^{-1}, calculated by Equation (S5), Supporting Information), and is greater than that of most state-of-the-art cathodes as shown in Figure 4d,e.[11,26–35] The high power density of our dual-ion batteries at 1 A g^{-1} in Figure 4e is attributed to high concentrations of electrolyte ions in the electrical double-layer near electrodes, which provide enough active materials for electrode reactions and alleviate the dependence of mass transfer. Comparisons of electrochemical performances between our dual-ion batteries and more devices are provided in Tables S3–S7, Supporting Information. Moreover, the cost of the WSOE$_{45}$-1 is much cheaper than that of previously reported concentrated electrolytes as shown in Tables S8 and S9, Supporting Information. The safety and environmental tolerance of DIBs are demonstrated by Movies S1–S3 and Figure S24, Supporting Information.

In situ Raman spectroscopy (100–500 cm^{-1}) was performed to probe the intercalated Br in graphene cathode (**Figure 5**a). A characteristic peak at 242 cm^{-1} was observed and gradually intensified with the SOC, corresponding to the stretch-mode of intercalated Br$_2$ in graphite lattice. Compared with free Br$_2$ (liquid) located at 318 cm^{-1}, a frequency downshift for intercalated Br$_2$ was found resulted from the interaction with graphene layer which weakens the interatomic bonds of halogen intercalants.[36] No free Br$_2$ peak was detected during charge/discharge processes, indicating that almost all of the oxidized bromines were intercalated into the graphitic structure of PGA cathode rather than simply absorbed on the surface of electrode, which is benefited from the ultrahigh concentration of electrolyte as abovementioned. When discharge process was carried out, the intercalated-Br peak is gradually weakened and even disappeared with the SOC at 0%, demonstrating a good reversibility of the intercalation and deintercalation process of Br. The intercalation of ions, atoms, and molecules into graphitic materials has an effect on their lattice parameters as well as Raman vibrations.[37] Figure 5b shows structural evolutions of the PGA cathode during charge/discharge processes by in situ Raman spectroscopy (1500–1650 cm^{-1}). Upon charging, Br intercalated into PGA cathode, meanwhile the graphite G band (1580 cm^{-1}) diminishes and first shifts to 1612 cm^{-1}, corresponding to a stage-2 Br-GIC structure.[38] The peak further shifts from 1612 to 1625 cm^{-1} at 100% SOC, indicating a stage-1 Br-GIC structure of the PGA cathode in this condition. Such a stage-1 Br-GIC was only previously observed in a single-layer graphene by

**ADVANCED
SCIENCE NEWS**
www.advancedsciencenews.com

**ADVANCED
MATERIALS**
www.advmat.de
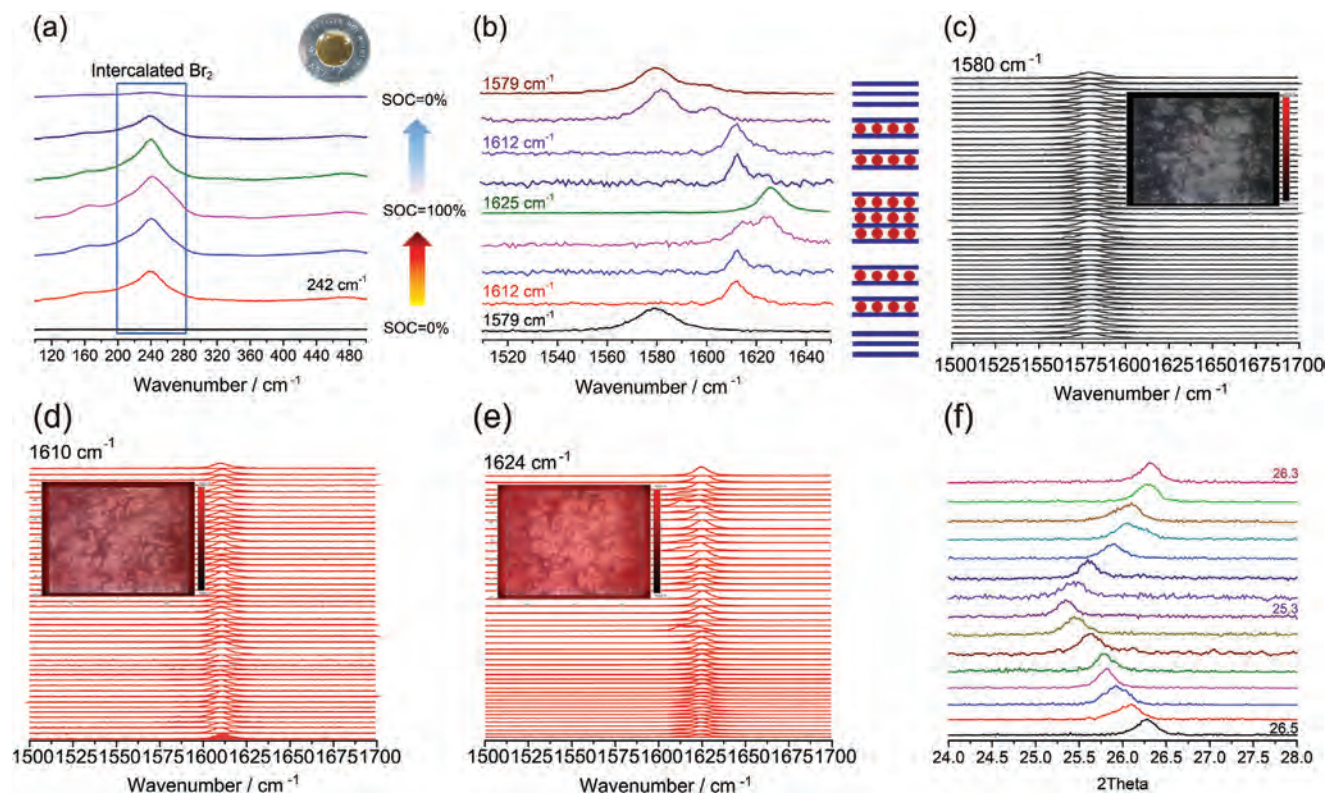
Figure 5. Energy storage mechanism. a,b) Raman spectra (100–500 cm^{-1} and 1510–1650 cm^{-1}) of Br-intercalated PGA cathode in situ during a charge–discharge cycle. c) Raman mapping and corresponding peaks of pristine PGA cathode before charge, d) stage-2 Br-intercalated PGA cathode during charge, and e) stage-1 Br-intercalated PGA cathode after charge. f) XRD profile of the Br-intercalated PGA cathode obtained in situ during a charge–discharge cycle. The color range of the maps in 5c-e refer to different Raman shift obtained on graphene cathode, and the wavenumber increases from blackness to redness.

Jung et al., whereas it is hardly to be achieved in macroscopic graphene assemblies (such as the PGA cathode) by chemical doping.[38] We attribute the stage-1 Br-GIC structure of PGA to the two reasons: 1) The activity of electrolyte (Br$^-$) is increased by salt molality,[39] that promotes the oxidation of Br$^-$ anions. 2) The dissolution of oxidized Br into electrolyte is suppressed by highly concentrated WSOE$_{45}$-1 (Figure S25, Supporting Information) that promotes the intercalation of Br into graphene lattice. Reversible process was observed during discharge. In addition, Raman mapping demonstrates uniform structures of pristine (Figure 5c) and Br-intercalated PGA cathode at different stages (Figure 5d,e).

X-ray diffraction (XRD) tests were also in situ performed with a DIB cell (Figure 5f). The (002) peak of PGA cathode experienced continuous shifting from 26.5° to 25.3° during charging process, indicating the gradual expansion of graphene interlayers with Br-intercalation. The d-spacing of PGA cathode at 100% SOC is calculated to be 0.352 nm, which is quite close to the theoretical value (0.35 nm) of stage-1 intercalated Br-GIC.[23] Upon discharging, de-intercalation of Br occurred and the expanded graphene layer gradually recovered to its pristine state again (d_{002} = 0.338 nm), representing the recovery of graphene structure in a complete charge/discharge cycle.

In summary, the polymer-like inorganic WSOEs consisted of acetate-capped water–salt oligomers break through physical solubility limits of aqueous electrolytes and demonstrate their advanced

performances for rechargeable batteries. In comparison to lithium-ion batteries (LIBs) that are troubled by limited amount and non-uniform distribution of lithium source on the earth, WSOE-based batteries driven by concentrated zinc and halogen elements provide a complement technology for low-cost and highly safe energy storages. Additionally, the WSOE may also be favored in other areas, such as polymer-free solid electrolyte and synthesis media.

Experimental Section

Materials: Zinc chloride (≥98.0%), zinc bromide (≥99.9%), and zinc acetate (≥99.0%) were purchased from Shanghai Aladdin Bio-Chem Technology Co., Ltd. Graphene oxide with average lateral size of 20 μm was acquired from GaoxiTech Co., Ltd. All reagents were used as received without any further treatment. Deionized water was generated by PW Ultrapure Water System and had a resistivity of 18 MΩ cm.

Preparation of Electrolyte: WSOE: Typically, the WSOE$_{45}$-1 was prepared by dissolving 9.200 g (0.0225 mol) $ZnCl_2$, 5.067 g (0.0675 mol) $ZnBr_2$, and 0.367 g (0.002 mol) $Zn(CH_3COO)_2$ in 2.0 g deionized water, and then heated at 60 °C for 2 h and then 120 °C for 72 h. Resultant solutions were cooled at room temperature before tests. Conventional electrolytes: 1–30 m $ZnCl_2$, 1–30 m $ZnBr_2$, and 1–35 m $ZnBr_{0.5}Cl_{1.5}$ aqueous solutions were prepared by dissolving zinc salts in water solvent at 60 °C under stirring, and cooled down at room temperature before tests.

NMR: NMR spectra were obtained on a Brulcer 500 MHz NMR spectrometer (DMX-500). Typically, 0.5 mL of electrolyte was added into a 5 mm glass NMR tube for characterization and chloroform-d (CDCl$_3$) in a sealed coaxial glass tube was used for reference. NMR

**ADVANCED
SCIENCE NEWS**

www.advancedsciencenews.com

**ADVANCED
MATERIALS**

www.advmat.de

tubes were immediately sealed with plastic septa wrapped with parafilm to limit exposure to atmospheric moisture. Data were processed in MestReNova 11.0.4.

Raman Spectroscopy for Electrolytes: Electrolyte was dropped in a dry glass slide and then immediately tested by inVia-Reflex (Renishaw plc) with a laser of 532 nm wavelength.

Electrospray Ionization Mass Spectrometry: The electrolytes were first diluted by anhydrous methyl alcohol (mass ratio = 1:50), and then used for analysis.

FTIR Spectroscopy: FTIR spectra were collected by a Nicolet 5700 spectrometer, mounted with an attenuated total reflectance accessory. Electrolyte solutions were analyzed using 16 scans with a 4 cm^{-1} resolution from 4000 to 650 cm^{-1}. Background correction was performed by measuring the ambient atmosphere in the same conditions.

DSC: DSC traces were obtained on a Perkin Elmer DSC4000. Electrolytes ($\approx$5–10 mg) were added into aluminum Tzero pans and hermetically sealed with a Tzero Sample press. Samples were cooled from room temperature to −80 °C at a rate of 5 °C min^{-1}.

MD Simulations: The simulation box consisted of a cube box with length of 50 Å containing several ion pairs and water molecules. Parameters of the atomistic models of OAc were based on the OPLS-AA force field.[40] The parameters of Zn^{2+} ion are shown in Table S10, Supporting Information. For water molecules, the four-site water model TIP4P/Ew was used.[41] 3D periodic boundary conditions were used to avoid the influence of the box boundary during simulations. The cut-off distance of non-bonded interactions was 13 Å and the long-range electrostatic interactions were calculated by the particle-mesh Ewald method.[42] Initial structures for molecular dynamic simulation were constructed by Packmol software package.[43] The ion pairs of salts and water molecules were randomly placed in a simulated box for providing homogeneous structures. Prior to the dynamics simulation, the steepest descent algorithm was used to pre-equalize the system for eliminating the excessive stress in initial structures.[44] After pre-equilibrium, an *NPT* ensemble was used to equilibrate the system under room conditions (298 K and 1 atm) for 10 ns which can converge the density of the system to a stable value. Then, 35 ns production simulation in the *NVT* ensemble at 298.15 K was carried out for data collection. The density and potential energy changes of the WSOE$_{45}$-1 system during the *NPT* process are shown in Figure S26a,b, Supporting Information. The mean square displacement of each species from 0 to 30 ns in the *NVT* process is shown in Figure S26c, Supporting Information. Both *NPT* and *NVT* simulations used time step of 1 fs. Temperature and pressure coupling were performed using v-rescale thermostat and Berendsen barostat.[45,46] All simulations were carried out by using the GROMACS 2018.6 software package.[47] All visualization structures are provided by VMD 1.9.3 software. Radial distribution functions (RDF) $g(r)_{A-B}$ was calculated by:

$$g(r)_{A-B} = \frac{1}{\rho_B} \frac{1}{N_A} \sum_{i=1}^{N_A} \sum_{j=1}^{N_B} \frac{\delta(r_{ij} - r)}{4\pi r^2} \tag{1}$$

with ρ_B the particle density of type B averaged over all spheres around particles A.

The coordination number is determined by the number of particles in the first solvation shell of the ion. Therefore, the integral value of the radial distribution function at the first valley is the coordination number. The corresponding integral number is calculated by the following equation:

$$N(r) = 4\pi\rho_N \int_0^r r^2 g(r) dr \tag{2}$$

where ρ_N is the average number density of coordination atoms. This method has been reported in the literature.[48–50] The corresponding valley used for calculating coordination numbers are provided in Table S11, Supporting Information.

Preparation of the Electrode: PGA cathode was obtained by previously reported method.[51] First, graphene oxide (GO) solution (5 mg mL^{-1})

was freeze-dried to get GO aerogel. It was then reduced by hydrazine hydrate at 95 °C and carbonized at 3000 °C for 1 h in a graphite furnace which was under the protection of argon flow to remove oxygen-containing groups and restore defects. The resulted aerogel was finally compressed into porous papers to get the PGA cathode. Zn/GFF anode was formed by in situ deposition of Zn on graphene fiber non-woven fabrics,[52] which was prepared by filtration of GO fibers in a mixture of water and ethanol (volume ratio of 3:1), followed by chemical reduction and high temperature carbonized at 3000 °C.

Electrochemical Measurements: In the three-electrode cells, the PGA cathode (Zn/GFF anode or Ti current collector) was used as the working electrode, Zn foil as the counter-electrode, and Ag/AgCl as the reference electrode. Cyclic voltammetry tests were carried out by a CHI 660E electrochemical work station. The EIS measurement was performed on the Multi Autolab M204 (Metrohm) using a 5-mV perturbation with frequency in the range of 0.01–1 000 000 Hz at room temperature. The dual-ion batteries were assembled as CR2025-type coin cells using PGA as the cathode (areal loadings were $\approx$2.79 mg cm^{-2}) and Zn/GFF as the anode. A titanium metal foil disk was placed between the cathode and the coin cell case to prevent corrosion. Glass microfiber filters (thickness of 435 µm; Whatman 934-AH) were used as the separator. After assembly, the electrochemical performances were evaluated by CHI 660E and Multi Autolab M204. The galvanostatic cycling measurements at 25 °C (in a constant temperature humidity chamber) were carried out on a Land BT2000 battery test system. The Zn|WSOE$_{45}$-1|Zn symmetric cell was assembled and tested in a similar way. Soft pack cells were fabricated with the PGA cathode, Zn/GFF anode, WSOE$_{45}$-1, titanium foil current collector (for cathode), and glass fiber filters.

In Situ Raman Spectroscopy for PGA Cathode: For the in situ Raman measurements, a Zn/GFF|WSOE$_{45}$-1|PGA cell with a kapton optical window on the cathode side was charged and discharged at 1 A g^{-1}. Raman spectra and mapping patterns were directly collected on the in Via-Reflex (Renishaw plc) using a laser of 532 nm wavelength.

In Situ XRD Study of PGA Cathodes: For the in situ XRD measurements, a Zn/GFF|WSOE$_{45}$-1|PGA cell with a Kapton window on the cathode side was charged and discharged at 1 A g^{-1}. During this process, the battery was directly put on the X-ray diffractometer to obtain immediate results. The d-spacing of PGA cathodes could be calculated from the diffraction angles by Bragg's law.

Supporting Information

Supporting Information is available from the Wiley Online Library or from the author.

Conflict of Interest

The authors declare no conflict of interest.

**ADVANCED
SCIENCE NEWS**
www.advancedsciencenews.com

**ADVANCED
MATERIALS**
www.advmat.de

[1] H. Kim, J. Hong, K. Y. Park, H. Kim, S. W. Kim, K. Kang, *Chem. Rev.* **2014**, *114*, 11788.

[2] W. Li, J. R. Dahn, D. S. Wainwright, *Science* **1994**, *264*, 1115.

[3] Y. Wang, J. Yi, Y. Xia, *Adv. Energy Mater.* **2012**, *2*, 830.

[4] F. Beck, P. Rüetschi, *Electrochim. Acta* **2000**, *45*, 15.

[5] O. Borodin, J. Self, K. A. Persson, C. S. Wang, K. Xu, *Joule* **2020**, *4*, 69.

[6] L. M. Suo, O. Borodin, T. Gao, M. Olguin, J. Ho, X. L. Fan, C. Luo, C. S. Wang, K. Xu, *Science* **2015**, *350*, 938.

[7] C. A. Angell, *J. Electrochem. Soc.* **1965**, *112*, 1224.

[8] L. M. Suo, O. Borodin, W. Sun, X. L. Fan, C. Y. Yang, F. Wang, T. Gao, Z. H. Ma, M. Schroeder, A. V. Cresce, S. M. Russell, M. Armand, A. Angell, K. Xu, C. S. Wang, *Angew. Chem., Int. Ed.* **2016**, *128*, 7252.

[9] Y. Yamada, K. Usui, K. Sodeyama, S. Ko, Y. Tateyama, A. Yamada, *Nat. Energy* **2016**, *1*, 16129.

[10] M. R. Lukatskaya, J. I. Feldblyum, D. G. Mackanic, F. Lissel, D. Michels, Y. Cui, Z. N. Bao, *Energy Environ. Sci.* **2018**, *11*, 2876.

[11] C. Zhang, J. Holoubek, X. Y. Wu, A. Daniyar, L. D. Zhu, C. Chen, D. P. Leonard, I. A. Rodríguez-Pérez, J. X. Jiang, C. Fang, X. L. Ji, *Chem. Commun.* **2018**, *54*, 14097.

[12] R. B. Ellis, *J. Electrochem. Soc.* **1966**, *113*, 485.

[13] H. Kanno, J. Hiraishi, *J. Raman Spectrosc.* **1980**, *9*, 85.

[14] F. Wang, O. Borodin, T. Gao, X. L. Fan, W. Sun, F. D. Han, A. Faraone, J. A. Dura, K. Xu, C. S. Wang, *Nature Mater.* **2018**, *17*, 543.

[15] D. E. Irish, T. F. Young, *J. Chem. Phys.* **1965**, *43*, 1765.

[16] K. Fukushima, H. Yokota, H. Ibaraki, T. Nakazawa, K. Noda, Y. Iwadate, *J. Alloys Compd.* **1998**, *266*, 145.

[17] B. M. Auer, J. L. Skinner, *J. Chem. Phys.* **2008**, *128*, 224511.

[18] L. M. Uriarte, J. Dubessy, P. Boulet, V. G. Baonza, I. Bihannic, P. Robert, *J. Raman Spectrosc.* **2015**, *46*, 822.

[19] Y.-H. Zhang, C. K. Chan, *J. Phys. Chem. A* **2003**, *107*, 5956.

[20] G. E. Walrafen, *J. Chem. Phys.* **1964**, *40*, 3249.

[21] M. H. Brooker, G. Hancock, B. C. Rice, J. Shapter, **1989**, *20*, 683.

[22] B. Auer, R. Kumar, J. R. Schmidt, J. L. Skinner, *P. Natl. Acad. Sci. U. S. A.* **2007**, *104*, 14215.

[23] C. Y. Yang, J. Chen, X. Ji, T. P. Pollard, X. J. Lü, C. J. Sun, S. Hou, Q. Liu, C. M. Liu, T. T. Qing, Y. Q. Wang, O. Borodin, Y. Ren, K. Xu, C. S. Wang, *Nature* **2019**, *569*, 245.

[24] L. G. Bulusheva, V. A. Tur, E. O. Fedorovskaya, I. P. Asanov, D. Pontiroli, M. Riccò, A. V. Okotrub, *Carbon* **2014**, *78*, 137.

[25] Y. J. Liu, Z. Xu, J. M. Zhan, P. G. Li, C. Gao, *Adv. Mater.* **2016**, *28*, 7941.

[26] P. K. Nayak, J. Grinblat, M. D. Levi, O. Haik, E. Levi, M. Talianker, B. Markovsky, Y. K. Sun, D. Aurbach, *Chem. Mater.* **2015**, *27*, 2600.

[27] R. Y. Chen, S. H. Ren, M. Knapp, D. Wang, R. Witter, M. Fichtner, H. Hahn, *Adv. Energy Mater.* **2015**, *5*, 1401814.

[28] P. K. Nayak, T. R. Penki, B. Markovsky, D. Aurbach, *ACS Energy Lett.* **2017**, *2*, 544.

[29] J. Lee, A. Urban, X. Li, D. Su, G. Hautier, G. Ceder, *Science* **2014**, *343*, 519.

[30] X. L. Fan, L. Chen, O. Borodin, X. Ji, J. Chen, S. Y. Hou, T. Deng, J. Zheng, C. Y. Yang, S. C. Liou, K. Amine, K. Xu, C. S. Wang, *Nat. Nanotechnol.* **2018**, *13*, 715.

[31] P. He, Y. Quan, X. Xu, M. Yan, W. Yang, Q. An, L. He, L. Mai, *Small* **2017**, *13*, 1702551.

[32] Y. Q. Yang, Y. Tang, G. Z. Fang, L. T. Shan, J. S. Guo, W. Y. Zhang, C. Wang, L. B. Wang, J. Zhou, S. Q. Liang, *Energy Environ. Sci.* **2018**, *11*, 3157.

[33] B. Wu, G. B. Zhang, M. Y. Yan, T. F. Xiong, P. He, L. He, X. Xu, L. Q. Mai, *Small* **2018**, *14*, 1703850.

[34] P. He, M. Y. Yan, G. B. Zhang, R. M. Sun, L. N. Chen, Q. Y. An, L. Q. Mai, *Adv. Energy Mater.* **2017**, *7*, 1601920.

[35] W. Li, K. L. Wang, S. J. Cheng, K. Jiang, *Energy Storage Mater.* **2018**, *15*, 14.

[36] A. Erbil, G. Dresselhaus, M. S. Dresselhaus, *Phys. Rev. B* **1982**, *25*, 5451.

[37] D. Zhan, L. Sun, Z. H. Ni, L. Liu, X. F. Fan, Y. Y. Wang, T. Yu, Y. M. L. , W. Huang, Z. X. Shen, *Adv. Funct. Mater.* **2010**, *20*, 3504.

[38] N. Jung, N. Kim, S. Jockusch, N. J. Turro, P. Kim, L. Brus, *Nano Lett.* **2009**, *9*, 4133.

[39] M. R. Ally, J. Braunstein, *Fluid Phase Equilibr.* **1996**, *120*, 131.

[40] W. L. Jorgensen, D. S. Maxwell, J. Tirado-Rives, *J. Am. Chem. Soc.* **1996**, *118*, 11225.

[41] H. W. Horn, W. C. Swope, J. W. Pitera, J. D. Madura, T. J. Dick, G. L. Hura, T. Head-Gordon, *J. Chem. Phys.* **2004**, *120*, 9665.

[42] L. Martínez, R. Andrade, E. G. Birgin, J. M. Martínez, *J. Comput. Chem.* **2009**, *30*, 2157.

[43] M. C. Payne, M. P. Teter, D. C. Allan, T. A. Arias, J. D. Joannopoulos, *Rev. Mod. Phys.* **1992**, *64*, 1045.

[44] G. Bussi, D. Donadio, M. Parrinello, *J. Chem. Phys.* **2007**, *126*, 014101.

[45] H. J. C. Berendsen, J. P. M. Postma, W. F. van Gunsteren, A. DiNola, J. R. Haak, *J. Chem. Phys.* **1984**, *81*, 3684.

[46] M. J. Abraham, T. Murtola, R. Schulz, S. Páll, J. C. Smith, B. Hess, E. Lindahl, *SoftwareX* **2015**, *1–2*, 19.

[47] W. Humphrey, A. Dalke, K. Schulten, *J. Mol. Graph.* **1996**, *14*, 33.

[48] Y. Liu, H. G. Lu, Y. B. Wu, T. P. Hu, Q. L. Li, *J. Chem. Phys.* **2010**, *132*, 1157.

[49] R. M. D. Souza, L. J. A. D. Siqueira, M. Karttunen, L. G. Dias, *J. Chem. Inf. Model.* **2019**, *60*, 485.

[50] M. Q. Fatmi, T. S. Hofer, B. M. Rode, *J. Chem. Phys.* **2010**, *12*, 9713.

[51] H. Chen, F. Guo, Y. J. Liu, T. Q. Huang, B. N. Zheng, N. Ananth, Z. Xu, W. W. Gao, C. Gao, *Adv. Mater.* **2017**, *29*, 1605958.

[52] Z. Li, Z. Xu, Y. J. Liu, R. Wang, C. Gao, *Nat. Commun.* **2016**, *7*, 13684.

RESEARCH ARTICLE

ENERGY STORAGE WILEY

A dendrite free Zn-Fe hybrid redox flow battery for renewable energy storage

C. Balakrishnan Jeena [ID] | P. Jose Elsa [ID] | P. Peter Moly [ID] |
K. Jacob Ambily [ID] | Vadakkan T. Joy [ID]

Department of Chemistry, Christ College (Autonomous, affiliated to University of Calicut), Irinjalakuda, Kerala, India

Correspondence
Vadakkan T. Joy, Department of Chemistry, Christ College (Autonomous, affiliated to University of Calicut), Irinjalakuda, Kerala 680125, India.
Email: joyvthomas@christcollegeijk.edu.in; joyvthomas2002@gmail.com

Abstract
About two thirds of global greenhouse emissions is caused by burning of fossil fuels for energy purposes and this has spurred great research interest to develop renewable energy technologies based on wind, solar power, and so on. Redox flow batteries (RFB) are receiving wide attention as scalable energy-storage systems to address the intermittency issues of renewable energy sources. However, for widespread commercialization, the redox flow batteries should be economically viable and environmentally friendly. Zinc based batteries are good choice for energy storage devices because zinc is earth abundant and zinc metal has a moderate specific capacity of 820 mA hg^{-1} and high volumetric capacity of 5851 mA h cm^{-3}. We herein report a zinc-iron (Zn-Fe) hybrid RFB employing Zn/Zn(II) and Fe(II)/Fe(III) redox couples as positive and negative redox systems, respectively, separated by a self-made anion exchange membrane (AEM). The battery delivers a good discharge voltage of approximately 1.34 V at 25 mA cm^{-2}, with a coulombic efficiency (CE) of 92%, voltage efficiency (VE) of 85% and energy efficiency (EE) of ~78% for 30 charge-discharge cycles. Repeated galvanostatic charge/discharge cycles show no degradation in performance, confirming the excellent stability of the system. A key advancement in the present Zn-Fe hybrid redox flow battery with AEM separator is that no dendrite growth was observed on zinc electrode on repeated charge-discharge cycles, which was the serious drawback of many previously reported zinc based redox flow batteries.

KEYWORDS
anion-exchange membrane, dendrite growth suppression, energy storage, redox flow battery, renewable energy, zinc deposition

1 | INTRODUCTION

Global climate change resulting from greenhouse emissions is causing increasingly severe risks for ecosystems, human safety and health. This combined with the large-scale demand for electricity expected during the coming decades has aroused great interest in the development of new technologies for energy production from renewable energy sources, such as wind, solar, and so on. However, these renewable energy sources are intermittent in nature and hence the success of these new renewable energy harvesting technologies needs to be associated with the introduction of competitive energy storage devices for grid scale energy storage. Unlike traditional batteries, the
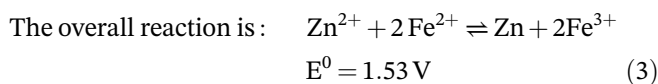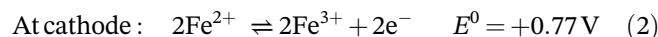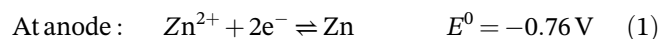
redox flow batteries (RFBs) are attractive electrochemical systems which store energy in two electrolyte solutions comprising of different redox couples separated by an ion-exchange membrane (IEM).[1–5] Among various traditional flow battery systems, the hybrid flow batteries involve the deposition of a metal coating on at least one of the electrodes.[4,6] The main advantages of RFBs over other battery systems are their safety, moderate cost, modularity, transportability and flexibility in charge-discharge cycles.[7–9] Unfortunately, the inadequate ionic selectivity of the existing IEMs leads to undesired crossover of redox species between negative and positive electrolytes through the membrane. This results a permanent loss of both coulombic efficiency (CE) and battery capacity and will lead to overall performance degradation of RFBs.[5,10–13]

There are many redox flow batteries under development and among which the vanadium redox flow battery (VRFB) reported by Skyllas-Kazacos et al. at the University of New South Wales (UNSW), Australia is considered as most successful RFBs to date but its commercialization is hindered mainly by the high costs of vanadium salts and perfluorosulfonic acid (PFSA) membrane.[14–16] Other RFBs that uses low-cost redox materials are all-copper,[17–20] all-iron[21,22] and all-lead[23–25] RFBs, but all these systems have low performances. Due to slow kinetics of Cu/Cu(I) redox couple, all-copper RFBs have low energy efficiency and low cell voltage.[17,26] In all-iron RFBs, the standard redox potential of Fe^{2+}/Fe (-0.44 V vs SHE) is more negative than that of hydrogen evolution reaction (HER) and lower hydrogen overpotential of iron causes hydrogen evolution and coulombic losses.[27–29]

Zinc-based redox flow batteries are generally more attractive due to favorable electrochemical properties of zinc such as its low cost, fast electrode kinetics, negative electrode potential ($E^0 = -0.76$ V vs SHE) and high overpotential for the hydrogen evolution reaction (HER).[30–32] A Zn-Fe flow battery system reported by Selverston et al. used mixed zinc-iron electrolytes and porous separator in place of expensive ion-exchange membranes.[31] Gong et al. reported a zinc-iron RFB based on double-membrane triple electrolyte design.[33] Yuan et al. reported a battery that employs $Zn(OH)_4^{2-}$/Zn and $Fe(CN)_6^{3-}$/Fe$(CN)_6^{4-}$ as the negative and positive redox couples, respectively, while a self-made polybenzimidazole (PBI) membrane was used as a separator. Xie et al. reported an energy efficiency of 71.1% over 50 cycles for a zinc-ferrum redox flow battery (Zn/Fe RFB) employing an ion exchange membrane as a separator.[34] Wu et al. developed a chloride acid-based tin-iron hybrid flow battery with good rate and cycle performance.[35,36] Wang and co-workers developed a zinc-polyiodide flow battery and reported high energy density.[29] During the charging process of Zn based flow batteries, zinc dendrites form and

ultimately pierce the separator, causing a short circuit and battery failure.[37–40] Additionally, zinc dendrites can easily fall from anodes, reducing efficiency, capacity and life time of the cell.[41] As a result, inhibiting the formation of zinc dendrites is essential for the successful commercialization of zinc based RFBs. Researchers have recently focused their efforts on modifying the electrolyte, anodes, electric field, and rate of zinc ion transfer to solve zinc dendrite formation.[37,39] To prevent negative effects of zinc dendrites on the performance and lifetime of zinc-based batteries, the separator should also have good mechanical stability to prevent the direct contact of the anode and cathode.[42] Thus, developing a high efficiency, dendrite free zinc based RFB electrical energy storage system having negligible crossover of the electroactive materials between the anode and cathode compartments, is an important goal towards widespread use of renewable energy sources.

Herein we report a novel zinc-iron hybrid redox flow battery (Zn/Fe hybrid RFB), in which Zn/Zn(II) and Fe(II)/Fe(III) redox couples act as negative and positive redox materials and the two redox couples are separated by a self-made anion exchange membrane. Both zinc and iron are the two advantageous elements for energy storage due to their low cost and high abundance.[33] The ferric/ferrous chloride redox pair, which has been used in a variety of flow battery systems, is promising as an active material on the positive side due to its rapid kinetics.[27] Electrodes were densified graphite sheets and cell housings were made of acrylic sheets. A schematic representation of the Zn-Fe hybrid redox flow battery is shown in Figure 1. The electrochemical reaction through which Zn-Fe RFB stores and releases electricity can be expressed by following reactions:

$$\text{At anode}: \quad Zn^{2+} + 2e^- \rightleftharpoons Zn \qquad E^0 = -0.76\,\text{V} \quad (1)$$

$$\text{At cathode}: \quad 2Fe^{2+} \rightleftharpoons 2Fe^{3+} + 2e^- \qquad E^0 = +0.77\,\text{V} \quad (2)$$

$$\text{The overall reaction is}: \quad Zn^{2+} + 2\,Fe^{2+} \rightleftharpoons Zn + 2Fe^{3+}$$
$$E^0 = 1.53\,\text{V} \qquad (3)$$

During the charging process, the Fe(II) ions at the positive electrode release the electrons, and get oxidized to Fe(III) ions; the Zn(II) ions at the negative electrode acquire these electrons from the external circuit, and electrodeposits onto the electrode as metallic Zn. The chloride ions move through the anion-exchange membrane from zinc compartment to the iron compartment, to maintain charge neutrality. During the discharge, the above electrochemical processes are reversed. At the
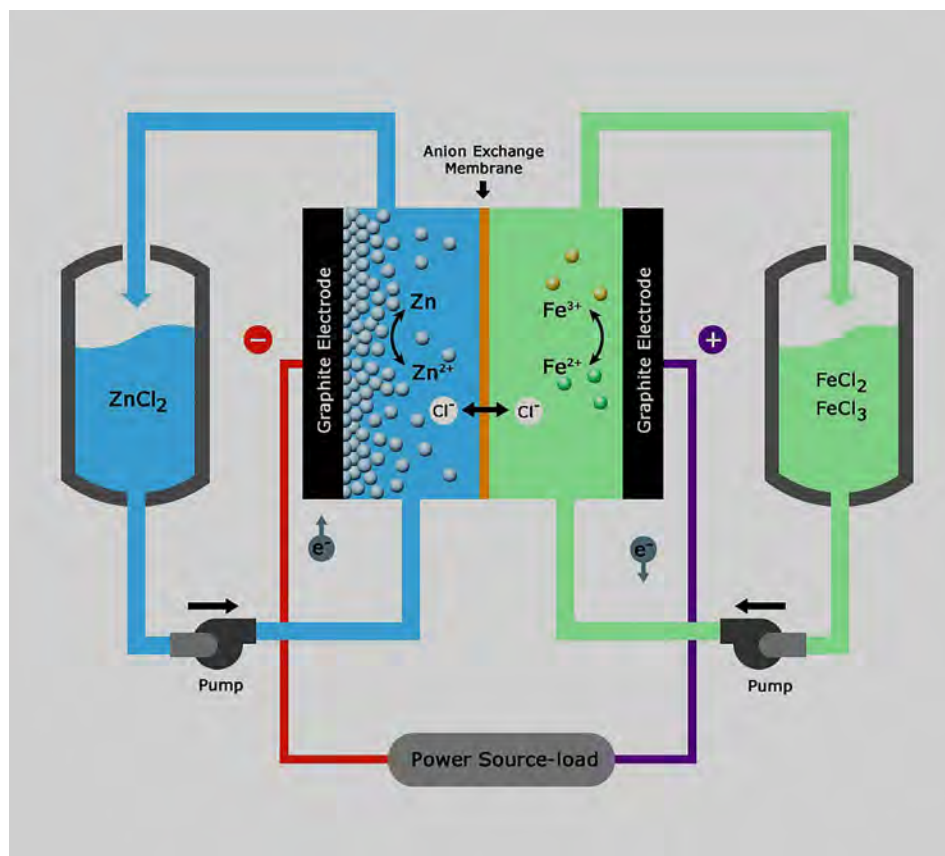
positive electrode, the Fe(II)/Fe(III) redox couple have good solubility in acidic media and exhibits facile kinetics.[33] At the negative electrode, the Zn/Zn(II) redox couple also exhibit fast kinetics and has high overpotential for hydrogen evolution reaction.

2 | EXPERIMENTAL

2.1 | Chemicals

All chemicals were of reagent grade and the electrolytes were prepared with deionized water. Iron(II) chloride tetrahydrate ($FeCl_2 \cdot 4H_2O$), iron(III) chloride ($FeCl_3$), ammonium chloride (NH_4Cl) and zinc chloride ($ZnCl_2$) were obtained from Merck India.

2.2 | Preparation of electrolyte

1 M Zn/Zn(II) electrolyte is prepared by dissolving Zn(II) chloride in deionized water (pH = 5.8). The positive electrolyte is a mixture of 0.5 M $FeCl_2$ and 0.5 M $FeCl_3$ with 2 M NH_4Cl in deionized water (pH = 1.7). The NH_4Cl was added to the positive electrolyte as a supporting electrolyte in order to improve conductivity of the solution.

2.3 | Preparation of anion-exchange membrane

The anion-exchange membrane was prepared by condensing guanidine carbonate with formaldehyde followed by cross-condensation with melamine. The dried powder was mixed with a polymer powder as a binder and made in to a homogeneous suspension and converted in to membrane by solvent casting method. The prepared membranes were highly flexible and had a thickness of ~120 μm. The prepared membranes exhibited hydroxide ion conductivity around 80 mS^{-1} at room temperature. The ion exchange value of the membrane was 1.2 mmol/g. To study the alkaline stability, the membranes were kept immersed in 2 M NaOH at room temperature for 2 weeks. The FT-IR and weight loss measurements of the washed, dried membrane after alkali treatment show no signs of degradation and weight loss indicating high alkaline stability. Figure 2 shows the SEM images of the membrane. More details about the membrane will be published elsewhere.

2.4 | Cyclic voltammetry

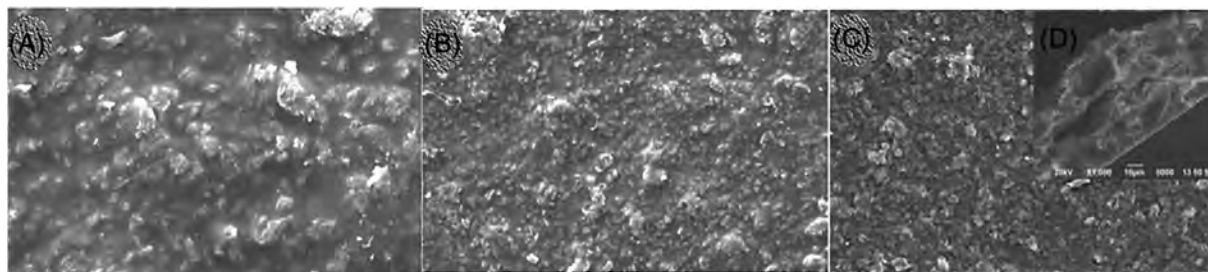Cyclic voltammetry (CV) experiments were conducted in a three-electrode cell as shown in Figure 3, using a

FIGURE 2 (A-C) The SEM images of the membrane and (D) cross-sectional image of membrane
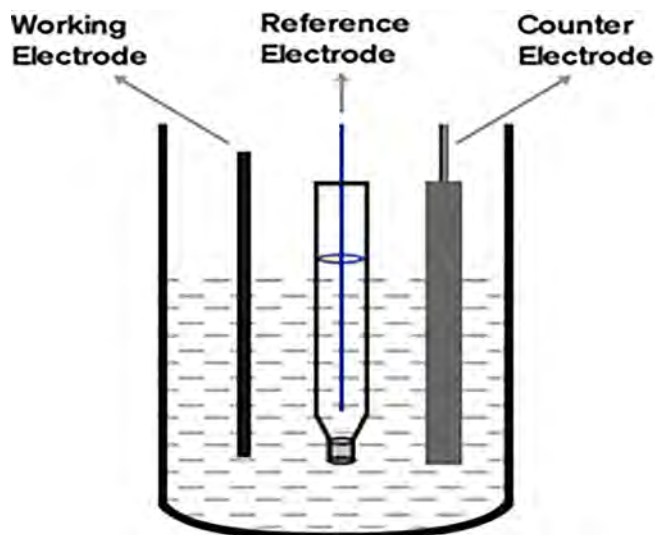

FIGURE 3 The electrochemical set-up of a three-electrode cell

potentiostat/galvanostat (Autolab PGSTAT, Metrohm 50519) instrument. A graphite sheet, platinum sheet and an Ag/AgCl electrode were used as working, counter and reference electrodes, respectively. The CV was measured from -1.6 to -0.2 V vs Ag/AgCl reference electrode using 0.085 M $ZnCl_2$ as the electrolyte at a scan rate of 50 mV/s. The measurement was performed at room temperature.

2.5 | Battery test

The redox flow battery consists of a reaction chamber (cell) and two reservoirs to store electrolytes externally. The cell was made of acrylic sheet and the positive and negative electrodes were densified graphite sheets with an area of 16 cm^2 and thickness of 2 mm. The negative and positive electrodes were separated by the self-made anion-exchange membrane. The total volume of each compartment of the cell is 3 cm $\times$ 3 cm $\times$ 1 cm. The negative electrolyte of this zinc-iron flow cell consisted of 1 M $ZnCl_2$ and the positive electrolyte is a mixture of 0.5 M $FeCl_2$ and 0.5 M $FeCl_3$ with 2 M NH_4Cl. The electrolytes were stored in two external reservoirs (each of 75 mL volume). Both positive and negative electrolytes were circulated through the cell using two peristaltic pumps. The cell performance was measured under a constant current charge-discharge measurement using an Autolab PGSTAT (Metrohm 50519 with NOVA 1.11 software) instrument connected to a PC. The charge-discharge measurements were carried out using a standard two-electrode setup as shown in Figure 4, in which the graphite sheets act as both working electrode and counter electrode, respectively.

The charge-discharge experiment of the zinc-iron redox flow cell is performed by charging the cell at a constant current of 25 mA cm^{-2} for 1800 seconds followed by discharge at the same current, until the cell reached a voltage of 0.0 V to completely strip off any deposited zinc. The cell parameters like coulombic efficiency (CE), voltage efficiency (VE) and energy efficiency (EE) of the battery are calculated using the following equations[43]:

$$CE = \frac{t_d}{t_c} \times 100\% \qquad (4)$$

$$VE = \frac{V_d}{V_c} \times 100\% \qquad (5)$$

$$EE = VE \times CE \qquad (6)$$

Here t_d represents the discharge time; t_c represents the charge time; V_d represents the average discharge voltage; and V_c represents the average charge voltage.

2.6 | Zn electrodeposit characterization

Electrodeposits are analyzed using scanning electron microscope (JEOL-JSM 6390 JED 2300 scanning electron microscope).

**FIGURE 4** The standard two-electrode setup for charge-discharge measurements
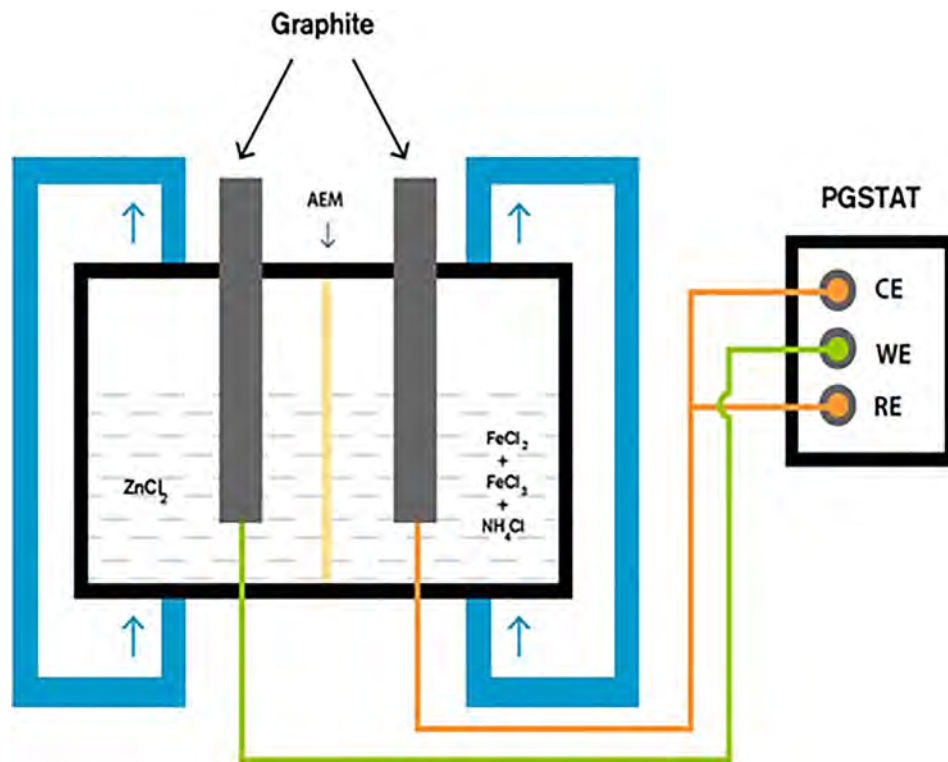
3 | RESULTS AND DISCUSSION

3.1 | Cyclic voltammograms

A cyclic voltammogram of 0.085 M electrolyte of $ZnCl_2$ on a graphite sheet working electrode in the range of -1.6 to -0.2 V (vs Ag/AgCl) at the scan rate of 50 mV s^{-1} is shown in Figure 5. From figure, it is clear that the cathodic peak at -1.28 V corresponds to the electrodeposition of zinc and the anodic peak at -0.74 V corresponds to the dissolution of zinc to the solution.

3.2 | Battery performance

The performance of a Zn-Fe RFB employing 1 M Zn(II) chloride aqueous solution as negative active species and 0.5 M $FeCl_2$ and 0.5 M $FeCl_3$ with 2 M NH_4Cl aqueous solution as positive species was evaluated with constant-current charge-discharge measurements. Figure 6 represents the characteristic charge/discharge curves during the 15th cycle at 25 mA cm^{-2}. This curve was obtained from 30 minutes of charging followed by 30 minutes of discharging under a current density of 25 mA cm^{-2} using graphite electrodes. It shows a relatively flat voltage profile for charge and discharge process. The charge-discharge measurements were repeated over 30 cycles and are shown in Figure 7. The cycling studies at 25 mA cm^{-2} revealed good stability of the
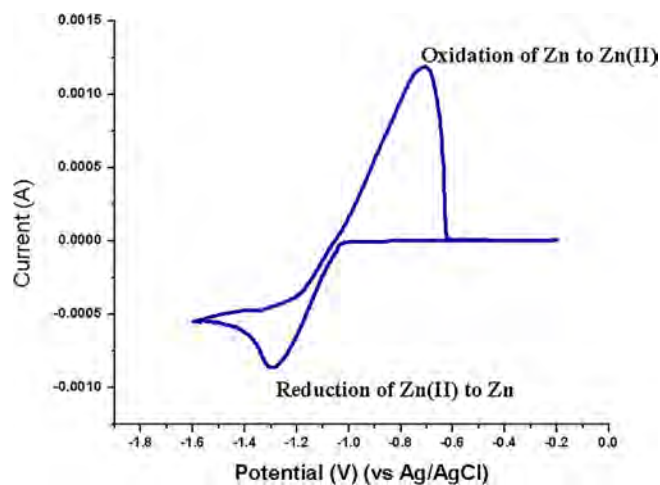
FIGURE 5 CV of 0.085 M $ZnCl_2$ on a graphite electrode at the scan rate of 50 mV s^{-1}

battery, without any evidence of degradation. The curves are identical with a charge voltage of approximately 1.59 V and a discharge voltage of 1.34 V.

Any crossover of Fe^{2+}/Fe^{3+} through the membrane to the anodic compartment will result in a gradual fading of coulombic efficiency on repeating the charge-discharge cycles.[31,34] However, this phenomenon is not observed in the present redox flow system indicating that the crossover of Fe^{2+}/Fe^{3+} does not occur appreciably. This may be due to the good cation-blocking ability of the anion exchange membrane. In this case, during charging,
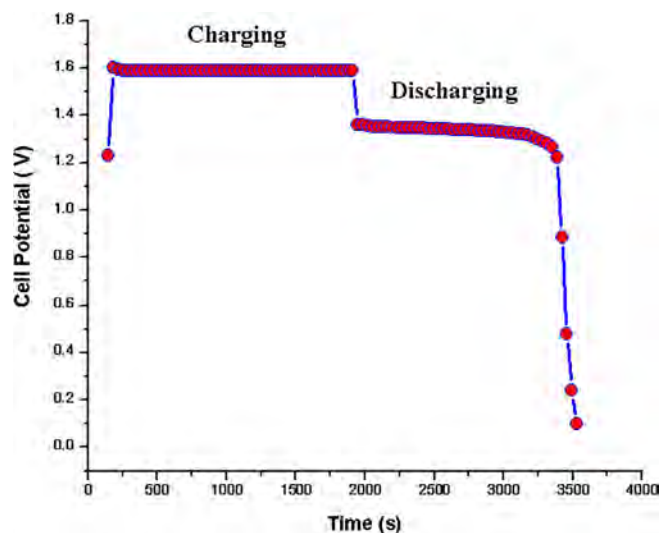
FIGURE 6 Cell potential vs time response for the 15th charge-discharge cycle at 25 mA cm^{-2}

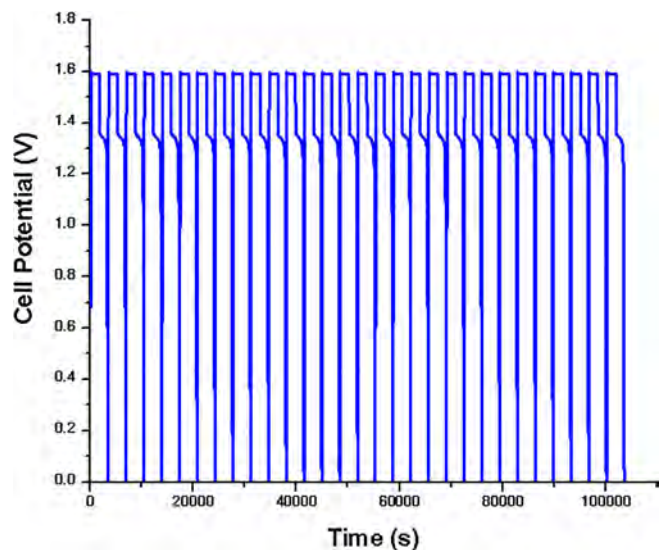**FIGURE 7** Cell potential vs time response for 30 cycles of Zn-Fe RFB at 25 mA cm^{-2}

excess chloride ions left in the anode compartment move towards cathode compartment through the membrane for electrical neutrality. During discharge process, opposite changes take place. When we repeated the experiments with a porous PVC membrane instead of an AEM, dendrite formation was observed on zinc electrodes even on first charging step. When an AEM is used, only chloride ions can diffuse from anode compartment to the cathode compartments through the AEM, during charging. From the above observations it clear that selective migration of chloride ions has a strong influence on the uniform deposition of the zinc. Similar results of suppression of dendrite formation in zinc RFBs with different

kinds of membranes have been reported by many other groups.[44–46]

The dependences of cell performance on concentration and current density were also investigated by performing the galvanostatic charge-discharge measurement at different electrolyte concentrations (1 M, 3 M and 5 M) and at different current densities (15, 25 and 50 mA cm^{-2}). The results are tabulated in Table 1 and 2.

From Table 1, it is found that the average discharge voltage decreases from 1.34 to 1.01 V on increasing concentration of ZnCl$_2$ from 1 M to 5 M, while the coulombic efficiency (CE) remains nearly constant at ~92 to 90%, which indicates the high anion selectivity of the membrane. A higher CE compared to that of the cells reported by other researchers is mainly due to the negligible crossover of Fe^{3+} ions through AEM used in our redox flow battery. This result also confirms the high anion selectivity of our anion exchange membrane when used as a separator in Zn-Fe redox flow battery. The decrease in energy efficiency (EE) values from 78.2% to 53.46% with increase in electrolyte concentration is mainly due to the decreasing voltage efficiency (VE) arising from the increased electrolyte resistance.[47,48]

The electrochemical performance of the Zn-Fe system with 1 M ZnCl$_2$ at different current densities (such as 15, 25, and 50 mA cm^{-2}) is given in Table 2. The coulombic efficiency is mainly influenced by three key factors: temperature, current and state-of-charge. The relationship between charge or discharge currents and coulomb efficiency can be expressed by the Peukert equation.[20] This states that the overall battery capacity or the total energy supplied by the battery, decreases disproportionately as the discharge current rises.

$$\eta_c = \frac{Q_d}{Q_N} = \left(\frac{I_d}{I_N}\right)^{1-n} \quad (7)$$

where I_d is discharge current, I_N is base current, Q_d is the capacity discharged by I_d and Q_N is the capacity discharged by base current I_N. The equation relating internal resistance, discharge current and energy efficiency can be written as

$$\eta_w = \eta_c \eta_v = \left(\frac{I_d}{I_N}\right)^{1-n} \frac{V_B - R_i I_d}{V_B + R_i I_c} \quad (8)$$

From Equations (7) and (8), it is clear that the internal resistance and discharge current values are obviously two key factors that reduce energy efficiency. Reducing internal resistance and maintaining an optimum charge and

TABLE 1   Zn-Fe RFB performance as a function of $ZnCl_2$ concentration at a current density of 25 mA cm^{-2}

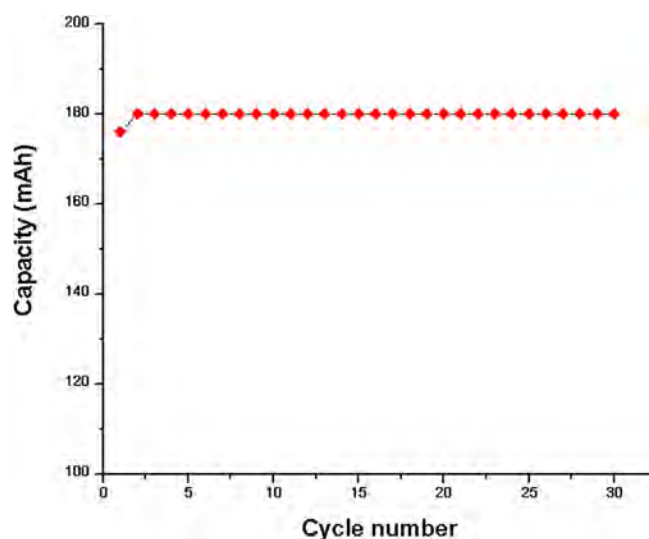| ZnCl$_2$ (M)	OCV (V)	Avg. charge voltage (V)	Avg. discharge voltage (V)	CE (%)	VE (%)	EE (%)
1 M	1.44	1.58	1.343	92	85	78.2
3 M	1.31	1.65	1.138	92	68.9	63.38
5 M	1.09	1.7	1.01	90	59.4	53.46

TABLE 2   The electrochemical performances for Zn-Fe cell with 1 M $ZnCl_2$ run at different charge/discharge current density

Current density (mA cm^{-2})	OCV (V)	Avg. charge voltage (V)	Avg. discharge voltage (V)	CE (%)	VE (%)	EE (%)
15	1.52	1.55	1.4	90	90	81
25	1.44	1.58	1.343	92	85	78.2
50	1.38	1.71	1.27	92	74	68.08
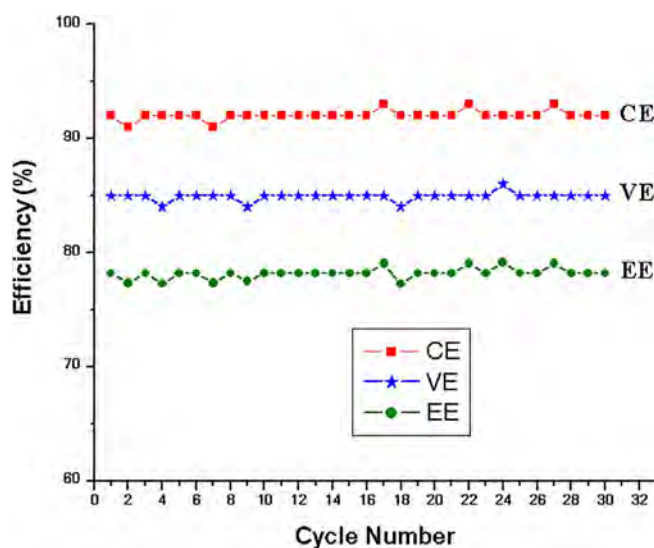
FIGURE 8   Efficiency of the cell with 1 M $ZnCl_2$ under the current density of 25 mA cm^{-2}

FIGURE 9   Discharge capacity vs number of cycles at a current density of 25 mA cm^{-2}

discharge current will help to increase the energy efficiency.

From charge-discharge plot, the coulombic, voltage and energy efficiencies were calculated and plotted vs cycle number in Figure 8. From the figure, it is clear that the Zn-Fe RFB shows no decrease of coulomb efficiency (92%), voltage efficiency (85%) or energy efficiency (78.2%) on 30 repeated charge-discharge cycles at 25 mA cm^{-2}. The average coulombic efficiency of about 92% in all the cycles indicates that the products formed during battery discharge return almost completely to their initial conditions on charging. Low coulombic efficiency in aqueous electrolytes is generally attributed to the side reactions due to water electrolysis.[5] The standard reduction potential of zinc in acid media is −0.76 V vs the standard hydrogen electrode (SHE). During the charging process, proton or water reduction leading to H$_2$

evolution is the preferred reaction, thermodynamically. However zinc is a relatively poor electrocatalyst for the H$_2$ evolution and hence high overpotential of zinc for hydrogen evolution increase the overall cell efficiency by suppressing hydrogen evolution reaction.[30] After repeated charge-discharge cycles, no appreciable changes in pH were observed. Hydrogen evolution reaction ($2H^+ + 2e^- \rightarrow H_2$ (g)) is a side reaction that decrease the efficiency of many redox flow batteries. This will also increase the pH of the anolyte. Higher coulombic efficiency and near consistency of the pH values after many charge-discharge cycles indicates that the hydrogen evolution on the anode is negligible in the present system. The cell capacity is also calculated for each discharge cycles at a current density of 25 mA cm^{-2} and plotted vs cycle number in Figure 9. From the figure, it is clear that the discharge capacity is almost constant even after
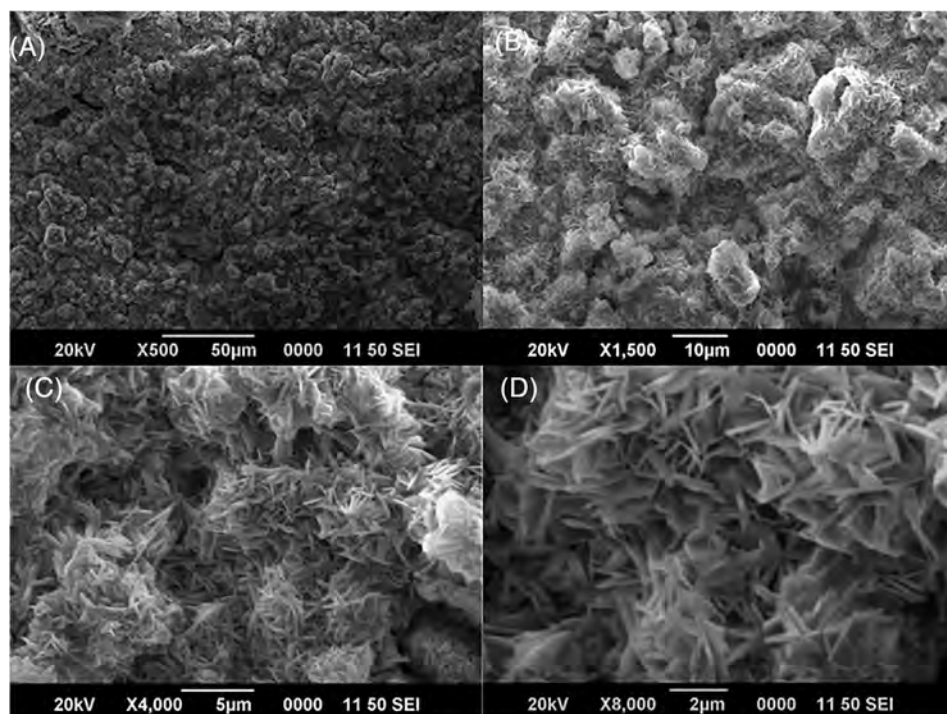
FIGURE 10 (A-D) SEM images of zinc deposition at various magnifications

30 charge-discharge cycles. No zinc dendrite formation was observed on increasing the current densities to 15, 25, 50, 100 and 150 mA cm^{-2}.

3.3 | SEM Analysis

The deposition of a uniform, thick zinc layer onto an inert current collector has become a necessity in all zinc-based redox flow batteries. Figure 10 shows SEM micrograph of zinc electrodeposit obtained during the charging phase of the zinc half-cell under a current density of 25 mA cm^{-2}. Visually, all the electrodeposited Zn coatings were homogeneous and metallic gray. It is pertinent to note that no dendrite growth occurs on the zinc electrode which was a severe drawback of previously reported zinc based rechargeable batteries. Absence of dendrite growth might be due to the fact that, only the chloride ions shuttles between two electrolyte solutions through AEM and this probably promotes uniform zinc deposition and prevent the dendrite growth.

4 | CONCLUSION

In conclusion, the feasibility of a Zn-Fe RFB system utilizing Zn(II)/Zn and Fe(III)/Fe(II) redox couples and an anion exchange membrane as a separator has been demonstrated. Densified graphite sheets were used both as positive and negative electrode current collectors and the performance of the test cell was evaluated with repeated constant current charge-discharge experiments. The cell delivered an average discharge voltage of ~1.34 V at 25 mA cm^{-2}, with a high average coulombic efficiency of 92%, voltage efficiency of 85% and energy efficiency of 78.2% over 30 cycles at 298 K. During charge-discharge cycles, only chloride ions shuttle between anode and cathode compartments through AEM, which eliminates the issue of cross contamination of electroactive materials and thus increase the performance of the battery. From SEM images, it was clear that the Zn coatings were homogeneous and dendrite-free.

The dependence of cell performance on concentration and current density was also investigated by performing the galvanostatic charge-discharge measurements at different electrolyte concentrations (1 M, 3 M and 5 M) and at different current densities (15, 25 and 50 mA cm^{-2}). The results show that the average discharge voltage decreases from 1.34 to 1.01 V on increasing concentration of ZnCl$_2$ from 1 M to 5 M, while the coulombic efficiency (CE) remains nearly constant (90-92%). Higher coulombic efficiency confirms negligible hydrogen evolution side reaction and high anion selectivity of AEM. The energy efficiency (EE) values, however, decrease from 78.2 to 53.46% with increase in electrolyte concentration and this is mainly due to the decreasing voltage efficiency (VE) arising from the increased electrolyte resistance. On increasing the current densities to 15 to 50 mA cm^{-2} the coulombic efficiency remained almost same (90-92%). However, voltage efficiency decreased from ~90% to 74%

and energy efficiency decreased from ~81% to 68%. The results show that the operating conditions are crucial impact factors for the cell performance and the Zn-Fe RFB can exhibit good performance at low concentration (1 M) and at low current density (15 mA cm^{-2}). Thus, we have successfully demonstrated working of a high efficiency and stable Zn-Fe hybrid redox flow battery with no dendrite growth during zinc deposition by optimizing charge-discharge conditions and employing an anion exchange membrane as separator.

ACKNOWLEDGEMENT

DATA AVAILABILITY STATEMENT

Data sharing is not applicable to this article as no new data were created or analyzed in this study.

ORCID

C. Balakrishnan Jeena https://orcid.org/0000-0001-7228-5891
P. Jose Elsa https://orcid.org/0000-0003-1427-1138
P. Peter Moly https://orcid.org/0000-0002-7549-4952
K. Jacob Ambily https://orcid.org/0000-0002-7499-4453
Vadakkan T. Joy https://orcid.org/0000-0001-9871-2900

REFERENCES

1. Bartolozzi M. Development of redox flow batteries. A historical bibliography. *J Power Sources*. 1989;27:219-234. https://doi.org/10.1016/0378-7753(89)80037-0
2. Noack J, Roznyatovskaya N, Herr T, Fischer P. The chemistry of redox-flow batteries. *Angewandte*. 2015;54(34):9776-9809. https://doi.org/10.1002/anie.201410823
3. Skyllas-kazacos M, Kazacos G, Poon G, Verseema H. Recent advances with UNSW vanadium-based redox flow batteries. *Energy Res*. 2010;34(2):182-189. https://doi.org/10.1002/er
4. Leung P, Li X, De Leo P, Berlouis L, John CT, Walsh FC. Progress in redox flow batteries, remaining challenges and their applications in energy storage. *RSC Adv*. 2012;2:10125-10156. https://doi.org/10.1039/c2ra21342g
5. Soloveichik GL. Flow batteries: current status and trends. *Chem Rev*. 2015;115(20):11533-11558. https://doi.org/10.1021/cr500720t
6. Van Nguyen T, Savinell RF. Flow batteries. *Electrochem Soc Interface*. 2010;19:54-56. https://doi.org/10.1021/ac200156s
7. Chen R, Kim S, Chang Z, Chen R, Kim S. Redox flow batteries: Fundamentals and applications. *Principles Adv Appl*. Rijeka, Croatia: InTech; 2017. https://doi.org/10.5772/intechopen.68752
8. De Le CP, Walsh FC. Redox flow cells for energy conversion. *J Power Sources*. 2006;160:716-732. https://doi.org/10.1016/j.jpowsour.2006.02.095
9. Shigematsu T. Recent development trends of redox flow batteries. *SEI Techn Rev*. 2019;89:5-11.

10. Zhang C, Zhang L. Progress and prospects of next-generation redox flow batteries. *Energy Storage Mater*. 2018;15:324-350. https://doi.org/10.1016/j.ensm.2018.06.008
11. Small LJ, Soc JE, Small LJ, Iii HDP, Anderson TM. Crossover in membranes for aqueous soluble organic redox flow batteries. *J Electrochem Soc*. 2019;166(12):A2436-A2542. https://doi.org/10.1149/2.0681912jes
12. Prifti H, Parasuraman A, Winardi S, Lim TM, Skyllas-kazacos M. Membranes for redox flow battery applications. *Membranes*. 2012;2(2):275-306. https://doi.org/10.3390/membranes2020275
13. Weber AZ, Mench MM, Meyers JP, Ross PN, Gostick JT, Liu Q. Redox flow batteries: a review. *J Appl Electrochem*. 2011;41:1137-1164. https://doi.org/10.1007/s10800-011-0348-2
14. Wei L, Zhao TS, Zeng L, Zhou XL, Zeng YK. Copper nanoparticle-deposited graphite felt electrodes for all vanadium redox flow batteries. *Appl Energy*. 2016;180:386-391. https://doi.org/10.1016/j.apenergy.2016.07.134
15. Mohammadi T, Kazacos MS. Evaluation of the chemical stability of some membranes in vanadium solution. *J Appl Electrochem*. 1997;27:153-160. https://doi.org/10.1023/A:1018495722379
16. Sukkar T, Skyllas-kazacos M. Membrane stability studies for vanadium redox cell applications. *J Appl Electrochem*. 2004;03430:137-145. https://doi.org/10.1023/B:JACH.0000009931.83368.dc
17. Sanz L, Lloyd D, Magdalena E, Palma J. Description and performance of a novel aqueous all-copper redox flow battery. *J Power Sources*. 2014;268:121-128. https://doi.org/10.1016/j.jpowsour.2014.06.008
18. Schaltin S, Li Y, Brooks NR, et al. Towards an all-copper redox flow battery based on a copper-containing ionic liquid. *Chem Commun*. 2015;52(2):414-417. https://doi.org/10.1039/C5CC06774J
19. Lloyd D, Magdalena E, Sanz L, Murtom L. Preparation of a cost-effective, scalable and energy efficient all-copper redox flow battery. *J Power Sources*. 2015;292:87-94. https://doi.org/10.1016/j.jpowsour.2015.04.176
20. Sanz L, Lloyd D, Magdalena E, Palma J, Anderson M. Study and characterization of positive electrolytes for application in the aqueous all-copper redox flow battery. *J Power Sources*. 2015;278:175-182. https://doi.org/10.1016/j.jpowsour.2014.12.034
21. Yensen N, Allen PB. HardwareX Open source all-iron battery for renewable energy storage. *HardwareX*. 2019;6:e00072. https://doi.org/10.1016/j.ohx.2019.e00072
22. Tucker MC, Phillips A, Weber AZ. All-iron redox flow battery tailored for off-grid portable applications. *ChemSusChem*. 2015;8(23):3996-4004. https://doi.org/10.1002/cssc.201500845
23. Banerjee A, Saha D, Row TNG, Shukla AK. A soluble-lead redox flow battery with corrugated graphite sheet and reticulated vitreous carbon as positive and negative current collectors. *Bull Mater Sci*. 2013;36:163-170.
24. Collins J, Li X, Pletcher D, et al. A novel flow battery: a lead acid battery based on an electrolyte with soluble lead (II). Part IX: Electrode and electrolyte conditioning with hydrogen peroxide. *J Power Sources*. 2010;195:2975-2978. https://doi.org/10.1016/j.jpowsour.2009.10.109
25. Cheng J, Gao C, Wen YH, Pan JQ, Xu Y, Cao GP. Performance improvement of the all—lead redox flow battery in fluoroboric acid electrolyte. *Int J Energy Sci*. 2013;3:165-168.

26. Ventosa E, Guarnieri M, Trov A, et al. Redox flow batteries: status and perspective towards sustainable stationary energy storage. 2021;481. https://doi.org/10.1016/j.jpowsour.2020.228804

27. Manohar AK, Kim KM, Plichta E, Hendrickson M, Rawlings S, Narayanan SR. A high efficiency iron-chloride redox flow battery for large-scale energy storage. *J Electrochem Soc.* 2016;163: A5118-A5125. https://doi.org/10.1149/2.0161601jes

28. Gong K, Xu F, Grunewald JB, et al. All-soluble all-iron aqueous redox-flow battery. *ACS Energy Lett.* 2016;1(1):89-93. https://doi.org/10.1021/acsenergylett.6b00049

29. Jayathilake BS, Plichta EJ, Hendrickson MA, Narayanan SR. Improvements to the coulombic efficiency of the iron electrode for an all-iron redox-flow battery. *J Electrochem Soc.* 2018;165: 1630-1638. https://doi.org/10.1149/2.0451809jes

30. Li X, De Le CP. Zinc-based flow batteries for medium- and large-scale energy storage. *Advances in Batteries for Medium and Large-Scale Energy Storage.* Woodhead Publishing; 2015;293-315. https://doi.org/10.1016/B978-1-78242-013-2.00008-X

31. Selverston S, Savinell RF, Wainright JS. Zinc-iron flow batteries with common electrolyte. *J Electrochem Soc.* 2017;164:1069-1075. https://doi.org/10.1149/2.0591706jes

32. Arenas LF, Loh A, Trudgeon DP, et al. The characteristics and performance of hybrid redox flow batteries with zinc negative electrodes for energy storage. *Renew Sustain Energy Rev.* 2018; 90:992-1016. https://doi.org/10.1016/j.rser.2018.03.016

33. Gong K, Ma X, Conforti KM, et al. A zinc-iron redox-flow battery under $100 per kW h of system capital cost. *Energ Environ Sci.* 2015;8:2941-2945. https://doi.org/10.1039/C5EE02315G

34. Xie Z, Su Q, Shi A, et al. High performance of zinc-ferrum redox flow battery with Ac−/HAc buffer solution. *J Energy Chem.* 2016;25(3):1-5. https://doi.org/10.1016/j.jechem.2016.02.009

35. Zhou X, Lin L, Lv Y, Zhang X, Fan L, Wu Q. Elucidating effects of component materials and flow fields on Sn-Fe hybrid flow battery performance. *J Power Sources.* 2020;450:227613. https://doi.org/10.1016/j.jpowsour.2019.227613

36. Zhou X, Lin L, Lv Y, Zhang X, Wu Q. A Sn-Fe flow battery with excellent rate and cycle performance. *J Power Sources.* 2018;404:89-95. https://doi.org/10.1016/j.jpowsour.2018.10.011

37. Xie C, Zhang H, Li X. Zinc dendrites inhibition for zinc-based battery. *ChemSusChem.* 2018;11:1-2. https://doi.org/10.1002/cssc.201801657

38. Wang K, Pei P, Ma Z, et al. Dendrite growth in the recharging process of zinc-air batteries. *J Mater Chem A.* 2015;3:22648-22655. https://doi.org/10.1039/C5TA06366C

39. Guo L, Guo H, Huang H, Tao S, Cheng Y. Inhibition of zinc dendrites in zinc-based flow batteries. *Front Chem.* 2020;8:1-8. https://doi.org/10.3389/fchem.2020.00557

40. Li C, Zhang X, He W, Xu G, Sun R. Cathode materials for rechargeable zinc-ion batteries: From synthesis to mechanism and applications. *J Power Sources.* 2020;449:227596. https://doi.org/10.1016/j.jpowsour.2019.227596

41. Cheng Y, Lai Q, Li X, Xi X, Zheng Q. Electrochimica Acta Zinc-nickel single flow batteries with improved cycling stability by eliminating zinc accumulation on the negative electrode. *Electrochim Acta.* 2014;145:109-111.

42. Li Q. Dendrites issues and advances in Zn anode for aqueous rechargeable Zn-based batteries. *EcoMat.* 2020;2(3):1-14. https://doi.org/10.1002/eom2.12035

43. Zeng YK, Zhao TS, Zhou XL, Wei L, Ren YX. A novel iron-lead redox flow battery for large-scale energy storage. *J Power Sources.* 2017;346:97-102. https://doi.org/10.1016/j.jpowsour.2017.02.018

44. Yuan Z, Liu X, Xu W, Duan Y, Zhang H, Li X. Negatively charged nanoporous membrane for a dendrite-free alkaline zinc-based flow battery with long cycle life. *Nat Commun.* 2018;9:1-11. https://doi.org/10.1038/s41467-018-06209-x

45. Lee B, Cui S, Xing X, et al. Energy, environmental, and catalysis applications dendrite suppression membranes for rechargeable zinc batteries dendrite suppression membranes for rechargeable zinc batteries. *ACS Appl Mater Interfaces.* 2018; 10(45):38928-38935. https://doi.org/10.1021/acsami.8b14022

46. Hao X, Hu J, Zhang Z, et al. Interfacial regulation of dendrite-free zinc anodes through a dynamic hydrophobic molecular. *J Mater Chem A.* 2021;9:14265-14269. https://doi.org/10.1039/d1ta01697k

47. Li B, Nie Z, Vijayakumar M, et al. Ambipolar zinc-polyiodide electrolyte for a high-energy density aqueous redox flow battery. *Nat Commun.* 2015;6:1-8. https://doi.org/10.1038/ncomms7303

48. Lu R, Yang A, Xue Y, Xu L, Zhu C. Analysis of the key factors affecting the energy efficiency of batteries in electric vehicle. *World Electr Veh J.* 2010;4:9-13.

Chemistry–A European Journal

Full Paper
doi.org/10.1002/chem.202005156

Chemistry Europe
European Chemical
Societies Publishing

▌ **Electrochemistry**

A High-Performance Asymmetric Supercapacitor Based on Tungsten Oxide Nanoplates and Highly Reduced Graphene Oxide Electrodes

Muhammad Ashraf,[a] Syed Shaheen Shah,[b, d] Ibrahim Khan,[c] Md. Abdul Aziz,[d] Nisar Ullah,[a] Mujeeb Khan,[e] Syed Farooq Adil,[e] Zainab Liaqat,[f] Muhammad Usman,[d] Wolfgang Tremel,*[f] and Muhammad Nawaz Tahir*[a]

Abstract: Tungsten oxide/graphene hybrid materials are attractive semiconductors for energy-related applications. Herein, we report an asymmetric supercapacitor (ASC, HRG//m-WO$_3$ ASC), fabricated from monoclinic tungsten oxide (m-WO$_3$) nanoplates as a negative electrode and highly reduced graphene oxide (HRG) as a positive electrode material. The supercapacitor performance of the prepared electrodes was evaluated in an aqueous electrolyte (1 M H$_2$SO$_4$) using three- and two-electrode systems. The HRG//m-WO$_3$ ASC exhibits a maximum specific capacitance of 389 F g^{-1} at a current density of 0.5 A g^{-1}, with an associated high energy density of 93 Wh kg^{-1} at a power density of 500 W kg^{-1} in a wide 1.6 V operating potential window. In addition, the HRG//m-WO$_3$ ASC displays long-term cycling stability, maintaining 92% of the original specific capacitance after 5000 galvanostatic charge–discharge cycles. The m-WO$_3$ nanoplates were prepared hydrothermally while HRG was synthesized by a modified Hummers method.

Introduction

Meeting the growing global energy demands is one of the future challenges because the current energy resources are coming to an end in the near future. In addition, the use of fossil fuels has a negative impact on the environment due to CO$_2$ emission that contributes to global warming.[1–3] The environmental problems have stimulated the interest in exploring new energy horizons.[4, 5] Renewable resources like solar and wind energy are considered the most suitable and reliable supplies of alternative energy.[6, 7] The energy harvested from these resources could generate enough electricity to power-up most daily energy requirements (including transportation and industrial systems),[8] but this requires strategies for high performance and efficient energy storage devices.[2, 8–10]

Supercapacitors are potential electrochemical energy storage devices (EESDs) that hold much promise because of their high-power density, long-term cycling stability, high-power attainment, low maintenance costs, and high stability.[11, 12] According to their method of operation, supercapacitors are classified as (i) electrode double-layer capacitors (EDLCs) and (ii) pseudocapacitors.[6, 13, 14] EDLCs uses electrostatic charge storage in the form of a double layer at the electrode–electrolyte interface (EEI), which leads to physical storage of charges by adsorption/desorption of electrolyte ions at the EEI.[13–15] The corresponding cyclic voltammetry (CV) curves show a characteristic rectangular shape. EDLC electrode materials contain carbonaceous materials like activated carbon (AC),[16–18] reduced graphene oxide (rGO),[19] carbon nanotubes (CNTs),[20] or carbon nanofibers (CNFs).[21] In contrast, fast and reversible redox reac-

[a] M. Ashraf, Prof. N. Ullah, Dr. M. N. Tahir
     Chemistry Department
     King Fahd University of Petroleum & Minerals
     Dharan 31261 (Kingdom of Saudi Arabia)
     E-mail: muhammad.tahir@kfupm.edu.sa

[b] S. S. Shah
     Physics Department
     King Fahd University of Petroleum & Minerals
     Dharan 31261 (Kingdom of Saudi Arabia)

[c] Dr. I. Khan
     Center of Integrative Petroleum Research
     King Fahd University of Petroleum & Minerals
     Dhahran 31261 (Saudi Arabia)

[d] S. S. Shah, Dr. M. A. Aziz, Dr. M. Usman
     Center of Research Excellence in Nanotechnology
     King Fahd University of Petroleum & Minerals Dhahran
      31262 (Saudi Arabia)

[e] Dr. M. Khan, Dr. S. F. Adil
     Department of Chemistry, College of Science
     King Saud University
     P.O. Box 2455, Riyadh 11451 (Kingdom of Saudi Arabia)

[f] Z. Liaqat, Prof. W. Tremel
     Institut für Anorganische Chemie und Analytische Chemie
     Johannes Gutenberg-Universität Mainz
     Duesbergweg 10–14, 55128 Mainz (Germany)
     E-mail: tremel@uni-mainz.de

     Supporting information and the ORCID identification number(s) for the author(s) of this article can be found under:
     https://doi.org/10.1002/chem.202005156.

     This manuscript is part of a special collection on Chemistry in Saudi Arabia.

Chemistry–A European Journal

Full Paper
doi.org/10.1002/chem.202005156

Chemistry Europe
European Chemical
Societies Publishing

tions occur at the electrode surfaces of pseudocapacitors giving rise to sharp peaks in the CV curves.[22] Typical active electrode materials in pseudocapacitors are metal oxides,[23] metal sulfides,[24] and conducting polymers.[25] Nanomaterials have shown great promise in energy conversion and storage[26–28] as their properties depend not only on composition but also on size and morphology.[10,29] Thus, their size- and morphology-controlled synthesis is crucial from a basic science and technological perspective.[10,18,30,31]

Tungsten oxides (WO_{3-x}) have been tested for energy storage devices because of their stability, availability, and economic viability. WO_3 is very promising because of its high theoretical capacity, good chemical stability, and relative better conductivity as already documented in literature.[32] It is an *n*-type semiconductor with variable oxidation states, high energy and packing density, and large pseudocapacitance.[33] It has been used not only in secondary batteries,[34] photocatalysis,[35] gas sensing,[36] or electrochemical[37] and solar[38] energy devices, but also as an electrode material for flexible and portable supercapacitors.[39] Much consideration has been devoted to its pseudocapacitor performance.[40] Particularly, its reversible valence change, that is, the change in the oxidation states between W^{6+} and W^{5+}, and especially towards low potential results in enhanced conductivity. Moreover, it is worth mentioning that nano-dimensions and morphology of the m-WO_3 plays important role in its energy storage applications.[41] Also m-WO_3 works best as negative electrode as already reported in the literature.[40] Gao et al. reported a hydrothermal synthesis of WO_3 nanowires supported over conductive carbon supports.[42] This nanocomposite was used to make a supercapacitor with a specific capacitance (C_{sp}) of up to 521 $F\,g^{-1}$ at a current density of 1 $A\,g^{-1}$.[43] Wu et al. prepared WO_3 nanotubes in a surfactant-free hydrothermal reaction. The prepared WO_3 nanotubes were applied as a negative electrode in asymmetric supercapacitors (ASCs) with polyaniline (PANI) as a positive electrode.[42] These ASCs showed a high energy density and long-term cycling stability with up to 10000 galvanostatic charge–discharge cycles.[42] Two dimensional (2D) monoclinic WO_3 (m-WO_3) showed an exceptional high surface area, which resulted in enhanced photocatalytic activities.[44]

Graphene has been used in many energy-related applications[26,45] because of its high specific surface area (SSA) and good electrical conductivity.[46] The SSA depends on the number of layers.[46] Single-layer graphene sheets can have theoretical surface areas of up to 2360 $m^2\,g^{-1}$[47] and a theoretical capacitance up to 550 $F\,g^{-1}$.[48] Based on the high SSA and electrical conductivity of around 2000 $S\,m^{-1}$[49] graphene-based supercapacitors exhibit EDLC behavior[48] with higher power densities and exceptional cycling stability compared to batteries.[50] Graphene is a superior support for flexible, transparent, and high-power density supercapacitors due to its high optical transmittance (ca. 98%), superior elastic modulus (ca. 1.0 TPa) mechanical strength of around 130 GP.[51,52] For instance, Zhaodong et al. reported hybrid supercapacitors with ultrafast charging capability and negligible self-discharge. The developed supercapacitors effectively resolved the critical self-dis-

charge challenge and provided more opportunities for applications of metallic-based electrodes in supercapacitors.[53,54]

In general, graphene oxide (GO) has attracted the attention due to its promising route towards production of large quantities of graphene-based materials because the intercalation of graphite with oxygen containing groups, gives the possibilities to nucleate and grow metal oxides to synthesis nanocomposites at ease for various.[55] However, the oxygen containing functionalities cause strong and robust electron localization which could result in shutting down the charge transport process in graphene oxide. In contrast, the reduction of graphene oxide (HRG) leads to a structure close to graphene having high electrical conductivity.[56] Therefore, HRG is a unique class of two-dimensional (2D) carbon nanostructures that has emerged as promising candidate for the energy storage devices because of large electrical conductivity, thermal and chemical stability with broad surface electrochemical window.[57,58]
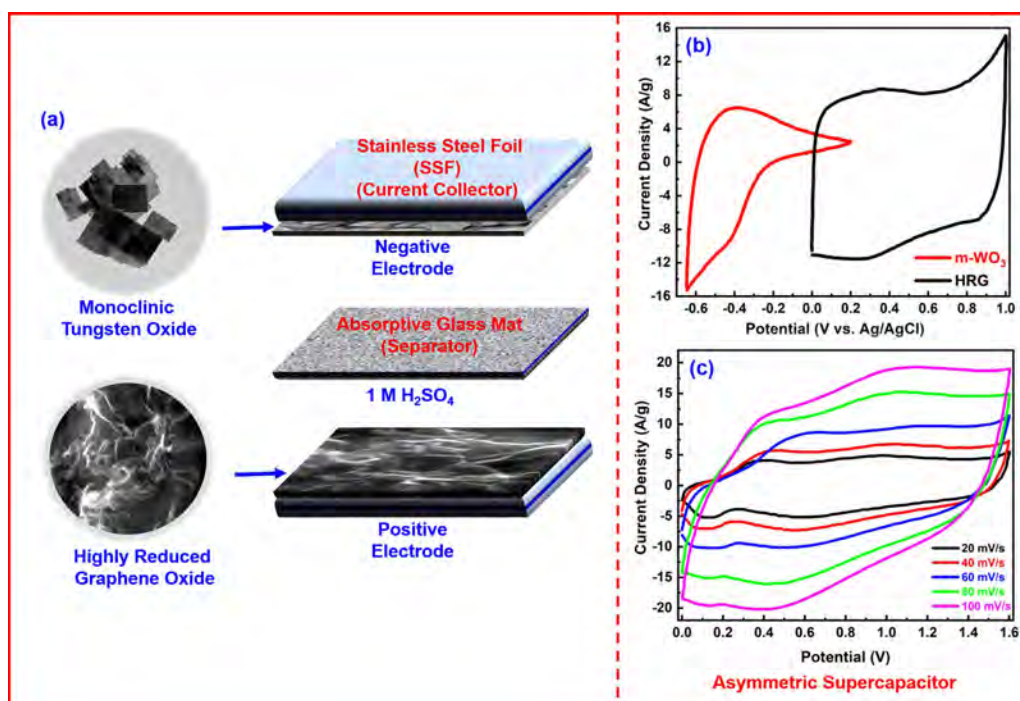
Supercapacitors with high energy density and excellent power density require a good ion diffusion and electrical conductivity of the electrode materials.[14,15] Therefore, HRG was used as positive electrode material. Matching both requirements in a single device can be accomplished in asymmetric supercapacitors by combining electrical double layers and pseudocapacitive materials.[59]

Here we report an asymmetric supercapacitor HRG//m-WO_3 serving as efficient EESD devices with a maximum C_{sp} of 389 $F\,g^{-1}$ at 0.5 $A\,g^{-1}$ (Scheme 1). Nanoparticles of m-WO_3 were prepared hydrothermally, highly reduced graphene oxide (HRG) by a modified Hummers method. The ACSs have a maximum energy density of 93 $Wh\,kg^{-1}$ at a power density of 500 $W\,kg^{-1}$ over a wide operating potential window (OPW). The ASCs show good cycling-stability and maintain 92% of its original C_{sp} after 5000 charge–discharge cycles.

Experimental Section

Materials: All chemicals and reagents, except stainless steel foil (SSF), were purchased from either Sigma–Aldrich or Alfa Aesar and used as received without further purification. SSF was purchased from Tmax Battery Equipments Limited, China, Absorptive Glass Mat (AGM) from Anhui Fengxin Industrial Co., Ltd., China.

Characterization: The morphology, phase structure and composition of the products were characterized by field-emission scanning electron microscopy FE-SEM (Tescan Lyra-3) at 20 kV. The energy dispersion spectrum (EDS) analysis of our samples was carried out on a Lyra 3 attachment to the FESEM using LINK INCA program system. Powder X-ray diffraction pattern (XRD) of the dried samples was recorded on Rigaku miniflex II X-ray diffractometer in step scan mode between 20 and 90° 2θ (scan rate 0.02° 2θ s^{-1}) using Cu Kα radiation ($\lambda = 1.5414$ Å). Raman Spectrometer (Tag no.340326 RR-1115) with charge-coupled device (CCD) detector at a spectrum window of 30–2000 cm^{-1}, laser (green type, 532 nm) was used for Raman spectra. A micro-focusing X-ray monochromator XPS (ESCALAB 250Xi XPS Microprobe, Thermo Fisher Scientific, USA) was applied for the chemical analysis of the prepared sample. TEM instrument FEI Tecnai G2 Spirit microscope operating at 120 kV (LaB6 filament), equipped with a Gatan US1000 CCD-camera (16-bit, 2048×2048 pixels), using the Gatan Digital Micrograph software was used to characterize the morphology.

Chemistry–A European Journal

Full Paper
doi.org/10.1002/chem.202005156

Chemistry Europe
European Chemical
Societies Publishing

Scheme 1. (a) Fabrication of an asymmetric supercapacitor using highly reduced graphene oxide (HRG) as a positive electrode and m-WO$_3$ as a negative electrode; (b) comparative CV curves of HRG and m-WO$_3$ electrodes (scan rate: 100 mV s^{-1}) and (c) CV curves at different scan rates in an OPW between 0.0 and 1.6 V.

Synthesis of m-WO$_3$ nanoplates: Na$_2$WO$_4$·2H$_2$O (2.5 g) was dissolved in 6 M aqueous HCl under constant magnetic stirring for 1 hour. NH$_4$NO$_3$ (2.00 g) was added to the 50 mL of the precursor solution to obtain the m-WO$_3$. The flask contents were transferred into a 100 mL Teflon-lined stainless-steel autoclave and kept in a preheated oven at 180 °C for 24 hours. Subsequently, the autoclave was cooled to room temperature, and the resultant green-yellow precipitate was filtered and washed successively with de-ionized (DI) water (100 mL) and ethanol (100 mL). m-WO$_3$ nanoplates were obtained after drying in an oven for 6 hours at 80 °C.

Synthesis of HRG: HRG was prepared by a modified Hummers method.[60] Graphite powder (GP) (0.7 g) and NaNO$_3$ (0.7 g) were added to a cold solution of H$_2$SO$_4$ (25 mL) at 0 °C. After stirring for 10 minutes, KMnO$_4$ (2.5 g) was added portion-wise to the reaction mixture. The mixture was then stirred at 37 °C for one hour, ensuring the thick paste formation. After adding 40 mL of DI water, stirring was continued for 30 min at 90 °C. Subsequently, more DI water (100 mL) was added to the reaction mixture, followed by the slow addition of H$_2$O$_2$ (2.5 mL), which led to a color change from dark brown to yellowish. The resulting mixture was cooled to room temperature, filtered, and washed with DI water (100 mL). The obtained thick brown paste was dispersed in DI water (80 mL) and centrifuged at a low speed (1000 rpm) for 2 minutes. In the last step, the product was dispersed in DI water, and centrifugation was repeated for 4 times until a clear supernatant layer was obtained. The same step was repeated by increasing the speed (8000 rpm) of centrifugation. The final product, a thick paste, was re-dispersed in DI water using mild sonication techniques to acquire a graphene oxide (GRO) solution for further processing. GRO was reduced according to our previously reported procedure.[61] Briefly, 100 mg of GRO was dispersed in DI water (30 mL) and sonicated for 30 min. The obtained suspension was heated at 100 °C, and 3 mL of hydrazine hydrate was added. After 2 minutes, the reaction temperature was dropped to 98 °C and stirring continued

for 24 hours. The resulting black powder formed was filtered and washed with water (100 mL). This suspension was centrifuged for 4 minutes at a slow speed (4000 rpm). The end product was filtered and dried under vacuum.

Fabrication of working electrodes and ASC cell assembly: Working electrodes were fabricated by mixing 90% of active materials (HRG or m-WO$_3$) with 10% of polyvinylidene fluoride (PVDF) as a binder. PVDF was dissolved in dimethyl sulfoxide at 80 °C, followed by the slow addition of active material into the solution. The stirring was continued for 4 hours until a homogeneous slurry was attained, which was then cast on a SSF (working area of 2×1 cm^2; used as a current collector) with an automatic film coater doctor blade (Shandong Gelon Lib Co., Ltd.). Subsequently, the coated electrodes were dried in an electric oven for 5 hours at 80 °C. Each of the fabricated electrodes contained 0.25 mg of the active materials. The HRG//m-WO$_3$ ASC was assembled with two electrodes in the sandwich-type cell assembly, where HRG coated SSF was used as a positive electrode and m-WO$_3$ nanoplates coated SSF was used as a negative electrode. The HRG//m-WO$_3$ ASC was assembled with two working electrodes separated by an AGM separator soaked in 1 M H$_2$SO$_4$ aqueous electrolyte.

Electrochemical measurements: Galvanostatic charge–discharge (GCD), CV, and electrochemical impedance spectroscopy (EIS) measurements of the prepared electrodes and HRG//m-WO$_3$ ASC were performed with an Autolab/PGSTAT302N Potentiostat/Galvanostat (Metrohm, Utrecht, Netherlands). The supercapacitor performances of the HRG and m-WO$_3$ electrodes were evaluated initially with a three-electrode system in an aqueous electrolyte of 1 M H$_2$SO$_4$. Where HRG or m-WO$_3$ coated on the SSF was used as a working electrode. Ag/AgCl (saturated KCl) and a platinum wire were used as reference and counter electrodes, respectively. In the three-electrode configuration the C_{sp} (F g^{-1}) values were calculated

Chemistry–A European Journal

Full Paper
doi.org/10.1002/chem.202005156

Chemistry
Europe
European Chemical
Societies Publishing

from CV and GCD profiles with Equations (1) and (2), respectively.[62–65]

$$C_{sp} = \frac{\int I dv}{2m_s \nu \Delta V} \tag{1}$$

$$C_{sp} = \frac{2I \int V dt}{m_s V^2 \big|_{V_i}^{V_f}} \tag{2}$$

in which, $\int I dv$, m_s, ν, ΔV, and I represent the integrated area under the CV curve over the whole OPW, the mass (g) of active material in the working electrode, the scan rate (mV s^{-1}), the OPW (V), and the discharging current (A), respectively. While $\int V dt$ represents area under the discharge curve and V_i and V_f are initial and final values of the applied potential (V).

The HRG//m-WO$_3$ ASC was also tested with a two-electrode electrochemical system using 1 M H$_2$SO$_4$ as an electrolyte. The C_{sp} values were obtained from the CV curves and GCD profiles using Equations (3) and (4), respectively.[63–65]

$$C_{sp} = \frac{\int I dv}{m_t \nu \Delta V} \tag{3}$$

$$C_{sp} = \frac{2I \int V dt}{m_t V^2 \big|_{V_i}^{V_f}} \tag{4}$$

in which, $\int I dv$, m_t, ν, ΔV, and I represent the integrated area under the CV curve over the whole OPW, the total active materials mass (g) of both positive and negative electrodes, the scan rate (mV s^{-1}), the OPW (V), and the discharging current (A), respectively. While $\int V dt$ represents the area under the discharge curve and V_i and V_f are initial and final values of the applied potential (V).

Whereas, energy density (E) and power density (P) derived from the GCD measurements of the HRG//m-WO$_3$ ASC in the two-electrode system were determined with the aid of Equations (5) and (6), respectively.[63–68]

$$E \; (Wh/kg) = \frac{C_{sp} \times \Delta V^2 \times 1000}{2 \times 3600} \tag{5}$$

$$P \; (W/kg) = \frac{E \times 3600}{\Delta t} \tag{6}$$

Here ΔV is the OPW (V), C_{sp} is given in F g^{-1}, and Δt is the discharging time (s) of the HRG//m-WO$_3$ ASC. EIS measurements were also performed in the two-electrode system for the HRG//m-WO$_3$ ASC.

Results and Discussion

Synthesis and characterization of m-WO$_3$ nanoplates

The synthesis of m-WO$_3$ nanoplates was carried as illustrated in Figure 1. Monoclinic WO$_3$ was synthesized hydrothermally[29] by adding 2.00 g of NH$_4$NO$_3$ to 50 mL of a precursor solution (H$_2$WO$_4$·H$_2$O). Subsequently, the mixture was heated under autogenous pressure for 24 hours at 180 °C. Under hydrothermal conditions, the decomposition of H$_2$WO$_4$ (formed by the reaction of Na$_2$WO$_4$·2H$_2$O and HCl) leads to the formation of WO$_3$ nuclei that serve as seeds for the growth of m-WO$_3$ nanoplates.

Figure 1. Schematic representation for synthesis of m-WO$_3$ nanoplates.

Phase purity and crystal structure of the as-synthesized m-WO$_3$ nanoplates was first demonstrated by X-ray powder diffraction (XRD). All intensities of the m-WO$_3$ nanoplates match well with the positions and intensities of monoclinic WO$_3$ (JCPDS No. 83–0950).[69] The well-defined and sharp intensities indicate are compatible with a highly crystalline product. The (002) main reflection centered at $2\theta = 23°$ (Figure 2 a) indicates the anisotropic growth of monoclinic WO$_3$ structure along the c axis. The concentration of NH$_4$NO$_3$ plays an important role for controlling the morphology of m-WO$_3$. Increasing NH$_4$NO$_3$ concentration leads to an increase of the intensities of the (022) and (202) reflections and to a decrease of the intensities of the (120) and (112) reflections, which indicates a plate-like growth of m-WO$_3$.[42]

The crystal structure of m-WO$_3$ was confirmed by Raman spectroscopy (Figure 2 b). The positions and intensities of the Raman bands match those reported for m-WO$_3$. The bands centered at 135 and 185 cm^{-1} are attributed to vibrations of the (W$_2$O$_2$)$_n$ backbone. The characteristic bands at 270 and
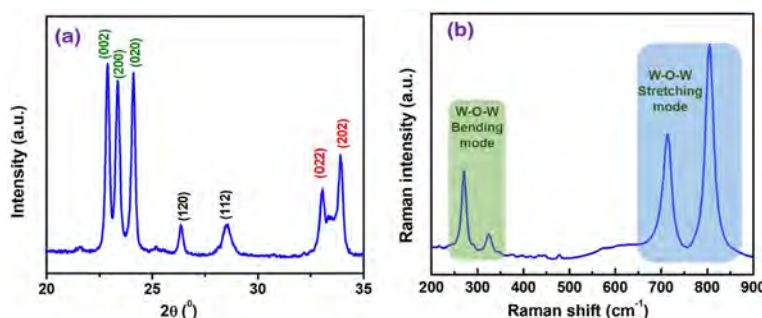

Figure 2. (a) X-ray powder diffractogram and (b) Raman spectrum of m-WO$_3$ nanoplates.

Chem. Eur. J. **2021**, *27*, 6973 – 6984   **www.chemeurj.org**

© 2021 Wiley-VCH GmbH

65

Chemistry–A European Journal

Full Paper
doi.org/10.1002/chem.202005156

Chemistry
Europe
European Chemical
Societies Publishing

$330 \, \text{cm}^{-1}$ are associated with the W-O-W bending vibrations. The sharp bands centered at 715 and 810 cm^{-1} were assigned to the W-O-W vibrational stretching modes.

Size and morphology of the m-WO_3 nanoplates were confirmed by field emission scanning electron microscopy (FESEM) and transmission electron microscopy (TEM). Figure 3 shows the TEM images confirming the plate-like morphology (Figure 3 a). Interestingly, some of the nanoplates were found lying at their lateral side on the TEM sample grid which give the chance to measure the thickness of these nanostructures. The average thickness of the nanoplates is around 13 nm (Figure 3 b). The high resolution TEM analysis (Figure 3 c&d) showed the d-spacing of around 0.38 nm corresponding to the (200) plane of the monoclinic phase of WO_3. The overview FESEM image (Figure S1a) also shows a plate-like morphology. The high-resolution FESEM micrograph (Figure S1b) revealed the dimensions of the nanoplates. The elemental mapping
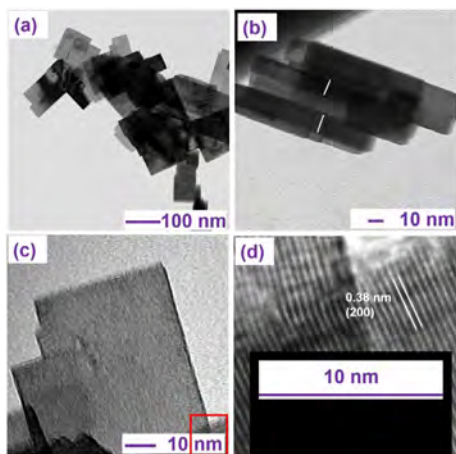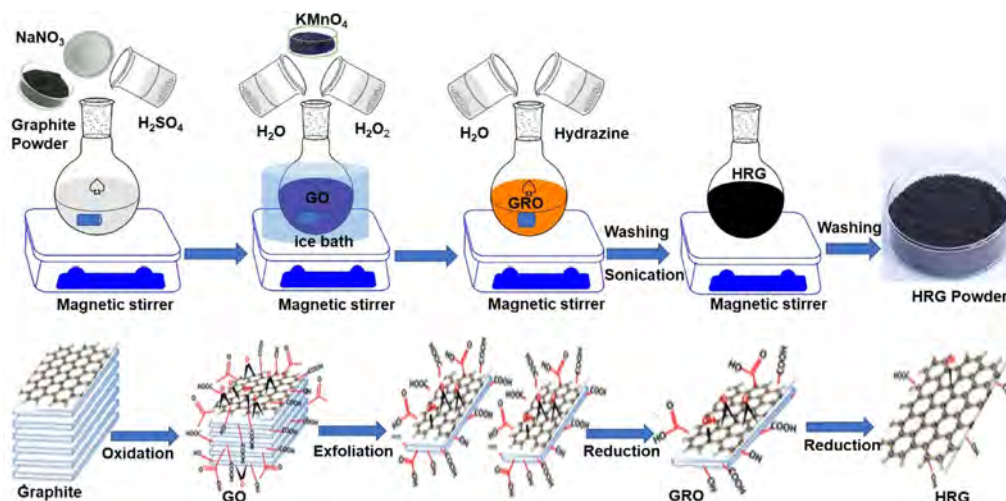
analysis using energy dispersive spectroscopy (EDS), of the m-WO_3 nanoplates confirmed the homogeneity of the product.

Synthesis and characterization of HRG

HRG was prepared as outlined in Figure 4. The crystallinity and phase purity of the as-synthesized HRG were confirmed by X-ray diffractometry. The XRD diffractogram of GP (Figure 5 a) displayed an intensive and narrow reflection at $2\theta = 26.4°$. Similarly, the HRG diffractogram showed a broad reflection at $2\theta = 26.4°$, which corresponds to the (002) reflection that is associated with the stacking of the graphene layers with a d spacing of 0.34 nm. Upon oxidation, different functional groups with oxygen atoms are generated within the carbon nanosheets, leading to an increase of the stacking distance and shift the GRO reflection to a lower Bragg angle ($2\theta = 10.9°$). Similarly, H_2O molecules between the graphene layers lead to an increase (almost twice that of GP) of the GRO d-spacing to 0.79 nm. GRO's main reflection at ($2\theta = 10.9°$) vanished in HRG due to the reduction, indicating a loss of long-range order.

The Raman spectra of GP, GRO, and HRG are presented in Figure 5 b. The GP (black line) spectrum shows a strong G and less intense D bands centered at 1589 cm^{-1} and 1345 cm^{-1}, respectively. After oxidation, GRO showed two bands which were broadened and slightly red-shifted by 10 cm^{-1}. After the reduction of GRO to HRG, the intensity of the D band increased, increasing the relative intensity ratio of the D/G bands. This indicates that the formation of SP^2 domains is more pronounced in HRG compared to GRO, because of the reduction of GRO to HRG.[26] The reduction of GRO to HRG was also confirmed using X-ray photoelectron spectroscopy (XPS). The core-level signals for C 1 s XPS spectrum of HRG, (Figure S2) shows four peaks corresponding to the four different carbon bonds. The strong peak centered at 284.8 eV correspond to the sp^2 carbon that is, C=C bond in graphene Skelton.[70–73] The peaks located at a position approximately 285.9 eV and 289 eV, are due to the C–O bond and C=O bond, respectively. The significant decrease in the peak intensities related to oxygen containing

Figure 3. Transmission electron microscopy (images) of as synthesis WO_3 nanoplates; (a) overview TEM image, (b) some of the image lying on the lateral axis which also shows the thickness of the nanoplates, and (c & d) corresponding HRTEM images confirming the d-spacing of 0.38 nm related to the (200) crystal plane of m-WO_3.

Figure 4. Synthetic Scheme for the oxidation of graphite powder and reduction of GO to GRO and HRG.

Chemistry–A European Journal

Full Paper
doi.org/10.1002/chem.202005156

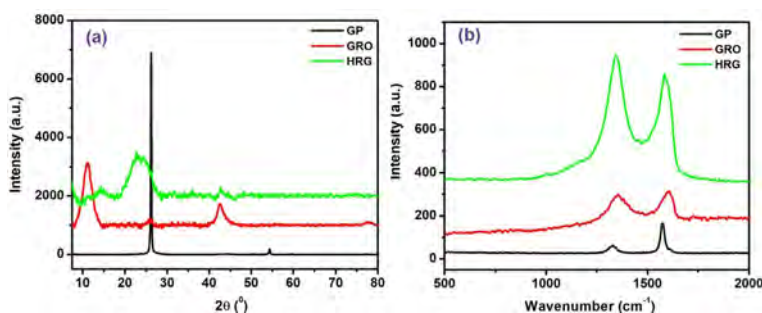**Chemistry Europe**
European Chemical
Societies Publishing

Figure 5. (a) XRD diffractograms and (b) Raman spectra of GP (black line), GRO (red line), and HRG (green line).

functional groups in C 1 s spectrum, indicate considerable reduction.

The surface topology and layering nature of HRG were confirmed by FESEM and transmission electron microscopy (TEM). The FESEM micrograph (Figure 6a) revealed the layered structure of HRG. Likewise, the TEM image (Figure 6b) suggests
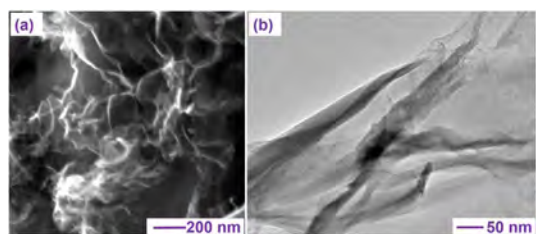

Figure 6. (a) FESEM and (b) TEM images of as-prepared HRG sheets.

that HRG contains graphene sheets that are only a few layers thick.

Electrochemical performance of HRG and m-WO₃ electrodes

The electrochemical performance of the HRG and m-WO$_3$ electrodes was evaluated individually with a three-electrode electrochemical cell in aqueous electrolyte, containing 1 M H$_2$SO$_4$ at various scan rates and OPWs. The CV curves of HRG electrode were recorded at different scan rates from 20–100 mV s^{-1} within an OPW from 0.0 to 1.0 V (vs. Ag/AgCl) (Figure 7a). The HRG electrode exhibited a capacitance behavior with CV curves of symmetrical quasi-rectangular shape due to the pure EDLC behavior, which is characteristic of a good reversible supercapacitor performance.[74] These results indicate fast ion diffusion and rapid transport during charging and discharging with a fast-current response to the change of potential from 0.0 to 1.0 V (vs. Ag/AgCl). In addition, the current densities and
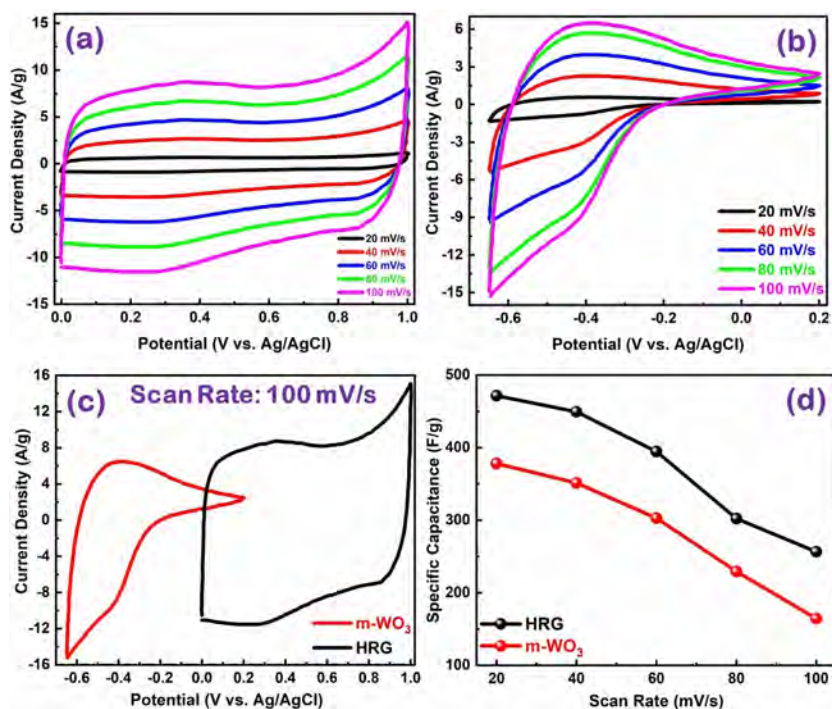

Figure 7. Electrochemical performance of the electrodes in the three-electrode system. CV curves of (a) HRG and (b) m-WO$_3$ electrodes at scan rates of 20, 40, 60, 80, and 100 mV s^{-1}, (c) comparative CV curves of HRG and m-WO$_3$ electrodes at a scan rate of 100 mV s^{-1}, and (d) specific capacitances calculated for each electrode in 1 M H$_2$SO$_4$ at different scan rates.

Chemistry–A European Journal

Full Paper
doi.org/10.1002/chem.202005156

Chemistry Europe
European Chemical
Societies Publishing

the area under the corresponding CV curves increased with increasing scan rate in order to keep C_{sp} constant. Equation (1) was used to calculate the C_{sp} values of HRG electrode at scan rates of 20, 40, 60, 80, and 100 mV s^{-1} leading to C_{sp} values of 472, 449, 395, 302, and 256 F g^{-1}, respectively.

To study the electrochemical performance of the m-WO$_3$ electrode, CV measurements were conducted in the aqueous electrolyte of 1 M H$_2$SO$_4$, using a three-electrode electrochemical system. Figure 7b indicates the CV curves of the m-WO$_3$ electrode at different scan rates from 20 to 100 mV s^{-1} over an OPW from -0.65 to 0.2 V. The CV curves of the m-WO$_3$ electrode exhibit characteristics redox peaks of m-WO$_3$ at around -0.41 V of the cathodic scan and -0.36 V of the anodic scan.[75,76] These redox peaks may be attributed to the reversible intercalation/deintercalation of H$^+$ ions into/out of the m-WO$_3$ structure during the charge (H$^+$ intercalation) and discharge (H$^+$ deintercalation) process (Equation (7)).[76]

$$WO_3 \cdot yH_2O + xH^+ \underset{\text{discharging}}{\overset{\text{charging}}{\rightleftharpoons}} H_xWO_3 \cdot yH_2O \tag{7}$$
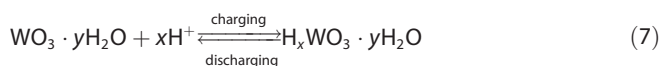
The current densities increased with increasing scan rates, and the anodic peaks were shifted to higher voltages in the applied OPW. Likewise, the cathodic peaks shifted to lower voltages. This shows the excellent electrochemical performance of the m-WO$_3$ electrode with a pseudocapacitance behavior. The C_{sp} of the m-WO$_3$ electrode was determined from the CV curves with equation 1, and the acquired C_{sp} values were 378, 351, 303, 229, and 164 F g^{-1} at scan rates of 20, 40, 60, 80, and 100 mV s^{-1}, respectively.

The CV performance of the HRG and m-WO$_3$ electrodes was analyzed in 1 M H$_2$SO$_4$ to assess the appropriate OPW of the negative and positive electrodes before the evaluation of the HRG//m-WO$_3$ ASC. The CV performance was in line with each electrode's behavior at a scan rate of 100 mV s^{-1} (Figure 7c). The HRG electrode exhibited a stable OPW between 0 and 1.0 V while the m-WO$_3$ electrode displayed a stable OPW between -0.65 and 0.2 V. Therefore, we estimated that the OPW might be extended to approximately 1.6 V after assembling both electrodes as HRG//m-WO$_3$ ASC. Likewise, the oxidation peak in the CV related to m-WO$_3$ electrode at around -0.4 V (vs. Ag/AgCl) represent its pseudocapacitance behavior and could be attributed to the H$^+$ insertion/storage in nanostructured m-WO$_3$ and also responsible for the reduction of W^{6+} and W^{5+}.[75,76] The small reduction peak in the CV of HRG at around 0.3 V may be attributed the irreversible reactions of oxygen functional groups attached to the HRG. Figure 7d shows the relationship between the specific capacitance and CV scan rate. The specific capacitance for both electrodes decreased with increasing CV scan rate. The lower values of the specific capacitance at high CV scan rates may be due to the slower ion diffusion at the electrode surface.

GCD measurements were performed to study the charge/discharge rate performance of HRG and m-WO$_3$ electrodes in a three-electrode system in 1 M H$_2$SO$_4$. The GCD profiles of the HRG electrode were studied at different current-densities, ranging from 0.5 to 5.0 A g^{-1} in an OPW and from 0.0 to 1.0 V (vs. Ag/AgCl) as shown in Figure 8a. All GCD curves are symmetric, corresponding to the typical pattern of a carbon-based capacitor. Similarly, the GCD curves of HRG electrode show good linearity with nearly isosceles-triangular behavior, which confirms their EDLC behavior.[77] The C_{sp} of the HRG electrode at different current densities were extracted from the GCD profiles
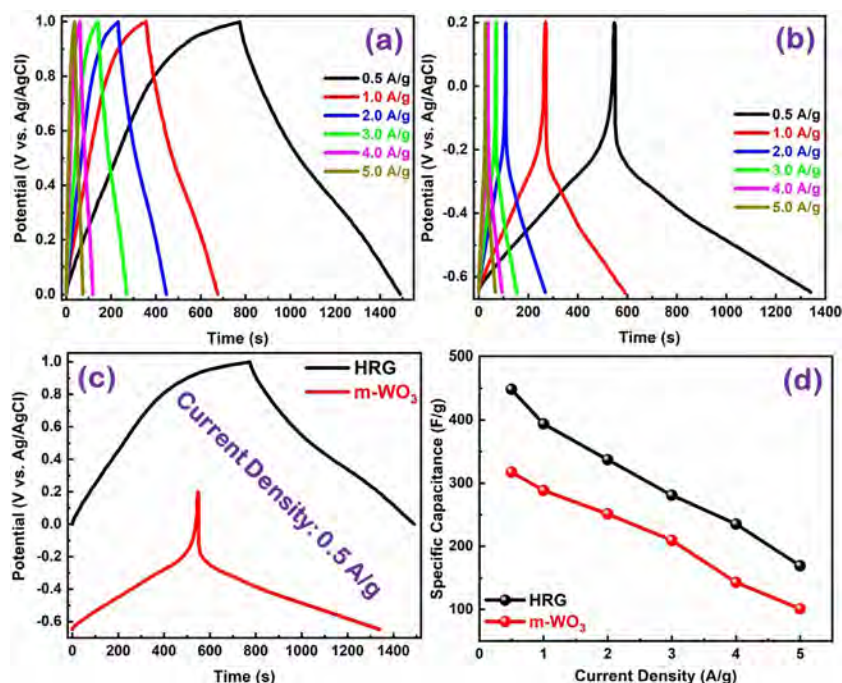
Figure 8. Electrochemical performance of HRG and m-WO$_3$ electrodes in a three-electrode setup. GCD profiles of (a) HRG and (b) m-WO$_3$ electrodes at current densities of 0.5, 1.0, 2.0, 3.0, 4.0, and 5.0 A g^{-1}). (c) Comparative GCD profiles of HRG and m-WO$_3$ electrodes measured at a current density of 0.5 A g^{-1} and (d) C_{sp} measured at different current densities for each electrode in 1 M H$_2$SO$_4$.

68

Chem. Eur. J. **2021**, *27*, 6973 – 6984   **www.chemeurj.org**

© 2021 Wiley-VCH GmbH

Chemistry–A European Journal

Full Paper
doi.org/10.1002/chem.202005156

**Chemistry
Europe**
European Chemical
Societies Publishing

using Equation (2). The HRG electrode exhibited a C_{sp} within the range from 448 F g^{-1} to 169 F g^{-1} at current densities of 0.5–5.0 A g^{-1} (Figure 8 a). Likewise, GCD curves of m-WO$_3$ electrode (Figure 8 b) at different current densities from 0.5 to 5.0 A g^{-1} in the OPW and from -0.65 to 0.2 V showed non-linearities owing to the pseudocapacitive behavior. In addition, the GCD profiles displayed plateau regions in the OPW range > -0.18 V. This, in turn, was in agreement with the observed decrease of the current densities at higher redox potentials in the CV curves (Figure 7 b). The C_{sp} calculated from Equation (2) based on the discharge profiles ranged between 317 F g^{-1} and 101 F g^{-1} at current densities between 0.5 and 5.0 A g^{-1}. To identify the optimum working OPW prior to the setup of the HRG//m-WO$_3$ ASC, separate GCD measurements of HRG and m-WO$_3$ electrodes were compared (recorded at 0.5 A g^{-1}, Figure 8 c). As the HRG and m-WO$_3$ electrodes have stable OPWs from 0.0 to 1.0 V and -0.65 to 0.2 V, respectively, one could anticipate a maximum OPW for HRG//m-WO$_3$ ASC cell of up to 1.6 V.[67]

One of the most appealing characteristics of supercapacitors is their capacity to operate at high current densities. A comparison of the specific capacitances measured at different current densities for the electrodes is illustrated in Figure 8 d. Although the specific capacitances decreased with increasing current densities, high specific capacitances with enhanced charge and discharge times compared to most established systems (Table 2) were achieved for both HRG and m-WO$_3$ electrodes, indicating superior capacitance performance.

Electrochemical performance of HRG//m-WO$_3$ ASC

To further assess the HRG and m-WO$_3$ electrodes supercapacitor performance in 1 M H$_2$SO$_4$, an HRG//m-WO$_3$ ASC was fabricated with m-WO$_3$ as negative and HRG as a positive electrode. The ASC revealed OPWs between 0.0 and 1.0 V and between -0.65 and 0.2 V, which is in accordance with the expected OPW of 1.6 V for the HRG//m-WO$_3$ ASC.[67] These results are in agreement with CV and GCD measurements of the single electrodes (Figure 7). Therefore, the HRG//m-WO$_3$ ASC was tested in an OPW from 0.0 to 1.6 V. The width of the OPW for two-electrode system is matched by the OPW for the three-electrode system. CV measurements of the HRG//m-WO$_3$ ASC were performed at scan rates between 20 and 100 mV s^{-1} (Figure 9 a). The CV curves show a symmetric rectangular behavior compatible with Faradaic pseudocapacitance behavior and an ideal and fast charge/discharge capacitive performance. Moreover, the CV curves revealed redox peaks in the OPW, ranging from 0.1 to 0.5 V and verified the pseudocapacitor performance of the m-WO$_3$ electrode. The specific capacitances were extracted from the CV measurements of the HRG//m-WO$_3$ ASC using Equation (3). The specific capacitances were 426, 412, 377, 286, and 190 F g^{-1} for scan rates of 20, 40, 60, 80, and 100 mV s^{-1}, respectively. Similarly, the current densities and the areas under the CV curve increased with increasing scan rate (required to keep C_{sp} values constant). The reversibility and stable OPW of the HRG//m-WO$_3$ ASC were tested in different OPWs between 1.0 and 1.8 V at a scan rate of 20 mV s^{-1}. The OPW of the HRG//m-WO$_3$ ASC may be extended to 1.8 V due to the combination of an EDLC and a pseudocapacitor electrode (Figure 9 b). The HRG//m-WO$_3$ ASC shows a typical
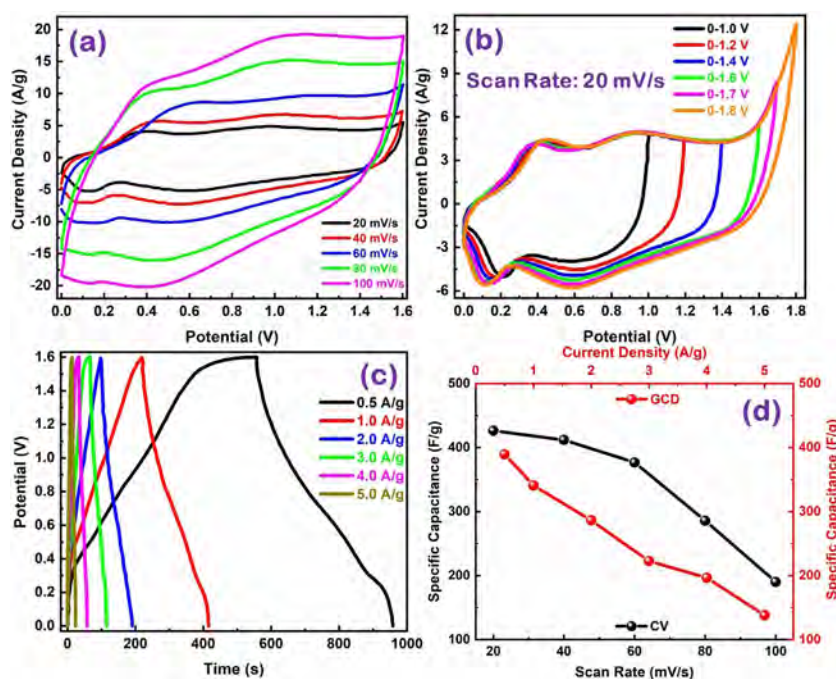
Figure 9. Electrochemical performance of HRG//m-WO$_3$ ASC. (a) CV curves at scan rates of 20, 40, 60, 80, and 100 mV s^{-1} tested in a maximum OPW between 0.0 and 1.6 V. (b) CV curves at constant (20 mV s^{-1}) scan rate with increasing OPWs between 1.0 and 1.8 V. (c) GCD profiles measured at different current densities, and (d) C_{sp} vs. scan rate (extracted from the CV curves) and current density (extracted from the GCD profiles).

Chemistry–A European Journal

Full Paper
doi.org/10.1002/chem.202005156

Chemistry Europe
European Chemical
Societies Publishing

capacitive behavior in all OPWs from 1.0 V to 1.6 V, with quasi-rectangular CV curves, compatible with an ideal capacitance performance with good reversibility. The current densities were strongly enhanced when the OPW was raised to values > 1.6 V owing to electrolyte decomposition coupled with hydrogen/oxygen evolution reactions. Therefore, the optimum stable OPW for a supercapacitor performance of HRG//m-WO$_3$ ASC is in the range between 0.0 and 1.6 V.

The supercapacitor evaluation of HRG//m-WO$_3$ ASC was assessed by the GCD technique at different current densities between 0.5 and 5.0 A g^{-1} in an OPW from 0.0 to 1.6 V (Figure 9 c). All GCD profiles show electrochemical reversibility and EDLC behavior in addition to a fast redox reaction at the electrode surface, indicating excellent capacitive performance for HRG//m-WO$_3$ ASC.

The plateau region validated the pseudocapacitor performance of the m-WO$_3$ electrode in the GCD profiles (Figure 9 c). Fast redox reactions occur due to charge transfer and the formation of an EDL at the EEI. Specific capacitances were calculated from the GCD profiles of HRG//m-WO$_3$ ASC using Equation (4). The C_{sp} values ranged from 389 F g^{-1} to 138 F g^{-1} at current densities between 0.5 and 5.0 A g^{-1}. During the GCD cycle, the electrical potential difference between the two ends of a conducting phase is called IR drop (V$_{drop}$).[78] A very small IR drop can be seen in the HRG//m-WO$_3$ ASC, which can be attributed to the low charge transfer resistance value (0.35 Ω, measured from the Nyquist plot), a key consideration for high power applications.[79] Figure 9 d presents the C_{sp} values as a function of scan rate (measured from the CV curves) and current-densities (measured from the GCD profiles) for HRG//m-WO$_3$ ASC. The C_{sp} values increase with increasing scan rate and current density because the time for charges to migrate through the electrodes (which leads to a lower capacitance) is not sufficient. Therefore, decreasing current density or scan rate may allow electrolyte ions to easily penetrate the electrodes, make better contact with the electrode material's internal surface, and produce higher C_{sp}.[80] Specific capacitance values extracted from GCD and CV measurements are compiled in Table 1.
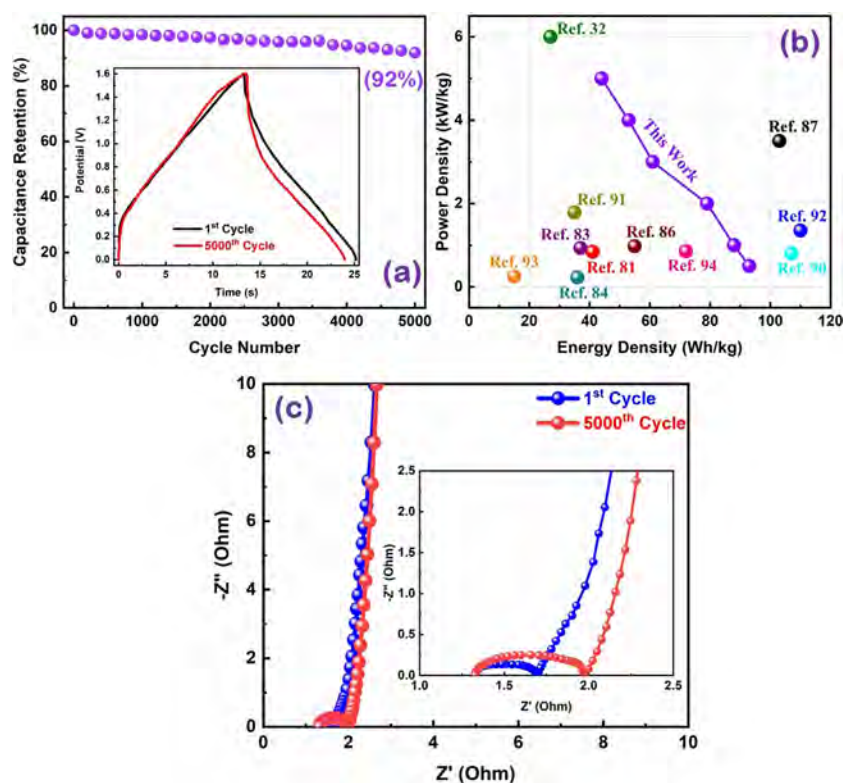
Electrochemical stability and long-term cycling performance are important criteria to evaluate supercapacitor performance for practical applications. The cycling performance of HRG//m-WO$_3$ ASC was tested in a maximum OPW between 0.0 and 1.6 V at a constant current density of 5.0 A g^{-1} for 5000 continuous GCD cycles (Figure 10 a). The C_{sp} at every 200th cycle was calculated and the respective values up to 5000 GCD cycles

are shown in Figure 10 a. The HRG//m-WO$_3$ ASC retained 92 % of its original C_{sp} even after 5000 GCD cycles, demonstrating a very stable charge storage capability. The GCD curves maintained their quasi-triangular shape with almost similar discharge time over 5000 GCD cycles. The 1st and 5000th GCD cycle are displayed in Figure 10 a for comparison.

Energy and power densities are critical factors for the performance of a supercapacitor. They are used in the form of a Ragone plot showing power density as a function of energy density. A Ragone plot comparing HRG//m-WO$_3$ ASC with other asymmetric supercapacitors is shown in Figure 10 b. The energy and power densities of HRG//m-WO$_3$ ASC, calculated from Equation (5) and Equation (6), show a maximum energy density of 93 Wh kg^{-1} for HRG//m-WO$_3$ ASC at a power density of 500 W kg^{-1}. The energy density remained 44 Wh kg^{-1} at a high power density of 5000 W kg^{-1}. The energy and power densities of HRG//m-WO$_3$ ASC are higher than those of most previously reported ASCs (compiled in Table 2). The exceptional supercapacitor performance of HRG//m-WO$_3$ ASC is attributed to the low diffusion resistance and the low charge-transfer resistance (R_{ct}) of the electrodes (determined by EIS). EIS is a valuable tool to determine the electronic conductivity of supercapacitors during the charge–discharge process. EIS was carried out to illustrate the advantages of HRG//m-WO$_3$ ASC. EIS data were recorded in the frequency range from 1.0 Hz to 1.0 MHz at an open-circuit potential of 5 mV impedance amplitude. Figure 10 c shows Nyquist plots of HRG//m-WO$_3$ ASC with an inset to compare EIS plots after the 1st and 5000th cycle. The Nyquist plots contain a semi-circle and a nearly straight line in the high- and low-frequency ranges, respectively. The semi-circle diameter on the abscissa of the Nyquist plot in the high-frequency range of the electrochemical system represents the charge-transfer resistance (R_{ct}).[81] The lower value of R_{ct} indicates a higher transfer or diffusion rate for ions into the electrodes.[82] The intercept of the Nyquist plot on the abscissa at high frequency indicates the equivalent series resistance (ESR) associated with the summation of the electrode material's intrinsic resistances, electrolyte-solution resistance, and contact resistance at the EEI. The R_{ct} values measured from the semi-circle diameter were 0.35 and 0.62 Ohm after the 1st and 5000th cycle, respectively. While the straight line at lower frequency represents the electrolyte ions' diffusion behavior in the electrode, the vertical curve acquired in the low-frequency range is associated with the ideal capacitance behavior along with a faster diffusion of electrolyte ions into the electrode.[82]

Table 1. The specific capacitances of the HRG electrode, the m-WO$_3$ electrode, and the HRG//m-WO$_3$ ASC, measured at different scan rates (from CV curves) and current-densities (from GCD profiles).

Scan Rate (mV/s)	Specific Capacitance (F/g)			Current Density (A/g)	Specific Capacitance (F/g)		
	HRG electrode	m-WO$_3$ electrode	HRG//m-WO$_3$ ASC		HRG electrode	m-WO$_3$ electrode	HRG//m-WO$_3$ ASC
20	472	378	426	0.5	448	317	389
40	449	351	412	1.0	394	288	341
60	395	303	377	2.0	337	251	286
80	302	229	286	3.0	281	209	223
100	256	164	190	4.0	235	143	197
				5.0	169	101	138

Chemistry–A European Journal

Full Paper
doi.org/10.1002/chem.202005156

Chemistry Europe
European Chemical
Societies Publishing

Figure 10. (a) Long term GCD cycling stability recorded at 5.0 A g^{-1} current density shows 92% stability of C_{sp} after 5000 GCD cycles (inset: GCD profiles of the 1st and 5000th cycle). (b) Ragone plot comparing energy density and power density of HRG//m-WO$_3$ ASC with other reported ASCs. (c) Nyquist plots of the HRG//m-WO$_3$ ASC after the 1st and 5000th cycle (inset: magnified region of the Nyquist plots in the high-frequency range).

Table 2. Comparison of the electrochemical performance of HRG//m-WO$_3$ ASC with previously reported ASCs.

Electrodes	Specific Capacitance (F/g)	Energy Density (Wh/kg)	Power Density (W/kg)	References
rGO/NiSe$_2$//AC	114 (1 A/g)	41	842	[81]
AC//MnMoO$_4$·n H$_2$O	945 (3 A/g)	37	935	[83]
AC//Co$_2$O$_3$@rGO	636 (1 A/g)	36	225	[84]
AC//MnOOH@rGO	116 (0.5 A/g)	41	400	[85]
Ni@rGO@Co$_3$S$_4$//Ni@rGO@sNi$_3$S$_2$	940 (1.5 A/g)	55	975	[86]
Ni(OH)$_2$@SiC@NiCo$_2$O$_4$//SiC@Fe$_2$O$_3$	712 (2 A/g)	103	3500	[87]
MnO$_2$/CNFs//CNFs	294 (0.5 A/g)	35	497	[88]
Ni(OH)$_2$@MoSe$_2$//AC	1175 (1 A/g)	43	8181	[89]
NF@MnMoO$_4$//AC	302 (1 A/g)	107	801	[90]
AC//Graphene@WO$_3$	465 (1 A/g)	27	6000	[32]
CoNi-LDH//AC	2616 (1 A/g)	35	1785	[91]
Na-FG-CC//C@Mn$_3$O$_4$-CC	318 (0.5 A/g)	110	1352	[92]
CAC/PANI//WO$_3$	597 (1 A/g)	15	252	[93]
NF@NiMoO$_4$@C//AC	201.3 (0.5 A/g)	72	852	[94]
HRG//m-WO$_3$	389 (0.5 A/g)	93	500	this Work

Conclusions

We have developed a new, simple, and effective approach to prepare highly efficient electrode materials that can be assembled directly into high-performance supercapacitors from m-WO$_3$ (acting as a negative electrode) and HRG (acting as a positive electrode). The HRG//m-WO$_3$ ASC showed superior electrochemical supercapacitor performance in an extensive OPW range of 0.0 to 1.6 V and demonstrated a maximum specific capacitance of 389 F g^{-1} at 0.5 A g^{-1}. A higher energy density of 93 Wh kg^{-1} was achieved at a power density of 500 W kg^{-1}, which remained at 44 Wh kg^{-1} with a 5000 W kg^{-1} power density. Moreover, the ASC showed outstanding cycling-stability by retaining 92% of its original C_{sp} value even after 5000 GCD cycles. The m-WO$_3$ and HRG-based electrodes provide a platform for the fabrication of high-performance ASC for efficient EESDs. The main finding is that the HRG and m-WO$_3$ are stable enough to be used as effective electrodes in supercapacitors for the growing requirements of high-performance and low-cost future generations of EESDs.

Author Contributions

M.A. and S.S.S. designed the project; M.A., Z.L. and M.K. carried out the preparation of electrode materials; S.F.A. helped with microscopy; I.K., M.U. and S.S.S. fabricated the devices and carried electrochemical characterizations; N.U. helped with characterizations and to draft the manuscript; M.A.A., W.T. and M.N.T. provided scientific guidance and wrote the paper. All authors read and approved the final manuscript.

Acknowledgements

Conflict of interest

The authors declare no conflict of interest.

[1] S. A. Khan, S. Ali, K. Saeed, M. Usman, I. Khan, *J. Mater. Chem. A* **2019**, *7*, 10159 – 10173.
[2] M. Dresselhaus, I. Thomas, *Nature* **2001**, *414*, 332 – 337.
[3] M. D. Garba, M. Usman, S. Khan, F. Shehzad, A. Galadima, M. F. Ehsan, A. S. Ghanem, M. Humayun, *J. Environ. Chem. Eng.* **2021**, *9*, 104756.
[4] M. Ashraf, I. Khan, M. Usman, A. Khan, S. S. Shah, A. Z. Khan, K. Saeed, M. Yaseen, M. F. Ehsan, M. N. Tahir, N. Ullah, *Chem. Res. Toxicol.* **2020**, *33*, 1292 – 1311.
[5] M. Usman, M. Ali, B. A. Al-Maythalony, A. S. Ghanem, O. W. Saadi, M. Ali, M. A. Jafar Mazumder, S. Abdel-Azeim, M. A. Habib, Z. H. Yamani, W. Ensinger, *ACS Appl. Mater. Interfaces* **2020**, *12*, 49992 – 50001.
[6] S. S. Shah, M. A. Alfasane, I. A. Bakare, M. A. Aziz, Z. H. Yamani, *J. Energy Storage* **2020**, *30*, 101562.
[7] V. Khare, S. Nema, P. Baredar, *Renewable Sustainable Energy Rev.* **2016**, *58*, 23 – 33.
[8] T. Janoschka, M. D. Hager, U. S. Schubert, *Adv. Mater.* **2012**, *24*, 6397 – 6409.
[9] L. Yaqoob, T. Noor, N. Iqbal, H. Nasir, M. Sohail, N. Zaman, M. Usman, *Renew. Energy* **2020**, *156*, 1040 – 1054.
[10] I. Khan, N. Baig, S. Ali, M. Usman, S. A. Khan, K. Saeed, *Energy Storage Mater.* **2021**, *35*, 443 – 469.
[11] X. Wang, C. Yan, A. Sumboja, P. S. Lee, *Nano Energy* **2014**, *3*, 119 – 126.
[12] W. Tian, X. Wang, C. Zhi, T. Zhai, D. Liu, C. Zhang, D. Golberg, Y. Bando, *Nano Energy* **2013**, *2*, 754 – 763.
[13] Y. Shao, M. F. El-Kady, J. Sun, Y. Li, Q. Zhang, M. Zhu, H. Wang, B. Dunn, R. B. Kaner, *Chem. Rev.* **2018**, *118*, 9233 – 9280.
[14] T. Islam, M. M. Hasan, S. S. Shah, M. R. Karim, F. S. Al-Mubaddel, M. H. Zahir, M. A. Dar, M. D. Hossain, M. A. Aziz, A. J. S. Ahammad, *J. Energy Storage* **2020**, *32*, 101908.
[15] C. K. Roy, S. S. Shah, A. H. Reaz, S. Sultana, A.-N. Chowdhury, S. H. Firoz, M. H. Zahir, M. A. A. Qasem, M. A. Aziz, *Chem. Asian J.* **2021**, *16*, 296 – 308.
[16] N. C. Deb Nath, S. S. Shah, M. A. A. Qasem, M. H. Zahir, M. A. Aziz, *ChemistrySelect* **2019**, *4*, 9079 – 9083.
[17] A. M. Abioye, F. N. Ani, *Renewable Sustainable Energy Rev.* **2015**, *52*, 1282 – 1293.
[18] A. Aziz, S. S. Shah, A. Kashem, *Chem. Rec.* **2020**, *20*, 1074 – 1098.
[19] L. L. Zhang, X. Zhao, M. D. Stoller, Y. Zhu, H. Ji, S. Murali, Y. Wu, S. Perales, B. Clevenger, R. S. Ruoff, *Nano Lett.* **2012**, *12*, 1806 – 1812.
[20] M. V. Kiamahalleh, S. H. S. Zein, G. Najafpour, S. A. Sata, S. Buniran, *Nano* **2012**, *7*, 1230002.
[21] V. Barranco, M. Lillo-Rodenas, A. Linares-Solano, A. Oya, F. Pico, J. Ibañez, F. Agullo-Rueda, J. M. Amarilla, J. Rojo, *J. Phys. Chem. C* **2010**, *114*, 10302 – 10307.
[22] E. Mourad, L. Coustan, P. Lannelongue, D. Zigah, A. Mehdi, A. Vioux, S. A. Freunberger, F. Favier, O. Fontaine, *Nat. Mater.* **2017**, *16*, 446 – 453.
[23] M. Zhi, C. Xiang, J. Li, M. Li, N. Wu, *Nanoscale* **2013**, *5*, 72 – 88.
[24] X. Y. Yu, X. W. Lou, *Adv. Energy Mater.* **2018**, *8*, 1701592.
[25] Q. Meng, K. Cai, Y. Chen, L. Chen, *Nano Energy* **2017**, *36*, 268 – 285.
[26] M. Khan, M. N. Tahir, S. F. Adil, H. U. Khan, M. R. H. Siddiqui, A. A. Al-warthan, W. Tremel, *J. Mater. Chem. A* **2015**, *3*, 18753 – 18808.
[27] A. K. Hussein, *Renewable Sustainable Energy Rev.* **2015**, *42*, 460 – 476.
[28] M. N. Tahir, B. Oschmann, D. Buchholz, X. Dou, I. Lieberwirth, M. Panthöfer, W. Tremel, R. Zentel, S. Passerini, *Adv. Energy Mater.* **2016**, *6*, 1501489.
[29] J. Jia, X. D. Liu, X. Li, L. Cao, M. Zhang, B. Wu, X. Zhou, *J. Alloys Compd.* **2020**, *823*, 153715.
[30] R. A. Berner, *Nature* **2003**, *426*, 323 – 326.
[31] Z. Yu, L. Tetard, L. Zhai, J. Thomas, *Energy Environ. Sci.* **2015**, *8*, 702 – 730.
[32] A. K. Nayak, A. K. Das, D. Pradhan, *ACS Sustainable Chem. Eng.* **2017**, *5*, 10128 – 10138.
[33] H. Zheng, Y. Tachibana, K. Kalantar-Zadeh, *Langmuir* **2010**, *26*, 19148 – 19152.
[34] W.-J. Li, Z.-W. Fu, *Appl. Surf. Sci.* **2010**, *256*, 2447 – 2452.
[35] M. A. Lange, Y. Krysiak, J. Hartmann, G. Dewald, G. Cerretti, M. N. Tahir, M. Panthöfer, B. Barton, T. Reich, W. G. Zeier, *Adv. Funct. Mater.* **2020**, *30*, 1909051.
[36] J. Ma, Y. Ren, X. Zhou, L. Liu, Y. Zhu, X. Cheng, P. Xu, X. Li, Y. Deng, D. Zhao, *Adv. Funct. Mater.* **2018**, *28*, 1705268.
[37] G. A. Niklasson, C. G. Granqvist, *J. Mater. Chem.* **2007**, *17*, 127 – 156.
[38] S. Yoon, E. Kang, J. K. Kim, C. W. Lee, J. Lee, *Chem. Commun.* **2011**, *47*, 1021 – 1023.
[39] K. Kourosh, Z. Jian, D. Torben, M. Arnan, S. Takayoshi, S. Michael, *Appl. Mater. Today* **2016**, *5*, 73 – 89.
[40] M. Qiu, P. Sun, L. Shen, K. Wang, S. Song, X. Yu, S. Tan, C. Zhao, W. Mai, *J. Mater. Chem. A* **2016**, *4*, 7266 – 7273.
[41] J. E. ten Elshof, H. Yuan, P. Gonzalez Rodriguez, *Adv. Energy Mater.* **2016**, *6*, 1600355.
[42] X. Wu, S. Yao, *Nano Energy* **2017**, *42*, 143 – 150.
[43] L. Gao, X. Wang, Z. Xie, W. Song, L. Wang, X. Wu, F. Qu, D. Chen, G. Shen, *J. Mater. Chem. A* **2013**, *1*, 7167 – 7173.
[44] D. Chen, L. Gao, A. Yasumori, K. Kuroda, Y. Sugahara, *Small* **2008**, *4*, 1813 – 1822.
[45] S. O. Adio, S. A. Ganiyu, M. Usman, I. Abdulazeez, K. Alhooshani, *Chem. Eng. J.* **2020**, *382*, 122964.
[46] A. C. Ferrari, F. Bonaccorso, V. Fal'Ko, K. S. Novoselov, S. Roche, P. Bøggild, S. Borini, F. H. Koppens, V. Palermo, N. Pugno, *Nanoscale* **2015**, *7*, 4598 – 4810.
[47] A. Peigney, C. Laurent, E. Flahaut, R. Bacsa, A. Rousset, *Carbon* **2001**, *39*, 507 – 514.
[48] C. Liu, Z. Yu, D. Neff, A. Zhamu, B. Z. Jang, *Nano Lett.* **2010**, *10*, 4863 – 4868.
[49] Z.-S. Wu, W. Ren, L. Gao, J. Zhao, Z. Chen, B. Liu, D. Tang, B. Yu, C. Jiang, H.-M. Cheng, *ACS Nano* **2009**, *3*, 411 – 417.
[50] C. Li, X. Zhang, K. Wang, X. Sun, G. Liu, J. Li, H. Tian, J. Li, Y. Ma, *Adv. Mater.* **2017**, *29*, 1604690.
[51] R. R. Nair, P. Blake, A. N. Grigorenko, K. S. Novoselov, T. J. Booth, T. Stauber, N. M. Peres, A. K. Geim, *Science* **2008**, *320*, 1308.
[52] C. Lee, X. Wei, J. W. Kysar, J. Hone, *Science* **2008**, *321*, 385 – 388.
[53] Z. Huang, T. Wang, H. Song, X. Li, G. Liang, D. Wang, Q. Yang, Z. Chen, L. Ma, Z. Liu, B. Gao, J. Fan, C. Zhi, *Angew. Chem. Int. Ed.* **2021**, *60*, 1011 – 1021.
[54] Z. Huang, A. Chen, F. Mo, G. Liang, X. Li, Q. Yang, Y. Guo, Z. Chen, Q. Li, B. Dong, C. Zhi, *Adv. Energy Mater.* **2020**, *10*, 2001024.
[55] Y. Zhu, S. Murali, W. Cai, X. Li, J. W. Suk, J. R. Potts, R. S. Ruoff, *Adv. Mater.* **2010**, *22*, 3906 – 3924.
[56] V. Skákalová, V. Vretenár, Ľ. Kopera, P. Kotrusz, C. Mangler, M. Meško, J. C. Meyer, M. Hulman, *Carbon* **2014**, *72*, 224 – 232.

[57] B. Lobato, V. Vretenár, P. Kotrusz, M. Hulman, T. A. Centeno, *J. Colloid Interface Sci.* **2015**, *446*, 203–207.

[58] H. Feng, R. Cheng, X. Zhao, X. Duan, J. Li, *Nat. Commun.* **2013**, *4*, 1539.

[59] B. G. Choi, S.-J. Chang, H.-W. Kang, C. P. Park, H. J. Kim, W. H. Hong, S. Lee, Y. S. Huh, *Nanoscale* **2012**, *4*, 4983–4988.

[60] S. William, J. Hummers, R. E. Offeman, *J. Am. Chem. Soc.* **1958**, *80*, 1339.

[61] M. Khan, M. R. Shaik, S. F. Adil, M. Kuniyil, M. Ashraf, H. Frerichs, M. A. Sarif, M. R. H. Siddiqui, A. Al-Warthan, J. P. Labis, *Sci. Rep.* **2020**, *10*, 11728.

[62] A. K. Mohamedkhair, M. A. Aziz, S. S. Shah, M. N. Shaikh, A. K. Jamil, M. A. A. Qasem, I. A. Buliyaminu, Z. H. Yamani, *Arab. J. Chem.* **2020**, *13*, 6161–6173.

[63] M. Grundy, Z. Ye, *J. Mater. Chem. A* **2014**, *2*, 20316–20330.

[64] Y. Cheng, B. Li, Z. Wei, Y. Wang, D. Wei, D. Jia, Y. Feng, Y. Zhou, *J. Power Sources* **2020**, *451*, 227775.

[65] L.-Q. Mai, A. Minhas-Khan, X. Tian, K. M. Hercule, Y.-L. Zhao, X. Lin, X. Xu, *Nat. Commun.* **2013**, *4*, 2923.

[66] P. M. Shafi, V. Ganesh, A. C. Bose, *ACS Appl. Energy Mater.* **2018**, *1*, 2802–2812.

[67] J. Y. Hwang, M. F. El-Kady, Y. Wang, L. Wang, Y. Shao, K. Marsh, J. M. Ko, R. B. Kaner, *Nano Energy* **2015**, *18*, 57–70.

[68] H. Wang, H. Yi, X. Chen, X. Wang, *J. Mater. Chem. A* **2014**, *2*, 3223–3230.

[69] C. Long, Q. Li, Y. Li, Y. Liu, A. Li, Q. Zhang, *Chem. Eng. J.* **2010**, *160*, 723–728.

[70] M. Khan, A. H. Al-Marri, M. Khan, N. Mohri, S. F. Adil, A. Al-Warthan, M. R. H. Siddiqui, H. Z. Alkhathlan, R. Berger, W. Tremel, M. N. Tahir, *RSC Adv.* **2014**, *4*, 24119–24125.

[71] C. Wang, J. Zhou, J. Ni, Y. Cheng, H. Li, *Chem. Eng. J.* **2014**, *253*, 130–137.

[72] Y. Xu, K. Sheng, C. Li, G. Shi, *ACS Nano* **2010**, *4*, 4324–4330.

[73] C. Wang, J. Zhou, F. Du, *J. Nanomater.* **2016**, 4840301.

[74] J.-S. M. Lee, M. E. Briggs, C.-C. Hu, A. I. Cooper, *Nano Energy* **2018**, *46*, 277–289.

[75] H. Qu, X. Zhang, H. Zhang, Y. Tian, N. Li, H. Lv, S. Hou, X. Li, J. Zhao, Y. Li, *Sol. Energy Mater. Sol. Cells* **2017**, *163*, 23–30.

[76] H. Farsi, F. Gobal, Z. Barzgari, *Ionics* **2013**, *19*, 287–294.

[77] Z. Ren, J. Li, Y. Ren, S. Wang, Y. Qiu, J. Yu, *Sci. Rep.* **2016**, *6*, 20021.

[78] X. Zhong, J. Tang, L. Cao, W. Kong, Z. Sun, H. Cheng, Z. Lu, H. Pan, B. Xu, *Electrochim. Acta* **2017**, *244*, 112–118.

[79] B. Hsia, M. S. Kim, C. Carraro, R. Maboudian, *J. Mater. Chem. A* **2013**, *1*, 10518–10523.

[80] A. B. Fuertes, F. Pico, J. M. Rojo, *J. Power Sources* **2004**, *133*, 329–336.

[81] Y. Gu, L.-Q. Fan, J.-L. Huang, C.-L. Geng, J.-M. Lin, M.-L. Huang, Y.-F. Huang, J.-H. Wu, *J. Power Sources* **2019**, *425*, 60–68.

[82] R. Vellacheri, A. Al-Haddad, H. Zhao, W. Wang, C. Wang, Y. Lei, *Nano Energy* **2014**, *8*, 231–237.

[83] X. Mu, Y. Zhang, H. Wang, B. Huang, P. Sun, T. Chen, J. Zhou, E. Xie, Z. Zhang, *Electrochim. Acta* **2016**, *211*, 217–224.

[84] L.-J. Xie, J.-F. Wu, C.-M. Chen, C.-M. Zhang, L. Wan, J.-L. Wang, Q.-Q. Kong, C.-X. Lv, K.-X. Li, G.-H. Sun, *J. Power Sources* **2013**, *242*, 148–156.

[85] Y. Cao, Y. Xiao, Y. Gong, C. Wang, F. Li, *Electrochim. Acta* **2014**, *127*, 200–207.

[86] D. Ghosh, C. K. Das, *ACS Appl. Mater. Interfaces* **2015**, *7*, 1122–1131.

[87] J. Zhao, Z. Li, X. Yuan, Z. Yang, M. Zhang, A. Meng, Q. Li, *Adv. Energy Mater.* **2018**, *8*, 1702787.

[88] P. Zhao, M. Yao, H. Ren, N. Wang, S. Komarneni, *Appl. Surf. Sci.* **2019**, *463*, 931–938.

[89] B. Kirubasankar, P. Palanisamy, S. Arunachalam, V. Murugadoss, S. Angaiah, *Chem. Eng. J.* **2019**, *355*, 881–890.

[90] Z. Xu, S. Sun, Y. Han, Z. Wei, Y. Cheng, S. Yin, W. Cui, *ACS Appl. Energy Mater.* **2020**, *3*, 5393–5404.

[91] L.-j. Xie, G.-h. Sun, L.-f. Xie, F.-Y. Su, X.-m. Li, Z. Liu, Q.-q. Kong, C.-X. Lu, K. − x. Li, C.-m. Chen, *New Carbon Mater.* **2016**, 31, 37–45.

[92] X. Wu, B. Huang, Q. Wang, Y. Wang, *J. Mater. Chem. A* **2019**, *7*, 19017–19025.

[93] H. Wang, G. Ma, Y. Tong, Z. Yang, *Ionics* **2018**, *24*, 3123–3131.

[94] Z. Wang, G. Wei, K. Du, X. Zhao, M. Liu, S. Wang, Y. Zhou, C. An, J. Zhang, *ACS Sustainable Chem. Eng.* **2017**, *5*, 5964–5971.